

**THERMAL AND MECHANICAL PROPERTIES OF INDIVIDUAL
POLYMER NANOFIBERS**

Submitted in partial fulfillment of the requirements for

the degree of

Doctor of Philosophy

in

Mechanical Engineering

Ramesh Shrestha

B.S., Physics, Southeastern Louisiana University

M.S., Mechanical Engineering, Carnegie Mellon University

Carnegie Mellon University
Pittsburgh, PA

August 2018

© Ramesh Shrestha, 2018
All Rights Reserved

ACKNOWLEDGMENTS

I would like to thank my Ph.D. co-advisers Prof. Maarten P. de Boer (Committee chair) and Prof. Sheng Shen for giving me the opportunity to join their research group. I am forever indebted to both of you for your patience and energy to explain me the scientific process, introduce me to the topics of nanomechanics and nanoscale heat transfer and your insightful comments that guided the course of my Ph.D.

I express gratitude to my thesis committee members Prof. Ioannis Chasiotis and Prof. Michael R. Bockstaller for their valuable comments and feedback on my work. I would also like to acknowledge my close collaborators Prof. Tengfei Luo for theoretical insight using MD simulations, Dr. Kedar Hippalgaonkar for providing me with the microthermal device, Prof. Mohammad Naraghi for providing me electrospun PAN nanofiber, Prof. Sukwon Choi for thermorefectance measurements of polyethylene nanofiber and Prof. Renkun Chen for high-temperature polyethylene measurement. I would particularly like to thank Dr. Teng Zhang, Sunmi Shin and Bikram Chatterjee, students of my collaborators, whose dedication and contribution was valuable for the completion of this work.

I would like to acknowledge the staffs of Mechanical engineering department whose help made this thesis work smooth especially John Fulmar, and Ed Wojciechowski for custom building parts in a machine shop and Chris Hertz, Ginny Barry and Bobbi Kostyak for administrative issues. I also thank CMU nanofabrication facility staffs Dr. Matthew T. Moneck, Norman Gottron and James Rosvanis for facilitating my requests in the cleanroom. I am grateful to Dr. Xiao Chuan Ong for training me in cleanroom equipment necessary for my research.

I also thank the funding agency for my research, the US National Science Foundation (NSF) under award CMMI-1334630. I am also thankful to Sandia National lab for fabricating the device which was vital for my research. I am also thankful to GSA/Provost office conference funding which helped me disseminate my research.

I would like to offer my special thanks to Prof. Tzahi Cohen-Karni for giving me access to his lab equipment which was essential for making specimen for my thermal measurements. I also thank Sahil Rastogi and Raghav Garg, doctoral students of Prof. Karni, who have been greatly tolerant to my constant disturbances in the lab.

My deepest appreciation goes to Dr. Sameer Shroff, Dr. Emreacan Soylemez, and Dr. Pengfei Li for training me in mechanical and thermal measurement systems which made this thesis possible. I would like to thank Prof. Elias Towe for giving me access to his micro-Raman system and Dr. Ibrahim Kimukin for training me. I also acknowledge Dr. Jennifer L. Gray for the acquisition of cryogenic transmission electron microscope images.

I am deeply grateful to Dr. Narayan Ramasubramanian for numerous consultations on mechanics and material science. I also thank my colleagues Prince Singh, Allen Changho Oh, Ryan Pocratsky, Longchang Ni, Dr. Francisco Ramirez, Shivang Shekhar, Bowen Yu, Wei Gong, Jiayu Li, Phil Smith, Qian Yang, Yuxuan Luan and Yusuf Mert Senturk whose camaraderie and support has helped me through my Ph.D.

On a personal note, I would like to thank my friends Bijay Tilak Bhattarai, Anuska Shrestha, Samikshya Subedi, Hardik Shah, Giancarlo Incorvaia, Regeant Panday, Judith Brand, Anurag Jhakotia, Krithi Shetty and Prathamesh Kini whose help, support and friendship have made

this journey a joyful one. I would also like to thank all my friends back at home and abroad for their endearing friendship.

I owe special thanks to India Carter for her constant love, warm encouragement, and support. I am eternally indebted to my family who has always shown me unconditional love and support to pursue my goal and aspirations. I dedicate this to my father, mother, brother, and sisters.

Abstract

Polymer nanofibers have garnered significant attention due to their nanoscale size effects. When their diameter is below $\sim 1 \mu\text{m}$, mechanical and thermal properties such as Young's modulus, tensile strength, and thermal conductivity are enhanced by several times to several orders of magnitude. This notable enhancement in the material properties coupled with their intrinsic properties such as low density, chemical resistance, and biocompatibility open applications in tissue engineering, sensors, textiles, composite reinforcements, ballistic armors, thermal management and other areas. The objective of this thesis is to study the thermal, mechanical and thermo-mechanical properties of individual nanofibers and couple the properties with their molecular structure.

Stress-induced crystallization using two-stage tip drawing technique is known to produce highly crystalline and oriented polymer nanofiber. However, it is time-consuming, low yield and lacks consistency. In this thesis, a local stretching technique is developed to produce highly crystalline and oriented polyethylene nanofibers consistently. Microstructure characterization using a transmission electron microscope (TEM) and micro-Raman analysis verified the evolution of microstructure from semi-crystalline to highly crystalline from microfiber to nanofiber.

The thermal transport in PE microfibers and nanofibers was studied using a previously demonstrated suspended micro-thermal device. Temperature-dependent thermal conductivity was measured over a broad temperature range from 20 K to 560 K. PE thermal conductivity increased from the bulk to the microfiber and then to the nanofiber form, consistent with an increase in crystallinity and molecular orientation. The PE nanofiber thermal conductivity increased with increasing temperature following an unusual $\sim T^1$ trend below 100 K, peaked around 130–150 K reaching a metal-like value of $90 \text{ W m}^{-1} \text{ K}^{-1}$, and then decayed as T^{-1} . It was found that thermal

transport in aligned PE chain bundles is highly anisotropic and is dominated by the chain backbone since the inter-chain Van der Waals interactions are much weaker than the covalent bonding along the backbone. The thermal contact resistance between a PE nanofiber and the suspended thermal device was found to be significant. A capillary-induced van der Waal contact method was developed to enhance grip and thermal contact. The experimentally measured thermal contact resistance was found to be consistent with the thermal contact resistance predicted using a line contact model.

A fully reversible thermal switching was discovered at 430 K in crystalline PE nanofibers due to a temperature-induced structural phase transition from the orthorhombic to the hexagonal lattice structure. The phase transition introduces segmental rotational disorder along the chain and leads to a switching factor (i.e., the ratio between on-state high and off-state low thermal conductance values) as high as 10 before and after the phase transition, which exceeds any previously reported experimental values for solid-solid or solid-liquid phase transition of materials. The phase transformation was found to be thermally stable. A high-performance nanoscale thermal diode was fabricated by creating a heterogeneous amorphous-crystalline PE nanofiber junction. A thermal rectification factor of 25 % was achieved, comparable to the existing solid-state nanoscale thermal diodes based on carbon nanotubes, boron nitride nanotubes, graphene and VO₂ nanobeams.

The tensile strength of individual PE nanofiber was tested in tension using a microelectromechanical system (MEMS) based device with an on-chip actuator. Since the crystalline polymer is sensitive to high-energy electron beams, an optical metrology based on sub-pixel pattern matching was employed. In the tensile tests, PE nanofibers could not be firmly gripped using a variety of adhesives because of the low surface energy of PE. Instead, slip

occurred before they were tested to failure. A microscale dog bone shape on a PE nanofiber was fabricated to provide additional grip by mechanical locking. The tensile strength of 11.4 ± 1.1 GPa was obtained for the nanofiber with a diameter of 85 nm. To our knowledge, this is the highest measured tensile strength for any polymer-based fiber including carbon fiber, Zylon, Kevlar and nylon fibers.

Polymer nanofibers exhibit viscoelastic behavior which is both dependent on time and temperature. A variable stress-based creep measurement technique was developed to remove the necessity of the feedback to keep a creep stress constant. From the temperature-dependent creep compliance curves, a master curve spanning 30 years was developed for polyacrylonitrile (PAN) nanofibers. A thin nanofiber (150 nm) exhibited an order of magnitude less creep compared to a thick fiber (250 nm) after 30 years at room temperature. The reduction in creep compliance for the thin fiber was attributed to the increased orientation within the core molecules. After removing the orientation of core PAN molecules by the exposure to high energy electron beam, higher creep compliance than that of the oriented sample was obtained. This was because of the globally lesser orientation of the PAN molecules.

TABLE OF CONTENTS

Acknowledgments	iii
Abstract	vi
List of tables	xiv
List of figures and illustrations	xv
Chapter 1: Introduction	1
1.1 Objectives.....	1
1.2 Organization of the thesis.....	4
1.3 Thesis contributions.....	5
1.4 Chapter references.....	8
Chapter 2: Background and literature review	12
2.1 Introduction.....	12
2.2 Polymer crystallization and drawing.....	12
2.2.1 Polymer crystallization.....	12
2.2.2 Stress-induced crystallization.....	14
2.2.3 Drawing.....	15
2.3 Fabrication of polymer micro/nanofiber.....	17
2.3.1 Gel spinning and Electrospinning.....	17
2.3.2 Two stage tip drawing.....	20
2.4 Thermal transport in polymers.....	22
2.4.1 Thermal enhancement in polymers.....	22
2.4.2 Temperature dependent behavior of crystalline polymer.....	25
2.4.3 Melting of PE.....	26

2.5 Mechanical characterization of polymer nanofiber.....	28
2.5.1 Elastic-plastic behavior of PE fiber.....	28
2.5.2 Viscoelastic behavior of polymer nanofiber.....	32
2.6 Summary.....	33
2.7 Chapter references.....	34

Chapter 3: Fabrication, manipulation and structural characterization of PE

nanofiber.....	44
3.1 Abstract.....	44
3.2 Local heat stretching/Local drawing of PENF.....	44
3.2.1 Fabrication of PENF.....	45
3.2.2 Temperature profile of the PEMF during local drawing.....	49
3.2.3 Estimation of strain rate during local drawing.....	51
3.3 Manipulation of an individual nanofiber.....	52
3.3.1 Sample collector.....	52
3.3.2 Micro heater.....	52
3.3.3 Positioning PENF on the MEMS devices.....	53
3.4 Structural characterization of PENF.....	60
3.4.1 PE powder characterization using DSC.....	61
3.4.2 Micro Raman characterization.....	62
3.4.3 Low-dose cryo-TEM.....	65
3.5 Morphological characterization of PENF.....	68
3.5.1 Diameter measurement and electron beam swelling in PE.....	68
3.5.2 Cross-section of PENFs fabricated by local drawing.....	71
3.5.3 PE Shape of PENF along the length evaluated by SEM.....	72
3.6 Summary.....	73
3.7 Chapter references.....	74

Chapter 4: Crystalline polymer nanofibers with ultra-high thermal conductivity.....77

4.1 Abstract.....77

4.2 Introduction.....77

4.3 Thermal measurement for 1D structures using PRT microthermal device.....78

 4.3.1 Overview of the measurement system.....79

 4.3.2 Electrical and thermal systems.....81

 4.3.3 Thermal conductance and thermal conductivity calculations.....83

4.4 Experimental results and discussion.....84

 4.4.1 Role of thermal contact resistance.....84

 4.4.2 contact width estimation.....86

 4.4.3 Noise equivalent thermal conductance of PRT microthermal device.....88

 4.4.4 Background thermal conductance.....89

 4.4.5 Uncertainty analysis in thermal conductivity.....90

 4.4.6 Thermal transport in crystalline PENF.....93

4.5 Discussion.....98

4.6 Summary.....99

4.7 Chapter references.....99

Chapter 5: Solid-state polyethylene nanofiber thermal switches and diodes using structural phase transition.....103

5.1 Abstract.....103

5.2 Introduction.....104

5.3 High contrast reversible thermal switch.....105

 5.3.1 Reversible thermal switching.....105

 5.3.2 Beyond the *O-H* phase transition: Melting of PENF.....109

5.4 PE thermal diode.....	110
5.5 Thermal contact resistance.....	112
5.7 Summary.....	113
5.8 Chapter references.....	114
Chapter 6: Ultra-high strength of crystalline polyethylene nanofiber.....	116
6.1 Abstract.....	116
6.2 Mechanical measurement of polymer nanofibers.....	116
6.3 Mechanical measurement MEMS platform.....	121
6.3.1 Fabrication.....	121
6.3.2 Stepper motor.....	122
6.3.3 Loadcell.....	124
6.4 Measurement method.....	125
6.4.1 Experimental setup	125
6.4.2 Sub-pixel pattern matching.....	126
6.4.3 Force and displacement measurement on the specimen.....	128
6.4.4 Stress-strain curve.....	129
6.4.5 Test method verification using silica nanofibers.....	129
6.5 Results and discussions.....	133
6.5.1 Overview of samples.....	133
6.5.2 Gripping by mechanical locking using a dog-bone.....	135
6.5.3 Evaluation of glue adhesion and performance of dog-bone.....	137
6.5.4 Ultra-high strength of crystalline PENF.....	138
6.5.5 Error analysis in stress using the nanotractor platform.....	140
6.5.6 SEM of PENF post measurement.....	142
6.5.7 Extreme necking.....	143
6.6 Summary.....	144
6.7 Chapter references.....	145

Chapter 7: Size-dependent creep master curve of electrospun polymer

nanofibers	150
7.1 Abstract.....	150
7.2 Introduction.....	150
7.3 Experimental methods.....	153
7.3.1 Specimen preparation and test platform.....	153
7.3.2 Mechanical test protocols.....	157
7.4 Results.....	166
7.4.1 Size-dependent tensile properties.....	166
7.4.2 Variable creep experiment.....	166
7.5 Summary and concluding remarks.....	171
7.6 Chapter references.....	173

Chapter 8: Summary and future directions.....179

8.1 Summary.....	179
8.2 Future directions.....	183
8.2.1 Thermo-mechanical measurement of a PENF.....	183
8.2.2 Conducting polymer nanofiber.....	184
8.3 Chapter references.....	184

Appendix.....186

A: Sample collector fabrication.....	186
B: Microheater.....	189

List of Tables

Table 3.1: Crystallinity of a PE powder particle from Raman measurements.....	64
Table 6.1: Estimated stiffness of the loadcells.....	125
Table 6.2: Verification of measurement set up using silica nanofibers.....	132

List of Figures and illustrations:

- Figure 2.1:** Hierarchy of polymer crystals a) Orthorhombic unit cell of polyethylene shown in the black box. [3] b) Stacked lamellae interconnected by tie molecules c) Spherulite.....13
- Figure 2.2:** a) Shish-kebab structures clearly seen in the SEM micrograph of PE fiber fabricated by shear-induced crystallization [4]. b) details of the shish-kebab structure where lamellar outgrowths are seen on a central fibrillar fiber. The arrow shows the direction of applied stress. c) grain boundaries on fibril where lamellar outgrowths occur [8].....15
- Figure 2.3:** A Wet spinning process in which polymer solution or gel is extruded through a spinneret and solidified in a coagulating bath. Image from Britannica Inc.....18
- Figure 2.4:** a) Basic electrospinning set up with a flat collector [60]. b) The random mat of polymer nanofibers [61] c) Aligned polymer nanofibers [61].....20
- Figure 2.5:** Schematic of two state tip drawing method [63].....22
- Figure 3.1:** Schematic of fabrication setup of tip drawing.....46
- Figure 3.2:** Schematic of local drawing of PE microfiber (PEMF) to PE nanofiber (PENF). a) Pre-stressed PEMF on sample collector. b) PENF formed on the PEMF using local drawing.....47
- Figure 3.3:** Fabrication of a PE nanofiber (PENF). a) Idealized schematics of localized drawing with a microheater to fabricate PENF from a PE microfiber (PEMF). Arrows indicate drawing directions whereas red lines highlight the defects in PEMF. b-c) Optical micrograph before and after localized drawing (in ©, nanofiber not resolved optically). Scale bars, 20 μm48
- Figure 3.4:** Temperature profile along the heater from ANSYS simulation.....49
- Figure 3.5:** Temperature profile of heater and a PEMF from ANSYS/FLUENT simulation. a) ANSYS/FLUENT simulation temperature map of heater and a PEMF. b) Temperature profile of the PEMF. The maximum temperature of the fiber reaches 450 K ($\sim 180^\circ\text{C}$).....50

Figure 3.6: PEMF undergoing high strain rate elongation. PENF (a) before and (b) after undergoing high strain rate elongation (diameter measured post measurement using Scanning electron microscopy (SEM)).....	51
Figure 3.7: Mounting of a nanofiber onto the Nanotractor using the sample collector. This is performed under an optical microscope using a 20X objective.....	54
Figure 3.8: Nanofiber section is aligned between triangular pads of a nanotractor and pre glued behind one of the pads.....	55
Figure 3.9: PE nanofiber on nanotractor ready for testing. a) fibers were glued onto pads after cutting process b) Zoomed image of the pads after gluing.....	56
Figure 3.10: Optical image of a PE nanofiber sample mounted on the thermal device.....	58
Figure 3.11: Schematics of mounting PE nanofiber onto thermal device. a) suspended platforms of the thermal device. b) a small drop of IPA is placed on the platforms c) after IPA evaporates, micro heater is used to cut the fibers and limit within platforms d) Fiber is conformal to the platform surface as the evaporating IPA pulls the fiber.....	60
Figure 3.12: a) SEM micrograph of PE powder particles. b) DSC curves of heating and cooling of PE powder. The melting point of PE powder is 141 °C. The enthalpy area of melting endotherm from 105 °C to 155 °C is found to be 1743.8 mJ. Scale bar, 100 μm.....	61
Figure 3.13: Micro Raman measurement of PE powder.....	63
Figure 3.14: Raman spectra of a PENF obtained at the same spot.	64
Figure 3.15: Morphological and structural characterizations. a) Micro-Raman spectra of PE powder, PEMF and PENF where the data is normalized to the highest peak of each spectrum. b) Ratio of integral areas of Raman band 1414 cm ⁻¹ to Raman bands 1293 cm ⁻¹ and 1305 cm ⁻¹ vs intensity ratio of Raman bands 1128 cm ⁻¹ to 1060 cm ⁻¹ . c) TEM micrograph of a PENF. d) SAED pattern of the PENF in c) Inset shows the distinct diffraction spots of (200) plane of parent crystal (subscript P) and (110) plane of twinned crystal (subscript T). Arrow indicates the drawing direction. e) Orthorhombic crystal structure of PE. Scale bar, 500 nm.....	66

Figure 3.16: SAED pattern of a PENF where a monoclinic phase is seen in addition to orthorhombic phase. Plane with subscript ‘O’ corresponds to the plane from orthorhombic structure whereas ‘M’ corresponds to the plane from monoclinic structure. Arrow indicates the drawing direction.....68

Figure 3.17: Electron beam swelling in PENF. a) AFM image of a nanofiber b) Height profile of lines drawn in (a). Horizontal distance is larger because of the convolution of the AFM tip. c) SEM image of PENF d) Magnified view of inset of (c). Scale bars 5 μm (c) and 500 nm (d).....69

Figure 3.18: Diameter measurement for k evaluation. a) SEM micrograph of the initial fiber b) SEM micrograph after SEM exposure. Scale bars, 5 μm70

Figure 3.19: Comparison of fiber dimensions measured using AFM and SEM. a) Height map measured using AFM. b) Zoom in of Inset of (a). c) Width measured using SEM at same region in (a). d) Zoom in inset of (c). e) Height profile of lines in (b). f) Ratio of SEM width to AFM height versus SEM width. Scale bars, 2 μm (c,d).....71

Figure 3.20: Diameter profile of a typical PENF fabricated using local drawing.....72

Figure 4.1: PRT based micro thermal device. Zoomed inset is the suspended PRT platforms supported by SiN_x beams. (Note gold wires bonded on PRT device for electrical connection to a chip carrier are visible.).....78

Figure 4.2: a) Resistance of the heating and sensing platforms in a device as the global temperature is lowered from room temperature to 10 K b) global temperature measured by a thermocouple on a copper finger. c) Resistance of the heating platform (blue line) and the global temperature (red line) as the global temperature is ramped up from 230 K to 240 K. Blue arrows indicate steady state at 240 K.....81

Figure 4.3: a) An electrical configuration of the thermal measurement system b) Thermal configuration at steady state. Figure obtained from [73].....82

Figure 4.4: a) Platinum coating using FIB on PENF. b) k of PENF with platinum contact. The k values are similar to that of bulk PE. Scalebar, 10 μm86

Figure 4.5: Thermal contact resistance ($2R_c$) as a function of axial thermal conductivity of a PENF.....88

Figure 4.6: Background thermal conductance of an empty device with gap 5 μm90

Figure 4.7: Thermal characterization of PENF. a) A PRT based micro-device with the heating and the sensing islands. Inset shows a PENF bridging the islands. b) Total measured thermal resistance vs L/A of crystalline (c) PENFs at 150 K and 300 K where the y-intercept represents $2R_c$. The error bars show the mean and standard deviation values of 250 measurements. c) $k(T)$ of a PENF. Blue circles are measured k of a c -PENF, black dotted lines are after adjusting for $2R_c$. Orange line is $1/T$ trend of c -PENF at high temperatures and pink line is T^1 trend at low temperatures. d) $k(T)$ of PEMF and amorphous (a) PENF. Red circles are PEMF before local drawing, and green circles are c -PENF amorphized due to exposure to FIB. e) $k(T)$ of all reported samples after adjusted for $2R_c$. Scale bars, 20 μm and 2 μm (inset).....96

Figure 4.8: Thermal transport in PENF. a) Thermoreflectance imaging of heating island (right) and sensing island (left) without a nanofiber and a PENF respectively, in laboratory air. Dotted white line is the PENF position. b) Phonon dispersion relation of the acoustic branches along the chain backbone calculated from the trajectory of MD simulations using two-dimensional Fourier transform. The contour is the raw data from calculation and colored lines are linear fits. The inset shows the acoustic branches close to the Brillouin zone center.....97

Figure 5.1: Orthorhombic to hexagonal phase transition in PE. A) All trans conformation in orthorhombic phase where r , θ and α represent C-C bond, C-C-C dihedral angle and C-C-C bond angle. B) Side view of PE in orthorhombic phase. Inset shows cross-section view where dotted line indicates the orthorhombic lattice of PE. C) After phase transition to hexagonal phase, gauche conformation is introduced in the chain. D) This makes PE conformationally disordered, however, it retains the along chain order as seen from the side view. Inset shows cross-section view where dotted line indicates the hexagonal lattice of PE.....106

Figure 5.2: Thermal switching in PENF. A) A TEM brightfield image. The inset shows orthorhombic crystal lattice. B) Thermal conductance behavior of crystalline PENF and amorphous PENF. C) A $Q-\Delta T$ transfer function shows non-linear behavior at the phase transition.

D) Thermal stability of the <i>O-H</i> phase transition shown after holding at 450 K for 10 h..	107
Figure 5.3: Thermal conductance measurement beyond the <i>O-H</i> phase transition. The insets show the thermal conductance trend after the <i>O-H</i> transition where T_m indicates the melting temperature of the hexagonal phase.....	110
Figure 5.4: Thermal rectification in amorphous-crystalline PENF. A) Device schematic B) Diode performance.....	112
Figure 5.5: Thermal contact resistance. A) The thermal conductivity of crystalline PENF and amorphous PENF. B) Thermal contact resistance obtained using line contact model. The inset shows the thermal contact resistance for thermal conductivity from 0 to 4 W m ⁻¹ K ⁻¹	113
Figure 6.1: Optical image of a nanotractor. A nanofiber is clamped between the triangular pads.....	122
Figure 6.2: Voltage sequence applied to the actuator to obtain a step motion. a) A leading clamp is locked due to electrostatic force from applied voltage b) Voltage is applied on an actuation plate that causes out of plane bending on the plate and pulls a trailing clamp by a step (~ 60 nm) c) Voltage is applied on the trailing clamp and locked d) Voltage is, then, released at the leading clamps and it moves by a step (~60 nm). Reprinted from [1].....	123
Figure 6.3: Load cell structure. Four guided beams and two combs with a fixed reference structure at the center. The scale bar is 40 μm.....	124
Figure 6.4: Customized probe station with a long distance working objective a) Image of the probe station b) Components of the probe station [2].....	126
Figure 6.5: Pattern matching results of a load cell displacement from images taken at 50X on a stationary device. The standard deviation is ~4 nm.....	127
Figure 6.6: Optical image at 50X objective of combs and a reference structure used for sub-pixel pattern matching. The scale bar is 40 μm.....	128

Figure 6.6: Silica fiber sample on a nanotractor a) Optical image of nanotractor sample with a silica fiber (20X objective) b) silica nanofiber gripped on a pad (50X objective) c) SEM image of the silica nanofiber.....130

Figure 6.7: Stress strain curve of the silica nanofibers. E = 67.72 GPa was obtained for d=108 nm sample and E = 76.53 GPa was obtained for d = 90.3 nm sample.....131

Figure 6.8: SEM image of a fractured silica fiber. Scale bar is 2 μm.....133

Figure 6.9: A representative sample ready for testing.....134

Figure 6.10: PE nanofiber (PENF) on the left side of the dog bone for additional mechanical gripping, with PE microfiber (PEMF) on the right. a) Schematic of mechanical locking of the dog bone within cured epoxy. b) Optical image of the dog bone before testing. c) SEM image of the same dog bone after testing. The streaks at the left edge of the dog bone in (c) are crazes due to the deformation of the cured epoxy. They are only on the left side of the dog bone, indicating successful gripping of the test sample. d) Atomic force microscopy (AFM) image of tip of a dog bone (SEM image not shown here). e) Height profile of the dog bone in (d) labelled ‘1’. Scale bars, 25 μm (b,c).....136

Figure 6.11: Estimation of glue shear strength. a) Shear force per unit glued length versus diameter of the fiber. The slope gives the shear modulus of glue with PE fiber. (b) and (c) are schematic cross section and longitudinal views of the fiber in the glue.....137

Figure 6.12 Mechanical characterization of PENF. a) A PENF gripped between two pads. b) Dog bone shape on a PENF which provides additional grip due to mechanical locking. High contrast at the edges of dog bone is from charging of cured epoxy. c) Stress-displacement curve. d) σ_{ts} of PENF compared to other fibers such as electrospun PE [3], CF1 [4] (Carbon fiber 1), CF2 (HexTow®/ Hexcel), CNTF [5] (Carbon nanotube fiber), PE [6] (Gel-spun PE fiber), Zylon®/ Toyobo, LCPF (Liquid crystal polymer fiber, Vectran™/ Kuraray), Kevlar®/ Du Pont, Dyneema®/ Royal DSM, and GF [7] (Graphene fiber). The error bars in PENF are calculated using uncertainty analysis (see Section 6.5.5). Scale bars, 25 μm (a), and 10 μm (b).....139

Figure 6.13: Diameter measurement for σ_{ts} evaluation. a) Fractured sample. b) Zoom in of inset of a. c) Extremely necked sample. The diameter is measured far away from necked region. The coiling is prominent in freely suspended sample compared to the sample on the substrate. Scale bars, 5 μm (a,c), 1 μm (b), 500 nm (d).....142

Figure 6.14: Extreme necking of PENF a) AFM image of the necked region b) Height profiles of lines shown in (a).....144

Figure 7.1: Test platform schematic (not to scale).....153

Figure 7.2: SEM images of (A) the full test platform with the stepper motor on the right, (B) the gauge section with a mounted nanofiber and (C) the comb fingers and reference gauge used for displacement metrology.....154

Figure 7.3: Data from a conventional creep test at RT. (A) Approximately constant creep stress as maintained by feedback (B) the corresponding creep compliance curve.....158

Figure 7.4: An example of variable creep stress.....160

Figure 7.5: Data taken to determine the limit of the linear viscoelasticity (LVE) regime at 100 °C (A) Multiple levels of variable stresses. The insets show individual levels of variable stress. (B) The corresponding strain. The insets show the respective strains. In the insets, the stress and strains values are shifted such that their origins begin at their initial value.....162

Figure 7.6: Isochronous engineering stress-strain curves at 100 °C to determine the limit of linear viscoelastic (LVE) behavior. A least squares linear fit with 95 % confidence interval on the 10 s stress-strain data is shown.....163

Figure 7.7: Elastic-plastic behavior of PAN nanofiber. (A) Engineering stress-strain curves for three different diameters. (B) Elastic modulus vs diameter. (C) Yield strength vs diameter. (D) The elastic modulus vs yield strength show a positive correlation. Dashed lines are exponential curves that indicate the data trends.....165

Figure 7.8: Representative sample with (A) stress and (B) strain curve fitting.....167

Figure 7.9: Creep compliance as a function of temperatures. The nanofiber diameters for each tested temperature of 24 °C, 53 °C, 85 °C and 104 °C were 240 nm, 190 nm, 232 nm and 375 nm respectively.....168

Figure 7.10: TTSP with RT as the reference temperature. (A) Master curve for nanofibers with an average diameter of 260 nm (B) Horizontal shift factor vs inverse of absolute temperature. The dashed line is a linear curve fit excluding the data close to T_g . (C) Master curve for nanofibers with average diameter of 150 nm. The nanofiber diameters for each tested temperature of 25 °C, 53 °C, and 95 °C were 160 nm, 145 nm, and 145 nm respectively. (D) Horizontal shift factor vs inverse of absolute temperature.....169

Figure 7.11: Comparison of the master curves of thick (average diameter 250 nm) and thin fiber (average diameter 150 nm). RT is the reference temperature.....170

Figure 7.12: Creep compliances of the partially oriented versus a randomly oriented PAN nanofiber.....171

Figure A.1: Microfabrication processes of the sample collector.....188

Figure B.1: Microheater used for local heat stretching and cutting PE fiber. a) micro heater b) tungsten tip of micro heater with diameter $\sim 3\mu\text{m}$190

Chapter 1: Introduction

1.1 Objectives

Polymer micro/nano fibers exhibit significantly different mechanical, thermal and thermo-mechanical properties compared to their bulk counterparts. Often referred to as the size effect in polymer micro/nanofibers, this different behavior stems from reorganization of the interior core molecules and increased surface to volume ratio. The increase in alignment of the core molecules (also referred as orientation) along the fiber-axis and crystallinity enhance the mechanical and thermal properties such as Young's modulus, tensile strength, and thermal conductivity in the fiber direction by several times to several orders of magnitude [2]–[7]. This notable enhancement in material properties coupled with its intrinsic properties such as low density, chemical resistance, and bio-compatibility open applications such as tissue engineering, filtration, sensing, textiles, composite reinforcements, ballistic armor and more [8]–[12]. In contrast, the increase in surface to volume ratio increases the volume fraction of higher mobility amorphous surface molecules which have the opposite effect. This leads to a decrease in the glass transition temperature, T_g , and the melting temperature, T_m [13], [14]. In addition, nanoscale confinement can also cause reduction in the melting temperature due to a reduction in the crystallite size [15]. The objective of this thesis is to study the thermal and mechanical properties of individual nanofibers and couple the properties with their molecular structure.

Several fiber processing techniques such as gel spinning [16]–[18], tip drawing [3], [5], [19] and electrospinning [20]–[22] have been developed to produce polymer micro/nanofiber with enhanced crystallinity and chain alignment and thus engineer the thermal and mechanical

properties of polymers. Using stress, linear isotactic polymers such as polyethylene (PE) crystallize and the chain backbone molecules become oriented. This dissertation is mainly focused on PE, specifically ultra-high molecular weight PE. Chapter 3 discusses a new fabrication technique developed to produce highly crystalline PE nanofiber.

Over the last half century, thermal and mechanical properties of PE have been thoroughly studied on thin film and microfibers. It has been observed that with increasing molecular weight and draw ratio, thermal and mechanical properties increase concurrently [23]. Bulk PE thermal conductivity is $0.1 \text{ W m}^{-1} \text{ K}^{-1}$ - $0.4 \text{ W m}^{-1} \text{ K}^{-1}$. With the development of micro/nanofabrication of polymer with post drawing, researchers have increased the crystallinity and alignment of backbone molecules which further reduce phonon scattering sites. Consequently, higher thermal conductivity in polymers such as PE has been achieved [5], [23], [24]. Recently, tip-drawn PE nanofibers at a draw ratio of 1400X have been reported to have a room-temperature thermal conductivity as high as $104 \text{ W m}^{-1} \text{ K}^{-1}$ [5]. This is comparable to metals and alloys such as platinum ($\sim 70 \text{ W m}^{-1} \text{ K}^{-1}$), nickel ($\sim 90 \text{ W m}^{-1} \text{ K}^{-1}$) and stainless steel ($\sim 12 - 45 \text{ W m}^{-1} \text{ K}^{-1}$). Such high thermal conductivity shows potential of using polymer as a cheaper alternative to conventional metallic heat transfer materials. However, temperature-dependent thermal transport in such ultra-drawn nanofibers, which is critical for not only elucidating the phonon physics in the nanofibers but also developing their applications in a wide temperature range, was not previously measured but is a focus of this thesis. Chapters 4 and 5 discuss the temperature dependent thermal property of crystalline PE nanofiber.

One of the major limitations of PE for heat transfer application is its low melting temperature ($T_m = 414 \text{ K}$). A properly designed PE fiber with high thermal stability can be used in applications such as heat exchangers, cell phone casings, plastic packaging for light emitting

diodes (LEDs) and flexible electronics. PE fiber can be used as an efficient heat transfer material, particularly where an electrically insulating material and directional heat transfer is concurrently desired. Chapter 5 discusses the thermal stability that can be achieved far beyond the equilibrium melting temperature in crystalline PE nanofiber.

Large scale molecular dynamics simulations suggest that increased segmental rotation can cause along chain disorder and lead to a thermal conductivity switching, a ratio of high thermal conductivity to low thermal conductivity, up to 12 [30]. This phenomenon is predicted to be tunable and fully reversible [31]. Such active control of thermal transport is of significant interest for a broad range of applications, including heating and cooling, energy conversion, materials processing, and data storage [32]. Based on literature review, there has not been any experimental evidence of such reversible thermal conductivity switching in PE. I discuss this in Chapter 5.

Just as defects such as amorphous region, entanglements, dangling chain ends, voids and impurities reduce thermal conductivity, they also explain low elastic modulus and strength in polymers. It has been long known that C–C bond is stiff and strong. Even though it contains a large concentration of C–C backbones, bulk PE has low modulus (~1 GPa) and strength (<50 MPa). Over the years, different crystallization and drawing methods have been developed to decrease these defects present in PE fibers to realize the enhancement of Young's modulus and strength. Recently, a near theoretical Young's modulus of 312 GPa has been reported in tip-drawn PE nanofibers [3]. However, the maximum tensile strength of such ultra-drawn nanofibers, which is the limiting factor in many applications such as textiles, composite reinforcement and ballistic armor, needs to be ascertained. Chapter 6 discusses the tensile strength measurement of individual highly crystalline PE nanofiber.

In addition to elastic/plastic behavior, polymer nanofibers also exhibit viscoelastic behavior which can be significantly different than bulk due to an increase in the relative amount of fluid-like molecules on the surface. The reorganization of the inner core molecules due to different fabrication methodologies can also play significant role. Most nanoscale viscoelastic measurements, creep or stress relaxation, are limited to thin films [40]. Recently, Naraghi et al. demonstrated an innovative technique based on optical metrology capable of measuring the creep response of a soft polymer nanofiber [41], [42]. They demonstrated a size effect on creep of electrospun polyacrylonitrile (PAN) nanofibers where an increased orientation overwhelmed the increased surface effect and suppressed the creep rate. Recently, stress relaxation tests were carried out on nylon nanofibers in an electron microscope which also exhibited size dependent behavior [43]. Long term viscoelastic behavior of polymer nanofibers which is important for long term application design has not yet been studied. Chapter 7 discusses a long term viscoelastic property prediction for 30 years using time temperature superposition.

1.2 Organization of the thesis:

The details of the molecular organization of the polymer at nanoscale is important and has impact on the mechanical, thermal and thermomechanical properties of polymer nanofiber. The focus of this dissertation is to study such behavior in both crystalline and amorphous polymer nanofibers and couple the properties with their molecular architecture. This dissertation is organized into nine chapters as follows:

Chapter 2 reviews literature on polymer crystallization, drawing, and different micro/nanofiber fabrication methods, with a focus on PE. Experimental progress regarding thermal, and mechanical properties in PE micro/nanofibers is reviewed. Several theoretical models

to understand the upper limit of mechanical and thermal enhancements are also discussed. Viscoelastic measurements performed on polymer nanofibers are also briefly reviewed.

Subsequently, Chapters 3-7 report on new developments achieved over the course of this thesis program. Chapter 3 focuses on specimen preparation techniques, Chapters 4-5 on nanofiber thermal properties and Chapters 6 and 7 on nanofiber mechanical properties. More detail on the subject matter covered in each chapter are given next.

Chapter 3 reports on a new fabrication method developed to make polyethylene nanofibers with high draw ratio. Manipulation and mounting of polymer nanofibers onto test devices are also discussed. Structural and morphological characterizations performed using a cryo-transmission electron microscope and a micro-Raman are also discussed. Chapter 4 reports on temperature-dependent thermal conductivity measurements on PE nanofibers from 20 K to 320 K using a microthermal device with suspended platinum resistance thermometers. Chapter 5 reports on a reversible phase transition measurement in a constrained PE nanofiber using the same device discussed in Chapter 4. The resulting thermal conductivity switch makes a high-performance nanoscale thermal diode, and is also discussed. Chapter 6 discusses strength measurements on PE nanofibers using a microelectromechanical device (MEMS). Chapter 7 discusses size dependent creep master curve of electrospun PAN nanofibers. Chapter 8 summarizes the dissertation and identifies the future directions.

1.3 Thesis Contributions:

This thesis contributes to the field of nanoscale mechanical experimentation and thermal transport in crystalline and glassy polymer nanofibers. One article has been published in a peer reviewed journal [4]. Two other journal articles (including information from Chapters 6 and 7) are

in preparation. A published paper and the tentative titles and journals of the other two papers are listed below.

- 1) R. Shrestha, P. Li, B. Chatterjee, T. Zheng, X. Wu, Z. Liu, T. Luo, S. Choi, K. Hippalgaonkar, M. P. de Boer and S. Shen, "Crystalline polymer nanofibers with ultra-high strength and thermal conductivity," *Nature communications*, vol. 9, 2018.
- 2) R. Shrestha, M. Naraghi and M. P. de Boer "Size-dependent creep master curve of electrospun polymer nanofibers," to be submitted to "Macromolecules."
- 3) R. Shrestha, Y. Luan, S. Shin, T. Zhang, K. Hippalgaonkar, T. Luo, R. Chen, and S. Shen "Solid-state polyethylene nanofiber thermal switches and diodes using structural phase transition," TBD.

Fabrication and characterization of crystalline polyethylene nanofiber (Chapter 3)

- A local stretching technique was developed to fabricate highly crystalline and oriented polyethylene (PE) nanofiber with a diameter in the range of 10 – 100 nm. The diameter could be controlled by tuning the pre-existing tensile stress or the heater temperature.

Thermal transport of a crystalline PE nanofiber (Chapter 4)

- A capillary-induced Van der Waals contact method was developed to minimize the contact resistance of a nanofiber with the measurement platform.
- A unique low dimensionality phonon physics for thermal transport in a crystalline PE nanofiber was demonstrated, where the thermal conductivity increased with increasing temperature following an unusual $\sim T^1$ trend below 100 K.

A solid-state PE thermal diode (Chapter 5)

- A new fully reversible, high-contrast PE nanofiber thermal switch at ~ 430 K has been demonstrated. An unprecedented thermal switching factor $f = 10$ is observed due to the structural phase transition, from orthorhombic to hexagonal lattice, in a crystalline PE nanofiber. The phase transformation was found to be thermally stable and fully reversible.
- A non-linear but symmetric heat transport due to orthorhombic to hexagonal phase transition was observed in a crystalline PE nanofiber. The non-linearity and an asymmetry are pre-requisites for a thermal diode design.
- By fabricating the heterogeneous amorphous-crystalline PE nanofiber, a high-performance solid-state nanoscale thermal diode with a rectification factor $R = 25$ %, comparable to the existing solid-state nanoscale thermal diodes based on carbon nanotubes, boron nitride nanotubes, graphene and VO_2 nanobeams is demonstrated.

Mechanical measurement of crystalline polyethylene nanofiber (Chapter 6)

- In the tensile tests, the grip strength to a PE nanofiber using an adhesive was insufficient because of the low surface energy of PE (31 mJ m^{-2}), and slip occurred before they were tested to failure. A dog-bone shaped nanofiber was designed and fabricated to provide additional grip due to mechanical locking, enabling tensile strength to be measured.
- High ultimate tensile strength (~ 11.4 GPa) was obtained. This is one of the highest tensile strengths measured to date for a polymer or a polymer composite.

The long-term viscoelastic behavior of glassy PAN nanofiber (Chapter 7)

- A variable stress-based creep measurement technique was developed to eliminate the necessity of the feedback to keep a creep stress constant. This was particularly important to measure the creep properties at an elevated temperature.
- From the temperature-dependent creep compliance curves, a master curve spanning 30 years was developed. A thin PAN nanofiber (~150 nm) is predicted to give rise to an order of magnitude less creep compared to a thick fiber (~250 nm) after 30 years at room temperature. The activation energy for creep process in thin PAN fiber was $\sim 152 \text{ kJ mol}^{-1}$, 50 % larger than the thick fiber. The reduction in creep compliance for the thin fiber was attributed to the increased orientation within the core molecules.
- After removing the orientation of core PAN molecules by the exposure to high energy electron beam, higher creep compliance than that of the oriented specimens was obtained. This indicates the role of globally random molecules.

1.4 Chapter references:

- [1] “CES Edupack 2016 (Granata Design Limited, 2013).”
- [2] M. Naraghi, I. Chasiotis, H. Kahn, Y. Wen, and Y. Dzenis, “Novel method for mechanical characterization of polymeric nanofibers,” *Cit. Rev. Sci. Instruments*, vol. 78, p. 85108, 2007.
- [3] P. Li, L. Hu, A. J. H. McGaughey, and S. Shen, “Crystalline polyethylene nanofibers with the theoretical limit of Young’s modulus,” *Adv. Mater.*, vol. 26, no. 7, pp. 1065–1070, 2014.
- [4] R. Shrestha, P. Li, B. Chatterjee, T. Zheng, X. Wu, Z. Liu, T. Luo, S. Choi, K. Hippalgaonkar, M. P. de Boer, and S. Shen, “Crystalline polymer nanofibers with ultra-high strength and thermal conductivity,” *Nat. Commun.*, vol. 9, no. 1, p. 1664, 2018.
- [5] S. Shen, A. Henry, J. Tong, R. Zheng, and G. Chen, “Polyethylene nanofibres with very high thermal conductivities,” *Nat. Nanotechnol.*, vol. 5, no. 4, pp. 251–255, 2010.

- [6] Z. Zhong, M. C. Wingert, J. Strzalka, H.-H. Wang, T. Sun, J. Wang, R. Chen, and Z. Jiang, "Structure-induced enhancement of thermal conductivities in electrospun polymer nanofibers," *Nanoscale*, vol. 6, no. 14, p. 8283, 2014.
- [7] V. Singh, T. L. Bougher, A. Weathers, Y. Cai, K. Bi, M. T. Pettes, S. A. McMenemy, W. Lv, D. P. Resler, T. R. Gattuso, D. H. Altman, K. H. Sandhage, L. Shi, A. Henry, and B. A. Cola, "High thermal conductivity of chain-oriented amorphous polythiophene.," *Nat. Nanotechnol.*, vol. 9, no. 5, pp. 384–90, 2014.
- [8] S. Agarwal, J. H. Wendorff, and A. Greiner, "Progress in the Field of Electrospinning for Tissue Engineering Applications," *Adv. Mater.*, vol. 21, no. 32–33, pp. 3343–3351, Sep. 2009.
- [9] I. S. Chronakis, "Novel nanocomposites and nanoceramics based on polymer nanofibers using electrospinning process—A review," *J. Mater. Process. Technol.*, vol. 167, no. 2, pp. 283–293, 2005.
- [10] Z.-M. Huang, Y. Z. Zhang, M. Kotaki, and S. Ramakrishna, "A review on polymer nanofibers by electrospinning and their applications in nanocomposites," *Compos. Sci. Technol.*, vol. 63, no. 15, pp. 2223–2253, Nov. 2003.
- [11] J. Fang, H. Niu, T. Lin, and X. Wang, "Applications of electrospun nanofibers," *Sci. Bull.*, vol. 53, no. 15, pp. 2265–2286, Aug. 2008.
- [12] M. Á. R. Calderón and W. Zhao, "Applications of Polymer Nanofibers in Bio-Materials, Biotechnology and Biomedicine: A Review," in *TMS 2014: 143rd Annual Meeting & Exhibition*, Cham: Springer International Publishing, 2014, pp. 401–414.
- [13] Z. Yang, Y. Fujii, F. K. Lee, C.-H. Lam, and O. K. C. Tsui, "Glass transition dynamics and surface layer mobility in unentangled polystyrene films.," *Science*, vol. 328, no. 5986, pp. 1676–9, Jun. 2010.
- [14] Y. Chai, T. Salez, J. D. McGraw, M. Benzaquen, K. Dalnoki-Veress, E. Raphaël, and J. A. Forrest, "A direct quantitative measure of surface mobility in a glassy polymer.," *Science*, vol. 343, no. 6174, pp. 994–9, Feb. 2014.
- [15] M. Alcoutlabi and G. B. McKenna, "Effects of confinement on material behaviour at the nanometre size scale," *J. Phys. Condens. Matter*, vol. 17, pp. R461–R524, 2005.
- [16] C. L. Choy, Y. W. Wong, G. W. Yang, and T. Kanamoto, "Elastic modulus and thermal conductivity of ultradrawn polyethylene," *J. Polym. Sci. Part B Polym. Phys.*, vol. 37, no. 23, pp. 3359–3367, Dec. 1999.
- [17] X. Wang, V. Ho, R. A. Segalman, and D. G. Cahill, "Thermal Conductivity of High-Modulus Polymer Fibers," 2013.
- [18] P. Smith and P. J. Lemstra, "Ultra-high-strength polyethylene filaments by solution spinning/drawing," *J. Mater. Sci.*, vol. 15, no. 2, pp. 505–514, 1980.

- [19] J. Ma, Q. Zhang, Y. Zhang, L. Zhou, J. Yang, and Z. Ni, "A rapid and simple method to draw polyethylene nanofibers with enhanced thermal conductivity," *Appl. Phys. Lett.*, vol. 109, no. 3, p. 033101, Jul. 2016.
- [20] J. Doshi and D. H. Reneker, "Electrospinning process and applications of electrospun fibers," *J. Electrostat.*, vol. 35, no. 2–3, pp. 151–160, Aug. 1995.
- [21] D. H. Reneker and I. Chun, "Nanometre diameter fibres of polymer, produced by electrospinning," *Nanotechnology*, vol. 7, no. 3, pp. 216–223, Sep. 1996.
- [22] Z. Sun, E. Zussman, A. L. Yarin, J. H. Wendorff, and A. Greiner, "Compound Core–Shell Polymer Nanofibers by Co-Electrospinning," *Adv. Mater.*, vol. 15, no. 22, pp. 1929–1932, Nov. 2003.
- [23] D. B. Mergenthaler, M. Pietralla, S. Roy, and H. G. Kilian, "Thermal conductivity in ultraoriented polyethylene," *Macromolecules*, vol. 25, no. 13, pp. 3500–3502, Jun. 1992.
- [24] C. L. Choy, Y. Fei, and T. G. Xi, "Thermal conductivity of gel-spun polyethylene fibers," *J. Polym. Sci. Part B Polym. Phys.*, vol. 31, no. 3, pp. 365–370, Mar. 1993.
- [25] S. Burgess and D. Greig, "The low-temperature thermal conductivity of polyethylene," *J. Phys. C Solid State Phys.*, vol. 8, no. 11, pp. 1637–1648, Jun. 1975.
- [26] A. J. Pennings and J. M. A. A. Van Der Marlc, "Hydrodynamically induced crystallization of polymers from solution IV. The melting of fibrillar polyethylene crystals*)," *Rheol. Acta*, vol. 10, pp. 174–186, 1971.
- [27] A. J. Pennings and A. Zwijnenburg, "Longitudinal growth of polymer crystals from flowing solutions. VI. Melting behavior of continuous fibrillar polyethylene crystals," *J. Polym. Sci. Polym. Phys. Ed.*, vol. 17, no. 6, pp. 1011–1932, 1979.
- [28] T. Yamamoto, H. Miyaji, and K. Asai, "Structure and Properties of High Pressure Phase of Polyethylene," *Jpn. J. Appl. Phys.*, vol. 16, no. 11, pp. 1891–1898, Nov. 1977.
- [29] S. Rastogi and J. A. Odell, "Stress stabilization of the orthorhombic and hexagonal phases of UHM PE gel-spun fibres," *Polymer (Guildf.)*, vol. 34, no. 7, pp. 1523–1527, 1993.
- [30] T. Zhang and T. Luo, "Morphology-influenced thermal conductivity of polyethylene single chains and crystalline fibers," *J. Appl. Phys.*, vol. 112, no. 9, p. 094304, 2012.
- [31] T. Zhang and T. Luo, "High-Contrast, Reversible Thermal Conductivity Regulation Utilizing the Phase Transition of Polyethylene Nanofibers," *ACS Nano*, vol. 7, no. 9, pp. 7592–7600, Sep. 2013.
- [32] G. Wehmeyer, T. Yabuki, C. Monachon, J. Wu, and C. Dames, "Thermal diodes, regulators, and switches: Physical mechanisms and potential applications," *Appl. Phys. Rev.*, vol. 4, no. 4, 2017.

- [33] J. Smook and J. Pennings, "Influence of draw ratio on morphological and structural changes in hot-drawing of UHMW polyethylene fibres as revealed by DSC," *Colloid Polym. Sci.*, vol. 262, no. 9, pp. 712–722, 1984.
- [34] J. P. Penning, H. van der Werff, M. Roukema, and A. J. Pennings, "On the theoretical strength of gelspun/hotdrawn ultra-high molecular weight polyethylene fibres," *Polym. Bull.*, vol. 23, no. 3, pp. 347–352, Mar. 1990.
- [35] M. Naraghi, T. Ozkan, I. Chasiotis, S. S. Hazra, and M. P. de Boer, "MEMS platform for on-chip nanomechanical experiments with strong and highly ductile nanofibers," *J. Micromech. Microeng.*, vol. 20, no. 12, p. 125022, 2010.
- [36] B. Wu, A. Heidelberg, and J. J. Boland, "Mechanical properties of ultrahigh-strength gold nanowires.," *Nat. Mater.*, vol. 4, no. 7, pp. 525–529, 2005.
- [37] G. Brambilla and D. N. Payne, "The Ultimate Strength of Glass Silica Nanowires," *Nano Lett.*, vol. 9, no. 2, pp. 831–835, Feb. 2009.
- [38] S. Hoffmann, F. Östlund, J. Michler, H. J. Fan, M. Zacharias, S. H. Christiansen, and C. Ballif, "Fracture strength and Young's modulus of ZnO nanowires," *Nanotechnology*, vol. 18, no. 20, p. 205503, 2007.
- [39] J. H. Park and G. C. Rutledge, "Ultrafine high performance polyethylene fibers," *J. Mater. Sci.*, vol. 53, 2017.
- [40] P. A. O'Connell and G. B. McKenna, "Novel nanobubble inflation method for determining the viscoelastic properties of ultrathin polymer films," *Rev. Sci. Instrum.*, vol. 78, no. 1, p. 013901, Jan. 2007.
- [41] M. Naraghi, P. V. Kolluru, and I. Chasiotis, "Time and strain rate dependent mechanical behavior of individual polymeric nanofibers," *J. Mech. Phys. Solids*, vol. 62, pp. 257–275, 2014.
- [42] M. Naraghi, I. Chasiotis, H. Kahn, Y. Wen, and Y. Dzenis, "Mechanical deformation and failure of electrospun polyacrylonitrile nanofibers as a function of strain rate," *Appl. Phys. Lett.*, vol. 91, no. 15, p. 151901, Oct. 2007.
- [43] M. C. Wingert, Z. Jiang, R. Chen, and S. Cai, "Strong size-dependent stress relaxation in electrospun polymer nanofibers."

Chapter 2: Background and literature review

2.1 Introduction

The mechanical and thermal behavior of a polymer micro/nano fiber depends on size and on the internal structure of the polymer molecules, which can be tuned by the crystallization process or the drawing process. In Chapters 3-7, I report on new developments achieved over the course of this thesis program. Chapter 3 focuses on fabrication of crystalline polymer nanofiber and its characterization, Chapters 4-5 on nanofiber thermal properties and Chapters 6 and 7 on nanofiber mechanical properties.

Therefore, in Section 2.2, I have reviewed the literature on the polymer crystallization and subsequent drawing process. In Section 2.3, several fabrication techniques capable of producing polymer micro/nanofibers is discussed. Since, this thesis is focused on polyethylene (PE), a common type of linear polymer easy to crystallize and draw, the review is performed with polyethylene as a reference. In Section 2.4, I have reviewed the literature on thermal enhancement achieved in PE using different fabrication techniques. In Section 2.5, mechanical behavior of polymer nanofiber is reviewed.

2.2 Polymer crystallization and drawing

2.2.1 Polymer crystallization

Unlike metal and ceramics where the unit cell repeats in 3D space, polymers generally crystallize in a hierarchy of three structural levels when cooled from the melt. On the first level, individual chain backbones pack with neighboring chains to form a unit cell as shown in Fig. 2.1a. The unit cell dimensions are usually between 2 – 20 Å [1] and pack in a low symmetry lattice.

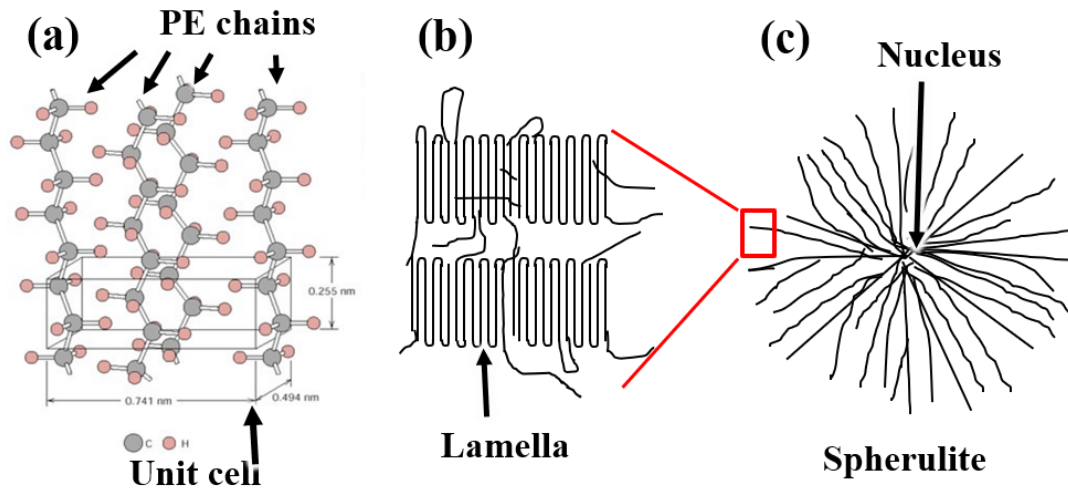


Figure 2.1: Hierarchy of polymer crystals a) Orthorhombic unit cell of polyethylene shown in the black box. [2] b) Stacked lamellae interconnected by tie molecules c) Spherulite.

For example, PE crystallizes most commonly in an orthorhombic lattice, as shown in Fig. 2.1a, with dimensions of 7.41 Å, 4.94 Å and 2.55 Å and sometimes in a monoclinic lattice with dimensions 8.09 Å, 2.53 Å and 4.79 Å [1]. In the second level, these unit cells pack into a thin sheet 10 – 50 nm thick and several microns wide, called lamella. Polymer backbones lie at some fixed angle in the lamella and often re-enter the lamella by folding 180° at the surfaces of the lamella or become a unit cell in another lamella. A backbone that connects two lamellae is also known as a tie molecule. Fig. 2.1b shows an example of a chain folded lamella, which is a unique morphological feature of a polymer. Finally, these lamellae arrange radially in a dendritic manner over a range of several hundreds of microns in a structure called a spherulite, as shown in Fig. 2.1c. All three levels of structures have been observed when a polymer melt is allowed to cool and crystallize [3]. Crystallization from dilute or very dilute polymer solution differs from bulk crystallization. Unlike the bulk case, crystallization from dilute solution can result in single lamellar crystals. The conformational changes of backbone molecules necessary for crystallization

occur more readily due to a reduced number of entanglements. Nucleation sites are also greatly reduced, so spherulites do not form.

2.2.2 Stress-induced crystallization

Polymers crystallize differently when the polymer solution is mechanically agitated or stressed compared to crystallization from bulk and dilute solutions [4]. The shear stress induced in the polymer solution preferentially aligns the crystals along the fiber axis [4]. We now focus on stress-induced crystallization in PE. A scanning electron micrograph (SEM) of the polyethylene fiber crystallized from mechanical agitation showed stacked lamellar crystals with oriented fibrils connecting them as shown in Fig. 2.2 [4]. Lamellar stacks, shown in Fig. 2.2b, grow transverse to the applied stress direction and are called kebabs while the oriented fibrils between the kebabs are called shish. Initial work by Pennings et al. on PE samples fabricated by stress-induced crystallization showed a high tensile strength and low elongation compared to that of drawn melt crystallized PE samples [4].

In the 1980s, research interest in stress-induced crystallization increased in the hope of obtaining highly stiff and strong polymer fibers. Hill et al. studied the crystallization of stressed melts and found that the highly oriented shish crystallizes before kebab and supports most of the load in a stress crystallized sample [5]. A. J. Pennings tested the tensile properties of PE fibers fabricated under Couette flow and found increased Young's modulus and strength, which he attributed to a decrease in the amount of lamellar overgrowth and an increase in the orientation of fibrils along the fiber axis [6]. It was later found that the lamella merely serves as "hairdressing" and the tensile modulus depends on the aligned fibrillar growth [7]. The main defect was the grain boundary between the fibrils (crystallites) where the lamella preferentially grew as shown in Fig.

2.2c [8]. Since then, several other methods with various degrees of crystallization and orientation have been developed. These include surface growth of polymer under Couette [9][10] or Poiseuille flow [11], melt/gel spinning [12], electrospinning [13][14], and two-stage tip drawing [15][16].

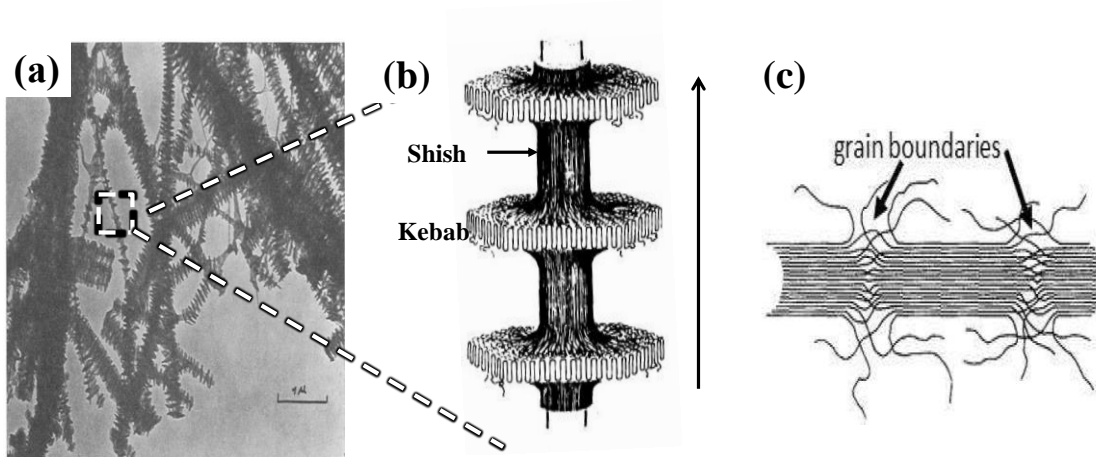


Figure 2.2: a) Shish-kebab structures clearly seen in the SEM micrograph of PE fiber fabricated by shear-induced crystallization [4]. b) details of the shish-kebab structure where lamellar outgrowths are seen on a central fibrillar fiber. The arrow shows the direction of applied stress. c) grain boundaries on fibril where lamellar outgrowths occur [8].

Stress-induced crystallization is not enough to fully eliminate the transverse lamellar growth or to create fully oriented fibrils along the fiber axis. Therefore, crystallization is accompanied by fiber drawing to further extend the molecules along the fiber axis and increase the crystallinity and orientation.

2.2.3 Drawing

While metal drawing has been done for centuries, polymer drawing only began in the 1930s. Carothers and Hill collected polyester fibers on a drum and applied some tension while they were wound at a room temperature (RT) or a slightly elevated temperature. They observed

higher breaking strength and higher crystallinity, which they attributed to the orientation of the molecules obtained due to drawing [17]. Initial work on a drawing of melt-crystallized PE showed a linear dependence on draw ratio (ratio of initial length to final length after drawing), where higher draw ratio gave stiffer and stronger fibers [18]. A similar trend was also seen in single crystal mat of high-density polyethylene (HDPE), however, the draw ratio was limited to ~30 to 40 when drawn from 90 °C to 110 °C [19]. Upon increasing the molecular weight to ultra-high molecular weight ($MW \geq 10^6$), drawability in crystalline mat increased to ~250 [20].

The drawing was also extensively used on fibers fabricated from stress-induced crystallization with shish-kebab morphology. Elastic modulus increased linearly with draw ratio just as in drawn single crystal mats. Even though these fibers exhibited increased crystallinity and orientation, they still displayed a lamellar structure (kebab). Smook et al. were able to transform the shish-kebab morphology into smooth fibrillar structure upon hot drawing at 148 °C at a draw ratio above 80 [21]. Although the gel initially contained a shish-kebab structure, the kebabs were mostly removed and pulled taut between the crystallites.

The orientation at the end of the drawing process is due to the extensional forces that orient the molecules along the fiber direction, compensating the molecular relaxation which tries to return the molecule to the isotropic state favored by entropy [22]. When followed by crystallization or solidification, the oriented taut-tie molecules (TTM) between the crystallites become locked in and remain in a metastable oriented state (local energy minimum state). Hot drawing is usually done in a heated chamber where the fiber is kept in tension and slowly wound in a drum. Heating near the crystallization temperature makes it easy to uncoil the molecules and orient them along the fiber axis. However, exposing a long section of the fiber at an elevated temperature could also reduce the orientation via entropic relaxation of the TTM bridging the crystallites [23].

2.3 Fabrication of polymer micro/nanofiber

Increased crystallinity and molecular alignment along the fiber axis have both been credited for the significant enhancement of mechanical and thermal properties in polymer micro/nanofibers [8], [15], [16], [24]–[26]. To realize these characteristics, numerous fabricating techniques have been developed such as longitudinal growth [9], [10], [27], spinning [8], [28], [29], template synthesis [30]–[32], electrospinning [13], [33]–[36] and two-stage tip drawing [15], [16]. For brevity and relevance, only spinning, electrospinning and two-stage tip drawing are reviewed.

2.3.1 Gel spinning and Electrospinning

Spinning is the most-frequently adopted technique. Based on the state of starting material, it can be classified as either (i) melt spinning, (ii) solution spinning or (iii) gel spinning. *Gel spinning* is similar to solution spinning except the starting material is in the gel state. The gel is a jelly-like solid where molecules form a network by cross-links or entanglements. Gel spinning is done at a temperature lower than the melting temperature (T_m) of polymer crystals so that the network remains intact. Ultra-high molecular weight polyethylene (UHMWPE, molecular weight $\sim 1 \times 10^6 - 3 \times 10^6$ g/mol) is commonly gel spun in the industry; it is challenging to melt spin because of its extremely long chain and a large number of entanglements, making it difficult to achieve significant chain extension [28].



Figure 2.3: A Wet spinning process in which polymer solution or gel is extruded through a spinneret and solidified in a coagulating bath. Image from Britannica Inc.

In *PE gel spinning*, PE is first dissolved in a suitable solvent (paraffin or decalin) at a temperature above the PE T_m , $>140^\circ\text{C}$. The solution is quenched to RT to obtain a PE gel. The gel is then spun through the spinneret to obtain a gel fiber. The gel fiber can be dry spun or wet spun. Gel spinning can also be done via dry-wet spinning where the gel fiber is first dried in air and then passed through a liquid bath to reabsorb solvent [37]. The filaments emerge with relatively high crystallinity and molecular alignment relative to other fabrication methods, providing high strength fibers. The fibers are further drawn at elevated temperature to enhance crystallinity and alignment. Example of wet spinning is shown in Fig. 2.3. DSM and Honeywell manufacture commercial high strength PE microfibers using this method and market them as products known as Dyneema and Spectra.

Electrospinning is now an established method for producing nanoscale polymer fibers in both the academic laboratory and at the industrial scale. Although electrospinning has its roots in the 1930s [14], it gained substantial academic attention in the 1990s nanotechnology boom when its multi-disciplinary potential was realized. An electrospun nanofiber has a high surface area to volume ratio and it can be fabricated as an aligned or entangled mat, making it ideal for catalysis

[38], tissue scaffold and drug delivery [39]–[41], filtration [42][43], high strength fiber applications [26], energy harvesting [44], fuel cells [45][46] and so on [14][33]. This method can be employed to make complex nanofiber structures such as core-shell fibers [47], hollow fibers [48][49], polymer composites [50]–[52] and polymer loaded with fluorescent dyes [49][53] or nanoparticles [54][55]. Unlike other spinning processes, which use mechanical force to continuously reduce the diameter and align the molecule in a solution or melt, it uses electrostatic force to reduce the diameter and align the molecules in a fiber.

There are many variants on the electrospinning set up. However, in general, it consists of three major components: a high voltage power supply, a syringe with a metallic needle, and a collector (often a metallic plate that serves as an electrode for high voltage power supply) as shown in Fig. 2.5. First, a polymer is dissolved with a suitable solvent to prepare a solution and the syringe is filled with it. Solution parameters such as concentration, viscosity, surface tension and surface charge density play a significant role in fiber diameter and its uniformity [35]. A high electric field, $\sim 100 - 500$ KV/m, is applied between the syringe needle and the collector. The polymer solution in needle experiences electrostatic repulsion due to the surface charges and electrostatic attraction due to the external field. As a result, the liquid drop will distort into a conical shape known as Taylor cone. When the field is large enough, an attractive force overcomes the surface tension and a liquid jet is formed. The electrified jet accelerates towards the collector while undergoing rapid a bending and whipping instability [34]. This instability along with the evaporation of the solvent stretches, aligns the molecules, and produces a nanoscale fiber. A fibrous mat of nanofibers or aligned fibers, depending on the collector geometry, is obtained as shown in Fig. 2-5. In practice, electrospinning gives a broad range of fiber diameters. Also, the fiber structure including molecular orientation and crystallinity vary significantly. Large arrays of polymers have been

electrospun, Examples include Nylon-6,6 [56], Polyacrylonitrile (PAN) [24], Polymethyl methacrylate (PMMA), PE [57], [58], polyimide [25] and others [33], [41], [59]. Electrospinning is a relatively cheap, easy, and scalable fabrication method for producing nanofibers, however, the fibers are only moderately crystalline and have moderate molecular orientation.

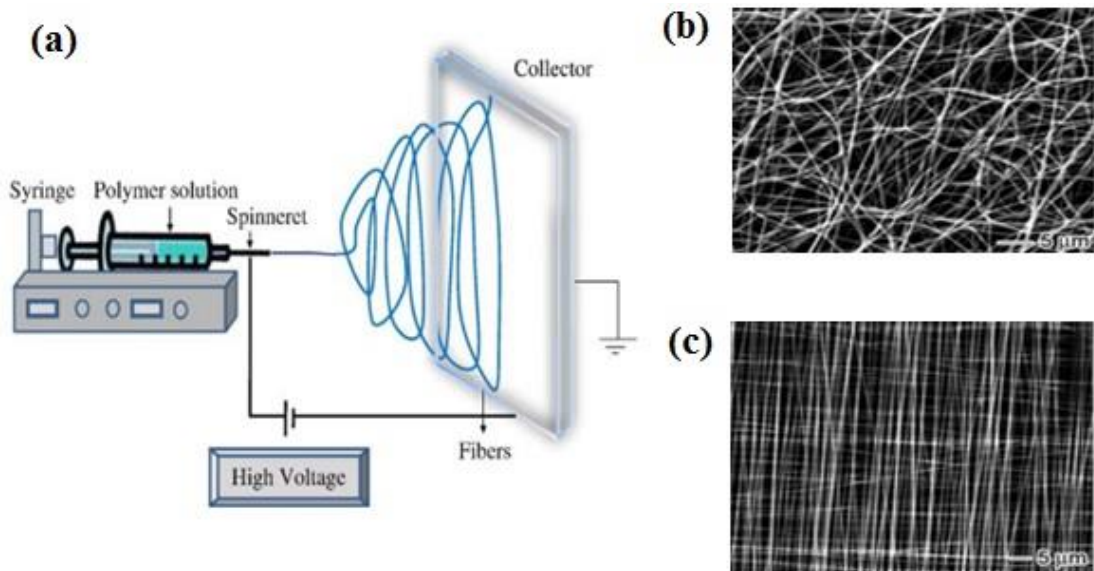


Figure 2.4: a) Basic electrospinning set up with a flat collector [60]. b) The random mat of polymer nanofibers [61] c) Aligned polymer nanofibers [61].

2.3.2 Two stage tip drawing

Among the methods discussed above, conventional spinning processes produce good quality fibers but are limited to microfibers. The electrospinning process produces nanoscale fibers, but they lack good alignment and crystallinity. A two-stage tip drawing method is an alternative technique that can produce high-quality nanoscale fibers [15], [16]. PE nanofibers fabricated with this method have been measured to have the highest recorded thermal conductivity ($\sim 104 \pm 30 \text{ W m}^{-1} \text{ K}^{-1}$) [15] and near theoretical Young's modulus ($\sim 312 \pm 108 \text{ GPa}$) [16].

In this method, a PE gel is first made. To make the PE gel, UHMWPE powder (average molecular weight $\sim 3 \times 10^6 - 6 \times 10^6 \text{ g mol}^{-1}$) is mixed with a decalin solvent at an optimum concentration of $\sim 0.8 \text{ wt } \%$ [62]. The mixture is constantly stirred and heated to 145°C to dissolve the PE powder. This process is done inside an argon filled glove box to avoid oxidation. The solution becomes transparent and viscous as the PE powder dissolves in the solvent. The solution is then quenched in a water bath to RT. When cooled, the solution turns into a translucent viscous gel.

The as-prepared gel is then used to draw individual PE nanofibers. A hot plate is used to set the air temperature to 90°C for the hot stretching of tip drawn fiber. A small heater is placed $\sim 1 \text{ cm}$ above the hot plate and the temperature is set to $120^\circ\text{C} - 130^\circ\text{C}$. A schematic of the process is shown in Fig. 2.5. When a gel-drop on the silicon chip melts, a microfiber with a length of hundreds of microns is drawn from the molten gel using a sharp glass tip (tip diameter $\sim 10 \mu\text{m}$). Convective current evaporates the solvent from the drawn microfiber, solidifying the viscous fiber and reducing its diameter to $< 5 \mu\text{m}$. The fiber is then further hot drawn at an ambient temperature of 90°C slowly until the desired length and diameter are achieved. This drawing process takes $\sim 1 - 2$ minutes and is done under a dark field stereo microscope. A large shear rate $> 1500 \text{ s}^{-1}$ and a small diameter significantly suppresses the growth of kebab, a lamellar structure within fiber [16], and enhance unfolding of the lamellae to oriented fibrillar crystals. Highly crystalline and aligned samples can be fabricated using this technique.

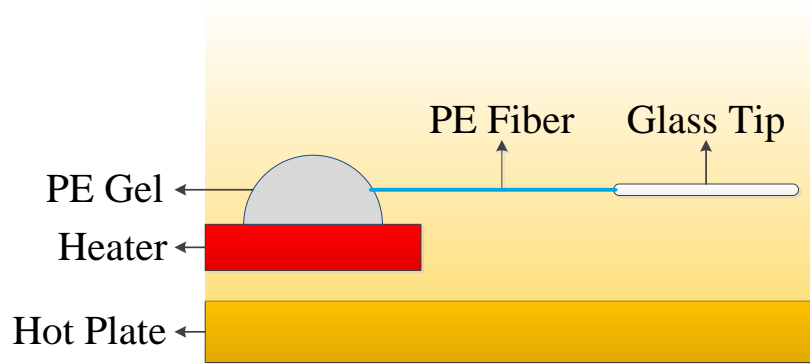


Figure 2.5: Schematic of two state tip drawing method [63].

2.4 Thermal transport in polymers

In a dielectric solid, heat is carried by quantized lattice vibrations also called as phonons. However, bulk polymers are amorphous with defects such as entanglements, dangling chain ends, voids and impurities which scatter the phonons. Therefore, bulk polymers have low thermal conductivity $0.1 \text{ W m}^{-1} \text{ K}^{-1} - 2 \text{ W m}^{-1} \text{ K}^{-1}$ [64]. Enhanced thermal transport in the polymer is desirable for many applications such as heat spreader, electronic packaging and thermal interface material. Their intrinsic properties such as low density, electrically insulating, chemically inert and easy to mass-produce give them a technological advantage over other classes of material.

2.4.1 Thermal enhancement in polymers

A typical approach to enhance the thermal conductivity of polymers has been to embed a high thermal conductivity material such as a metal, a ceramic, a carbon nanotube, graphene and recently, liquid metal droplets in a polymer resin [65]–[68]. However, this approach can yield only limited enhancement of $\sim 10\text{X}$, even though the fillers such as carbon nanotubes and graphene may

have ~1000X higher thermal conductivity. This is because of the high interfacial thermal resistance between the additive and the polymer matrix [69].

Alternatively, it has been found that a large enhancement in thermal properties is achievable by increasing crystallinity and alignment of polymer molecules [70]. With the development of several fabrication methods such as gel spinning and two-stage tip drawing along with drawing, researchers have been able to increase the crystallinity and align the backbone chain which significantly reduces phonon scattering sites. Consequently, higher thermal conductivity in polymers such as PE has been achieved [15], [71], [72].

The alignment of chain molecules due to drawing also introduces anisotropic thermal conductivity. Burgess and Greig extruded PE samples up to a draw ratio of 4 and measured the thermal conductivity in directions parallel and perpendicular to the fiber axis at temperatures from 2 K to 100 K. They obtained anisotropic conductivity at 100 K with a maximum thermal conductivity of $2.1 \text{ W m}^{-1} \text{ K}^{-1}$ along the drawing direction [73]. It has been observed that increasing the draw ratio increases the anisotropy as well as the thermal conductivity. Gibson et al. increased the draw ratio in LMWPE up to 20 and measured an anisotropy ratio of 18.5, with a maximum thermal conductivity of $9.1 \text{ W m}^{-1} \text{ K}^{-1}$ [74]. Mergenthaler et al. were able to achieve a larger draw ratio (250) in ultra-high molecular weight polyethylene (UHMWPE) and thus higher thermal conductivity ($37.5 \text{ W m}^{-1} \text{ K}^{-1}$) [71]. Choy et al. stretched the single crystal mat up to draw ratio of 400 and obtained even higher thermal conductivity in the stretching direction. The thermal conductivity at RT was $41 \text{ W m}^{-1} \text{ K}^{-1}$ [75]. In addition to crystallinity, Xu et al. and Zhu et al. demonstrated that alignment of amorphous chains also plays an important role in thermal transport and could improve the thermal conductivity of PE to as high as $50\text{--}60 \text{ W m}^{-1} \text{ K}^{-1}$ in a nanostructured thin film and a microfiber.

These works were done on microfibers or on thin films. As the dimensions' decrease, the defect density tends to reduce as well. Recently, Singh et al. demonstrated a nanoscale size effect in an amorphous polythiophene nanofiber [76]. Increased molecular orientation along the fiber axis due to electropolymerization on nanopore channels was attributed to a ~20X increase in thermal conductivity below 100 nm. In electrospun PE nanofibers, Ma et al. obtained a moderate enhancement compared to gel spun and drawn PE microfibers. The thermal conductivity value was as high as $9.3 \text{ W m}^{-1} \text{ K}^{-1}$ at RT [57]. Note that, electrospinning also gives only moderately crystalline and aligned specimen. In addition, Ma et al. did not have a post-drawing process to further align molecules and increase the crystallinity. Using a two-stage tip drawing method, Shen et al. fabricated nanofibers with a high draw ratio of 410 and achieved the highest reported metal like thermal conductivity of $104 \text{ W m}^{-1} \text{ K}^{-1}$ at RT [15]. This is higher than the conductivities of several metals and alloys including platinum ($\sim 70 \text{ W m}^{-1} \text{ K}^{-1}$), nickel ($\sim 90 \text{ W m}^{-1} \text{ K}^{-1}$) and stainless steel ($\sim 12 - 45 \text{ W m}^{-1} \text{ K}^{-1}$) [64]. This is still lower than a theoretical estimate based on molecular dynamics simulation for a bulk crystal which suggests that the thermal conductivity can be as high as $180 \pm 65 \text{ W m}^{-1} \text{ K}^{-1}$ [15].

Henry and Chen performed molecular dynamics simulation on a single PE chain allowing the internal degree of freedom for hydrogen atoms in a backbone chain [77]. A very high thermal conductivity of $350 \text{ W m}^{-1} \text{ K}^{-1}$ was estimated. They also noted that it could even be divergent in longer simulation domain where low-frequency modes do not fully attenuate [77]. Ab-initio calculations done by Jiang et al. show similar high value ($\sim 310 \text{ W m}^{-1} \text{ K}^{-1}$ at RT) of the thermal conductivity of a PE chain [78]. The experimental value, at best $\sim 100 \text{ W m}^{-1} \text{ K}^{-1}$, is only one-third of the theoretical estimate. This suggests there is still plenty of room for improvement for PE.

2.4.2 Temperature dependent behavior of PE

For a dielectric crystal at very low temperature, the thermal conductivity behavior is dominated by the heat capacity. So, thermal conductivity increases with T^3 as predicted by the Debye T^3 law [79]. For long-wavelength excitations at very low temperatures ($<10\text{K}$), polymer chains can interact through the weak Vander Waal forces. In such case, vibrations will be isotropic and can be explained by Debye T^3 law. However, the Debye model does not explain the thermal conductivity behavior of polymer crystals at intermediate temperatures. This is because of the one-dimensional nature of the polymer chains since the covalent bonding along the backbone is much stronger than the inter-chain Van der Waal interactions. For shorter wavelength and higher frequency, strong along-chain interactions dominate, so specific heat becomes one-dimensional. Therefore, thermal conductivity also increases as T^1 . A simple continuum model to explain both three-dimensional behavior at very low temperatures, and one-dimensional behavior at intermediate temperatures, was first developed by Tarasov [80]. Detailed review on temperature dependent thermal properties of polymers at low temperatures has been done by Reese [81], Wunderlich and Baur [82] and Choy [83].

At low temperatures, where the anharmonic phonon scattering is weak, the mean free path is usually limited by extrinsic scattering mechanisms, such as defect and boundary scattering [84]. The thermal conductivity trend at low temperatures, therefore, also depends on size. For example, at low temperatures, the thermal conductivity of bulk silicon and relatively large silicon nanowires ($\sim 110\text{ nm}$) follow the Debye T^3 law. However, when the size of the nanowire is reduced to $\sim 30\text{ nm}$, the thermal conductivity trend becomes T^1 . This linear trend on thin silicon nanowires has been attributed to several mechanisms, including frequency-dependent boundary scattering rates [85], surface oxidation [86], phonon confinement and reduced phonon group velocity [87], [88].

Such size effects may also exist in crystalline polymer nanofibers, which have not been explored. This effect is explored in Chapter 4.

As the temperature increases, the number of phonon modes at any given frequency increases, increasing the thermal conductivity. However, as the number of phonon modes increases, the probability of scattering events also increases. This anharmonic phonon-phonon scattering, known as Umklapp scattering, begins to dominate and reduce the thermal conductivity after a certain temperature threshold ($\sim\theta_D/10$), where θ_D is the Debye temperature. The thermal conductivity begins to drop with a $1/T$ dependence [79]. This is significant for crystalline materials with low defects [79], and has been demonstrated in a gel spun PE microfiber [89].

When the temperature further increases but before it reaches the T_m (where the crystal domain becomes amorphous), the chain molecule gains an additional degree of freedom from the segmental rotation. This conformational change can further increase phonon scattering events. Segmental rotation in combination with the Umklapp scattering sharply reduces the thermal conductivity. This abrupt change in thermal conductivity is predicted at ~ 400 K [90]. Such conformation scattering phenomenon has not been experimentally studied. I have explored this in Chapter 5. Recently, Wang et al. demonstrated that gel spun PE microfiber has thermal conductivity decreases faster than that Umklapp scattering alone can predict, however, the detailed interpretation was absent. Their PE microfiber melted at ~ 415 K.

2.4.3 Melting of polyethylene

One of the major limitations of PE for heat transfer applications is its low melting temperature (for UHMWPE $T_m = 414$ K). Wunderlich and Czornyj studied the equilibrium melting temperature of an orthorhombic PE and found it to be 414.6 K, which is consistent with the

previous estimate based on the extrapolation of melting temperatures of n-paraffins to infinity by Broadhurst [91], [92]. On fibers firmly clamped between glass plates or glued to a glass using epoxy, Pennings and van der Mark observed persistent birefringence up to 453 K, significantly higher than the equilibrium T_m [93]. Further detailed study on the melting process of constrained PE fibers using differential scanning calorimeter (DSC) and X-ray diffraction (XRD) revealed a phase transition from an orthorhombic to a hexagonal phase prior to melting at 428 K [9]. A hexagonal phase was also found in PE under high pressure above 300 MPa by Yasuniwa et al. [94]. This hexagonal phase exhibited a long-range order, however, it lacked a short range order due to conformational disorder [95]. Tsubakihara et al. verified that the hexagonal phase under high pressure is the same as the hexagonal phase in a constrained PE fiber [96]. In addition, Rastogi and Odell found that the stress can be used to stabilize an oriented PE fiber against melting up to 452 K [97]. The transformation of the orthorhombic phase to the hexagonal phase and the stabilization of the hexagonal phase is studied in Chapter 5.

During the phase transformation from the orthorhombic to the hexagonal phase, the chain molecules gain an additional degree of freedom from the segmental rotation. Segmental rotation introduces gauche conformations. This conformational change act as a structural defect along the chain increasing phonon scattering events. Large-scale molecular dynamics simulation suggest that increased segmental rotation can cause disorder along the chains and lead to a thermal conductivity switching up to 12 [90]. In addition, this thermal conductivity switching is predicted to be tunable and fully reversible [98]. Such active control of thermal transport is of significant interest for a broad range of applications, including heating and cooling, energy conversion, materials processing, and data storage [99]. Based on a literature survey, there has not been any

experimental evidence of such reversible thermal conductivity switching in PE. I have explored the reversible thermal switching in PE in Chapter 5.

2.5 Mechanical characterization of polymer nanofiber

Just as defects such as entanglements, dangling chain ends, voids and impurities reduce thermal conductivity, they also explain low elastic modulus and strength in polymers. It has been long known that C–C bond is stiff and strong. Even with C–C backbone, bulk PE has low modulus (~1 GPa) and strength (<50 MPa). Mechanical properties are generally enhanced as we extend from the micrometer to the nanometer scale [16], [100]–[103]. This is often attributed to the small volume in which the probability of a critical flaw size is significantly reduced.

2.5.1 Elastic-plastic behavior of PE fiber

Over the years, different crystallization and drawing methods have been developed to decrease the defects present in PE fibers with a goal of realizing an enhancement of Young's modulus and strength. This section reviews those methods in detail.

Early works on modulus and strength were carried out in the 1960s on single crystal mats of normal weight linear PE by Statton where the author observed Young's modulus of 10 GPa and a strength of 0.67 GPa [104]. These samples were hot drawn at 125 °C up to a draw ratio of 40 [104]. These were very high compared to a modulus of ~3 GPa at a more typical contemporary draw ratio of 4 and attracted significant attention. Kenamoto et al. extruded single crystal mats of PE with MW of 58,000 (LMWPE) up to 45X at 90 – 110 °C and obtained Young's modulus as high as 60 GPa [19]. With the shorter backbone chain, the maximum draw ratio achieved was between 30 and 40 [8]. With UHMWPE dissolved in solution, researchers were able to obtain

stiffer, stronger fibers. Smook et al. developed surface growth fibers and achieved a modulus of 120 GPa and a strength of 4.7 GPa [105]. Even though UHMWPE solution-drawn fibers were stiffer and much stronger than the LMWPE fibers, the fiber production rate was too low for commercial interest.

This issue was solved by Smith and Lemstra in 1980, who developed the gel spinning method [106] discussed in Section 2.3.1 Here, at a draw ratio of 30, Young's modulus of 90 GPa, and a tensile strength of 3 GPa were achieved [106]. Kanamoto et al., in 1983, used two-stage heating to extrude and draw UHMWPE single crystal mats from dilute solutions in xylene reaching a draw ratio up to 250 [20]. The Young's modulus was reported to be 220 GPa, however, the sample broke at the grips at 0.9 GPa to 2 GPa so the authors did not report a value for the tensile strength [20].

Smook and Pennings also developed a gel spinning method where they were able to transform the shish-kebab morphology into smooth fibrillar structure upon hot drawing at 148 °C to draw ratio above 80 [21]. Using differential scanning calorimetry [21], the measured peak T_m increased from 135 °C to 143 °C as draw ratio increased, and the heat of fusion at the highest draw ratio closely approached that of crystalline PE. Here, it was learned that although the gel initially contains shish kebab structures, they are largely removed at a draw ratio of 80, folded chain lamellae unfolded during the drawing process, and were pulled taut between remaining entanglements. Impressive values of 210 GPa and tensile strength of 6 GPa were achieved [107]. As draw ratio is increased, it is possible to obtain fibers of even higher crystallinity. These, in turn, will be stiffer and stronger. Werff and Pennings achieved the highest reported strength of 7.2 GPa in a gel spun fiber with Young's modulus of 264 GPa [108].

All the above-described measurements were made on microfibers. By optimizing the gel electrospinning process at an elevated temperature, Park and Rutledge achieved tensile strength up to 6.3 GPa and elastic modulus up to 110 GPa on a fiber of 490 nm diameter. Recently, Li et al. fabricated UHMWPE nanofibers using a two-stage tip drawing (discussed in Section 2.3.2) method drawn at 90 °C up to 1400X [16]. Selected area electron diffraction (SAED) revealed the nanofiber to be highly crystalline showing distinct spots in the diffraction pattern. The samples exhibited high stiffness 312 ± 108 GPa, near to the theoretical limit [16]. The samples were measured using an atomic force microscope (AFM) based three-point bending method and probed only to a small displacement, so strength values were not reported.

There has been considerable interest to understand the upper limit of strength in these highly drawn PE fibers. A semi-empirical model was established by Smook et al. where they asserted that strength was determined by the defects in the fibrillar structure and surface imperfections such as kink bands. When the diameter was reduced, both surface imperfections and fibrillar structure defects reduced significantly. They analyzed a Griffith-like scenario where the strength of a material is limited due to the flaws and imperfections that induce a crack which propagates once it reaches a critical size. They plotted the strength versus diameter and extrapolated it until the diameter reaches zero which results in a flawless fiber strength (theoretical strength) corresponding to 26 GPa [109]. Similar to Smook's method, Pennings et al. used extrapolation of experimentally obtained data to estimate the theoretical strength. They used a morphological model first proposed by Dijkstra et al. which assumes that the strength of a fiber is determined by the volume fraction of load carrying TTM in the disordered domain and the failure is the result of rupture of TTM. They obtained a linear relationship between strength and volume

fraction of TTM. Extrapolating the load bearing chains to unity, they estimated the theoretical strength to be 30 ± 3 GPa [107].

Even though the field is mostly driven by experimental work, extensive work has been carried out to predict the theoretical limit for the modulus and strength of a fully extended crystalline PE chains. Ab initio calculations predicted an upper limit in Young's modulus of PE chains to be 374.5 GPa [78]. Experimentally obtained unit cell dimensions have also been used to estimate crystal theoretical limit. X-ray, neutron, and Raman scattering have been used to obtain values of c-axis (crystal axis along the fiber axis) that corresponded to theoretical Young's moduli of 240 GPa, 329 GPa and 358 GPa, respectively [110]. In the X-ray based method, the basic assumption that macroscopic stress is same as the microscopic stress on the crystal was found to be prone to errors due to the presence of amorphous material where the stress was lower. When the material is cooled below the glass transition temperature, the amorphous material stiffens and a higher estimate for Young's modulus can be obtained with X-ray studies while minimal increase has been obtained in Raman and neutron scattering [110]. In light of these, Fanconi and Rabolt concluded that neutron and Raman scattering to be a correct benchmark for chain-axis Young's modulus estimate [110].

There have also been several approaches to estimate the theoretical strength of PE. First-principle calculations based on C–C bond scission predict strength ~ 30 GPa [111]. Tianbai calculated the theoretical strength of PE using a kinetic theory of fracture and estimated a strength of 32 GPa [112]. Quantum mechanical ab initio molecular orbital theory yielded a maximum stress at 34 GPa [111]. While impressive strength value is estimated, most experimental strengths are limited to 7 GPa [108]. Chain slip originating at the chain ends is thought to be the dominant failure mechanism limiting the upper limit of strength to $\sim 6 - 10$ GPa [111], [113].

2.5.2 Viscoelastic behavior of polymer nanofiber

While most of the discussions above on mechanical behavior are limited to the elastic-plastic properties, nanofibers also exhibit viscoelastic behavior significantly different than the bulk. At the nanoscale, the reorganization of the interior core polymer chains and an increase in the relative amount of fluid-like chains on the surface contribute to a size-effect observed in elastic-plastic as well as rheological behavior [114]–[120], both of which affect the viscoelastic behavior.

McKenna and Jackson discovered that the confinement of the polymer into nanoscale pores can lead to depression in the glass transition temperature [121]. A detailed review on the effect of spatial confinement on polymer rheological behavior by Alcoutlabi and McKenna can be found in [122]. Numerous viscoelastic studies [123]–[125] have been done on thin films since the pioneering work of O’Connell and McKenna [126], who developed a nano-bubble inflation technique.

However, viscoelastic measurements on polymer nanofibers are few. One of the major reasons is the lack of experimental tools with temporal, spatial and force resolution. Recently, Naraghi et al. designed and developed a surface micromachined platform capable of performing creep and high strain rate measurements [128], [129]. Creep measurement on as-electrospun polyacrylonitrile (PAN) nanofibers with a diameter between 200–700 nm was performed. Due to a finite ramp time of 10 s to apply a creep stress, creep measurement gave reliable creep compliance above 10 s. They demonstrated size dependent creep compliance on electrospun nanofiber where a smaller fiber exhibited suppressed creep compliance [129]. This was attributed to the increased molecular orientation with the reduction in nanofiber diameter. In addition to creep measurement, strain rate measurements spanning six decades from $2.5 \times 10^{-4} \text{ s}^{-1}$ to 200 s^{-1} were performed, where the energy dissipation capacity of the nanofiber increased significantly with the

strain rate. Furthermore, strain rate experiments along with a spring-dashpot model were used to obtain creep behavior with time constants from as small as 1 ms up to 500 s. From the strain rate and creep measurements, size-dependent creep compliance master curve spanning 8 decades from 0.1 ms to 10000 s were computed. Recently, Wingert et al. used AFM probes to measure stress relaxation of electrospun nylon-11 nanofibers from 65 to 500 nm in a SEM where they found increased relaxation modulus with reducing diameter [130]. Using a standard linear solid model, relaxation modulus and time constant were analyzed. Stress-relaxation experiments were done over a strain range of 1.5 % – 7 %, whereas the elastic limit was determined to be less than 6 %–8 % [130]. Therefore, a careful examination is necessary for high strain measurements to ensure within the linear viscoelastic limit. In Chapter 7, new methods to study linear viscoelasticity in PAN nanofibers will be proposed and investigated, and a time-temperature superposition curves will be constructed for these fibers.

2.6 Chapter summary

In this chapter, polymer crystallization, drawing, micro/nanofiber fabrication and their mechanical and thermal characterization have been extensively reviewed with UHMWPE as a reference. Several fabrication methods and post drawing techniques have been developed over the years to enhance the mechanical and thermal properties of PE. Two-stage tip drawing was found to be most promising to achieve a highly crystalline PE nanofiber with a very high draw ratio ~1400. Thermal conductivity as high as $\sim 100 \text{ W m}^{-1} \text{ K}^{-1}$ and a near theoretical Young's modulus $\sim 312 \text{ GPa}$ [16] has been achieved. To achieve high thermal conductivity and strength, molecular alignment of TTM in the amorphous region is important [131], [132]. Under constraint, PE microfiber exhibits an orthorhombic – hexagonal phase transition at $\sim 423 \text{ K}$ prior to melting [133].

The hexagonal phase has a long-range order, however, lacks short-range conformational order [95]. Elastic-plastic and viscoelastic measurements of polymer nanofibers have been briefly reviewed as well.

2.7 Chapter references:

- [1] P. C. Hiemenz and T. P. Lodge, *Polymer Chemistry, Second Edition*. Taylor & Francis, 2007.
- [2] W. D. Callister Jr, *Materials Science and Engineering*. 1940.
- [3] D. R. Norton and A. Keller, “The spherulitic and lamellar morphology of melt-crystallized isotactic polypropylene,” *Polymer (Guildf)*., vol. 26, no. 5, pp. 704–716, May 1985.
- [4] A. J. Pennings and A. M. Kiel, “Fractionation of polymers by crystallization from solution, III. On the morphology of fibrillar polyethylene crystals grown in solution,” *Kolloid-Zeitschrift und Zeitschrift für Polym.*, vol. 205, no. 2, pp. 160–162, 1965.
- [5] M. J. Hill and A. Keller, “Direct evidence for distinctive, stress-induced nucleus crystals in the crystallization of oriented polymer melts,” *J. Macromol. Sci. Part B*, vol. 3, no. 1, pp. 153–169, Mar. 1969.
- [6] A. J. Pennings, C. J. H. Schouteten, and A. M. Kiel, “Hydrodynamically induced crystallization of polymers from solution. V. Tensile properties of fibrillar polyethylene crystals,” *J. Polym. Sci. Part C Polym. Symp.*, vol. 38, no. 1, pp. 167–193, Mar. 2007.
- [7] M. J. Hill, P. J. Barham, and A. Keller, “On the hairdressing of shish-kebabs,” *Colloid Polym. Sci.*, vol. 258, no. 9, pp. 1023–1037, Sep. 1980.
- [8] P. J. Barham and A. Keller, “High-strength polyethylene fibres from solution and gel spinning,” *J. Mater. Sci.*, vol. 20, no. 7, pp. 2281–2302, 1985.
- [9] A. J. Pennings and A. Zwijnenburg, “Longitudinal growth of polymer crystals from flowing solutions. VI. Melting behavior of continuous fibrillar polyethylene crystals,” *J. Polym. Sci. Polym. Phys. Ed.*, vol. 17, no. 6, pp. 1011–1032, 1979.
- [10] A. Zwijnenburg, P. F. van Hutten, A. J. Pennings, and H. D. Chanzy, “Longitudinal growth of polymer crystals from flowing solutions V.: Structure and morphology of fibrillar polyethylene crystals,” *Colloid Polym. Sci. Kolloid Zeitschrift Zeitschrift für Polym.*, vol. 256, no. 8, pp. 729–740, 1978.
- [11] S. K. Smoukov, T. Tian, N. Vitchuli, S. Gangwal, P. Geisen, M. Wright, E. Shim, M. Marquez, J. Fowler, and O. D. Velev, “Scalable liquid shear-driven fabrication of polymer

- nanofibers,” *Adv. Mater.*, vol. 27, no. 16, pp. 2642–2647, 2015.
- [12] A. J. Pennings, R. J. Hooft, A. R. Postema, W. Hoogsteen, and G. Brinke, “High-speed gel-spinning of ultra-high molecular weight polyethylene,” *Polym. Bull.*, vol. 16, no. 2–3, pp. 167–174, 1986.
- [13] J. Doshi and D. H. Reneker, “Electrospinning process and applications of electrospun fibers,” *J. Electrostat.*, vol. 35, no. 2–3, pp. 151–160, Aug. 1995.
- [14] T. Subbiah, G. S. Bhat, R. W. Tock, S. Parameswaran, and S. S. Ramkumar, “Electrospinning of nanofibers,” *J. Appl. Polym. Sci.*, vol. 96, no. 2, pp. 557–569, 2005.
- [15] S. Shen, A. Henry, J. Tong, R. Zheng, and G. Chen, “Polyethylene nanofibres with very high thermal conductivities,” *Nat. Nanotechnol.*, vol. 5, no. 4, pp. 251–255, 2010.
- [16] P. Li, L. Hu, A. J. H. McGaughey, and S. Shen, “Crystalline polyethylene nanofibers with the theoretical limit of Young’s modulus,” *Adv. Mater.*, vol. 26, no. 7, pp. 1065–1070, 2014.
- [17] W. H. Carothers and J. W. Hill, “Studies of Polymerization and Ring Formation. XV. Artificial Fibers From Synthetic Linear Condensation Superpolymers,” *J. Am. Chem. Soc.*, vol. 54, no. 4, pp. 1579–1587, 1932.
- [18] P. J. Barham and A. Keller, “A study on the achievement of high-modulus polyethylene fibres by drawing,” *J. Mater. Sci.*, vol. 11, no. 1, pp. 27–35, 1976.
- [19] T. Kanamoto, E. S. Sherman, and R. S. Porter, “Extrusion of Polyethylene Single Crystals,” *Polym. J.*, vol. 11, no. 6, pp. 497–502, Jun. 1979.
- [20] T. Kanamoto, A. Tsuruta, K. Tanaka, M. Takeda, and R. S. Porter, “On Ultra-High Tensile Modulus by Drawing Single Crystal Mats of High Molecular Weight Polyethylene,” *Polym. J.*, vol. 15, no. 4, pp. 327–329, Apr. 1983.
- [21] J. Smook and J. Pennings, “Influence of draw ratio on morphological and structural changes in hot-drawing of UHMW polyethylene fibres as revealed by DSC,” *Colloid Polym. Sci.*, vol. 262, no. 9, pp. 712–722, 1984.
- [22] M. Richard-Lacroix and C. Pellerin, “Molecular Orientation in Electrospun Fibers: From Mats to Single Fibers,” *Macromolecules*, vol. 46, no. 24, pp. 9473–9493, Dec. 2013.
- [23] G. Capaccio and I. M. Ward, “Polymer Science Shrinkage, shrinkage force and the structure of ultra high modulus polyethylenes *),” *Colloid Polym. Sci.*, vol. 260, pp. 46–55, 1982.
- [24] E. Zussman, X. Chen, W. Ding, L. Calabri, D. A. Dikin, J. P. Quintana, and R. S. Ruoff, “Mechanical and structural characterization of electrospun PAN-derived carbon nanofibers,” *Carbon N. Y.*, vol. 43, no. 10, pp. 2175–2185, 2005.

- [25] F. Chen, X. Peng, T. Li, S. Chen, X.-F. Wu, D. H. Reneker, and H. Hou, “Mechanical characterization of single high-strength electrospun polyimide nanofibres,” *J. Phys. D. Appl. Phys.*, vol. 41, no. 2, p. 25308, Jan. 2008.
- [26] J. Yao, C. Bastiaansen, and T. Peijs, “High Strength and High Modulus Electrospun Nanofibers,” *Fibers*, vol. 2, no. 2, pp. 158–186, Apr. 2014.
- [27] A. Zwijnenburg, A. J. Pennings, and R. September, “Department of Polymer Chemistry , Stale University of Groningen , Groningen (The Netherlands) L o n g i t u d i n a l g r o w t h o f p o l y m e r c r y s t a l s f r o m f l o w i n g s o l u t i o n s I I I . P o l y e t h y l e n e c r y s t a l s i n C o u e t t e f l o w f i b r i l l a r p o l y e t h y l e n e c r y s ,” vol. 881, pp. 868–881, 1976.
- [28] Z. Yufeng, X. Changfa, J. I. A. Guangxia, and A. N. Shulin, “Study on Gel-Spinning Process of Ultra-High Molecular,” no. 670, pp. 670–675, 1999.
- [29] J. R. Dees and Spruiell .E., “Structure Development During Melt Spinning of Linear Polyethylene Fibers.,” *J. Appl. Polym. Sci.*, vol. 18, no. 4, pp. 1053–1078, 1974.
- [30] J. H. Wendorff, A. Greiner, and R. B. Wehrspohn, “Polymer Nanotubes by Wetting of Ordered Porous Templates,” *Science (80-.)*, vol. 296, no. 5575, p. 1997, 2002.
- [31] B. Y. Cao, Y. W. Li, J. Kong, H. Chen, Y. Xu, K. L. Yung, and A. Cai, “High thermal conductivity of polyethylene nanowire arrays fabricated by an improved nanoporous template wetting technique,” *Polymer (Guildf)*, vol. 52, no. 8, pp. 1711–1715, 2011.
- [32] J. Martín, J. Maiz, J. Sacristan, and C. Mijangos, “Tailored polymer-based nanorods and nanotubes by "template synthesis": From preparation to applications,” *Polymer (Guildf)*, vol. 53, no. 6, pp. 1149–1166, 2012.
- [33] N. Bhardwaj and S. C. Kundu, “Electrospinning: A fascinating fiber fabrication technique,” *Biotechnol. Adv.*, vol. 28, no. 3, pp. 325–347, 2010.
- [34] A. Greiner and J. H. Wendorff, “Electrospinning: A fascinating method for the preparation of ultrathin fibers,” *Angew. Chemie - Int. Ed.*, vol. 46, no. 30, pp. 5670–5703, 2007.
- [35] S. H. Tan, R. Inai, M. Kotaki, and S. Ramakrishna, “Systematic parameter study for ultra-fine fiber fabrication via electrospinning process,” *Polymer (Guildf)*, vol. 46, no. 16, pp. 6128–6134, 2005.
- [36] D. H. Reneker and I. Chun, “Nanometre diameter fibres of polymer, produced by electrospinning,” *Nanotechnology*, vol. 7, no. 3, pp. 216–223, Sep. 1996.
- [37] H. Blades, “Dry jet wet spinning process.” Google Patents, 1973.
- [38] H. Jia, G. Zhu, B. Vugrinovich, W. Kataphinan, D. H. Reneker, and P. Wang, “Enzyme-Carrying Polymeric Nanofibers Prepared via Electrospinning for Use as Unique Biocatalysts,” *Biotechnol. Prog.*, vol. 18, no. 5, pp. 1027–1032, Oct. 2002.

- [39] J. Zeng, X. Xu, X. Chen, Q. Liang, X. Bian, L. Yang, and X. Jing, "Biodegradable electrospun fibers for drug delivery," 2003.
- [40] H. Yoshimoto, Y. M. Shin, H. Terai, and J. P. Vacanti, "A biodegradable nanofiber scaffold by electrospinning and its potential for bone tissue engineering," 2003.
- [41] W.-J. Li, C. T. Laurencin, E. J. Caterson, R. S. Tuan, and F. K. Ko, "Electrospun nanofibrous structure: A novel scaffold for tissue engineering," *J. Biomed. Mater. Res.*, vol. 60, no. 4, pp. 613–621, Jun. 2002.
- [42] R. Gopal, S. Kaur, Z. Ma, C. Chan, S. Ramakrishna, and T. Matsuura, "Electrospun nanofibrous filtration membrane," *J. Memb. Sci.*, vol. 281, no. 1, pp. 581–586, 2006.
- [43] R. S. Barhate and S. Ramakrishna, "Nanofibrous filtering media: Filtration problems and solutions from tiny materials," *J. Memb. Sci.*, vol. 296, no. 1, pp. 1–8, 2007.
- [44] J. Fang, H. Niu, H. Wang, X. Wang, and T. Lin, "Enhanced mechanical energy harvesting using needleless electrospun poly(vinylidene fluoride) nanofibre webs," *Energy Environ. Sci.*, vol. 6, no. 7, p. 2196, 2013.
- [45] J. B. Ballengee and P. N. Pintauro, "Composite Fuel Cell Membranes from Dual-Nanofiber Electrospun Mats," *Macromolecules*, vol. 44, no. 18, pp. 7307–7314, Sep. 2011.
- [46] T. Tamura and H. Kawakami, "Aligned Electrospun Nanofiber Composite Membranes for Fuel Cell Electrolytes," *Nano Lett.*, vol. 10, no. 4, pp. 1324–1328, Apr. 2010.
- [47] Z. Sun, E. Zussman, A. L. Yarin, J. H. Wendorff, and A. Greiner, "Compound Core–Shell Polymer Nanofibers by Co-Electrospinning," *Adv. Mater.*, vol. 15, no. 22, pp. 1929–1932, Nov. 2003.
- [48] D. Li and Y. Xia, "Direct Fabrication of Composite and Ceramic Hollow Nanofibers by Electrospinning," *Nano Lett.*, vol. 4, no. 5, pp. 933–938, May 2004.
- [49] J. T. McCann, D. Li, and Y. Xia, "Electrospinning of nanofibers with core-sheath, hollow, or porous structures," *J. Mater. Chem.*, vol. 15, no. 7, p. 735, 2005.
- [50] I. S. Chronakis, "Novel nanocomposites and nanoceramics based on polymer nanofibers using electrospinning process—A review," *J. Mater. Process. Technol.*, vol. 167, no. 2, pp. 283–293, 2005.
- [51] Y. Zhang, H. Ouyang, C. T. Lim, S. Ramakrishna, and Z.-M. Huang, "Electrospinning of gelatin fibers and gelatin/PCL composite fibrous scaffolds," *J. Biomed. Mater. Res.*, vol. 72B, no. 1, pp. 156–165, Jan. 2005.
- [52] Q. Zhao, Z. Huang, C. Wang, Q. Zhao, H. Sun, and D. Wang, "Preparation of PVP/MEH-PPV composite polymer fibers by electrospinning and study of their photoelectronic character," 2007.

- [53] I. Cucchi, F. Spano, U. Giovanella, M. Catellani, A. Varesano, G. Calzaferri, and C. Botta, “Fluorescent Electrospun Nanofibers Embedding Dye-Loaded Zeolite Crystals,” *Small*, vol. 3, no. 2, pp. 305–309, Feb. 2007.
- [54] X. Xu, Q. Yang, Y. Wang, H. Yu, X. Chen, and X. Jing, “Biodegradable electrospun poly(l-lactide) fibers containing antibacterial silver nanoparticles,” *Eur. Polym. J.*, vol. 42, no. 9, pp. 2081–2087, 2006.
- [55] X. Lu, Y. Zhao, and C. Wang, “Fabrication of PbS Nanoparticles in Polymer-Fiber Matrices by Electrospinning,” *Adv. Mater.*, vol. 17, no. 20, pp. 2485–2488, Oct. 2005.
- [56] E. Zussman, M. Burman, A. L. Yarin, R. Khalfin, and Y. Cohen, “Tensile deformation of electrospun nylon-6,6 nanofibers,” *J. Polym. Sci. Part B Polym. Phys.*, vol. 44, no. 10, pp. 1482–1489, May 2006.
- [57] J. Ma, Q. Zhang, A. Mayo, Z. Ni, H. Yi, Y. Chen, R. Mu, L. M. Bellan, and D. Li, “Thermal conductivity of electrospun polyethylene nanofibers,” *Nanoscale*, vol. 7, no. 40, pp. 16899–16908, 2015.
- [58] J. H. Park and G. C. Rutledge, “Ultrafine high performance polyethylene fibers,” *J. Mater. Sci.*, vol. 53, 2017.
- [59] R. Inai, M. Kotaki, and S. Ramakrishna, “Structure and properties of electrospun PLLA single nanofibres,” *Nanotechnology*, vol. 16, no. 2, pp. 208–213, Feb. 2005.
- [60] N. Zhu and X. Che, “Biofabrication of Tissue Scaffolds,” in *Advances in Biomaterials Science and Biomedical Applications*, InTech, 2013.
- [61] J. Xie, M. R. MacEwan, A. G. Schwartz, and Y. Xia, “Electrospun nanofibers for neural tissue engineering,” *Nanoscale*, vol. 2, no. 1, pp. 35–44, Jan. 2010.
- [62] X. M. Shi, Y. Z. Bin, D. S. Hou, Y. F. Men, and M. Matsuo, “Gelation/crystallization mechanisms of UHMWPE solutions and structures of ultradrawn gel films,” *Polym. J.*, vol. 46, no. 1, pp. 21–35, 2014.
- [63] P. Li, “Mechanical and Thermal Characterizations of Crystalline Polymer Micro/Nanofibers,” Carnegie Mellon University, 2015.
- [64] “CES Edupack 2016 (Granata Design Limited, 2013).”
- [65] D. M. Bigg, “Thermally conductive polymer compositions,” *Polym. Compos.*, vol. 7, no. 3, pp. 125–140, Jun. 1986.
- [66] R. F. Hill and P. H. Supancic, “Thermal Conductivity of Platelet-Filled Polymer Composites,” *J. Am. Ceram. Soc.*, vol. 85, no. 4, pp. 851–857, Dec. 2004.
- [67] M. J. Biercuk, M. C. Llaguno, M. Radosavljevic, J. K. Hyun, A. T. Johnson, and J. E. Fischer, “Carbon nanotube composites for thermal management,” *Appl. Phys. Lett.*, vol.

- 80, no. 15, pp. 2767–2769, Apr. 2002.
- [68] M. D. Bartlett, N. Kazem, M. J. Powell-Palm, X. Huang, W. Sun, J. A. Malen, and C. Majidi, “High thermal conductivity in soft elastomers with elongated liquid metal inclusions,” *Proc. Natl. Acad. Sci. U. S. A.*, vol. 114, no. 9, pp. 2143–2148, Feb. 2017.
- [69] S. T. Huxtable, D. G. Cahill, S. Shenogin, L. Xue, R. Ozisik, P. Barone, M. Usrey, M. S. Strano, G. Siddons, M. Shim, and P. Keblinski, “Interfacial heat flow in carbon nanotube suspensions,” *Nat. Mater.*, vol. 2, no. 11, pp. 731–734, Nov. 2003.
- [70] C. . Choy, W. . Luk, and F. . Chen, “Thermal conductivity of highly oriented polyethylene,” *Polymer (Guildf)*, vol. 19, no. 2, pp. 155–162, Feb. 1978.
- [71] D. B. Mergenthaler, M. Pietralla, S. Roy, and H. G. Kilian, “Thermal conductivity in ultraoriented polyethylene,” *Macromolecules*, vol. 25, no. 13, pp. 3500–3502, Jun. 1992.
- [72] C. L. Choy, Y. Fei, and T. G. Xi, “Thermal conductivity of gel-spun polyethylene fibers,” *J. Polym. Sci. Part B Polym. Phys.*, vol. 31, no. 3, pp. 365–370, Mar. 1993.
- [73] S. Burgess and D. Greig, “The low-temperature thermal conductivity of polyethylene,” *J. Phys. C Solid State Phys.*, vol. 8, no. 11, pp. 1637–1648, Jun. 1975.
- [74] A. G. Gibson, D. Greig, M. Sahota, I. M. Ward, and C. L. Choy, “Thermal conductivity of ultrahigh-modulus polyethylene,” *J. Polym. Sci. Polym. Lett. Ed.*, vol. 15, no. 4, pp. 183–192, Apr. 1977.
- [75] C. L. Choy, Y. W. Wong, G. W. Yang, and T. Kanamoto, “Elastic modulus and thermal conductivity of ultradrawn polyethylene,” *J. Polym. Sci. Part B Polym. Phys.*, vol. 37, no. 23, pp. 3359–3367, Dec. 1999.
- [76] V. Singh, T. L. Bougher, A. Weathers, Y. Cai, K. Bi, M. T. Pettes, S. A. McMenamin, W. Lv, D. P. Resler, T. R. Gattuso, D. H. Altman, K. H. Sandhage, L. Shi, A. Henry, and B. A. Cola, “High thermal conductivity of chain-oriented amorphous polythiophene,” *Nat. Nanotechnol.*, vol. 9, no. 5, pp. 384–90, 2014.
- [77] A. Henry and G. Chen, “High Thermal Conductivity of Single Polyethylene Chains Using Molecular Dynamics Simulations,” *Phys. Rev. Lett.*, vol. 101, no. 23, p. 235502, Dec. 2008.
- [78] J.-W. Jiang, J. Zhao, K. Zhou, and T. Rabczuk, “Superior thermal conductivity and extremely high mechanical strength in polyethylene chains from ab initio calculation,” *J. Appl. Phys.*, vol. 111, no. 12, p. 124304, 2012.
- [79] C. Kittel, *Introduction to solid state physics*. Wiley, 2005.
- [80] V. . Tarasov and G. . Yunitskii, “Theory of heat capacity of chain and layer structures,” *Zh. fiz. khim*, vol. 24, no. 1, pp. 111–128, 1950.

- [81] W. Reese, "Thermal Properties of Polymers at Low Temperatures," *J. Macromol. Sci.*, vol. 3, no. 7, pp. 1257–1295, 1969.
- [82] B. Wunderlich and H. Baur, "Heat Capacities of Linear High Polymers," vol. 7/2, Berlin/Heidelberg: Springer-Verlag, 1970.
- [83] C. L. Choy, "Thermal conductivity of polymers," *Polymer (Guildf.)*, vol. 18, no. 10, pp. 984–1004, Oct. 1977.
- [84] C. L. Choy, S. P. Wong, and K. Young, "Model calculation of the thermal conductivity of polymer crystals," *J. Polym. Sci. Polym. Phys. Ed.*, vol. 23, no. 8, pp. 1495–1504, Aug. 1985.
- [85] R. Chen, A. I. Hochbaum, P. Murphy, J. Moore, P. Yang, and A. Majumdar, "Thermal Conductance of Thin Silicon Nanowires," *Phys. Rev. Lett.*, vol. 101, no. 105501, 2008.
- [86] N. Mingo, L. Yang, D. Li, and A. Majumdar, "Predicting the Thermal Conductivity of Si and Ge Nanowires," 2003.
- [87] A. Khitun, A. Balandin, and K. L. Wang, "Modification of the lattice thermal conductivity in silicon quantum wires due to spatial confinement of acoustic phonons," 1999.
- [88] J. Zou and A. Balandin, "Phonon heat conduction in semiconductor nanowire," *Nanoscale Therm. Transp. J. Appl. Phys.*, vol. 89, p. 2056, 2001.
- [89] X. Wang, V. Ho, R. A. Segalman, and D. G. Cahill, "Thermal Conductivity of High-Modulus Polymer Fibers," 2013.
- [90] T. Zhang and T. Luo, "Morphology-influenced thermal conductivity of polyethylene single chains and crystalline fibers," *J. Appl. Phys.*, vol. 112, no. 9, p. 094304, 2012.
- [91] B. Wunderlich and G. Czornyj, "A Study of Equilibrium Melting of Polyethylene," UTC, 1975.
- [92] M. G. Broadhurst, "The Melting Temperatures of the n-Paraffins and the Convergence Temperature for Polyethylene," *J. Res. Natl. Bur. Stand. - A. Phys. Chem.*, vol. 70A, no. 6, pp. 481–486, 1966.
- [93] A. J. Pennings and J. M. A. A. Van Der Marlc, "Hydrodynamically induced crystallization of polymers from solution IV. The melting of fibrillar polyethylene crystals*)," *Rheol. Acta*, vol. 10, pp. 174–186, 1971.
- [94] M. Yasuniwa, C. Nakafuku, and T. Takemura, "Melting and Crystallization Process of Polyethylene under High Pressure," *Polym. J.*, vol. 4, no. 5, pp. 526–533, May 1973.
- [95] T. Yamamoto, H. Miyaji, and K. Asai, "Structure and Properties of High Pressure Phase of Polyethylene," *Jpn. J. Appl. Phys.*, vol. 16, no. 11, pp. 1891–1898, Nov. 1977.

- [96] S. Tsubakihara, A. Nakamura, and M. Yasuniwa, "Hexagonal Phase of Polyethylene Fibers under High Pressure," *Polym. J.*, vol. 23, no. 11, pp. 1317–1324, Nov. 1991.
- [97] S. Rastogi and J. A. Odell, "Stress stabilization of the orthorhombic and hexagonal phases of UHM PE gel-spun fibres," *Polymer (Guildf)*, vol. 34, no. 7, pp. 1523–1527, 1993.
- [98] T. Zhang and T. Luo, "High-Contrast, Reversible Thermal Conductivity Regulation Utilizing the Phase Transition of Polyethylene Nanofibers," *ACS Nano*, vol. 7, no. 9, pp. 7592–7600, Sep. 2013.
- [99] G. Wehmeyer, T. Yabuki, C. Monachon, J. Wu, and C. Dames, "Thermal diodes, regulators, and switches: Physical mechanisms and potential applications," *Appl. Phys. Rev.*, vol. 4, no. 4, 2017.
- [100] M. Naraghi, T. Ozkan, I. Chasiotis, S. S. Hazra, and M. P. de Boer, "MEMS platform for on-chip nanomechanical experiments with strong and highly ductile nanofibers," *J. Micromech. Microeng.*, vol. 20, no. 12, p. 125022, 2010.
- [101] B. Wu, A. Heidelberg, and J. J. Boland, "Mechanical properties of ultrahigh-strength gold nanowires," *Nat. Mater.*, vol. 4, no. 7, pp. 525–529, 2005.
- [102] G. Brambilla and D. N. Payne, "The Ultimate Strength of Glass Silica Nanowires," *Nano Lett.*, vol. 9, no. 2, pp. 831–835, Feb. 2009.
- [103] S. Hoffmann, F. Östlund, J. Michler, H. J. Fan, M. Zacharias, S. H. Christiansen, and C. Ballif, "Fracture strength and Young's modulus of ZnO nanowires," *Nanotechnology*, vol. 18, no. 20, p. 205503, 2007.
- [104] W. O. Statton, "Coherence and Deformation of Lamellar Crystals after Annealing," *J. Appl. Phys.*, vol. 38, no. 11, p. 4149, 1967.
- [105] J. Smook, J. C. Torfs, P. F. van Hutten, and A. J. Pennings, "Ultra-high strength polyethylene by hot drawing of surface growth fibers," *Polym. Bull.*, vol. 2, no. 5, pp. 293–300, 1980.
- [106] P. Smith and P. J. Lemstra, "Ultra-high-strength polyethylene filaments by solution spinning/drawing," *J. Mater. Sci.*, vol. 15, no. 2, pp. 505–514, 1980.
- [107] J. P. Penning, H. van der Werff, M. Roukema, and A. J. Pennings, "On the theoretical strength of gelspun/hotdrawn ultra-high molecular weight polyethylene fibres," *Polym. Bull.*, vol. 23, no. 3, pp. 347–352, Mar. 1990.
- [108] H. Van der Werff and A. J. Pennings, "Tensile deformation of high strength and high modulus polyethylene fibers," *Colloid Polym. Sci.*, vol. 269, no. 8, pp. 747–763, Aug. 1991.
- [109] J. Smook, W. Hamersma, and A. J. Pennings, "The fracture process of ultra-high strength polyethylene fibres," *J. Mater. Sci.*, vol. 19, no. 4, pp. 1359–1373, Apr. 1984.

- [110] B. Fanconi and J. F. Rabolt, “The determination of longitudinal crystal moduli in polymers by spectroscopic methods,” *J. Polym. Sci. Polym. Phys. Ed.*, vol. 23, no. 6, pp. 1201–1215, Jun. 1985.
- [111] B. Crist, “The Ultimate Strength and Stiffness of Polymers,” *Annu. Rev. Mater. Sci.*, vol. 25, no. 1, pp. 295–323, Aug. 1995.
- [112] T. He, “An estimate of the strength of polymers,” *Polymer (Guildf.)*, vol. 27, no. 2, pp. 253–255, Feb. 1986.
- [113] T. C. O’connor and M. O. Robbins, “Chain Ends and the Ultimate Strength of Polyethylene Fibers,” vol. 5, p. 51, 2016.
- [114] R. Shrestha, P. Li, B. Chatterjee, T. Zheng, X. Wu, Z. Liu, T. Luo, S. Choi, K. Hippalgaonkar, M. P. de Boer, and S. Shen, “Crystalline polymer nanofibers with ultra-high strength and thermal conductivity,” *Nat. Commun.*, vol. 9, no. 1, p. 1664, 2018.
- [115] M. Naraghi, S. N. Arshad, and I. Chasiotis, “Molecular orientation and mechanical property size effects in electrospun polyacrylonitrile nanofibers,” *Polymer (Guildf.)*, vol. 52, no. 7, pp. 1612–1618, 2011.
- [116] C. T. Lim, E. P. S. Tan, and S. Y. Ng, “Effects of crystalline morphology on the tensile properties of electrospun polymer nanofibers,” *Cit. Appl. Phys. Lett*, vol. 92, p. 141908, 2008.
- [117] M. D. Shelby and G. L. Wilkes, “The effect of molecular orientation on the physical ageing of amorphous polymers—dilatometric and mechanical creep behaviour,” *Polymer (Guildf.)*, vol. 39, no. 26, pp. 6767–6779, Dec. 1998.
- [118] Z. Yang, Y. Fujii, F. K. Lee, C.-H. Lam, and O. K. C. Tsui, “Glass transition dynamics and surface layer mobility in unentangled polystyrene films,” *Science*, vol. 328, no. 5986, pp. 1676–9, Jun. 2010.
- [119] Y. Chai, T. Salez, J. D. McGraw, M. Benzaquen, K. Dalnoki-Veress, E. Raphaël, and J. A. Forrest, “A direct quantitative measure of surface mobility in a glassy polymer,” *Science*, vol. 343, no. 6174, pp. 994–9, Feb. 2014.
- [120] K. Paeng, S. F. Swallen, and M. D. Ediger, “Direct Measurement of Molecular Motion in Freestanding Polystyrene Thin Films,” *J. Am. Chem. Soc.*, vol. 133, p. 16, 2011.
- [121] C. L. Jackson and G. B. McKenna, “The glass transition of organic liquids confined to small pores,” 1991.
- [122] M. Alcoutlabi and G. B. McKenna, “Effects of confinement on material behaviour at the nanometre size scale,” *J. Phys. Condens. Matter*, vol. 17, pp. R461–R524, 2005.
- [123] P. A. O’Connell, S. A. Hutcheson, and G. B. McKenna, “Creep behavior of ultra-thin polymer films,” *J. Polym. Sci. Part B Polym. Phys.*, vol. 46, no. 18, pp. 1952–1965, Sep.

2008.

- [124] † and Hugues Bodiguel* and C. Fretigny, “Viscoelastic Properties of Ultrathin Polystyrene Films,” 2007.
- [125] P. A. O’Connell and G. B. McKenna, “Dramatic stiffening of ultrathin polymer films in the rubbery regime,” *Eur. Phys. J. E*, vol. 20, no. 2, pp. 143–150, Jun. 2006.
- [126] P. A. O’Connell and G. B. McKenna, “Rheological Measurements of the Thermoviscoelastic Response of Ultrathin Polymer Films,” *Science*, vol. 307, no. 5716, pp. 1760–1763, Mar. 2005.
- [127] P. A. O’Connell and G. B. McKenna, “Novel nanobubble inflation method for determining the viscoelastic properties of ultrathin polymer films,” *Rev. Sci. Instrum.*, vol. 78, no. 1, p. 013901, Jan. 2007.
- [128] M. Naraghi, I. Chasiotis, H. Kahn, Y. Wen, and Y. Dzenis, “Mechanical deformation and failure of electrospun polyacrylonitrile nanofibers as a function of strain rate,” *Appl. Phys. Lett.*, vol. 91, no. 15, p. 151901, Oct. 2007.
- [129] M. Naraghi, P. V. Kolluru, and I. Chasiotis, “Time and strain rate dependent mechanical behavior of individual polymeric nanofibers,” *J. Mech. Phys. Solids*, vol. 62, pp. 257–275, 2014.
- [130] M. C. Wingert, Z. Jiang, R. Chen, and S. Cai, “Strong size-dependent stress relaxation in electrospun polymer nanofibers.”
- [131] B. Zhu, J. Liu, T. Wang, M. Han, S. Valloppilly, S. Xu, and X. Wang, “Novel Polyethylene Fibers of Very High Thermal Conductivity Enabled by Amorphous Restructuring,” *ACS Omega*, vol. 2, no. 7, pp. 3931–3944, Jul. 2017.
- [132] D. J. Dijkstra and A. J. Pennings, “The role of taut tie molecules on the mechanical properties of gel-spun UHMWPE fibres,” *Polym. Bull.*, vol. 19, no. 1, pp. 73–80, 1988.
- [133] Kohji Tashiro, A. Sono Sasaki, and M. Kobayashi, “Structural Investigation of Orthorhombic-to-Hexagonal Phase Transition in Polyethylene Crystal: The Experimental Confirmation of the Conformationally Disordered Structure by X-ray Diffraction and Infrared/Raman Spectroscopic Measurements,” *Macromolecules*, vol. 29, no. 23, pp. 7460–7469, 1996.

Chapter 3: Fabrication, manipulation and structural characterization of PE nanofiber

3.1 Abstract

In this chapter, the development of new fabrication processes for ultra-high molecular weight polyethylene (UHMWPE) nanofibers for mechanical and thermal characterization are reported. Their mounting onto two different MEMS devices is also discussed. In addition, structural characterization using micro-Raman analysis revealed the increase in crystallinity and chain backbone orientation along the fiber direction. Selected area electron diffraction patterns obtained using low dose transmission electron microscopy confirmed an orthorhombic lattice structure, as expected for polyethylene (PE). Furthermore, morphological and electron-beam-induced damage in the crystalline PE nanofiber is also discussed.

3.2 Local heat stretching/Local drawing of PENF

The two-stage tip drawing method described in Section 2.3.2 in Chapter 2 produces nanofibers with high crystallinity and molecular alignment. However, it has low yield and lacks consistency in fiber quality. The local heat stretching/local drawing method developed in this chapter has a number of advantages over two-stage tip drawing and gel spinning methods discussed in Section 2.3.1 in Chapter 2, where the whole fiber was heated and stretched over an oven or hot plate until reaching a micro/nanoscale diameter [1], [2]. The thermal conductivity (k) of PE is directly correlated with the crystallinity and molecular alignment along the fiber axis of the sample. The steady-state extension of molecules increases with the strain rate [3]. With the drawing by local heating, a strain rate up to 1400 s^{-1} can be achieved (Section 3.2.3 in Chapter 3)

compared to $\sim 1000 \text{ s}^{-1}$ in gel electrospinning [4] and $\sim 1 \text{ s}^{-1}$ in gel spinning [5]. Another important aspect is the relaxation of molecules, which competes with stretching. In local heating, the fiber is rapidly quenched to minimize the relaxation. The resulting high degree of alignment, coupled with high crystallinity, leads to the improved tensile strength (σ_{ts}) and k . The fiber drawing by local heating yields a segment of nanofiber ($\sim 100 \text{ }\mu\text{m}$ long) that spans between microfibers. Using the microfiber segments for tracking, the nanofiber can be precisely manipulated onto the test platforms. In addition, the fabrication yield is much higher with local drawing. In two-stage tip drawing, hot air flow rising from the hot plate/oven makes the fiber stretching susceptible to local hot spots. A fiber with various hot spots is more likely to have different local stress and strain, increasing the likelihood of premature breakage. The fabrication of polyethylene nanofiber (PENF) using local drawing is detailed below.

3.2.1 Fabrication of polyethylene nanofiber (PENF)

The fabrication of polyethylene nanofibers (PENFs) was conducted in two steps where a microfiber, polyethylene microfibers (PEMF), was tip drawn from a PE/decalin gel and then further stretched to the nanometer scale by localized heating in air.

In this fabrication method, we first produce the PE gel by the same procedure as local tip drawing discussed in Section 2.3.2 in Chapter 2. To make the PE gel, we used 0.8 wt % UHMWPE powder (average molecular weight $3 - 6 \times 10^6 \text{ g mol}^{-1}$ purchased from Sigma Aldrich) and mixed it with a decalin solvent. The mixture is heated on a hot plate to $145 \text{ }^\circ\text{C}$. It becomes transparent and viscous as the PE powder dissolves in the solvent. A glass rod is used to constantly stir the solution. To avoid oxidation and subsequent molecular degradation, this process is carried out

inside an argon-filled glove box. The solution is then quenched in a room temperature water bath, and the gel forms.

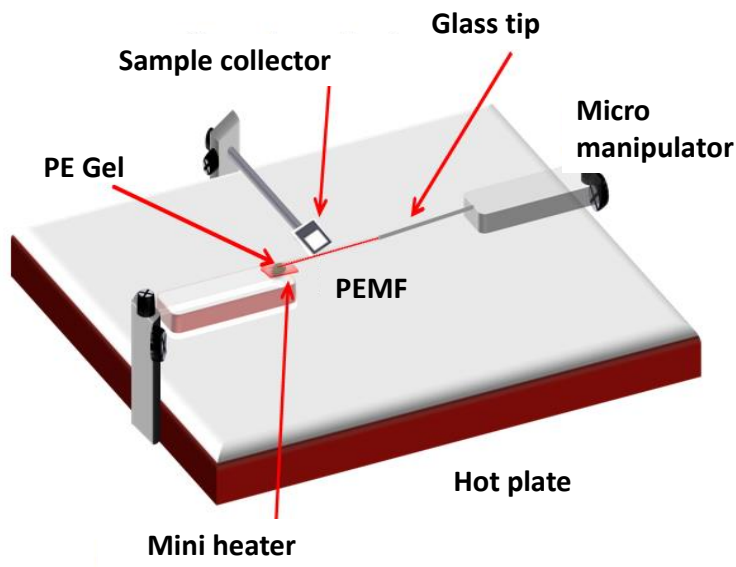


Figure 3.1: Schematic of tip drawing fabrication setup.

After gel preparation, the two-stage tip drawing method is used to form a PEMF. A 5 mm \times 5 mm silicon chip with a thin film heater attached on the backside is used to heat the gel to 120 – 130 $^{\circ}$ C. A hot plate placed 1 cm below the silicon chip heats the overhead air to 90 $^{\circ}$ C to prepare for hot-stretching. The fabrication setup is shown in Fig. 3.1. The translucent gel turns to a transparent solution as it is heated to 130 $^{\circ}$ C. As the solution turns clear, a sharp glass tip (10 μ m) is used to draw a short length (several hundreds of microns) of PEMF. Tip drawing of PEMF from PE/decalin gel at an elevated temperature results in the unfolding of the chain lamellae into micro fibrils that are pulled taut between entanglements [1]. The fiber undergoes stress-induced crystallization as discussed in Section 2.2.2 in Chapter 2. During crystallization, the decalin evaporates, aided by the convective current from the hot plate. Decalin syneresis further facilitates

crystallization [6]. The PEMF is then further drawn to a length of 1 cm after which it is quenched to room temperature to minimize relaxation of the extended chain.

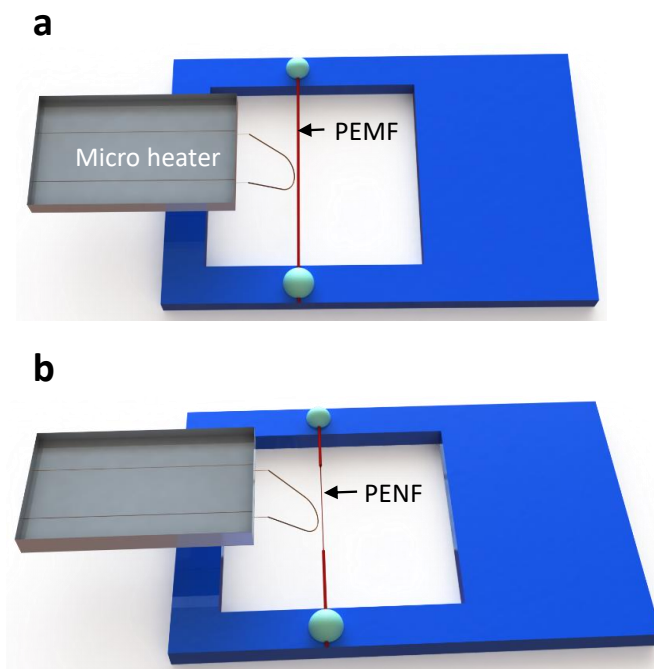


Figure 3.2: Schematic of PE microfiber (PEMF) to PE nanofiber (PENF) local drawing a) Pre-stressed PEMF on sample collector. b) PENF formed on the PEMF using local drawing.

The PEMF was kept taut and attached to a sample collector, which is a bulk micromachined rectangular silicon frame with a square hole (Section 3.3.1 in Chapter 3 and Fig. 3.2). The pre-stressed PEMF on the sample collector was locally heated and stretched to a nanoscale diameter using a home built microheater, which is a sharply bent tungsten microwire with an etched tip (Section 3.3.2 in Chapter 3 and Fig. 3.2). When a small segment of the PEMF was placed in proximity to the tip of the heater and heated close to the melting point, the pre-existing tensile stress immediately stretched the PEMF to the nanoscale diameter (Fig 3.2). A section of 80 to 100 μm long nanofiber was usually obtained in a PEMF using this two-step method. The eventual

diameter of the nanofiber can be controlled by tuning the pre-existing stress or the temperature of the heater. Per the schematic in Fig. 3.3a, amorphous regions are stretched and recrystallized, leaving a nearly defect-free aligned crystalline PENF.

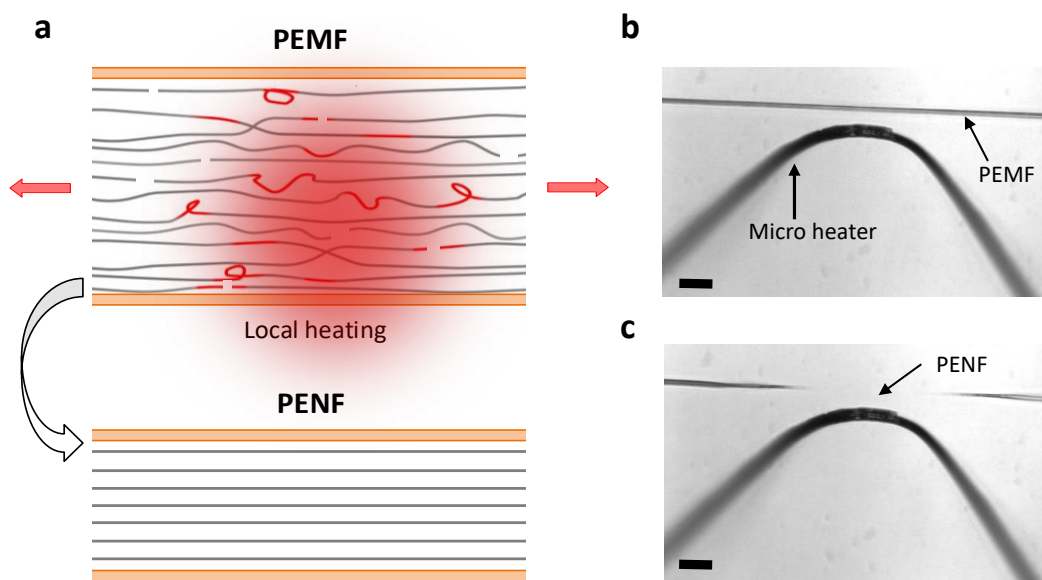


Figure 3.3: Fabrication of a PE nanofiber (PENF). a) Idealized schematics of localized drawing with a microheater to fabricate PENF from a PE microfibrillar film (PEMF). Arrows indicate drawing directions whereas red lines highlight the defects in PEMF. b-c) Optical micrograph before and after localized drawing (in (c), nanofiber not resolved optically). Scale bars, 20 μm .

In the presence of large micrometer current and/or high tensile stress, local stretching is rapid (<1 second). An 80-100 μm long nanofiber section is obtained with tapered ends. When the current is lowered, below a threshold current we see the local stretching process becoming 3-5 times slower. In this case, we obtain a nanofiber section 30 – 50 μm long with micro blobs at the ends. This could be because when the current is high, the fiber heats up more quickly and less volume is stretched. The force due to surface tension force is not enough to overcome the viscous drag to form micro blobs. When the current is lower, the slower process allows more time for the

heat to spread so more surface and volume take part in stretching. In this case, the surface tension force can overcome viscous drag and form micro blobs at the ends of the nanofiber section. In both these cases, a locally melted small volume of fiber near the microheater tip takes part in elongation and stretches to tens-hundreds of microns within in a time frame on the order of seconds, leading to a high draw ratio and a large elongation rate. This leads to a highly oriented and crystalline sample.

The high temporal and spatial resolution necessary to measure the temperature at the fiber during the drawing process limits any direct measurement. Here, we used ANSYS modeling to estimate the temperature during the local drawing process, which is described below.

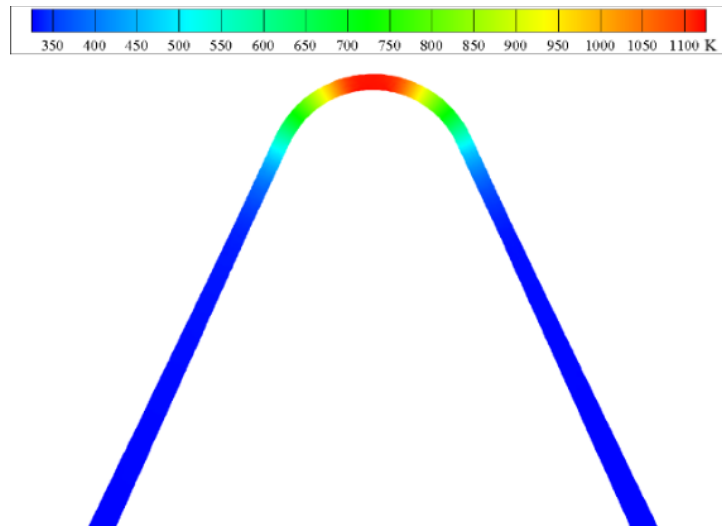


Figure 3.4: Temperature profile along the heater from ANSYS simulation.

3.2.2 Temperature profile of the PEMF during local drawing

Here, we estimate the maximum temperature attained by the fiber during local heating. First, we simulated the temperature profile of the microheater in ANSYS. Electrothermal modeling with a potential bias 0.7 V was applied to the heater, the same as in our experiment. Both

convective and radiative heat losses were considered. At the microscale, the boundary layer becomes smaller than at the macroscale. Thus, the heat transfer coefficient (h) greatly increases. Here, we used $h = 1000 \text{ W m}^{-2} \text{ K}^{-1}$ and emissivity = 0.1 in our simulation [7]. Fig. 3.4 shows the simulated temperature profile of the heater.

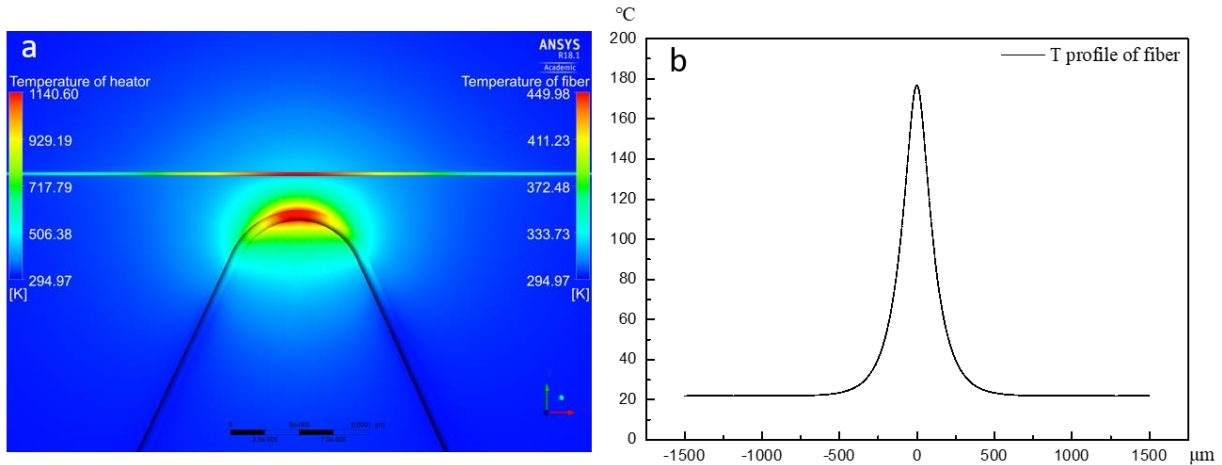


Figure 3.5: Temperature profile of heater and of a PEMF from ANSYS/FLUENT simulation. a) ANSYS/FLUENT simulation temperature map of the heater and a PEMF. b) The temperature profile of the PEMF. The maximum temperature of the fiber reaches 450 K (~180 °C).

Next, we added a PEMF with a diameter of 3 μm and set a 20 μm gap between the heater and the fiber. The thermal conductivity of the PEMF was modeled using gel spun microfibers with $k = 20 \text{ W m}^{-1} \text{ K}^{-1}$ [8]. We used an emissivity value of the PEMF of 0.2 [9]. A constant k of air of $0.02 \text{ W m}^{-1} \text{ K}^{-1}$ was used. The temperature of the fiber reached 450 K (~180 °C). The temperature profile along the fiber is shown in Fig 3.5.

3.2.3 Estimate of strain rate during local drawing

The molecular alignment within the fiber is correlated with increasing strain rate. We estimate that the strain rate in local drawing reaches up to 1400 s^{-1} compared to $\sim 1000 \text{ s}^{-1}$ in electrospinning [4] and $\sim 1 \text{ s}^{-1}$ in gel spinning [10]. Strain rate is defined as $\Delta l / (L_1 \Delta t)$ where Δl is the extension of the fiber segment of length L_1 within Δt seconds.

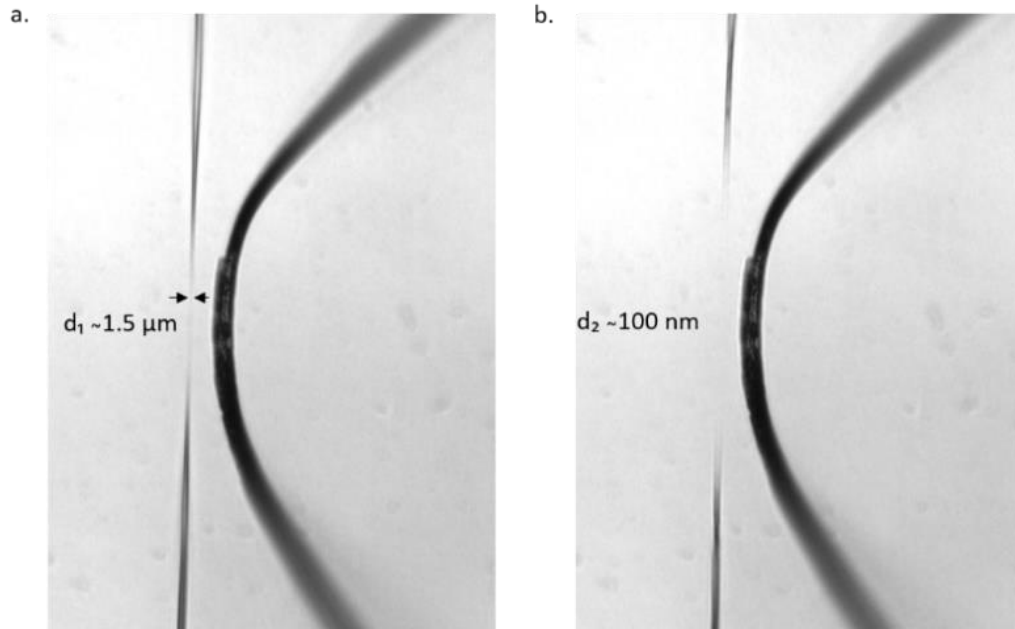


Figure 3.6: PEMF undergoing high strain rate elongation. PEMF (a) before and (b) after undergoing high strain rate elongation (diameter measured post measurement using Scanning electron microscopy (SEM)).

To estimate the strain rate during the local drawing, we used two consecutive image frames captured during the local drawing process (Fig. 3.6). Assuming volume conservation and a cylindrical fiber, $\pi d_1^2 L_1 / 4 = \pi d_2^2 L_2 / 4$ where d_1 is the initial diameter, d_2 is the final diameter after the local drawing, and L_2 is the final length of the fiber. Assuming, $\Delta l \gg L_1$, we can show

that $L_2/L_1 = (L_2 + \Delta l)/L_1 \approx (\Delta l)/L_1 \approx d_1^2/d_2^2$. The fiber starts thinning at a lower strain rate from 3 μm to around 1.5 μm before undergoing peak strain rate drawing. A video was obtained at an average frame rate of 6.3 frames per second. Therefore, the strain rate was estimated to be $(1.5 \mu\text{m})^2 / ((100 \text{ nm})^2 \times 0.16 \text{ s}) \approx 1400 \text{ s}^{-1}$. Next, I discuss a technique developed in this thesis to manipulate PENF onto the mechanical and thermal test platforms.

3.3 Manipulation of an individual nanofiber

3.3.1 Sample collector

Commonly, a micro/nanofiber is manipulated with a sharp glass/tungsten tip which is tedious, low yield and time-consuming. The sample collector, Fig. 3.2, makes manipulation of the fiber easy as we are manipulating a larger structure rather than just an individual fiber. The sample collector is a bulk micro-machined silicon frame with a through-etched hole of 4.5 mm \times 4.5 mm. The overall size of the sample collector is $\sim 7 \text{ mm} \times 10 \text{ mm}$. Its fabrication is described in Appendix A.

3.3.2 Microheater

The microheater is a sharply bent tungsten wire locally etched at the tip to 5 – 10 μm . It is joule-heated to a temperature exceeding 500 $^\circ\text{C}$ (Fig. 3.4) locally at the tip. It is used to fabricate a PENF by locally heating a PEMF stressed under tension and also later to cut the PENF by local melting to limit its length to that of the test platform. The steps used to make it are described in the Appendix B.

3.3.3 Positioning PENF on the MEMS devices

As the fiber diameter decreases, it becomes more challenging to precisely locate and position it onto the MEMS test platforms. Electron microscopes cannot be used because of the sensitivity of polymer samples to electron beam radiation [11], [12], which impairs the mechanical and thermal property enhancement [13], [14]. Therefore, the manipulation of the PENF is limited to optical methods. The sample must also be properly aligned. For example, during tensile testing, an unwanted bending moment can cause the load cell to rotate and the fiber force will be underestimated. The minuscule sample size, the limited resolution of the optical microscope and unpredictable forces such as van der Waals, triboelectric and capillary forces due to moisture are factors that make it difficult to successfully place nanofibers. Instead of manipulating the PENF directly, the sample collector with a suspended PENF is maneuvered as shown in Fig. 3.7. The microfiber in the undrawn section is used as a reference to align the nanofiber. After aligning the PENF, the sample is cut by local melting a suitable distance away from the region tested using a microheater.

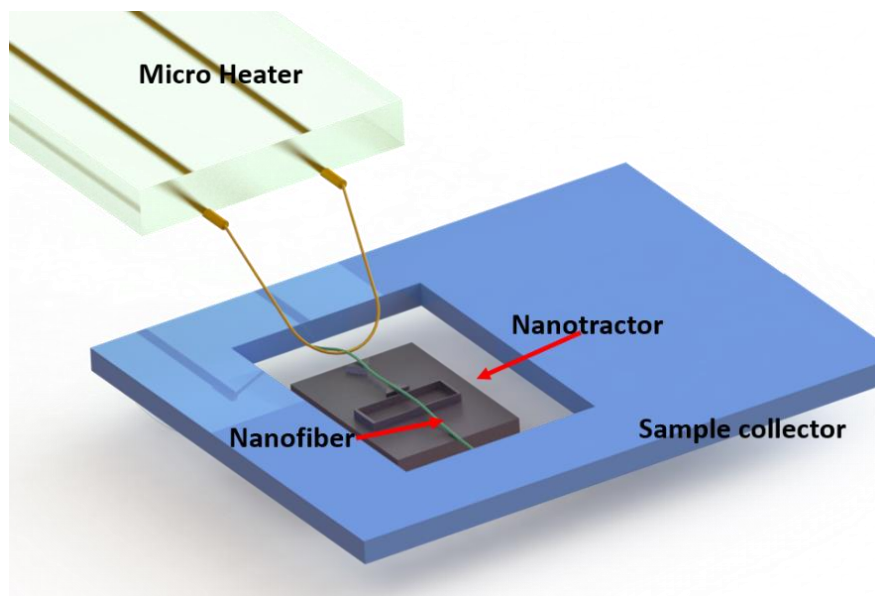


Figure 3.7: Mounting and cutting of a nanofiber onto the Nanotractor using the sample collector. This is performed under an optical microscope using a 20X objective.

3.3.3.1 Mounting onto Nanotractor

The mechanical properties of these nanofibers were tested using a MEMS device. It is called the “nanotractor” and it is a micromachined stepper motor with ~ 60 nm step size and high in-plane force (up to ~ 1 mN). It was fabricated in the SUMMiT VTM (Sandia Ultra-planar Multi-level MEMS Technology 5) process. The metrology used has a displacement resolution of 4 nm with a 50X objective and a force resolution of ~ 25 nN. The actuator is capable of stretching the nanofiber up to $75 \mu\text{m}$ and applying 250 % strain on these $30 \mu\text{m}$ gage length nanofibers. Details of the device are given in Chapter 6.

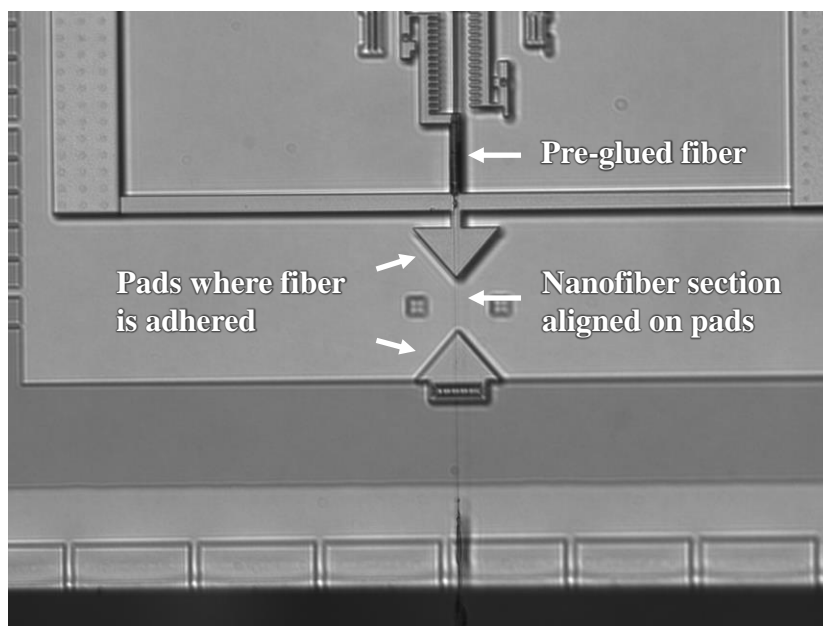


Figure 3.8: Nanofiber section is aligned between the triangular pads of a nanotractor and pre-glued behind one of the pads.

Two triangular pads to which the sample must adhere are behind the nanotractor, as seen in Figs. 3.7 and 3.8, one is fixed to the substrate while the other is connected to a load cell. A sample is placed between these pads and clamped onto them. When a specified voltage sequence is applied on the electrodes, the actuator plate moves one end of the load cell spring. The load cell spring transfers force onto the sample. Optical images of the load cell displacement provide the sample elongation and the force applied to the sample to deduce the stress and strain on the fiber. Next, we discuss the process to mount the nanofiber sample onto the nanotractor pads and clamp them for the tensile test.

3.3.1.1.1 Pre-gluing

Pre-gluing is the first step in mounting the nanofiber onto the nanotractor. A small amount of cyanoacrylate glue ($\sim 20 \mu\text{m} \times 5 \mu\text{m} \times 5 \mu\text{m}$) is placed on load cell beam of the nanotractor

using a compliant tungsten tip manipulated by a precise motorized micromanipulator. This glue is used to hold the sample while aligning and cutting the fiber. The sample collector is attached to another micro-manipulator and aligned along triangular pads under the 50X objective. The sample collector is lowered until the fiber makes contact with the glue. It is kept fixed at that position for ~20 minutes until the glue cures enough to hold the fiber while cutting. Fig. 3.8 shows a pre-glued PE nanofiber on a nanotractor.

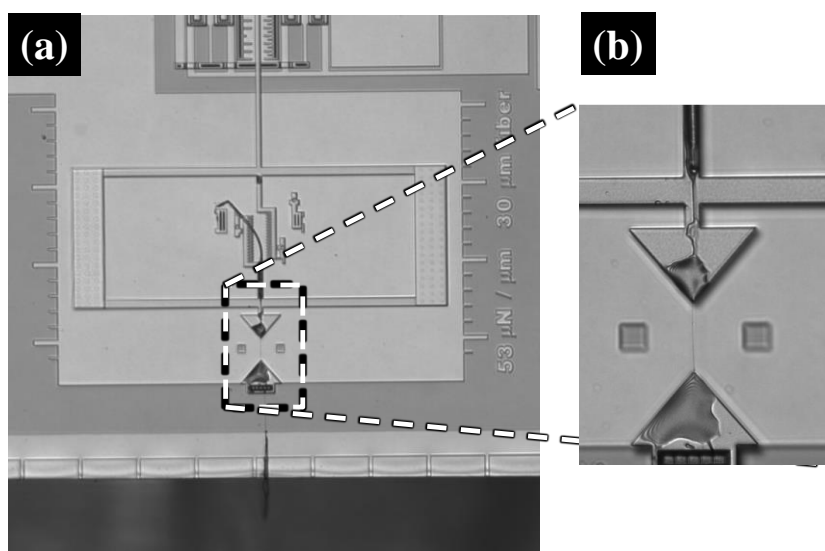


Figure 3.9: PE nanofiber on nanotractor ready for testing. a) fibers were glued onto pads after cutting process b) Zoomed image of the pads after gluing.

3.3.1.1.2 Cutting the fiber

After the glue has been allowed to partially cure for 15 m, the fiber is cut to 200 – 300 μm in length, which is much longer than the gauge length. Fig. 3.9 shows the specimen before the cutting process of the fiber. The microheater is used to cut the fibers. The fiber end on the fixed pad side is cut by local heating using the joule heated microheater. A DC power of 8 – 15 mW cuts the fibers. As the heater makes contact with the fiber, it melts it locally and thereby cutting it. Due

to some residual stress, the fiber is slightly pulled towards the pad. Similarly, the other end of the fiber is cut limiting the fiber within the pads with extra length beyond the glue.

3.3.1.1.3 Gluing the fibers

In this step, the fibers are glued onto the pads. Using a sharp compliant tungsten tip, glue is manipulated onto the aligned fiber on top of the pads. If the fiber comes out of alignment, it can be nudged using the same tungsten tip. Since the working time of the glue is ~8 minutes, this process should be finished within 6–8 minutes. As the glue becomes more viscous, manipulating it becomes difficult and overall yield decreases. After the fibers have been glued, they are cured in ambient temperature and humidity for 36 to 48 hours. Fig. 3.9 shows a sample that is ready for measurement.

3.3.3.2 Mounting onto the thermal device

Thermal characterization is done using suspended platinum resistance thermometers (PRT) based microdevice [15]. A total of seven SiN_x beams with platinum deposited on them hold each of two suspended SiN_x platforms. Serpentine platinum coils are fabricated on top of the SiN_x platforms that connect to the electrode membranes on the chip. A change in resistance of these PRTs indicates minute temperature changes; it thereby acts as a thermometer. A nanofiber is placed across these platforms to conduct heat from the heated side to the sensing side. Details of the measurement system are given in Section 4.3 in Chapter 4. Fig. 3.10 shows an optical image of a mounted nanofiber on the device. PENF that is significantly thinner and not resolvable under the optical microscope can be manipulated and mounted onto the test platform but is not shown here. Mounting processes are discussed next.

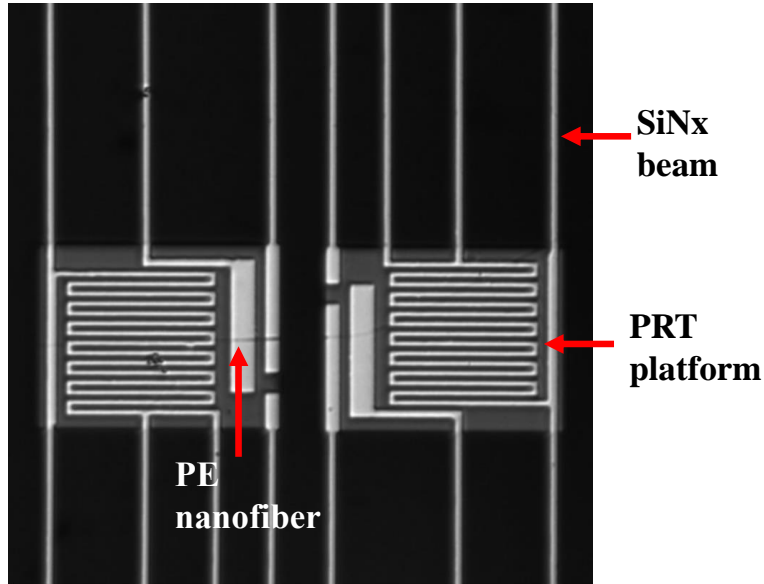


Figure 3.10: Optical image of a PE nanofiber sample mounted on the thermal device.

A nanofiber must be fixed onto the substrate before cutting; otherwise lateral forces will pull the nanofiber off the platforms. As adhesives can introduce higher thermal contact resistance by making a layer between the nanofiber and the platform, we used surface tension from an evaporating isopropanol (IPA) to fix the fiber onto the substrate. As the liquid evaporates, it pulls the fiber down and creates adhesion sufficiently strong to keep it fixed during the cutting process. Here, this adhesion process is defined as capillary-assisted adhesion and is discussed next.

3.3.3.2.1 Capillary assisted adhesion

Besides stronger adhesion for the cutting process, capillary-assisted adhesion plays an important role in reducing thermal contact resistance. Thermal contact resistance affects the k measurement. Glue and focused ion beam (FIB) deposited Pt have been previously used to bond PENF [16]. Glue wets the Pt wire surface, creating an insulating layer between the nanofiber and

the suspended pad, which increases the thermal contact resistance. Even though successfully used to make good contact for metal nanowires [17], carbon nanofiber [18] and other compatible materials [15], FIB-deposited Pt or electron beam-induced Pt/graphite deposition degrades polymer nanofiber as the electron/ion irradiation damages or even amorphizes the crystal structure. It is known that a large contact length and area of the fiber with the suspended pad decreases the thermal contact resistance. We used this capillary-assisted adhesion method to increase the contact area of the fiber with the suspended pad and thus decrease the thermal contact resistance.

Schematics of these steps are given in Fig. 3.11. In this process, first, an IPA liquid drop is placed on top of the thermal device. As the suspended beams are stiff, the van der Waals force does not keep them together after evaporation of the liquid. Evaporation of IPA from the device is closely monitored under the optical microscope. After the liquid meniscus connecting the platforms breaks but before the liquid layer from the suspended platform evaporates, a pre-aligned nanofiber is brought into focus and contact is made with the pads. The liquid wets the fiber and the evaporating liquid surface pulls the fiber down due to surface tension and adheres onto the pads. This surface tension with van der Waals force increases the contact width of the fiber on the pads. Also, the fiber conforms to the undulating surface, increasing the contact length significantly. Increased contact width and contact length due to capillary assisted adhesion reduce the thermal contact resistance.

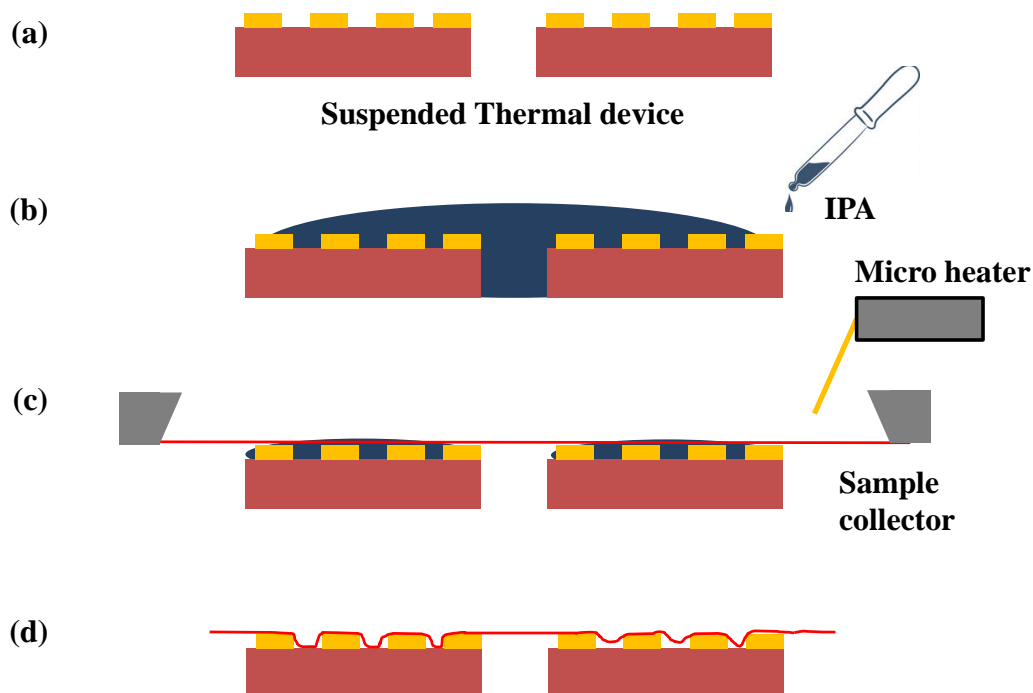


Figure 3.11: Schematics showing the mounting PE the nanofiber onto the thermal device. a) suspended platforms of the thermal device. b) a small drop of IPA is placed on the platforms c) after IPA evaporates, microheater is used to cut the fibers and limit within platforms d) Fiber is conformal with the platform surface as the evaporating IPA pulls the fiber in.

3.3.3.2.2 Cutting the fiber

This process is similar to that of cutting the fiber in nanotractor in Section 3.3.1.1.2.

3.4 Structural characterization of crystalline PENF

The crystallinity and orientation evolution within the PE powder, the PEMF and PENF are studied using differential scanning calorimetry (DSC), micro-Raman and low dose transmission electron microscope at cryogenic temperature.

3.4.1 PE powder characterization using DSC

The PE powder (Sigma Aldrich, $M_w = 3 - 6 \times 10^6 \text{ g mol}^{-1}$) (Fig. 3.12a) used as a control was characterized using differential scanning calorimetry (DSC) to understand its initial crystallinity, as seen in Fig. 3.12b.

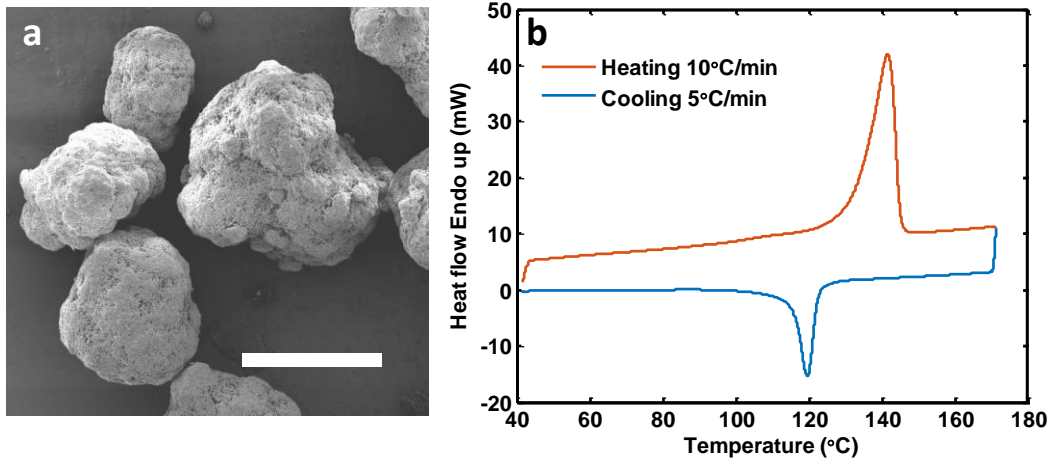


Figure 3.12: a) SEM micrograph of PE powder particles. b) DSC curves of the heating and cooling of PE powder. The melting point of PE powder is 141 °C. The enthalpy area of melting endotherm from 105 °C to 155 °C is found to be 1743.8 mJ. Scale bar, 100 μm .

A melting endotherm from the DSC can be used to measure the enthalpy of fusion of the polymer. The enthalpy of fusion of the sample can be compared with the theoretical crystal enthalpy of fusion to obtain the crystallinity of the sample as shown below[19].

$$\% \chi_c = \frac{\Delta H_s}{\Delta H_f} \times 100 \quad (1)$$

Here $\% \chi_c$ is the % crystallinity of the sample, ΔH_s is the enthalpy of fusion of the sample and ΔH_f is the enthalpy of fusion of pure crystal 289.3 J g⁻¹. The enthalpy of fusion of PE powder was obtained to be 157.1 J g⁻¹. Therefore, the crystallinity is 54.3 %. Next, the structural evolution

during drawing from starting material (PE powder) to PEMF and then PENF, using micro Raman is discussed.

3.4.2 Micro Raman characterization

We used a Renishaw InVia Raman Microscope with a 532 nm laser illumination. The sample was aligned using a low laser power of 2.5 mW to reduce the irradiation damage prior to characterization. An incident laser with 25 mW power was focused with a 50X objective onto a PE fiber suspended across a sample collector. A backscattered Raman spectrum was accumulated for 60 s at room temperature. The Raman spectra were collected with a spectral resolution of 0.9 cm^{-1} between 1000 cm^{-1} and 1500 cm^{-1} . A qualitative measure of molecular orientation can be obtained from the peak intensity ratio of 1128 cm^{-1} and 1060 cm^{-1} Raman bands [20]. Similarly, the crystallinity can be measured by the ratio of the integral areas under Raman bands of 1414 cm^{-1} to 1293 cm^{-1} and 1305 cm^{-1} , where Raman band 1414 cm^{-1} and Raman bands 1293 cm^{-1} and 1305 cm^{-1} correspond to the orthorhombic crystal and an internal standard independent of chain conformation, respectively [20]. First, the crystallinity in the PE powder is measured to establish a control.

3.4.2.1 PE powder crystallinity characterization from micro-Raman

Following the method of Strobl and Hagedorn [20], the crystallinity of unoriented PE powder can be determined using micro Raman as follows:

$$\% \chi_c = \frac{A_{1415}}{A_{(1295+1305)}} \times \frac{100}{0.45} \quad (2)$$

where A_{1415} is the integral area under 1415 cm^{-1} Raman band and $A_{(1295+1305)}$ is the integral area of 1295 cm^{-1} and 1305 cm^{-1} Raman bands, which act as an internal standard. A spectrum is shown in Fig. 3.13.

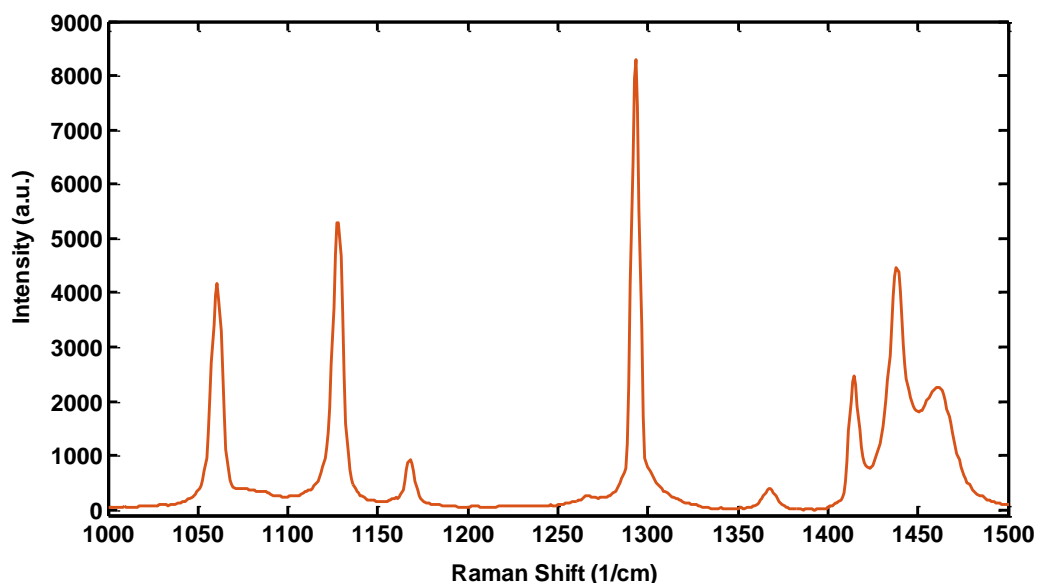


Figure 3.13: Micro Raman measurement of PE powder.

The Raman spectrum of PE powder was deconvoluted and the integral area under the 1295 cm^{-1} , 1305 cm^{-1} and 1415 cm^{-1} Raman bands were measured using curve fitting with Renishaw's Windows-based Raman environment (WiRE) software (WiRETM/ Renishaw). Three separate Raman spectrum measurements of PE powder are tabulated in Table 3.1 below:

Table 3.1: Crystallinity of a PE powder particle from Raman measurements

	A_{1415}	$A_{(1295+1305)}$	% χ_c
1	16435.2	58746.2	54.6
2	16843.8	57660.6	56.9
3	17493.8	58383.1	59.8

An average crystallinity of 57.1 % was obtained from the analysis of Raman bands of PE powder, in good agreement with the crystallinity obtained from the DSC analysis. The small difference of 3% could be because the DSC measurement is an average of bulk while micro Raman measurement is for a local area of a powder particle.

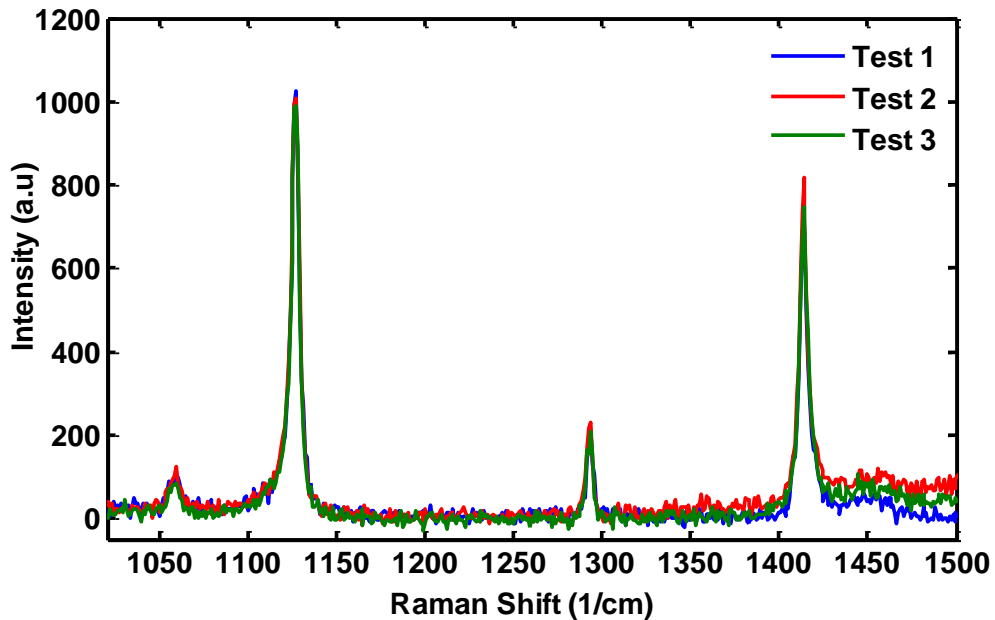


Figure 3.14: Raman spectra of a PENF obtained at the same spot.

3.4.2.2 Structural damage of PENF during Raman characterization

Fig. 3.14 shows repeated Raman spectra of a PENF obtained at the same location. In spite of the increasing irradiation, the spectra essentially overlap (within 5 %), suggesting that the fiber undergoes minimal structural damage during the characterization.

3.4.2.3 Structural evolution in PEMF and PENF from powder

The micro-Raman was used to understand the orientation and crystallinity of PE during different stages of drawing. Fig. 3.15a shows the typical Raman spectra of PE powder, PEMF and PENF. The spectra show that the area under 1414 cm^{-1} band increases from powder to PEMF and then to PENF, indicating that the amorphous phase is significantly reduced, and that crystallization is promoted (Fig. 3.15b). In addition to crystallinity, molecular orientation also increases from powder to PEMF and then PENF as indicated by the increase in the ratio of the intensity of Raman bands at 1128 cm^{-1} to 1060 cm^{-1} .

3.4.3 Low dose cryo-TEM:

Structural characterization of the crystalline polymer under an electron beam leads to fading and evolution of the diffraction spots into an amorphous halo ring because the radiation damages the sample crystallinity. The damage can be observed on a PE crystal at a dose as low as $25 \times 10^{-4}\text{ C cm}^{-2}$, and complete loss of Bragg spots occurs at a critical dose of 0.01 C cm^{-2} at an accelerating voltage of 100 kV [21]. The critical dose can be increased by reducing the temperature; in PE crystals it can be increased by a factor of 2.5 by cooling the sample from RT down to 100 K [21]. To reduce the electron beam damage and characterize morphological and structural features, we used low dose cryo-TEM. The sample was cooled to 100 K using a liquid

nitrogen cooled sample holder. The sample was inspected at a low dose $8 \times 10^{-5} \text{ C cm}^{-2}$, whereas selected aperture electron diffraction (SAED) patterns were obtained at a dose close to critical dose. Bright field images and SAED pattern were obtained at 80 kV.

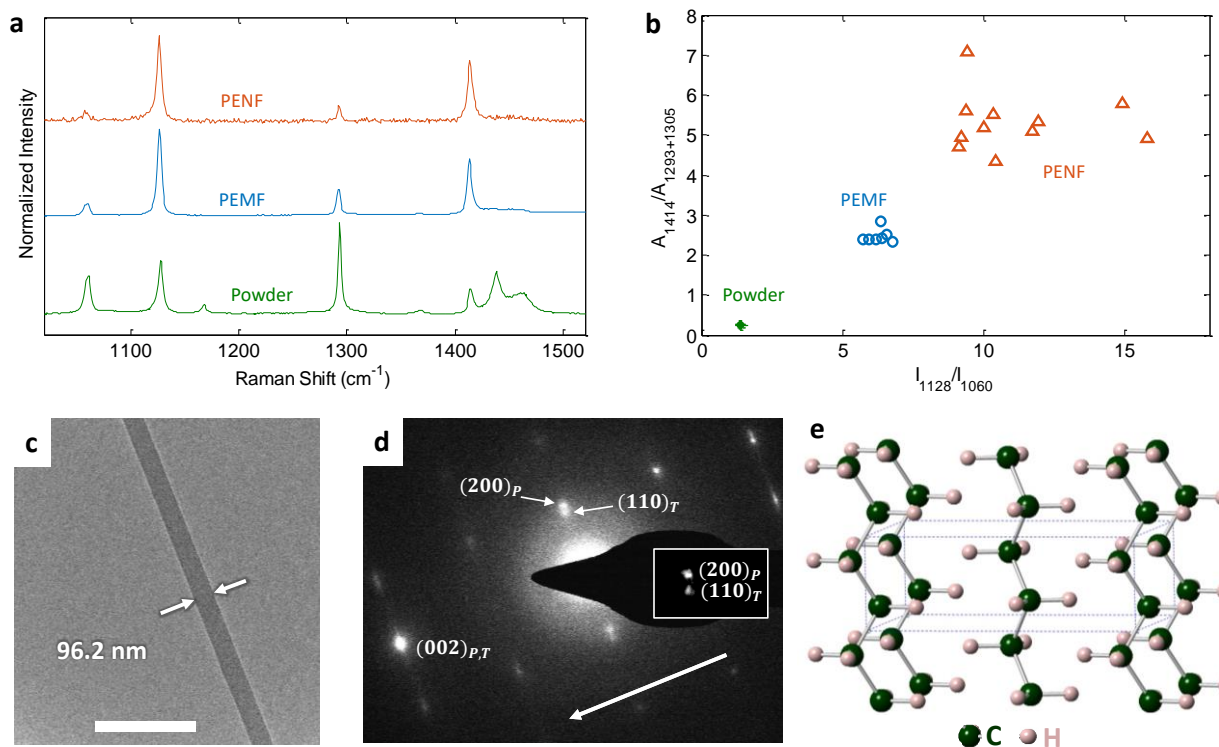


Figure 3.15: Morphological and structural characterizations. a) Micro-Raman spectra of PE powder, PEMF and PENF where the data is normalized to the highest peak of each spectrum. b) The ratio of integral areas of Raman band 1414 cm^{-1} to Raman bands 1293 cm^{-1} and 1305 cm^{-1} vs intensity ratio of Raman bands 1128 cm^{-1} to 1060 cm^{-1} . c) TEM micrograph of a PENF. d) SAED pattern of the PENF in c Inset shows the distinct diffraction spots of (200) plane of parent crystal (subscript P) and (110) plane of twinned crystal (subscript T). Arrow indicates the drawing direction. e) Orthorhombic crystal structure of PE. Scale bar, 500 nm.

3.4.3.1 Crystal structure of PE

The structural and morphological properties of PENF were further characterized using low-dose cryo-TEM. Fig. 3.15c shows the TEM micrograph of a typical PENF sample. Selected area electron diffraction (SAED) patterns (Fig. 3.15d) with an orthorhombic crystal structure (Fig. 3.15e) of crystalline PE with lattice constants $a = 7.301 \text{ \AA}$, $b = 4.893 \text{ \AA}$ and $c = 2.550 \text{ \AA}$ were indexed. These constants agree well with literature values from experiments and molecular simulations [22]–[24]. The arrow indicates the drawing direction, which is along the c -axis, and shows that the fiber axis is aligned with the $[001]$ c -axis direction. During the highly localized heating and drawing, the PEMF is stretched at very high strain rate while undergoing plastic deformation, which can occur via slip, twinning or martensitic phase transformation [25], [26]. Among the principal $\{110\}$ and $\{310\}$ twin planes that can be activated in PE, $\{310\}$ twinning may occur at high strain under which the morphology changes from lamellar to fibrillar [27]. The SAED pattern (Fig. 3.15d) indicates that in oriented PENF $\{310\}$ twinning occurs. Because the twinning involves rotations about the c -axis (54°) and the properties in this work are measured along that axis, the effects are expected to be negligible.

During the high strain rate fabrication step, PE crystals can undergo a phase transformation from the orthorhombic to a monoclinic phase [25]. The presence of a monoclinic phase was also observed in the SAED pattern (Fig. 3.16). Most SAED images indicated only the orthorhombic phase. One SAED pattern, Fig. 3.16, reveals the monoclinic phase, in the orthorhombic matrix. We did not evaluate the weight fraction of the monoclinic phase, however, we expect it to be small. It has been measured for a highly drawn PE microfiber using Wide angle X-Ray scattering (WAXS) and was found to be 4.3 % [28].

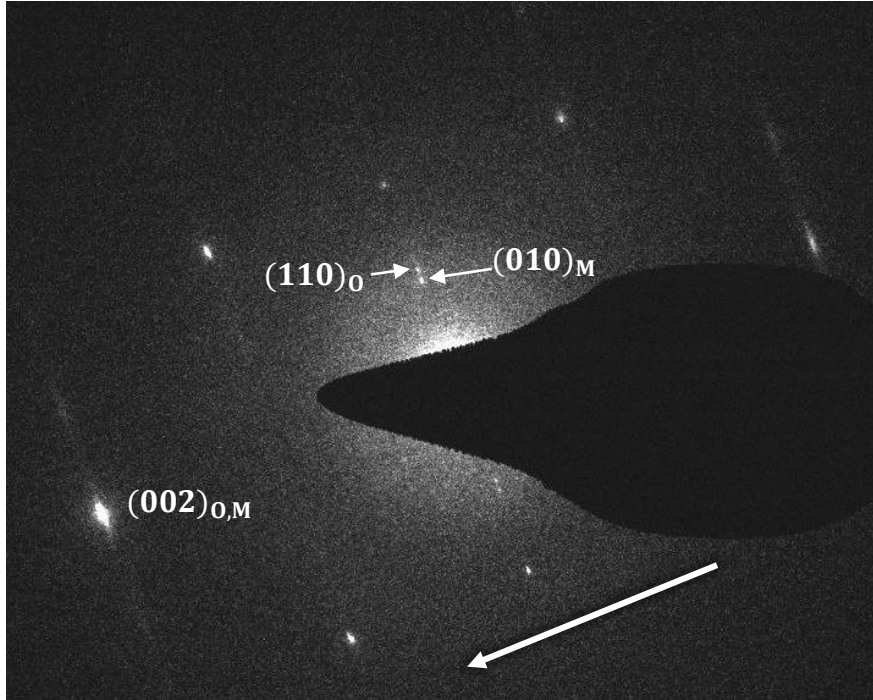


Figure 3.16: SAED pattern of a PENF where a monoclinic phase is seen in addition to the orthorhombic phase. Plane with subscript ‘O’ corresponds to the plane from orthorhombic structure whereas ‘M’ corresponds to the plane from monoclinic structure. Arrow indicates the drawing direction.

3.5 Morphological characterization of PENF

3.5.1 Diameter measurement and electron beam swelling in PE

Both the k and σ_{ts} measurements in Chapter 4–7 depend on the diameter of the PENF, so it is crucial to characterize its value accurately. However, swelling of the PENF due to electron beam irradiation during the SEM imaging makes the measurement challenging.

To characterize the SEM damage as well as the morphology of the fiber, the diameter of an as-drawn PENF was first measured in an atomic force microscope (AFM) followed by SEM. Prior to SEM, the nanofiber was coated with 3 nm platinum to minimize charging during SEM.

This does not significantly change the diameter of the nanofiber as the platinum deposition is not conformal.

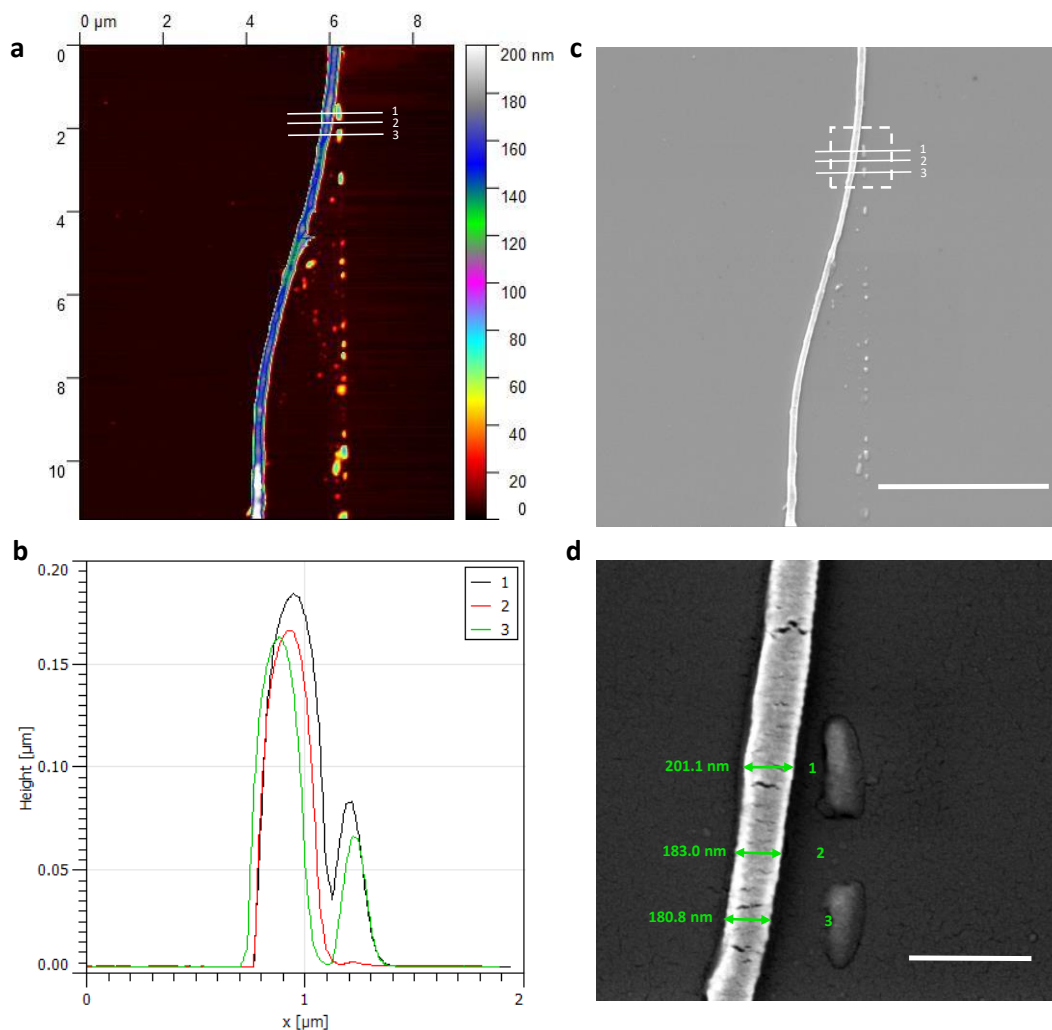


Figure 3.17: Electron beam swelling in PENF. a) AFM image of a nanofiber b) Height profile of lines drawn in (a). Horizontal distance is larger because of the convolution of the AFM tip. c) SEM image of PENF d) Magnified view of inset of (c). Scale bars 5 μm (c) and 500 nm (d).

AFM (Figs. 3.17a and b) and SEM (Figs. 3.17c and d) show images and data from the same three regions. A region with distinct debris pattern from the silicon chip was chosen so it would be easy to find in both AFM and SEM. The SEM measured diameters are 10.7 %, 11.9 % and 11.9

% larger than the heights measured from AFM. Fig. 3.17d also shows the morphological damage in the PE nanofiber. The irradiation scissions the chains in the as-drawn fiber. The observed ripples show the sheesh-kebab structure that evolves thereafter.

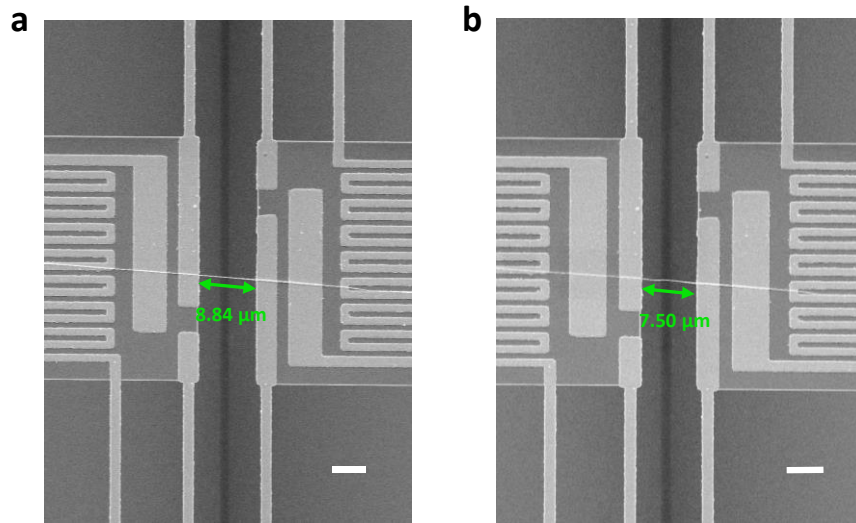


Figure 3.18: Diameter measurement for k evaluation. a) SEM micrograph of the initial fiber b) SEM micrograph after SEM exposure. Scale bars, 5 μm .

Figs. 3.18a and b show the separation between the thermal measurement platforms due to increased electron beam irradiation. The length of the fiber decreases in (b) relative to (a). The diameter of the swollen fiber is measured. Assuming that the volume does not change, one can obtain the initial diameter, d_{ini} , of the nanofiber using the formula $d_{\text{ini}} = d_{\text{swoln}} \sqrt{\text{length}_{\text{swoln}} / \text{length}_{\text{ini}}}$. Fig. 3.18 show a PENF specimen whose diameter increased by 8 %. The swelling of a PENF on a substrate was found larger than the PENF with constrained ends. Even though the swelling was evaluated, the PENF diameter was corrected only for k .

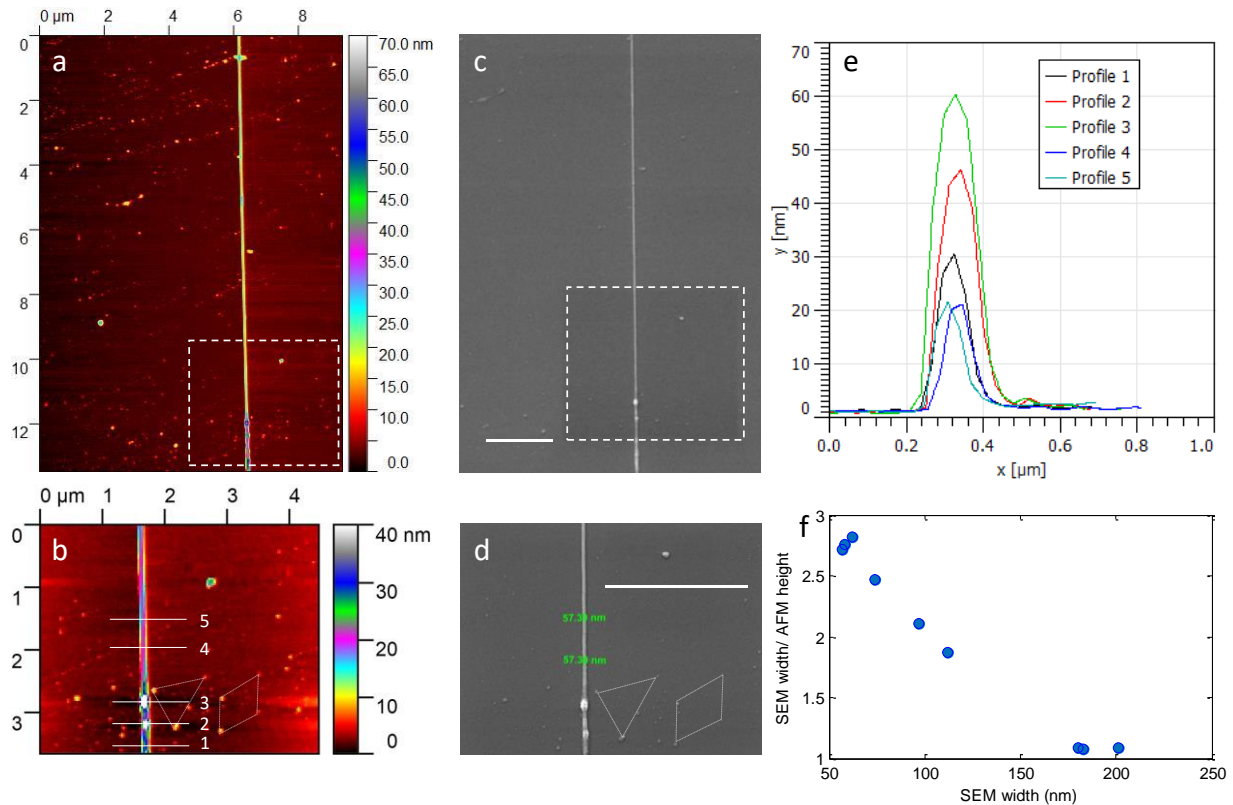


Figure 3.19: Comparison of fiber dimensions measured using AFM and SEM. a) Height map measured using AFM. b) Zoom in of Inset of (a). c) Width measured using SEM at the same region in (a). d) Zoom in inset of (c). e) Height profile of lines in (b). f) The ratio of SEM width to AFM height versus SEM width. Scale bars, 2 μm (c,d).

3.5.2 Cross section of PENFs fabricated by local drawing

The fiber cross-section was assumed to be circular. Hence, the PENFs diameters in the Chapters 4–7 are reported based on the width measured using SEM. However, upon measuring the height using atomic force microscopy (AFM), we found that the sample cross-section is non-circular at SEM measured widths below 150 nm, where the measured height using AFM is around 1.5 times smaller than the measured width by SEM, as shown in Fig. 3.19. However, when calculating the k 's of the PENFs from the measured thermal conductances, we assumed the fibers to have a cylindrical shape with uniform diameters that correspond to the widths measured by

SEM. The same situation is true for σ_{ts} measurements as well. Hence, the k and σ_{ts} reported in the Chapters 4–7 should be taken as a lower bound for the PENF.

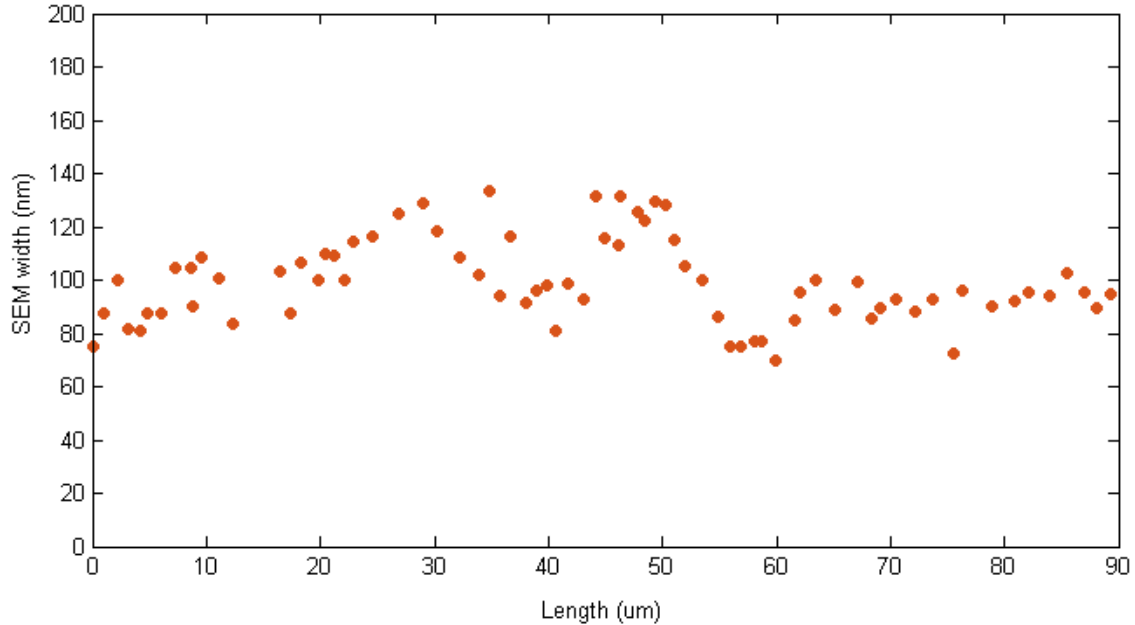


Figure 3.20: Diameter profile of a typical PENF fabricated using local drawing.

3.5.3 Shape of a PENF along the length evaluated by SEM

Fig. 3.20 shows a typical diameter measurement using SEM along a PENF fabricated using local drawing. It can be seen that the diameter is fairly uniform. The sample excludes the dog bone and the tapered region shown in Fig. 6.10. For thermal measurements, since the test length is less than 10 μm , we often obtain relatively uniform diameter. Samples with a standard deviation of nanofiber diameter larger than 15% are excluded from thermal measurements. However, for mechanical measurements the nominal gage length is 30 μm , so the sample always exhibits some non-uniformity.

3.6 Summary

To achieve significant mechanical and thermal enhancement, we have developed a new local heat stretching method where we can obtain large draw ratio PENFs. A micro/sub-micron UHMWPE fiber was rapidly (~1 s) stretched to the nanometer scale by local drawing.

Due to the size scale, methods to manipulate and mount individual nanofibers must be developed. High-resolution microscopy methods such as SEM and TEM to visualize and manipulate samples are not feasible as these polymer nanofibers are sensitive to electron beam irradiation. Therefore, manipulation of the nanofiber and mounting onto test device under an optical microscope is a must. We have developed a new robust method for manipulating and mounting polymer nanofibers onto test device under an optical microscope. In this method, a macrostructure (polymer nanofiber on bulk micro-machined silicon frame) is manipulated instead of the individual nanostructure.

In addition, we have characterized the structural and morphological evolution of PE powder to PEMF and PENF. PE powder crystallinity ($\% \chi_c = 54.3 \%$) was evaluated using DSC which was also verified using Micro-Raman ($\% \chi_c = 57.1 \%$). Micro-Raman study verified that the molecular orientation of backbone chains along the fiber axis increase as the powder is drawn to PEMF then PENF. Increase in crystallinity was also observed in accordance with the molecular orientation of the backbone. Due to the high strain rate fabrication technique, {310} twinning was observed in the orthorhombic parent crystal. In addition, the monoclinic phase was also detected.

The electron beam induced swelling was also studied on a PENF specimen by measuring AFM height prior to SEM. The electron beam induced swelling caused the diameter to increase by 11 to 12 %. The electron beam swelling was further investigated on a PENF suspended on a thermal measurement platform. The diameter increased by 8 % upon exposure to the electron

beam. Even though the swelling of PENF was evaluated, it was not corrected during the k and σ_{ts} analysis. Detailed analysis of height map using AFM and SEM width suggested that PENF has a non-circular cross-section. At SEM measured widths below 150 nm, the measured height using AFM is around 1.5 times smaller than the measured width by SEM. Both the k and σ_{ts} measurements in Chapters 4–7 depend on the diameter of the PENF, which has been assumed to be circular and SEM width used as the diameter. Therefore, the reported k and σ_{ts} measurements in Chapters 4–7 should be taken as a lower bound.

3.7 Chapter references:

- [1] S. Shen, A. Henry, J. Tong, R. Zheng, and G. Chen, “Polyethylene nanofibres with very high thermal conductivities.,” *Nat. Nanotechnol.*, vol. 5, no. 4, pp. 251–255, 2010.
- [2] P. Li, L. Hu, A. J. H. McGaughey, and S. Shen, “Crystalline polyethylene nanofibers with the theoretical limit of Young’s modulus,” *Adv. Mater.*, vol. 26, no. 7, pp. 1065–1070, 2014.
- [3] T. T. Perkins, D. E. Smith, and S. Chu, “Single polymer dynamics in an elongational flow.,” *Science*, vol. 276, no. 5321, pp. 2016–21, Jun. 1997.
- [4] J. H. Park and G. C. Rutledge, “Ultrafine high performance polyethylene fibers,” *J. Mater. Sci.*, vol. 53, 2017.
- [5] P. Smith and P. J. Lemstra, “Ultra-high-strength polyethylene filaments by solution spinning/drawing,” *J. Mater. Sci.*, vol. 15, no. 2, pp. 505–514, 1980.
- [6] X. M. Shi, Y. Z. Bin, D. S. Hou, Y. F. Men, and M. Matsuo, “Gelation/crystallization mechanisms of UHMWPE solutions and structures of ultradrawn gel films,” *Polym. J.*, vol. 46, no. 1, pp. 21–35, 2014.
- [7] A. Narayanaswamy and N. Gu, “Heat Transfer From Freely Suspended Bimaterial Microcantilevers,” *J. Heat Transfer*, vol. 133, no. 4, p. 042401, Apr. 2011.
- [8] DSM, “Dyneema Fact Sheet,” pp. 1–4, 2008.
- [9] Y. Fujikura, T. Suzuki, and M. Matsumoto, “Emissivity of chlorinated polyethylene,” *J. Appl. Polym. Sci.*, vol. 27, no. 4, pp. 1293–1300, Apr. 1982.

- [10] P. Smith and P. J. Lemstra, "Ultrahigh-Strength Polyethylene Filaments by Solution Spinning/Drawing, 2 Influence of Solvent on the Drawability," *Makromol Chem*, vol. 180, pp. 2983–2986, 1979.
- [11] L. C. Sawyer, D. T. Grubb, and G. F. Meyers, *Polymer Microscopy*. New York, NY: Springer New York, 2008.
- [12] J.-F. Revol and R. S. J. Manley, "Lattice imaging in polyethylene single crystals," *J. Mater. Sci. Lett.*, vol. 5, no. 3, pp. 249–251, Mar. 1986.
- [13] J. Ma, Q. Zhang, A. Mayo, Z. Ni, H. Yi, Y. Chen, R. Mu, L. M. Bellan, and D. Li, "Thermal conductivity of electrospun polyethylene nanofibers," *Nanoscale*, vol. 7, no. 40, pp. 16899–16908, 2015.
- [14] M. Naraghi, T. Ozkan, I. Chasiotis, S. S. Hazra, and M. P. de Boer, "MEMS platform for on-chip nanomechanical experiments with strong and highly ductile nanofibers," *J. Micromech. Microeng.*, vol. 20, no. 12, p. 125022, 2010.
- [15] D. Li, Y. Wu, P. Kim, L. Shi, P. Yang, and A. Majumdar, "Thermal conductivity of individual silicon nanowires," *Appl. Phys. Lett.*, vol. 83, no. 14, p. 2934, 2003.
- [16] P. Li, "Mechanical and Thermal Characterizations of Crystalline Polymer Micro/Nanofibers," Carnegie Mellon University, 2015.
- [17] Z. Cheng, L. Liu, S. Xu, M. Lu, and X. Wang, "Temperature Dependence of Electrical and Thermal Conduction in Single Silver Nanowire," *Sci. Rep.*, vol. 5, p. 10718, Jun. 2015.
- [18] C. Yu, S. Saha, J. Zhou, L. Shi, A. M. Cassell, B. A. Cruden, Q. Ngo, and J. Li, "Thermal Contact Resistance and Thermal Conductivity of a Carbon Nanofiber," *J. Heat Transfer*, vol. 128, no. 3, p. 234, 2006.
- [19] "Standard Test Method for Measurement of Enthalpy of Fusion, Percent Crystallinity, and Melting Point of Ultra-High-Molecular Weight Polyethylene by Means of Differential Scanning Calorimetry 1," *ASTM Int. West Conshohocken, PA*, , 2016.
- [20] G. R. Strobl and W. Hagedorn, "Raman spectroscopic method for determining the crystallinity of polyethylene," *J. Polym. Sci. Polym. Phys. Ed.*, vol. 16, no. 7, pp. 1181–1193, Jul. 1978.
- [21] D. T. Grubb and G. W. Groves, "Rate of damage of polymer crystals in the electron microscope: Dependence on temperature and beam voltage," *Phil. Mag.*, vol. 24, pp. 815–828, 1971.

- [22] B. C. W Bunn, "The crystal structure of long-chain normal paraffin hydrocarbons. The 'shape' of the CH₂ group," *Trans. Faraday Soc.*, vol. 35, pp. 482–491, 1939.
- [23] A. Kawaguchi, R. Matsui, and K. Kobayashi, "The Crystal Structure of Polyethylene at 4.5°K," *Bull. Inst. Chem. Res., Kyoto Univ*, vol. 55, no. 2, 1977.
- [24] T. Zhang and T. Luo, "High-Contrast, Reversible Thermal Conductivity Regulation Utilizing the Phase Transition of Polyethylene Nanofibers," *ACS Nano*, vol. 7, no. 9, pp. 7592–7600, Sep. 2013.
- [25] F. C. Frank, A. Keller, A. O 'connor, and H. H. Wills, "Deformation Processes in Polyethylene Interpreted in terms of Crystal Plasticity," *Phil. Mag.*, vol. 3, no. 25, 1958.
- [26] H. Kiho, A. Peterlin, and P. H. Geil, "Polymer Deformation. VI. Twinning and Phase Transformation of Polyethylene Single Crystals as a Function of Stretching Direction," *J. Appl. Phys.*, vol. 35, no. 5, pp. 1599–1605, May 1964.
- [27] J. E. Preedy and E. J. Wheeler, "A study of twinning in polyethylene," *J. Mater. Sci.*, vol. 12, no. 4, pp. 810–815, Apr. 1977.
- [28] V. M. Litvinov, J. Xu, C. Melian, D. E. Demco, M. Möller, and J. Simmelink, "Morphology, Chain Dynamics, and Domain Sizes in Highly Drawn Gel-Spun Ultrahigh Molecular Weight Polyethylene Fibers at the Final Stages of Drawing by SAXS, WAXS, and ¹H Solid-State NMR," *Macromolecules*, vol. 44, no. 23, pp. 9254–9266, Dec. 2011.

Chapter 4: Crystalline polymer nanofibers with ultra-high thermal conductivity

4.1 Abstract

Polymers are widely used in daily life, but exhibit low thermal conductivity as compared to most structural materials such as metals. In this work, we demonstrate that crystalline PENF fabricated in Chapter 3 exhibit a high metal like thermal conductivity. Specifically, we demonstrate unique low-dimensionality phonon physics for thermal transport in the nanofibers by measuring their thermal conductivity in a broad temperature range from 20 to 320 K, where the thermal conductivity increases with increasing temperature following an unusual $\sim T^1$ trend below 100 K and eventually peaks around 130–150 K reaching a metal-like value of $90 \text{ W m}^{-1} \text{ K}^{-1}$, and then decays as $1/T$. The polymer nanofibers are purely electrically insulating and bio-compatible. Combined with their remarkable lightweight-thermal-mechanical concurrent functionality, unique applications in electronics and biology emerge.

4.2 Introduction

With the advancement of nanotechnology, various polymer fibers have been developed with enhanced thermal properties. Enhancing thermal conductivity in polymer fibers has been mainly focused on polymer composites [1], [2] and polymer nanofibers with increased crystallinity and alignment [3]–[6]. In polymer composites, low thermal conductivity polymer matrix is filled with high thermal conductivity materials such as metallic nanoparticles and carbon nanotubes. Recent studies on the high thermal conductivities of carbon nanotubes and graphene have motivated researchers to use them as filler materials. However, enhancement of thermal conductivity of polymer composites is generally limited within an order of magnitude due to the

high thermal interface resistance between the filler and the matrix, and the decrease of the additives' thermal conductivity affected by the surrounding [7]. In addition, reduced defects in crystalline polymer nanofibers with a high degree of molecular alignment also enhance thermal properties [3], [6], [8]. On the other hand, measuring thermal properties in 1D materials using suspended platinum resistance thermometer (PRT) based micro thermal device is now routine [4], [9]–[11].

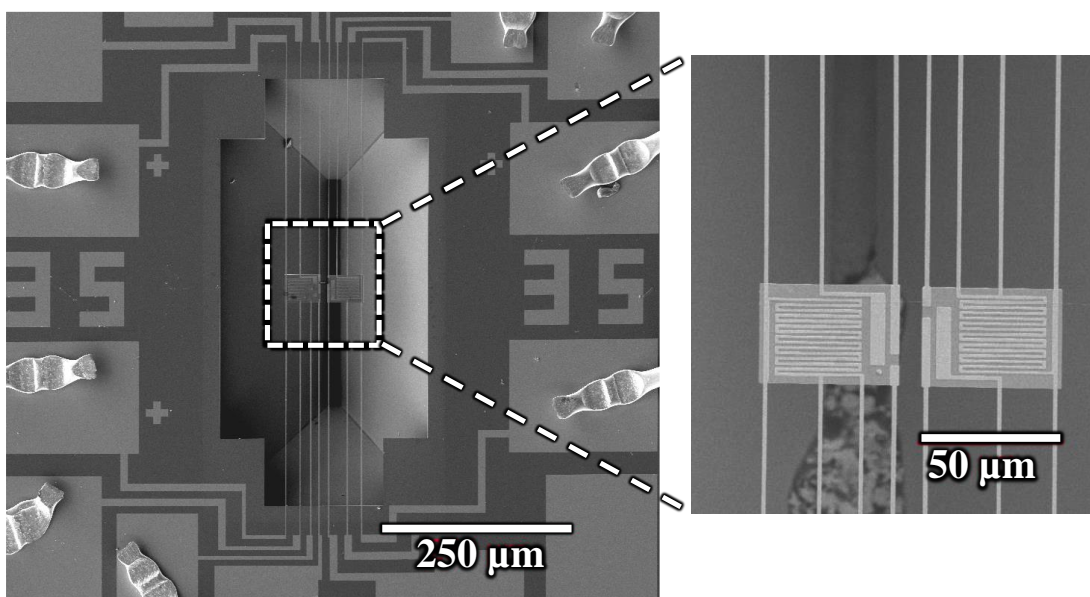


Figure 4.1: PRT based micro thermal device. Zoomed inset is the suspended PRT platforms supported by SiN_x beams. (Note gold wires bonded on PRT device for electrical connection to a chip carrier are visible.)

4.3 Thermal measurement for 1D structures using PRT based micro thermal device

PRT based micro thermal device has been used to measure the thermal/thermoelectric properties of various 1D materials such as carbon nanotubes, Si nanowire and polymer nanofibers

[4], [9]–[11]. Detailed fabrication and working principle can be found in [12]. Briefly, the microdevice consists of two suspended $30\ \mu\text{m} \times 40\ \mu\text{m}$ SiN_x platforms each supported by $0.3\ \mu\text{m}$ thick, $1.6\ \mu\text{m}$ wide and $320\ \mu\text{m}$ long five to seven SiN_x beams connected to the substrate as shown in Fig. 4.1. Serpentine platinum coils, $50\ \text{nm}$ thick and $1\ \mu\text{m}$ wide, are patterned on SiN_x platforms and functions as heaters and resistive thermometers. The temperature of a heating platform is raised by applying a DC current. The heat is transferred from the heating platform to the other platform (sensing platform) by a nanofiber placed across these two platforms. With known heat flux, temperature difference obtained from measured resistances and temperature coefficient of resistance (TCR) and nanofiber geometry (obtained from SEM image), one can calculate thermal conductivity from steady-state heat transfer solutions. Details of the measurement system of the micro thermal device are described below.

4.3.1 Overview of the measurement system

Sample mounting onto a PRT micro thermal device has been explained in detail in Chapter 3. After the sample mounting, the device is placed on a 24 lead side brazed ceramic dual-in-line package (DIP) (Addison Engineering inc.) using a small drop of silver epoxy. Conductive epoxy is used to reduce the thermal contact resistance between the device and the package. The package is connected with the contact pads of the device using $25\ \mu\text{m}$ gold wires with wedge wire bonder (West Bond Inc.). The packaged device is, then, mounted on a copper finger in a cryostat (CCS-450 Optical high-temperature refrigerator system, Janis research Co.) using a thermally conductive epoxy. The thermal contact resistance between the copper finger and the DIP is further minimized by a thermal interface material between the copper finger and the DIP with custom built copper clamps. The cryostat is covered with radiation shield and vacuum shroud. The cryostat chamber is

evacuated to a vacuum level of 1×10^{-7} Torr while the global temperature of the cryostat is lowered down to 10 K with a closed liquid helium compressor (CTI-Cryogenics 8200 Compressor, Brooks automation Inc.). The global temperature is recorded using a thermocouple mounted on the copper finger. The resistance of the PRT platforms are recorded as the device cools down to 10 K. The electrical configuration to measure the resistance of the platforms are discussed in the next section. The resistance drop of the PRT device indicates its transient heat conduction behavior which is compared with the temperature measured by a thermocouple as shown in Fig. 4.2. A similar trend of resistance drop on PRT platforms and a temperature drop of the copper finger without any lag indicates a good thermal contact of the device with the copper finger.

After the good thermal contact is established, the measurements are taken from 20 K to 320 K at an interval of 10 K. Using a heater, the temperature of the copper finger is increased by 10 K and stabilized using a PID controller. For example, Fig. 4.2c shows an increase in the temperature of the copper finger from 230 K to 240 K. Resistance measurement of the heating platform follows the same trend as the temperature rise of the copper finger without any noticeable lag, showing excellent thermal contact and negligible thermal resistance. With a negligible radiation loss, we can reasonably assume that the temperature of the thermal diode is the same as the temperature of the device. In Fig. 4.2c blue line indicates the steady state of the device. These resistance measurements at different steady-state temperatures are used to measure the temperature coefficient of resistance (TCR). A 10th order polynomial fit is used to minimize the residual error from curve fitting [13]. Next, the detailed electrical and thermal configuration to measure thermal conductivity is described.

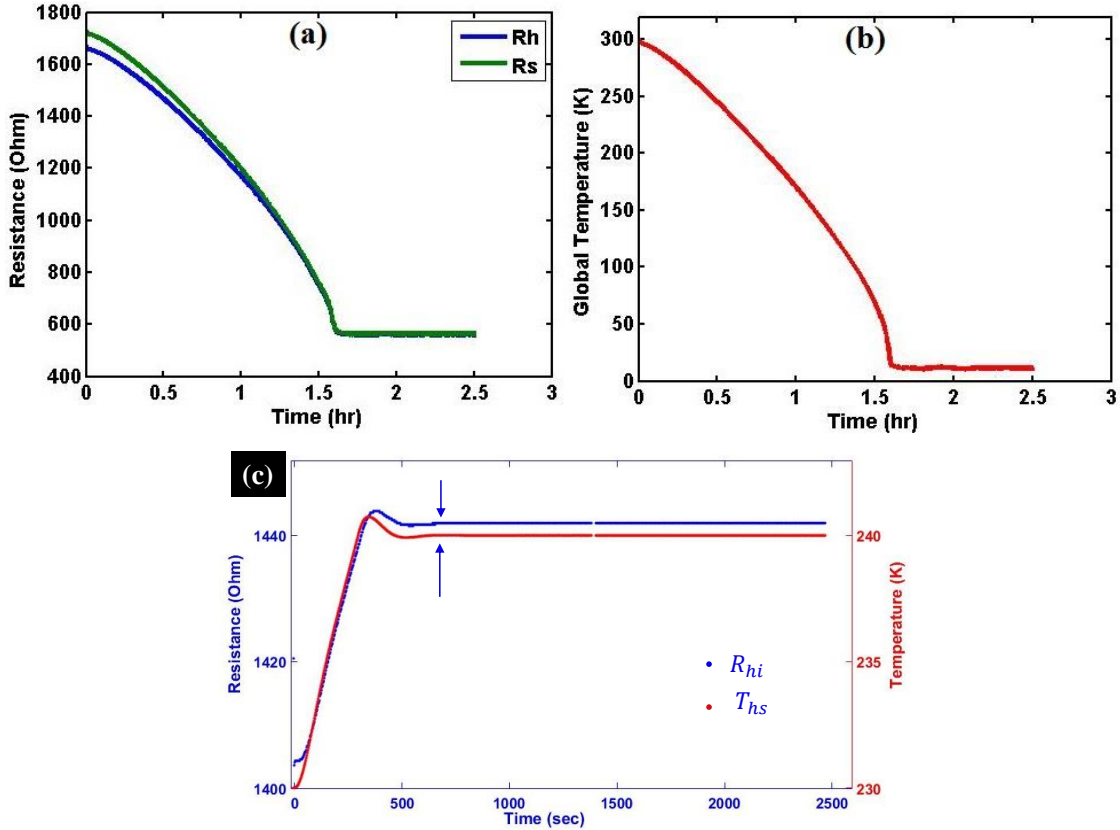


Figure 4.2: a) Resistance of the heating and sensing platforms in a device as the global temperature is lowered from room temperature to 10 K. b) global temperature measured by a thermocouple on a copper finger. c) The resistance of the heating platform (blue line) and the global temperature (red line) as the global temperature is ramped up from 230 K to 240 K. Blue arrows indicate steady state at 240 K.

4.3.2 Electrical and thermal systems

The electrical and thermal configuration for measuring the thermal conductivity of a nanofiber is shown in Fig. 4.3. The dc current I (supplied from a source meter, Keithley 2400) passing through a Pt coil generates the Joule heat ($I^2 R_{hi}$) where R_{hi} is the resistance of the PRT coil in the heating platform. Joule heat of $2Q_l = 2I^2 R_l$ (R_l is the resistance of a beam or leg) is also generated in the two Pt legs that supply the dc current to the heating platform. It can be shown by solving the diffusive heat transfer equation that only $I^2 R_l$ is utilized in heating up the heating

platform while another I^2R_l is dissipated to the heat sink. We assume that the heating platform reaches a uniform temperature T_{hi} . This assumption can be justified as the internal thermal resistance of the platform is smaller compared to the beams that connect it to the heat sink at temperature T_{hs} . The applied dc current ranges from 0 A to the value such that the temperature difference $\Delta T_h = T_{hi} - T_{hs} < 5K$, so that heat radiation can be neglected. Heat transferred through the specimen raises the temperature of the sensing platform $\Delta T_s = T_{si} - T_{hs}$ to a uniform temperature T_{si} .

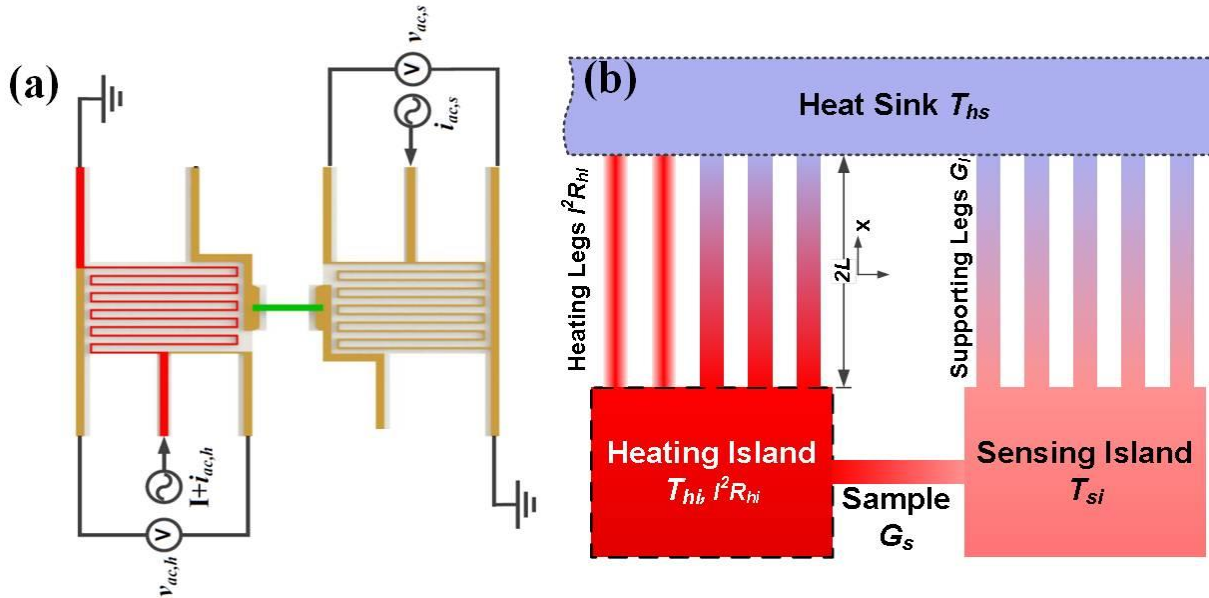


Figure 4.3: a) An electrical configuration of the thermal measurement system b) Thermal configuration at steady state. Figure obtained from [73].

Simultaneously, resistance measurements of both the heating platform and the sensing platform are done using four-probe measurements. Ac currents i_{ac} with an amplitude in nanoamperes (~ 50 nA) are applied to two Pt coils separately as shown in Fig. 4.3a and the first harmonic component of the ac voltage drop across the coils are measured using lock-in amplifiers. The joule heating from the ac current is several orders of magnitude smaller than dc and therefore

negligible. The ac frequencies used are 1.1 KHz for the heating platform and 149 Hz for the sensing platform. These frequencies are chosen to avoid interference with other noise sources, for example, power line noise. To complete an electrical circuit for thermal measurement purposes, only four Pt beams on each platform are required. Even though other beams are not necessary for this work (they are used for thermoelectric measurements), they provide extra rigidity to the platforms. The solution derived here does not depend on the number of legs.

4.3.3 Thermal conductance and thermal conductivity calculations

The entire system is placed in a cryostat with a vacuum level of 1×10^{-7} Torr, so that heat transfer due to residue air molecules can be neglected. Detailed thermal conductance derivation can be found in [12]. Briefly, following the analysis of Shi et al. [12], the total heat generated (Q) on the heating platform due to the current carrying suspended beam and the platform can be shown to be

$$Q = I^2(R_h + R_l) \quad (4.1)$$

Now, considering the energy conservation in the heating platform

$$Q = G_b \Delta T_h + G_s (\Delta T_h - \Delta T_s) \quad (4.2)$$

where G_b and G_s are the total thermal conductance of the suspended beams in the heating platform and thermal conductance of the specimen. Since the suspended beams are fabricated with identical geometry, they are assumed to have the same thermal conductance.

Considering energy conservation in the sensing platform,

$$G_s (\Delta T_h - \Delta T_s) = G_b \Delta T_s \quad (4.2)$$

From Equation 4.2 and 4.3, these can be shown,

$$G_s = G_b \frac{\Delta T_s}{(\Delta T_h - \Delta T_s)} \quad (4.3)$$

$$G_b = \frac{Q}{(\Delta T_h - \Delta T_s)} \quad (4.4)$$

Combining equation 4.3 and 4.4, it can be shown that,

$$G_s = \frac{Q}{(\Delta T_h - \Delta T_s)} \left(\frac{\Delta T_s}{\Delta T_h + \Delta T_s} \right) \quad (4.5)$$

From the measured thermal conductance given in Equation 4.5, the effective thermal conductivity k_{eff} of the specimen is, then, solved by

$$k_{\text{eff}} = \frac{L_s}{\pi d_s^2/4} G_s \quad (4.6)$$

where d_s is the diameter of the nanofiber and L_s is the length of the nanofiber measured using the SEM after a 3 nm Pt coating. Thermal contact resistances always exist between the nanofiber and the suspended platforms which can lower the sample's measured thermal conductance. Effective thermal conductivity k_{eff} equivalent to the sample's thermal conductivity k only if the thermal contact resistance is negligible as compared to the intrinsic thermal resistance of the nanofiber. This is discussed in detail in the next section.

4.4 Experimental results and discussions

4.4.1 Role of thermal contact resistance

The thermal conductance measurement system uses two-probes and includes thermal contact resistance. The thermal contact resistance between the sample and the islands can result in an underestimation of the sample's k . The total thermal resistance of the system at steady state is the sum of thermal contact resistance between the heating island and the nanofiber ($R_{c,hi}$), the

intrinsic thermal resistance of nanofiber (R_s) and the thermal contact resistance between the sensing island and the nanofiber ($R_{c,si}$). Therefore, the total thermal resistance ($R_{tot} = 1/G_s$) can be written as

$$R_{tot} = R_s + R_{c,hi} + R_{c,si} \quad (4.7)$$

The heating (h) and sensing (s) sides have the same geometrical properties and same contact mechanism, so we assume that $R_{c,hi} \approx R_{c,si} \approx R_c$. Then

$$R_{tot} = R_s + 2R_c \quad (4.8)$$

To measure the sample's k accurately, $2R_c$ should be negligible compared to the sample's intrinsic thermal resistance ($R_s = 4L_s/\pi d_s^2 k_s$). To achieve $2R_c \ll R_s$, either R_s can be increased or $2R_c$ can be lowered. For high k samples, such as PENF, intrinsic thermal resistance (R_s) can be increased by making the nanofiber long and the cross-section area small. However, this will also reduce the heat flux significantly. Consequently, the temperature rise of sensing side ΔT_s will be lessened, making accurate measurement difficult. Alternatively, thermal contact resistance can be decreased to make $2R_c \ll R_s$. A platinum or graphite coating, using an electron beam or focused ion beam (FIB), has been extensively used in literature to reduce $2R_c$ [11], [14]. However, high-energy electron/ion beam amorphized our sample and reduced the thermal conductivity enhancement to bulk as shown in Fig. 4.4.

Due to the sensitivity of our samples to the electron/ion beam, we used capillary-assisted adhesion (described in Section 3.3.3 of Chapter 3) to minimize $2R_c$. However, $2R_c$ remains significant comparable to R_s . Following the analysis of Yu *et al.*, the total $2R_c$ is given as [11]

$$2R_c = \frac{2}{\sqrt{\frac{k_{||}A_{cr}}{R'_c} \tanh\left(l_c \sqrt{\frac{1}{k_{||}A_{cr}R'_c}}\right)}} \quad (4.9)$$

where $k_{//}$ is axial thermal conductivity of the nanofiber sample, A_{cr} is the cross-sectional area, R'_c is the constriction resistance per unit axial length in contact and l_c is the total length of nanofiber in contact with an island. R'_c is calculated using the line contact model of McGee *et al.* for a cylinder on a flat substrate [15], [16]

$$R'_c = \frac{1}{\pi k_{\perp}} \ln\left(\frac{4d}{w}\right) - \left(\frac{1}{2k_{\perp}}\right) + \frac{1}{\pi k_{pt}} \ln\left(\frac{2d}{\pi w}\right) \quad (4.10)$$

where k_{\perp} ($0.33 \text{ W m}^{-1} \text{ K}^{-1}$ [6]) is the radial thermal conductivity of the nanofiber sample, d is the diameter of the sample, w is the contact width of nanofiber on the substrate and k_{pt} ($70 \text{ W m}^{-1} \text{ K}^{-1}$) is the thermal conductivity of platinum.

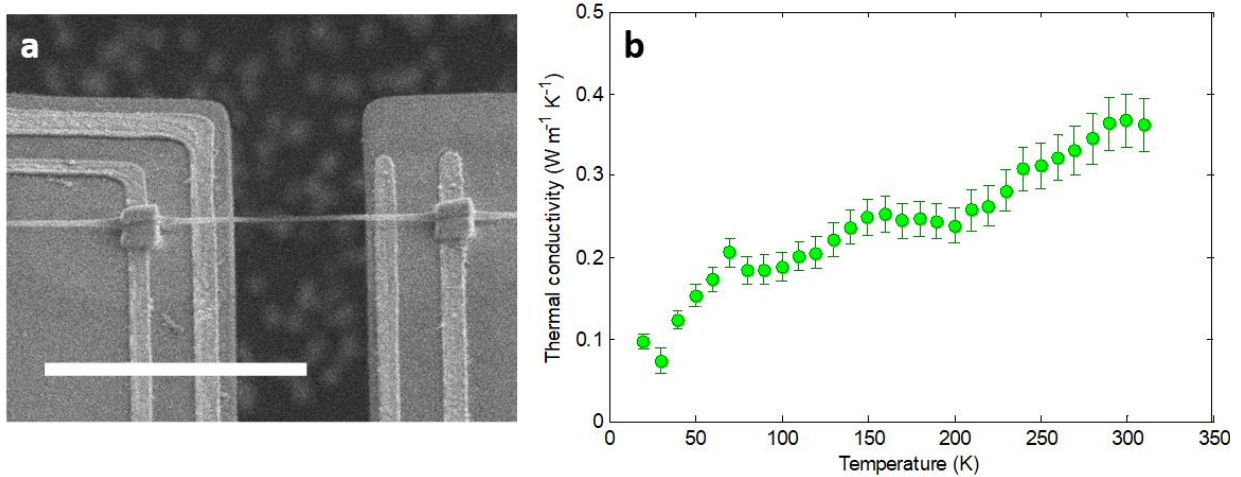


Figure 4.4: a) Platinum coating using FIB on PENF. b) k of PENF with platinum contact. The k values are similar to that of bulk PE. Scalebar, $10 \mu\text{m}$.

4.4.2 Contact width estimation

We need to know the contact width (w) between a nanofiber sample and an island to calculate $2R_c$ using Equations 4.9 and 4.10. Elastic plane strain analysis can be applied to obtain w assuming the van der Waals force represents the applied force [15], [16].

For an elastic cylinder on a flat substrate, Bahadur *et al.* [16] derived w due to elastic deformation from the van der Waals force given as:

$$w = \sqrt{\left(\frac{16F_{\text{vdw}}E_m d}{\pi}\right)} \quad (4.11)$$

where F_{vdw} is the van der Waals force per unit contact length between the nanofiber and the island, and E_m is the effective modulus defined as

$$E_m = \frac{1}{2} \left(\frac{1 - \nu_s^2}{E_s} + \frac{1 - \nu_{\text{Pt}}^2}{E_{\text{Pt}}} \right) \quad (4.12)$$

where $\nu_s = 0.4$ [17] is the Poisson's ratio of PE in cross plane-axial direction, $E_s \approx 3.5$ GPa [6] is the elastic modulus of the highly drawn PE in cross-plane direction, $\nu_{\text{Pt}} = 0.36$ [18] is the Poisson's ratio of thin Pt film and $E_{\text{Pt}} \approx 140$ GPa [19] is the elastic modulus of nanoscale Pt film. The van der Waals force per unit contact length for a cylinder-flat substrate is given as [20]

$$F_{\text{vdw}} = \frac{A_{\text{PE-Pt}}\sqrt{d}}{16h^{5/2}} \quad (4.13)$$

where $A_{\text{PE-Pt}}$ is a Hamaker constant for a PE-Pt interface and h is the separation distance between the PE nanofiber and Pt estimated as the sum of van der Waal's radii of Pt and C [21]. The Hamaker constant for a PE-Pt interface is

$$A_{\text{PE-Pt}} = \sqrt{A_{\text{PE-PE}}A_{\text{Pt-Pt}}} \quad (4.14)$$

Hamaker constant value for a PE-PE interface is 8.43×10^{-20} J at room temperature [22]. Similarly, we used the Hamaker constant for Pt-Pt interface (20×10^{-20} J) interacting in water at room temperature [23]. $A_{\text{PE-Pt}}$ was estimated to be 13×10^{-20} J.

Higher $k_{||}$ of the sample leads to a lower $2R_c$ (per Equation 4.9) as shown in Fig. 4.5. We chose upper ($100 \text{ W m}^{-1} \text{ K}^{-1}$) and lower bound ($50 \text{ W m}^{-1} \text{ K}^{-1}$) from previously reported $k_{||}$ values at RT for an ultra-drawn PE nanofiber [3] to estimate the range of $2R_c$ of our specimen.

For a typical 100 nm PE specimen, the w was found to be approximately 8.3 nm resulting in $2R_c \approx 3.31 \times 10^6 - 4.63 \times 10^6 \text{ K W}^{-1}$. This is, 10 – 30 % of R_{tot} , as can be seen by applying $R_s = 4L_s/(\pi d_s^2 k_s)$ to the data Fig. 4.7.

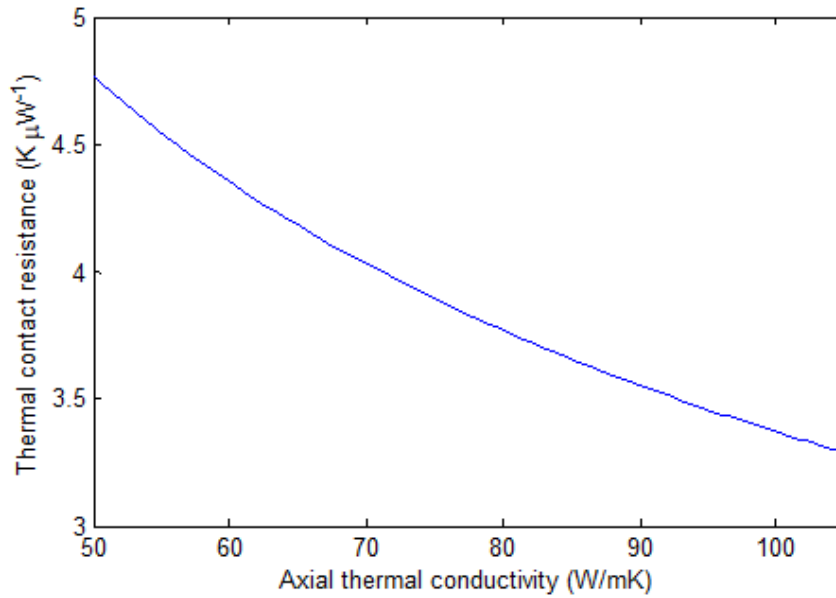


Figure 4.5: Thermal contact resistance ($2R_c$) as a function of axial thermal conductivity of a PENF.

4.4.3 Noise equivalent thermal conductance of PRT microthermal devices

The thermal conductance assessment is limited by the ability to measure the temperature rise in the sensing island (denoted by subscript s) accurately. Following the sensitivity analysis of Shi *et al.* [12], the noise-equivalent thermal conductance (NEG_s) in the sensing island can be shown as

$$NEG_s = G_b \frac{NET_s}{(\Delta T_h - \Delta T_s)} \quad (4.15)$$

where NET_s is the noise-equivalent temperature (K) of the sensing island. Also,

$$NET_s = \frac{NER_s/R_s}{TCR} \quad (4.16)$$

where NER_s is the noise-equivalent resistance (Ω) of the sensing island. Through measurement of a precision 1 M Ω resistor, NER_s/R_s was found to be $\sim 7.5 \times 10^{-5}$. The temperature coefficient of resistance (TCR) of the PRT was found to be $\sim 2.6 \times 10^{-3} \text{ K}^{-1}$ at 150 K and $\sim 2.1 \times 10^{-3} \text{ K}^{-1}$ at 300 K. Therefore, NET_s is $\sim 29 \text{ mK}$ at 150 K and $\sim 36 \text{ mK}$ at 300 K. The temperature fluctuation in the cryostat is $\sim 10 \text{ mK}$ after waiting for the global temperature to stabilize for an hour at temperatures above 150 K.

The thermal conductance of the suspended PRT beams, G_b , is 70 – 90 nW K $^{-1}$ at 150 K and 90 – 110 nW K $^{-1}$ at 300 K. The temperature difference between heating and sensing islands ($\Delta T_h - \Delta T_{hs}$) is kept within 5 K. The NEG_s of the measurement system can be now found from Equation 4.15. At 300 K, the NEG_s is $\sim 0.85 \text{ nW K}^{-1}$ and at 150 K it is $\sim 0.52 \text{ nW K}^{-1}$. This is around 1 % of the of the measured conductance, hence noise is not an issue in the measurements.

4.4.4 Background thermal conductance

Because the thermal conduction experiment was carried out at a high vacuum level of 2×10^{-7} Torr and the temperature difference between the islands was limited to 5 K, we expect negligible heat transfer from residual gas and radiation. A background thermal conductance, G_{bgd} , measurement of an empty micro thermal device in the same experimental conditions verifies that G_{bgd} is within the NEG_s as shown in Fig. 4.6.

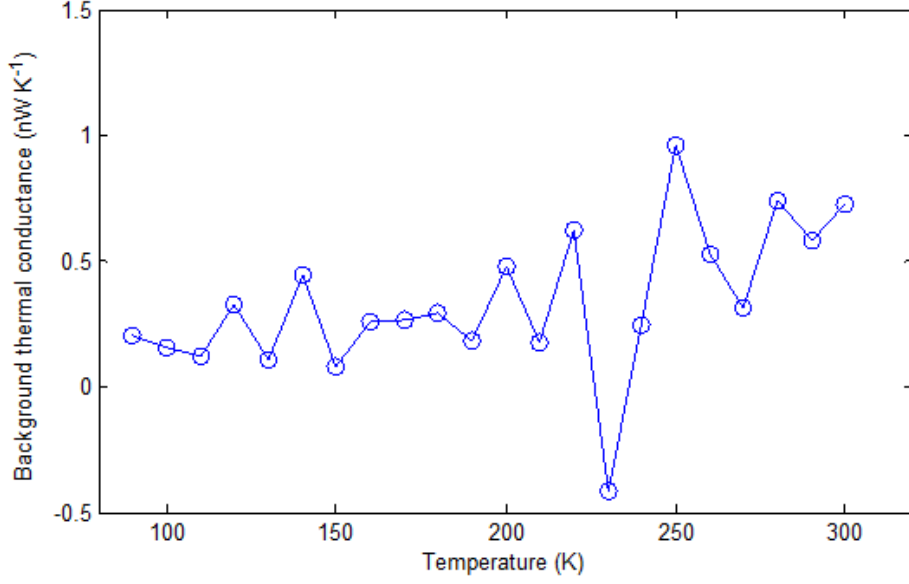


Figure 4.6: Background thermal conductance of an empty device with gap 5 μm .

4.4.5 Uncertainty analysis in thermal conductivity

The thermal conductivity of an individual PENF is given by

$$k = \frac{GL}{A} = \frac{4GL}{\pi d^2} \quad (4.17)$$

where G is its thermal conductance and L and A are its length and cross-sectional area. Using the uncertainty propagation rule, the error in k can be expressed as

$$\left(\frac{\delta k}{k}\right)^2 = \left(\frac{\delta G}{G}\right)^2 + \left(\frac{\delta L}{L}\right)^2 + \left(2\frac{\delta d}{d}\right)^2 \quad (4.18)$$

where δ is the uncertainty. The values for $\left(\frac{\delta L}{L}\right)^2$ and $\left(2\frac{\delta d}{d}\right)^2$ are obtained from the SEM images as described later. From the analysis of Shi *et al.* [10], [12],

$$G = \frac{Q}{(\Delta T_h - \Delta T_s)} \left(\frac{\Delta T_s}{\Delta T_h + \Delta T_s} \right) \quad (4.19)$$

where Q is the heat transferred to the heating island. The error in G can be written as

$$\left(\frac{\delta G}{G}\right)^2 = \left(\frac{\delta Q}{Q}\right)^2 + \left(\frac{\delta \Delta T_s}{\Delta T_s}\right)^2 + \left(\frac{\delta(\Delta T_h - \Delta T_s)}{(\Delta T_h - \Delta T_s)}\right)^2 + \left(\frac{\delta(\Delta T_h + \Delta T_s)}{(\Delta T_h + \Delta T_s)}\right)^2. \quad (4.20)$$

When a dc current I is applied to the heating island, it can be shown that the heat transferred to the heating island is equivalent to

$$Q = I^2(R_h + R_l) = I^2 \frac{(R_h + R_l)}{R_h} R_h = I^2 \gamma R_h, \quad (4.21)$$

where R_h is the resistance of the heating island and R_l is the resistance of a current carrying SiN_x beam. The error in DC power in the heating island is given by,

$$\left(\frac{\delta Q}{Q}\right)^2 = \left(2 \frac{\delta I}{I}\right)^2 + \left(\frac{\delta R_h}{R_h}\right)^2 \quad (4.22)$$

DC current up to 20 μ A is applied with a Keithley 2400 source measurement unit with a high accuracy of ± 5 nA. Thus, the uncertainty ($< 0.07\%$) due to heat input into the heating island (Q) is low. The error in temperature rise in the heating or sensing island can be shown to be

$$\left(\frac{\delta \Delta T_i}{\Delta T_i}\right)^2 = \left(\frac{\delta \Delta R_i}{\Delta R_i}\right)^2 + \left(\frac{\delta \alpha_i}{\alpha_i}\right)^2 \quad (4.23)$$

where $i = s$ (sensing) or h (heating), and $\alpha_i \equiv dR_i/dT$. A value for α_i is obtained from curve fitting of R_i and T where $\Delta T = 10$ K. The noise in R_i is small compared to T as $\left(\frac{\delta R_i}{R_i}\right) \approx 7.5 \times 10^{-5}$. Then, $\delta(\Delta T) = \sqrt{2} \delta(T)$. Assuming the worst-case scenario, NET is added with the temperature fluctuation in the cryostat, $\delta(T) \approx 36$ mK + 10 mK ≈ 50 mK. Then, $\delta(\Delta T) = \sqrt{2} \cdot 50$ mK = 71 mK. Hence, $\left(\frac{\delta \alpha_s}{\alpha_s}\right) \approx 71 \times 10^{-3} \text{ mK} / 10 \text{ K} = 0.71\%$. Zhu *et al.* [24] estimated $\left(\frac{\delta \alpha_i}{\alpha_i}\right)$ from the least square linear fit of five R_i vs T measurements within 10 K for a 95 % confidence interval to be $< 0.76\%$, which is consistent with our calculation.

The error in $\frac{\delta\Delta R_i}{\Delta R_i} \approx \frac{\sqrt{2}\delta(R_i)}{\Delta R_i}$ can be estimated from the change in resistance during a heating ramp. At 100 K, $\frac{\delta\Delta R_h}{\Delta R_h} \approx \frac{\sqrt{2} \cdot 0.1275}{30} \approx 0.56\%$; $\frac{\delta\Delta R_s}{\Delta R_s} \approx \frac{\sqrt{2} \cdot 0.1275}{11} \approx 1.6\%$. Similarly, at 300 K, $\frac{\delta\Delta R_h}{\Delta R_h} \approx 0.6\%$; $\frac{\delta\Delta R_s}{\Delta R_s} \approx 2.15\%$.

Then, the error in ΔT_s and ΔT_h can now be estimated. At 100 K,

$$\left(\frac{\delta(\Delta T_h)}{\Delta T_h}\right) = \sqrt{(0.56 \times 10^{-2})^2 + (0.71 \times 10^{-2})^2} \approx 0.90\%$$

$$\left(\frac{\delta(\Delta T_s)}{\Delta T_s}\right) = \sqrt{(1.6 \times 10^{-2})^2 + (0.71 \times 10^{-2})^2} \approx 1.75\%$$

Similarly, at 300 K,

$$\left(\frac{\delta(\Delta T_h)}{\Delta T_h}\right) = \sqrt{(0.6 \times 10^{-2})^2 + (0.71 \times 10^{-2})^2} \approx 0.93\%$$

$$\left(\frac{\delta(\Delta T_s)}{\Delta T_s}\right) = \sqrt{(2.15 \times 10^{-2})^2 + (0.71 \times 10^{-2})^2} \approx 2.26\%$$

Now, using $a_h = \left(\frac{\delta(\Delta T_h)}{\Delta T_h}\right)$ and $a_s = \left(\frac{\delta(\Delta T_s)}{\Delta T_s}\right)$

$$\left(\frac{\delta(\Delta T_h - \Delta T_s)}{(\Delta T_h - \Delta T_s)}\right) = \frac{\sqrt{[\delta(\Delta T_h)]^2 + [\delta(\Delta T_s)]^2}}{(\Delta T_h - \Delta T_s)} = \frac{\sqrt{(a_h \cdot \Delta T_h)^2 + (a_s \cdot \Delta T_s)^2}}{(\Delta T_h - \Delta T_s)}$$

Similarly,

$$\left(\frac{\delta(\Delta T_h + \Delta T_s)}{(\Delta T_h + \Delta T_s)}\right) = \frac{\sqrt{[\delta(\Delta T_h)]^2 + [\delta(\Delta T_s)]^2}}{(\Delta T_h + \Delta T_s)} = \frac{\sqrt{(a_h \cdot \Delta T_h)^2 + (a_s \cdot \Delta T_s)^2}}{(\Delta T_h + \Delta T_s)}$$

To estimate the error of above two expressions, let us consider the typical case of PE nanofibers at 100 K and 300 K. At 100K, we observe that for $\Delta T_h \approx 4.5$ K, $\Delta T_s \approx 2.0$ K. Thus, $\Delta T_h + \Delta T_s \approx 6.5$ K and $\Delta T_h - \Delta T_s \approx 2.5$ K

$$\left(\frac{\delta(\Delta T_h - \Delta T_s)}{(\Delta T_h - \Delta T_s)}\right) = \frac{\sqrt{(0.9 \times 10^{-2} \times 4.5)^2 + (1.75 \times 10^{-2} \times 2.0)^2}}{(2.5)} = 2.14\%$$

Similarly,

$$\left(\frac{\delta(\Delta T_h + \Delta T_s)}{(\Delta T_h + \Delta T_s)} \right) = \frac{\sqrt{(0.9 \times 10^{-2} \times 4.5)^2 + (1.75 \times 10^{-2} \times 2.0)^2}}{(6.5)} = 0.82 \%$$

The total error in thermal conductance is then, using Equation 4.20,

$$\left(\frac{\delta G}{G} \right) = \sqrt{(0.07 \times 10^{-2})^2 + (1.75 \times 10^{-2})^2 + (2.14 \times 10^{-2})^2 + (0.82 \times 10^{-2})^2} = 2.88 \%$$

At 300 K, we observe that for $\Delta T_h \approx 5 \text{ K}$, $\Delta T_s \approx 1.4 \text{ K}$. Thus, $\Delta T_h + \Delta T_s \approx 6.4 \text{ K}$ and $\Delta T_h - \Delta T_s \approx 3.6 \text{ K}$. The total error in thermal conductance is then, using Equation 4.20,

$$\left(\frac{\delta G}{G} \right) = \sqrt{(0.07 \times 10^{-2})^2 + (2.26 \times 10^{-2})^2 + (1.71 \times 10^{-2})^2 + (0.96 \times 10^{-2})^2} = 2.99 \%$$

This error is for a single measurement of $G = \frac{Q}{(\Delta T_h - \Delta T_s)} \left(\frac{\Delta T_s}{\Delta T_h + \Delta T_s} \right)$, where heat flux (Q) is determined by an applied dc current I . In our measurement, we collect 250 data points for current from 10 – 20 μA to get the sample conductance more accurately.

For a typical sample with a diameter of 100 nm and length 8 μm , the standard deviation in the diameter is found to be around 4 % and negligible in length. Then, the total error in the thermal conductivity at 300 K is

$$\left(\frac{\delta k}{k} \right) = \sqrt{(2.99 \times 10^{-2})^2 + (2 \times 4 \times 10^{-2})^2} = 8.54 \%$$

4.4.6 Thermal transport in crystalline PENF.

Fig. 4.7a shows a specimen mounted on the thermal platform with a new mounting technique developed in Section 3.3.3 of Chapter 3 ready for thermal measurement. The equivalent PENF thermal circuit can be expressed as a series of thermal resistances, namely intrinsic thermal resistance of the nanofiber R_s , the thermal contact resistance between the nanofiber and the heating

island $R_{c,hi}$ and the sensing island $R_{c,si}$. The heating and sensing islands have the same geometrical and material properties and undergo the same contact mechanism, so we can assume that $R_{c,hi} \approx R_{c,si} \approx R_c$. The measured R_{tot} is the total thermal resistance of this circuit. Therefore,

$$R_{tot} = R_s + 2R_c = \frac{L}{kA} + 2R_c \quad (1)$$

where L is the gap length between the heating and the sensing islands, A is the cross-sectional area of the fiber and $2R_c$ is the total thermal contact resistance. Assuming similar k for the samples with similar diameter, we estimate $2R_c$ by extrapolating the linear fit between R_{tot} and L/A to $L = 0 \mu\text{m}$. The linear fits (Fig. 4.7b) at 150 K and 300 K show that $2R_c$ is $3.6 \times 10^6 \text{ K W}^{-1}$ and is approximately temperature-independent above 100 K [25]. This value is consistent with ($2R_c \approx 4 \times 10^6 \text{ K W}^{-1}$) predicted using a line-contact model (see Fig. 4.5). Fig. 4.7c show the $k(T)$ of a typical nanofiber, which increases as $\sim T^1$ and reaches a maximum of $\sim 90 \text{ W m}^{-1} \text{ K}^{-1}$ at 130 K – 160 K. It then decreases as $1/T$ on further increasing the temperature. RT values were 50 – 70 $\text{W m}^{-1} \text{ K}^{-1}$, which is on the same order as those of tip drawn nanofibers [3]. This is a remarkable enhancement (10 – 14 \times) using local drawing as the PEMF RT k is $5 \text{ W m}^{-1} \text{ K}^{-1}$ (see Fig. 4.7d). However, PENFs with similar diameter show scattering in RT k values which may be because of the variation in crystallinity and orientation among the nanofibers as shown by micro Raman measurement discussed in Section 3.4.2 of Chapter 3. Recent studies on ultra-drawn PEMF and films have also obtained k around 50 – 60 $\text{W m}^{-1} \text{ K}^{-1}$ at RT [26]–[28]. After careful characterization on the cross section of the PENFs, we observed that samples with diameters below 150 nm generally have a non-circular cross-section (see Section 3.5.3 of Chapter 3), where we provide extensive documentation detailing how this was characterized), in which the measured height is about 1.5 times smaller than the measured width. We assumed the fibers to have a cylindrical shape

and used the measured width for calculating k of PENFs from the measured thermal conductance. Hence, the k reported in Figs. 4.7c and e should be taken as a lower bound.

To directly demonstrate the heat transfer along the PENF we used high-resolution thermoreflectance imaging (Microsanj NT-210B) to precisely map the temperature distribution of the micro thermal device in Fig. 4.8a, in which the island on the right-hand side was electrically heated. We compared the following two cases for the same batch of devices at the same heating power in laboratory air. In the absence of a nanofiber bridging the two islands, the left island was heated negligibly due to the low thermal conductivity of the air gap (Fig. 4.8a). In the case of our fabricated PENF with a diameter of ~ 500 nm (Fig. 4.8b), the left island of the microdevice was dramatically thermalized because of the extremely high thermal conductivity ($\sim 70 \text{ W m}^{-1} \text{ K}^{-1}$) of the PENF shown in our work. This experiment clearly demonstrated that the PENF can potentially be used as efficient heat spreaders for microelectronics. More importantly, compared with existing nanoscale heat spreaders like carbon nanotubes and graphene, the PENF have a practical advantage because they are purely electrically insulating.

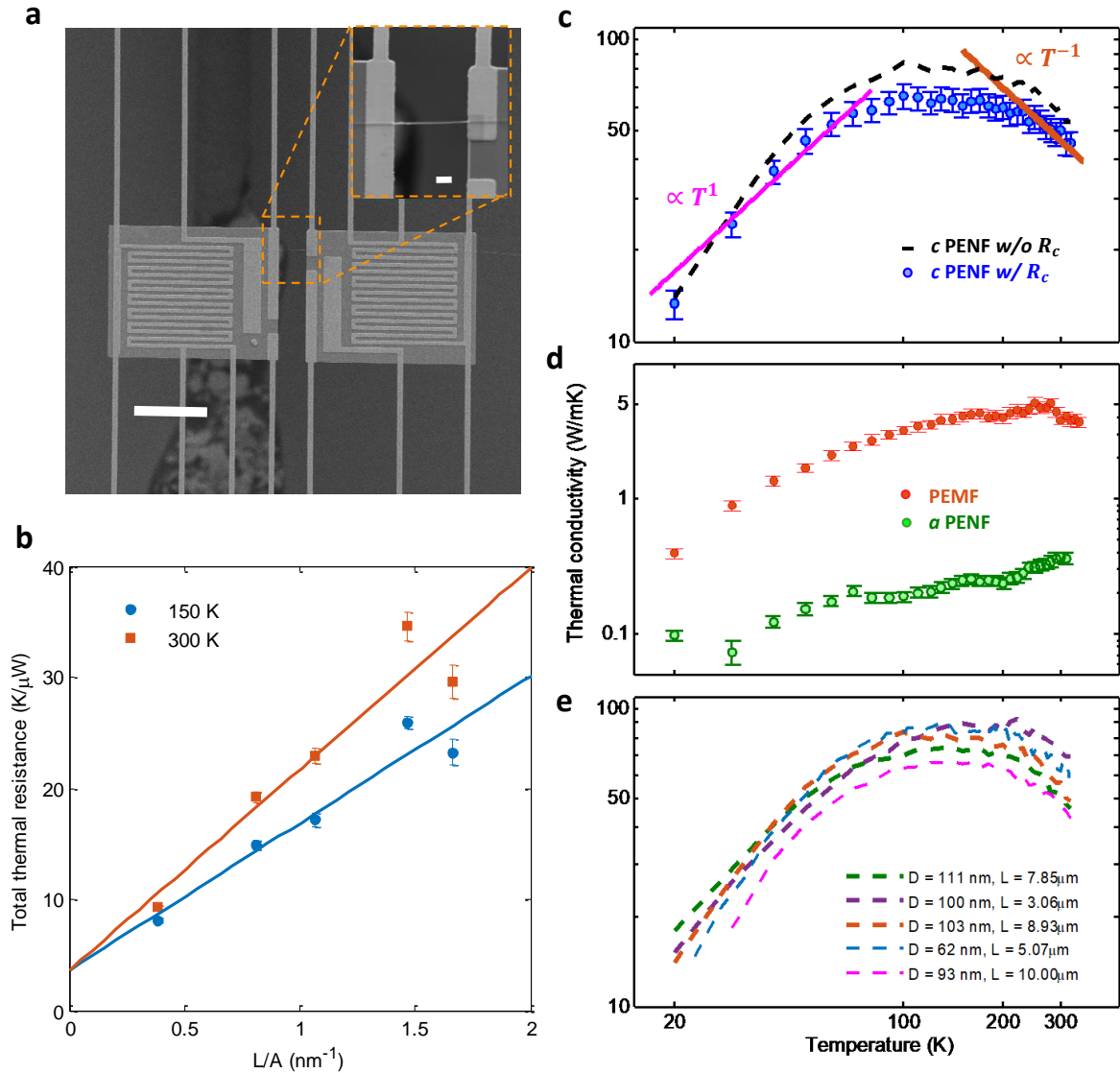


Figure 4.7: Thermal characterization of PENF. a) A PRT based micro-device with the heating and the sensing islands. Inset shows a PENF bridging the islands. b) Total measured thermal resistance vs L/A of crystalline (c) PENFs at 150 K and 300 K where the y-intercept represents $2R_c$. The error bars show the mean and standard deviation values of 250 measurements. c) $k(T)$ of a PENF. Blue circles are measured k of a c -PENF, black dotted lines are after adjusting for $2R_c$. Orange line is $1/T$ trend of c -PENF at high temperatures and pink line is T^1 trend at low temperatures. d) $k(T)$ of PEMF and amorphous (a) PENF. Red circles are PEMF before local drawing, and green circles are c -PENF amorphized due to exposure to FIB. e) $k(T)$ of all reported samples after adjusted for $2R_c$. Scale bars, 20 μm and 2 μm (inset).

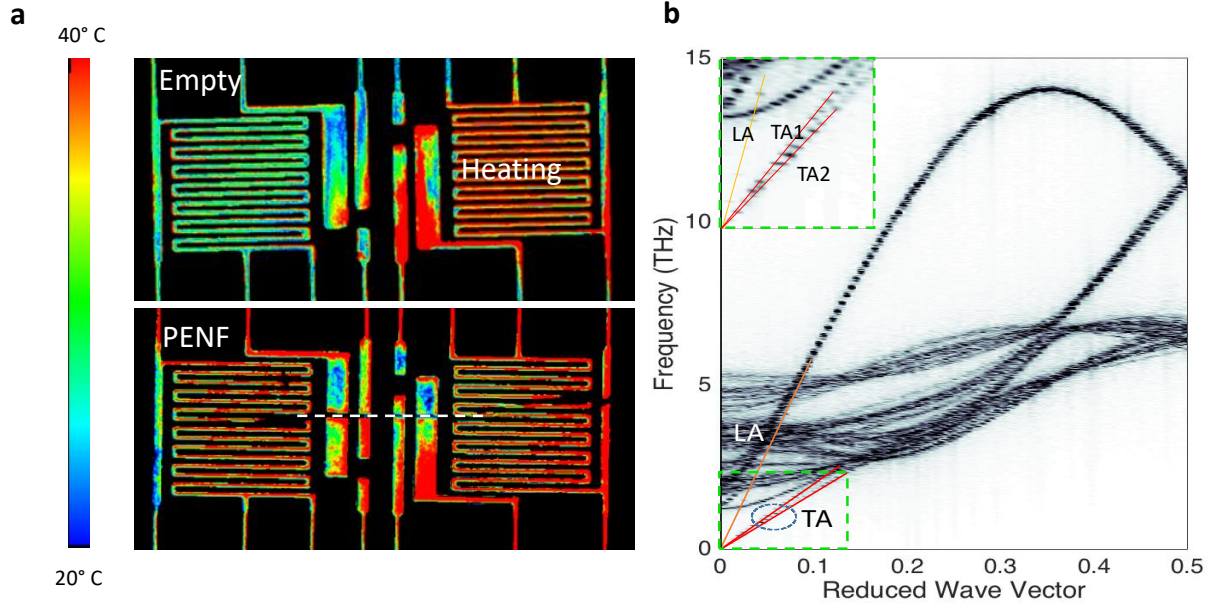


Figure 4.8: Thermal transport in PENF. a) Thermoreflectance imaging of heating island (right) and sensing island (left) without a nanofiber and a PENF respectively, in laboratory air. The dotted white line is the PENF position. b) Phonon dispersion relation of the acoustic branches along the chain backbone calculated from the trajectory of MD simulations using a two-dimensional Fourier transform. The contour is the raw data from the calculation and colored lines are linear fits. The inset shows the acoustic branches close to the Brillouin zone center.

While it is well understood that the $1/T$ relation of k at high temperatures is due to anharmonic phonon scattering in crystals, the T^1 relation at low temperatures is uncommon in crystalline materials [29], [30]. To understand this unusual $k(T)$ trend of PENFs, Zhang and Luo performed an atomistic simulation to analyze the phonon properties in a perfect PE crystal with extended chains and found that the heat capacity scales as T^1 because of 1 D behavior of backbone chain where strong covalent bond dominate over van der Waal interactions. At low temperatures, where the anharmonic phonon scattering is weak, the mean free path is usually limited by extrinsic scattering mechanisms, such as defect and boundary scattering. In PENF, these can be from polymer chain ends or other defects along the chain backbone, such as segment rotation, which

are much stronger scattering centers than point defects [31], [32]. Under such a condition, the mean free path is the same for all phonons, which is also a common assumption made for 3D crystals at low temperatures [33]. As a result, $k(T)$ is purely from that of the heat capacity. For the linear phonon branches in a 1D system, k should scale as T^1 [33]. Thermal transport in aligned PE chain bundles is highly anisotropic and is dominated by the chain backbone since the inter-chain van der Waal interactions are much weaker than the covalent bonding along the backbone. However, phonons with wavevectors not strictly aligned along the chain backbone direction can still contribute to k though in a much smaller proportion. This 3D effect of phonon dispersion can result in k scaling slightly greater than T^1 at the low temperature limit, which can be seen in Fig. 4.7c. At the high temperature end, the experimental data also matches well with results from early MD simulations [32] where non-equilibrium MD was used to calculate the k of crystalline PE. The high temperature data can be reasonably fit by a $1/T$ relation.

4.5 Discussion

In summary, values of $k(T)$ from 20 K to 320 K for a highly crystalline PENF verified by micro Raman and low-dose cryo-TEM in Sections 3.4.2 and 3.4.3 of Chapter 3 fabricated with a new technique as discussed in Section 3.2 of Chapter 3 are reported, where k reaches up to 90 W m⁻¹ K⁻¹ at 130 K. This suggests that PENF can be used as an efficient heat transfer material for cryogenic purposes particularly where an electrically insulating material is concurrently desired [34]. At low temperatures, k increases as $\sim T^1$, which stems from one dimensionality of phonon transport and extrinsic scattering (e.g. defects, boundary). The values k are critically dependent on the cross-section area, which is challenging to measure at this scale. As stated above and detailed in the Section 3.5.3 of Chapter 3, the cross-sections are non-circular. However, when calculating

k of PENF from the measured thermal conductance we have assumed the fibers to have a circular cross-section that corresponds to the larger dimension. Hence, the k reported in Figs. 4.7c and e a should be taken as a lower bound for PENF.

4.6 Summary

In this chapter, the temperature dependent thermal conductivity measurement of PENF from 20 K to 320 K is discussed. The thermal contact resistance $2R_c$ between PENF and the suspended platforms was found to be significant. Following the analysis of Bahadur *et al.*, a contact width of ~ 8 nm was estimated between a PENF with a diameter of 100 nm and the suspended platform. A line contact model by McGee *et al.* and analysis by Yu *et al.* was used to estimate the $2R_c \approx 4 \times 10^6$ K W⁻¹. The thermal contact resistance $2R_c$ was measured to be $\sim 3.6 \times 10^6$ K W⁻¹ consistent with the prediction. The thermal conductivity increased with increasing temperature following an unusual $\sim T^1$ trend below 100 K and eventually peaked around 130–150 K reaching a metal-like value of 90 W m⁻¹ K⁻¹, and then decays as $1/T$. At low temperatures (<100 K), k increases as $\sim T^1$, which stems from one dimensionality of phonon transport and extrinsic scattering (e.g. defects, boundary). The $1/T$ trend at a higher temperature (>150 K) was due to Umklapp scattering, consistent for a low defect-density crystalline sample. The thermal conductivity values are couple orders of magnitude higher than bulk opening potential as a heat spreader for flexible and wearable electronics.

4.7 Chapter references:

- [1] K. I. Winey, T. Kashiwagi, and M. Mu, “Improving Electrical Conductivity and Thermal Properties of Polymers by the Addition of Carbon Nanotubes as Fillers,” *MRS Bull.*, vol. 32, no. 04, pp. 348–353, Apr. 2007.

- [2] M. M. and K. I. Winey*, “Polymer Nanocomposites Containing Carbon Nanotubes,” 2006.
- [3] S. Shen, A. Henry, J. Tong, R. Zheng, and G. Chen, “Polyethylene nanofibres with very high thermal conductivities.,” *Nat. Nanotechnol.*, vol. 5, no. 4, pp. 251–255, 2010.
- [4] V. Singh, T. L. Bougher, A. Weathers, Y. Cai, K. Bi, M. T. Pettes, S. A. McMennamin, W. Lv, D. P. Resler, T. R. Gattuso, D. H. Altman, K. H. Sandhage, L. Shi, A. Henry, and B. A. Cola, “High thermal conductivity of chain-oriented amorphous polythiophene.,” *Nat. Nanotechnol.*, vol. 9, no. 5, pp. 384–90, 2014.
- [5] A. G. Gibson, D. Greig, M. Sahota, I. M. Ward, and C. L. Choy, “Thermal conductivity of ultrahigh-modulus polyethylene,” *J. Polym. Sci. Polym. Lett. Ed.*, vol. 15, no. 4, pp. 183–192, Apr. 1977.
- [6] C. L. Choy, Y. W. Wong, G. W. Yang, and T. Kanamoto, “Elastic modulus and thermal conductivity of ultradrawn polyethylene,” *J. Polym. Sci. Part B Polym. Phys.*, vol. 37, no. 23, pp. 3359–3367, Dec. 1999.
- [7] S. T. Huxtable, D. G. Cahill, S. Shenogin, L. Xue, R. Ozisik, P. Barone, M. Usrey, M. S. Strano, G. Siddons, M. Shim, and P. Keblinski, “Interfacial heat flow in carbon nanotube suspensions,” *Nat. Mater.*, vol. 2, no. 11, pp. 731–734, Nov. 2003.
- [8] C. L. Choy, Y. Fei, and T. G. Xi, “Thermal conductivity of gel-spun polyethylene fibers,” *J. Polym. Sci. Part B Polym. Phys.*, vol. 31, no. 3, pp. 365–370, Mar. 1993.
- [9] J. Ma, Q. Zhang, A. Mayo, Z. Ni, H. Yi, Y. Chen, R. Mu, L. M. Bellan, and D. Li, “Thermal conductivity of electrospun polyethylene nanofibers,” *Nanoscale*, vol. 7, no. 40, pp. 16899–16908, 2015.
- [10] D. Li, Y. Wu, P. Kim, L. Shi, P. Yang, and A. Majumdar, “Thermal conductivity of individual silicon nanowires,” *Appl. Phys. Lett.*, vol. 83, no. 14, p. 2934, 2003.
- [11] C. Yu, S. Saha, J. Zhou, L. Shi, A. M. Cassell, B. A. Cruden, Q. Ngo, and J. Li, “Thermal Contact Resistance and Thermal Conductivity of a Carbon Nanofiber,” *J. Heat Transfer*, vol. 128, no. 3, p. 234, 2006.
- [12] L. Shi, D. Li, C. Yu, W. Jang, D. Kim, Z. Yao, P. Kim, and A. Majumdar, “Measuring Thermal and Thermoelectric Properties of One-Dimensional Nanostructures Using a Microfabricated Device,” *J. Heat Transfer*, vol. 125, no. 5, p. 881, 2003.
- [13] J. Wu, X. Wang, M. Chen, D. Xu, and J. Yang, “Estimation of temperature coefficient of resistance for microfabricated platinum thermometers in thermal conductivity

- measurements of one-dimensional nanostructures,” *Meas. Sci. Technol.*, vol. 25, p. 5, 2014.
- [14] Z. Cheng, L. Liu, S. Xu, M. Lu, and X. Wang, “Temperature Dependence of Electrical and Thermal Conduction in Single Silver Nanowire,” *Sci. Rep.*, vol. 5, p. 10718, Jun. 2015.
- [15] G. R. McGee, M. H. Schankula, and M. M. Yovanovich, “Thermal resistance of cylinder-flat contacts: Theoretical analysis and experimental verification of a line-contact model,” *Nucl. Eng. Des.*, vol. 86, no. 3, pp. 369–381, Jun. 1985.
- [16] V. Bahadur, J. Xu, Y. Liu, and T. S. Fisher, “Thermal Resistance of Nanowire-Plane Interfaces,” *J. Heat Transfer*, vol. 127, no. 6, p. 664, 2005.
- [17] A. M. Zihlif, R. A. Duckett, and I. M. Ward, “The Poisson’s ratio of ultra-drawn polyethylene and polypropylene fibres using Michelson interferometry,” *J. Mater. Sci.*, vol. 13, no. 8, pp. 1837–1840, Aug. 1978.
- [18] K. Schwieker, J. Frye, and B. C. Prorok, “New Insight into Pile-Up in Thin Film Indentation,” in *MEMS and nanotechnology Volume 6*, Springer, New York, NY, 2013, pp. 41–46.
- [19] M. C. Salvadori, I. G. Brown, A. R. Vaz, L. L. Melo, and M. Cattani, “Measurement of the elastic modulus of nanostructured gold and platinum thin films,” *Phys. Rev. B*, vol. 67, no. 15, p. 153404, Apr. 2003.
- [20] J. N. Israelachvili, “Chapter 13 – Van der Waals Forces between Particles and Surfaces,” in *Intermolecular and Surface Forces*, 2011, pp. 253–289.
- [21] S. S. Batsanov, “Van der Waals Radii of Elements,” *Inorg. Mater.*, vol. 37, no. 9, pp. 871–885, 2001.
- [22] A. W. Neumann, S. N. Omenyi, and C. J. Van Oss, “Negative Hamaker coefficients I. Particle engulfment or rejection at solidification fronts,” *Colloid Polym. Sci.*, vol. 257, pp. 413–419, 1979.
- [23] B. . Derjaguin, Y. . Rabinovich, and N. V. Churaev, “Direct measurement of molecular forces,” *Nature*, vol. 272, no. 23, pp. 313–318, 1978.
- [24] J. Zhu, K. Hippalgaonkar, S. Shen, K. Wang, Y. Abate, S. Lee, J. Wu, X. Yin, A. Majumdar, and X. Zhang, “Temperature-Gated Thermal Rectifier for Active Heat Flow Control,” *Nano Lett.*, vol. 14, pp. 4867–4872, 2014.
- [25] J. Yang, S. Waltermire, Y. Chen, A. A. Zinn, T. T. Xu, and D. Li, “Contact thermal resistance between individual multiwall carbon nanotubes,” *Appl. Phys. Lett.*, vol. 96, no.

- 99, pp. 23109–224308, 2010.
- [26] Y. Xu, D. Kraemer, B. Song, Z. Jiang, J. Zhou, J. Loomis, J. Wang, M. Li, H. Ghasemi, X. Huang, X. Li, and G. Chen, “Nanostructured Polymer Films with Metal-like Thermal Conductivity,” *arXiv:1708.06416*, Aug. 2017.
- [27] S. Ronca, T. Igarashi, G. Forte, and S. Rastogi, “Metallic-like thermal conductivity in a lightweight insulator: Solid-state processed Ultra High Molecular Weight Polyethylene tapes and films,” *Polymer (Guildf)*, vol. 123, pp. 203–210, Aug. 2017.
- [28] B. Zhu, J. Liu, T. Wang, M. Han, S. Valloppilly, S. Xu, and X. Wang, “Novel Polyethylene Fibers of Very High Thermal Conductivity Enabled by Amorphous Restructuring,” *ACS Omega*, vol. 2, no. 7, pp. 3931–3944, Jul. 2017.
- [29] R. Chen, A. I. Hochbaum, P. Murphy, J. Moore, P. Yang, and A. Majumdar, “Thermal Conductance of Thin Silicon Nanowires,” *Phys. Rev. Lett.*, vol. 101, no. 105501, 2008.
- [30] K. Gofryk, S. Du, C. R. Stanek, J. C. Lashley, X.-Y. Liu, R. K. Schulze, J. L. Smith, D. J. Safarik, D. D. Byler, K. J. McClellan, B. P. Uberuaga, B. L. Scott, and D. A. Andersson, “Anisotropic thermal conductivity in uranium dioxide,” *Nat. Commun.*, vol. 5, p. 4551, Aug. 2014.
- [31] T. Zhang and T. Luo, “High-Contrast, Reversible Thermal Conductivity Regulation Utilizing the Phase Transition of Polyethylene Nanofibers,” *ACS Nano*, vol. 7, no. 9, pp. 7592–7600, Sep. 2013.
- [32] T. Zhang and T. Luo, “Morphology-influenced thermal conductivity of polyethylene single chains and crystalline fibers,” *J. Appl. Phys.*, vol. 112, no. 9, p. 094304, 2012.
- [33] C. Kittel, *Introduction to solid state physics*. Wiley, 2005.
- [34] A. Yamanaka, T. Takao, A. Yamanaka, and T. Takao, “Thermal Conductivity of High-Strength Polyethylene Fiber and Applications for Cryogenic Use,” *ISRN Mater. Sci.*, vol. 2011, pp. 1–10, 2011.

Chapter 5: Solid-state polyethylene nanofiber thermal switches and diodes using structural phase transition

5.1 Abstract

Here, we report an experimental demonstration of fully reversible thermal switching in crystalline PENF developed in Chapter 3 by a temperature-induced structural phase transition from orthorhombic – hexagonal (*O-H*) phase. We find that the phase transition introduces along-chain segmental rotational disorder, and leads to a switching factor (i.e., the ratio between on-state high and off-state low thermal conductance values) as high as 10 before and after the phase transition, which exceeds any previously reported experimental values for solid-solid or solid-liquid phase transition of materials [1], [2]. By utilizing the sharp thermal conductance change, we also demonstrate a high-performance nanoscale thermal diode by fabricating a heterogeneous amorphous-crystalline PE nanofiber junction, and achieve a thermal rectification factor up to 25 %, comparable to the existing nanoscale solid-state thermal diodes based on carbon nanotubes (2 %), boron nitride nanotubes (7 %), graphene (28 %) and VO₂ nanobeams (28 %) [3]–[5]. Moreover, the thermal rectification of the nanofiber thermal diode can be actively modulated by the environmental temperature and only requires a small temperature difference (<10 K) across the device. This active control of heat flow at the nanoscale opens up new possibilities for developing switchable thermal devices for autonomous thermal management, solid-state refrigeration, waste heat scavenging, thermal circuits, and phononic computing.

5.2 Introduction

Active control of thermal transport is of significant interest for a broad range of applications, including heating and cooling, energy conversion, materials processing, and data storage. However, compared with the rich selection of switchable, nonlinear, and active electrical components, advanced solid-state thermal components for actively controlling heat flow have been rare. As driven by Moore's law in the past decades, continuous miniaturization of electrical components such as transistors and diodes down to nanometer scale has enabled concurrent size reduction and operating speed increase in modern electronics, accelerating information revolution. In stark contrast, elementary building blocks for thermal control, particularly at the nanoscale, are few.

Recently, Shin et al. demonstrated a switchable liquid crystal network with a magnetic field above the glass transition temperature (~ 65 °C) [6]. However, the switching factor (~ 1.5) and thermal conductivity between on ($0.34 \text{ W m}^{-1} \text{ K}^{-1}$) and off ($0.22 \text{ W m}^{-1} \text{ K}^{-1}$) states were low. Solid to liquid phase transition in water can have a switching factor as high as 3.5 [1]. It has also been reported that metal alloys such as Ge, Sb and Te which possess phase change memory have similar thermal switching factor [1]. Metal to insulator transition in tungsten (W) doped vanadium dioxide (VO_2) also has a similar switching factor (~ 1.5) [7]. In crystalline PE, a high thermal conductivity switching up to 12 [8] is predicted due to the phase transformation from the orthorhombic to the hexagonal (*O-H*) phase. During the phase transformation, chain molecules gain an additional degree of freedom from the segmental rotation. Segmental rotation introduces gauche conformations. This conformational change acts as a structural defect along the chain increasing phonon scattering events and thus a large switching factor is obtained. Here, using the same

thermal measurement technique discussed in Chapter 4, we have observed a reversible high contrast thermal switching factor as high as 10. The details are discussed next.

5.3 High contrast reversible thermal switch

5.3.1 Reversible thermal switching

In an orthorhombic PE crystal (Fig. 5.1A and B) with extended molecular chains, the structural property of its molecular chains is highly anisotropic with strong carbon-carbon bonds along the chain but weak van der Waals bonds between chains. These strong carbon bonds give rise to high energy constants for bond stretching ($E_r = 299.67 \text{ kcal mol}^{-1}$) and bond bending ($E_\alpha = 39.52 \text{ kcal mol}^{-1}$). However, the dihedral angle energy ($E_\theta = 0.243 \text{ kcal mol}^{-1}$) is very low (Fig. 5.1A) [9]. As a result, the PE chains are soft in terms of the rotational degree of freedom, but stiff for bond stretching and bending degrees of freedom. This important feature makes PE crystals an ideal platform for the control of thermal transport. At low temperature, they have an intrinsic metal-like thermal conductivity along the chain direction as demonstrated in Chapter 4 due to the aligned and highly ordered carbon segmental arrangement (Figs. 5.1A, B) [10]. However, when temperature increases to allow the atomic kinetic energy to overcome the relative weak dihedral energy barrier, chain segmental rotations occur. This introduces morphology disorder along the chains that can significantly interrupt phonon transport along the chains and therefore results in a low thermal conductivity [8], [9]. In Figs. 5.1C and D, dramatic changes in morphology can be observed after the phase transition, where the PE chains transition from a highly ordered *all-trans* conformation (Figs. 5.1A, B) to the one with the rotational disorder, namely, combined *trans* and *gauche* conformation.

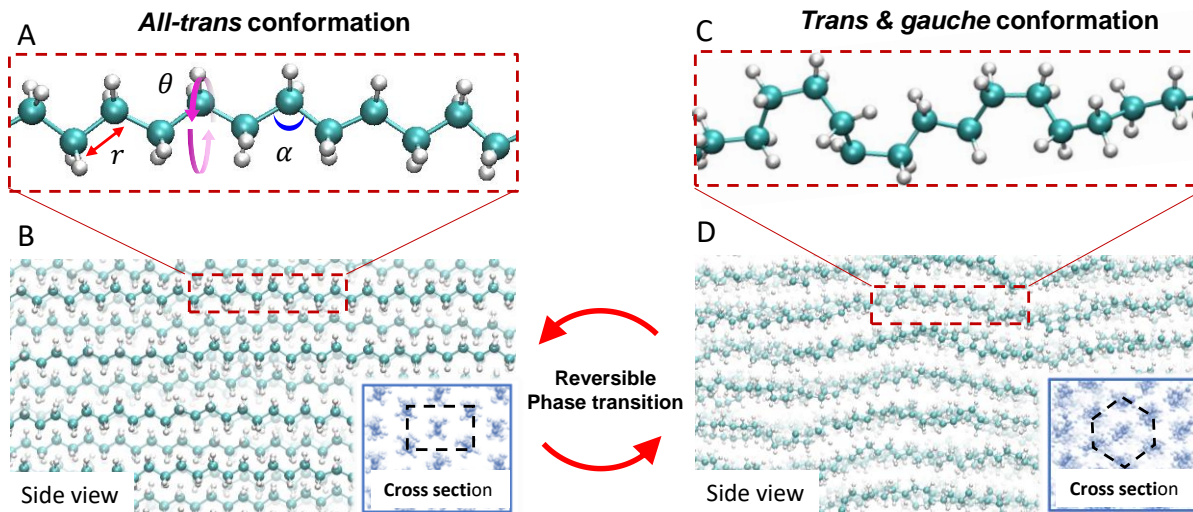


Figure 5.1: *O-H* phase transition in PE. A) All-trans conformation in an orthorhombic phase where r , θ and α represent a C-C bond, C-C-C dihedral angle and C-C-C bond angle. B) Side view the orthorhombic phase. The inset shows the cross-section view where the dotted line indicates the orthorhombic lattice of PE. C) A single molecule with trans and gauche conformation. D) Side view of the hexagonal phase. The inset shows the cross-section view where the dotted line indicates the hexagonal lattice of PE.

Crystalline PE nanofibers (PENF) with extended molecular chains were fabricated using local drawing as described in Chapter 3. Due to the high strain rate fabrication technique as shown in Section 3.2.3 of Chapter 3, these nanofibers have a diameter in the range of 10 – 100 nm, in which molecular chains are extended by stretching and aligned along the fiber direction. The structural and morphological properties of the crystalline PE nanofibers are characterized using low-dose transmission electron microscopy at cryogenic temperatures (Section 3.4.3 of Chapter 3) and show orthorhombic lattice structure (Fig. 5.2A).

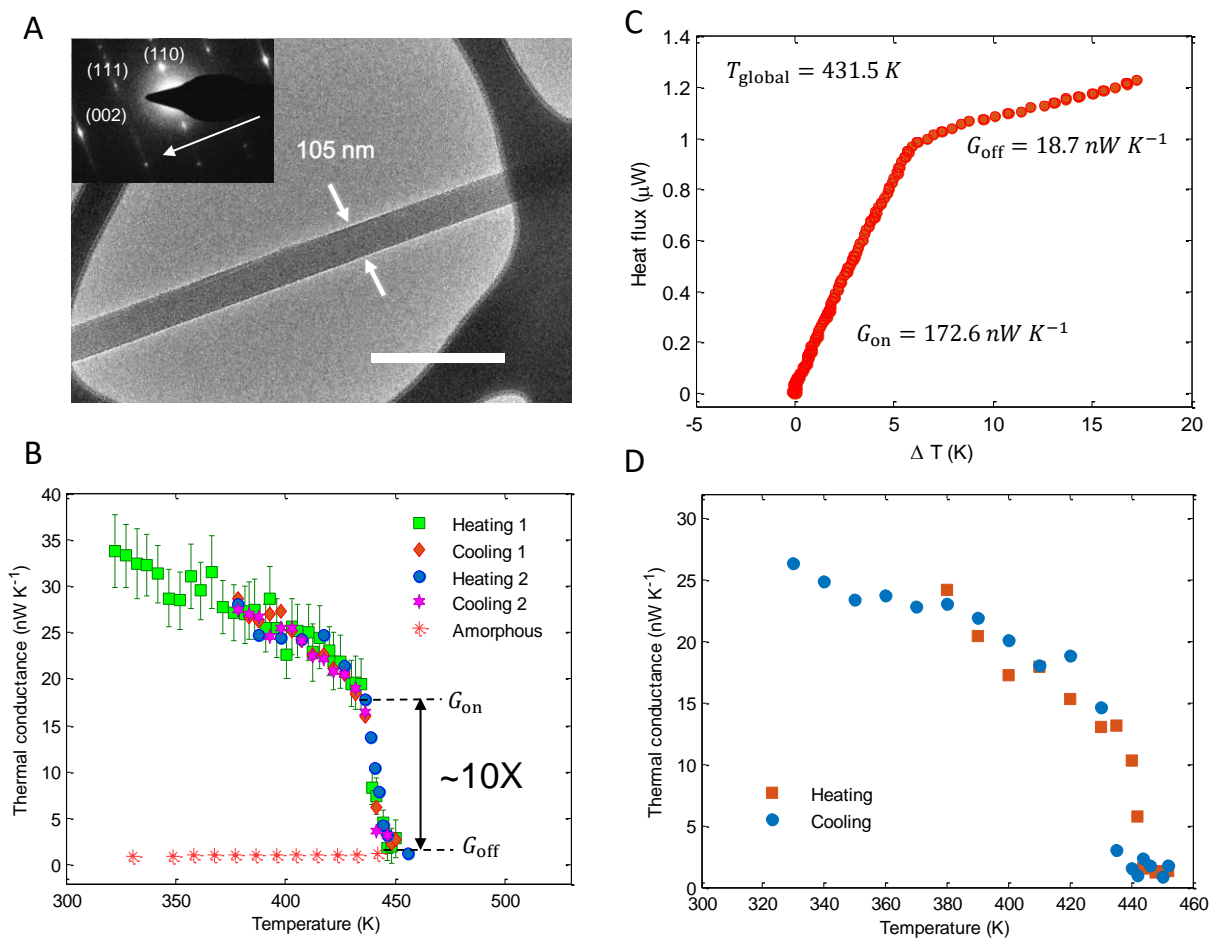


Figure 5.2: Thermal switching in PENF. A) A TEM brightfield image. The inset shows orthorhombic crystal lattice. B) Thermal conductance behavior of crystalline PENF and amorphous PENF. C) A $Q-\Delta T$ transfer function shows non-linear behavior at the phase transition. D) Thermal stability of the $O-H$ phase transition shown after holding at 450 K for 10 h.

We measure the temperature-dependent thermal conductance of PENF using the same suspended platinum resistance thermometer microdevice discussed in Section 4.3 of Chapter 4. To enhance the thermal contact between the PE nanofiber and the measurement device, we employ capillary assisted adhesion discussed in Section 3.3.3 of Chapter 3. In order to avoid the heating rate effect on the phase transition [11], the specimen is heated at 1 K min^{-1} until the system reaches

the desired ambient temperature. The ambient temperature is held for an hour before conducting the steady state thermal measurement as discussed in Chapter 4. Fig. 5.2B shows the strong non-linear heat flux (Q) – thermal bias (ΔT) transfer function. The $Q - \Delta T$ transfer function should be plotted at a fixed $T_{\text{avg}} = (T_{\text{h}} + T_{\text{s}})/2$, where T_{h} is the temperature of the hot side and T_{s} is the temperature of the sensing side. Since T_{s} cannot be controlled, T_{avg} increases with ΔT . However, the increase in T_{avg} is less than 2 % and has a negligible effect on the trend of the transfer function. Fig 5.2B shows that at an ambient temperature of 431.5 K, the PENF specimen has a high thermal conductance of 172.6 nW K^{-1} under $\Delta T < 5\text{K}$, which can be found from the slope of the transfer function ($G = \Delta Q/\Delta T$). When the specimen undergoes a phase transition, the thermal conductance drops to 18.7 nW K^{-1} . This corresponds to a thermal conductance switching factor $f = 9.2$, where the switching factor $f = G_{\text{on}}/G_{\text{off}}$ is defined as the ratio of on-state high thermal conductance G_{on} to off-state low thermal the conductance G_{off} .

To our knowledge, the high switching factor observed in crystalline PE nanofibers exceeds experimental values of the solid-solid phase transition in typical phase change materials like VO_2 and $\text{Ge}_2\text{Sb}_2\text{Te}_5$, and that of the solid-liquid phase transition in conventional materials [1]. We also measured the thermal conductance of the nanofiber in the temperature range of 320-455 K as shown in Fig 5.2C. As the temperature increases (the "heating" data points), the thermal conductance of the nanofiber first decreases due to the well-known Umklapp scattering of phonons in crystals, and then abruptly drops from 17.8 nW K^{-1} to 1.8 nW K^{-1} in a small temperature range between 435 K and 445 K. This corresponds to a thermal conductance switching factor $f \sim 10$, even higher than the specimen reported in Fig. 5.2B. Moreover, this sharp change on thermal transport is fully reversible, as shown by the "cooling" data points (Fig. 5.2C) where the temperature decreases. The specimen also exhibited full reversibility upon cycling up to 2 cycles that it was

tested. In order to verify the thermal stability of the *O-H* transition, we held a specimen at 450 K for 10 h and measured the thermal conductance while cooling it. The overlap of heating and cooling data points (Fig. 5.2D) suggest good thermal stability of the *O-H* transition.

The observed reversible, high-contrast thermal switching is attributed to the phase transformation from orthorhombic to rotationally disordered phase. This mesophase is also referred to as a conformationally disordered crystal (condis) phase with the hexagonal lattice, which has also been reported in constrained PE microfibers using in-situ X-ray diffraction (XRD) and Raman scattering [12], [13]. In terms of molecular structure, the mesophase still has the long-range order of molecular chains (Fig. 5.1D) but lacks the short-range conformation order of CH₂ units due to *trans* – *gauche* conformation rotations (Fig. 5.1B).

5.3.3 Beyond the *O-H* phase transition: Melting of PENF

For a crystalline material undergoing a first-order phase transition i.e. melting, the specific heat increases abruptly and then decreases [14]. In a thermal conductance measurement, this competes with the Umklapp scattering and morphology disorder scattering both of which reduces the thermal conductance. Consequently, the thermal conductance increases abruptly with increasing temperature and then decreases after reaching maximum [14]. The melting temperature, T_m , of the hexagonal phase in Fig. 5.3A is 441 K and T_m in Fig. 5.3B is 461 K. It is, possibly, because of the different levels of stress present in the specimens.

The melting transition observed in Figs. 5.3A and B is well above the equilibrium T_m of the orthorhombic lattice (414 K) [15] and the hexagonal phase in constrained PE microfiber (427 K) [12]. Stress on the specimen can cause to shift both the *O-H* transition phase transition temperature and T_m of the hexagonal [16], [17]. In a gel spun PE microfiber, Rastogi and Odell

stabilized orthorhombic phase up to 437 K after which the lattice transformed to hexagonal phase. The T_m of the hexagonal phase was 452 K [17]. The *O-H* phase transition occurs at a similar temperature (~ 436 K) in our experiments (Fig. 5.3B), however, T_m of hexagonal phase occurs at an even higher temperature (461 K).

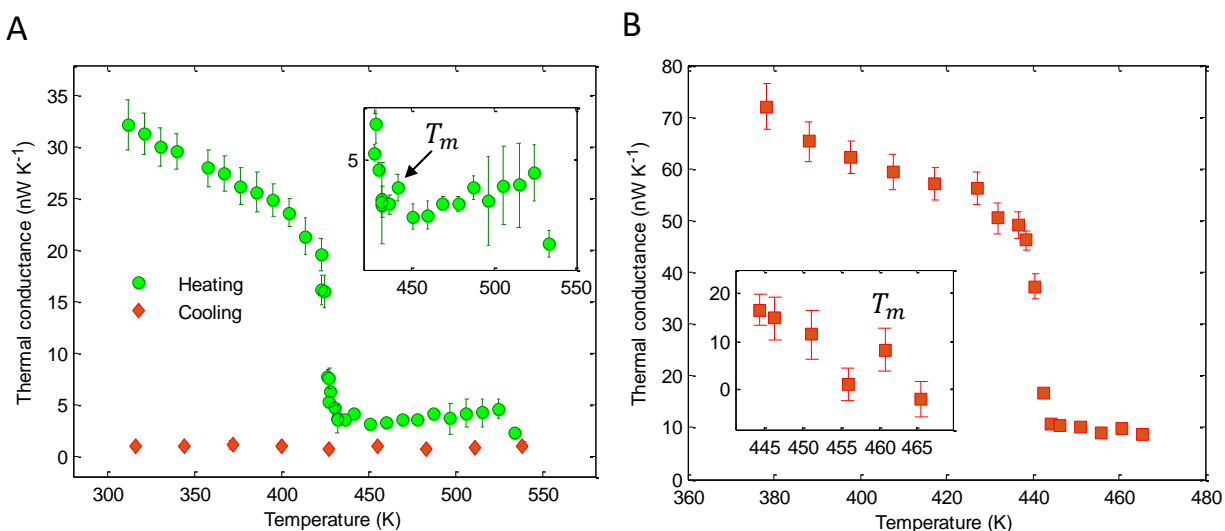


Figure 5.3: Thermal conductance measurement beyond the *O-H* phase transition. The insets show the thermal conductance trend after the *O-H* transition where T_m indicates the melting temperature of the hexagonal phase.

After the melting transition, PENF shows increasing thermal conductance with increasing temperature (Fig. 5.3A). At 520 K, the PENF shows an abrupt reduction in thermal conductance. This sudden drop is because the polymer becomes rubbery and undergoes a solid-liquid phase transition. The cooling trend corresponds to the background, implying the breakage of the fiber.

5.4 PE thermal diode

Utilizing the sharp thermal switching factor in crystalline PE and the nearly temperature-independent thermal conductivity of amorphous PE (Fig. 5.2C), we demonstrate a solid-state

nanoscale thermal diode in which we selectively amorphize ~15 % length of a crystalline PE nanofiber using electron beam irradiation to fabricate a heterogenous amorphous-crystalline junction. Fig. 5.4A shows a false-colored SEM micrograph where the magenta region is the amorphous section and the green region is the crystalline section. The device functionality schematic is also shown in Fig. 5.4A. For the forward bias in which heat transfers from left to right, the amorphous section is hot while the crystalline section is cold and it stays in the high thermal conductivity orthorhombic phase. The effective thermal conductance of the nanofiber is thus high. When the temperature bias or heat transport direction is reversed, the high temperature in the crystalline section enables the phase transition and thus leads to a low effective thermal conductance of the nanofiber. Fig. 5.4B shows the temperature-dependent thermal rectification factor R at a temperature difference of 10 K across the two pads of the thermal device, where the rectification factor R is defined as $R = (Q_{\text{fwd}} - Q_{\text{rev}})/Q_{\text{rev}}$. In Fig. 3B, in the presence of amorphous-crystalline junction, inversion symmetry for thermal transport breaks and thermal rectification is achieved, whereas crystalline PENF shows no thermal rectification. Here, an increasing thermal rectification is observed until ~432 K, the highest R is attained when the crystalline section has no phase transition in the forward bias but undergoes the phase transition in the reverse bias. The maximum thermal rectification of 25 % is achieved. This value is comparable to previously reported solid-state nanoscale thermal diodes based on carbon nanotubes, boron nitride nanotubes [3] and vanadium dioxide nanowire [5].

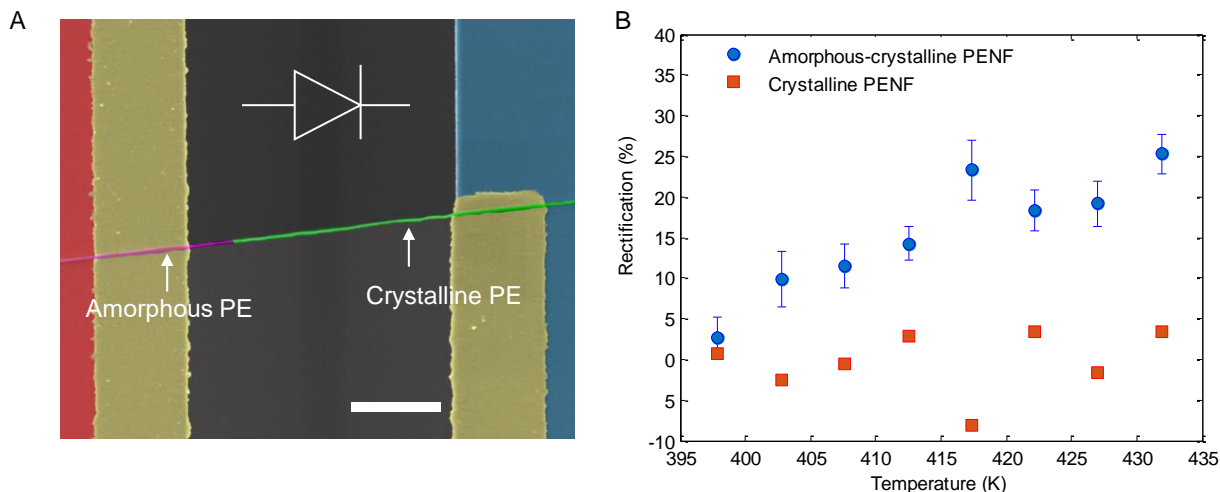


Figure 5.4: Thermal rectification in amorphous-crystalline PENF. A) Device schematic B) Diode performance.

5.5 Thermal contact resistance

While PENF shows excellent thermal switching behavior, the thermal rectification factor is only comparable at best to previously reported nanoscale thermal diodes. The molecular dynamics simulation by Zheng and Luo predicts a much higher thermal rectification ($\sim 120\%$) [18]. On further study onto the low rectification factor, it was found that while only $\sim 15\%$ of suspended PENF length was exposed to the electron beam, the apparent amorphous length was $\sim 90\%$, which is significantly far from optimal amorphous length predicted from the molecular dynamics simulation [18]. The PENF on the suspended platform was also exposed to SEM during the process and became amorphized. The contact resistance between amorphous PENF and the suspended pad (shown in left in Fig 5.4A) was found to be significantly higher than the contact resistance between crystalline PENF and the suspended pad (right in Fig. 5.4A). This increased thermal resistance due to the amorphous region on the suspended platform was attributed for low thermal rectification.

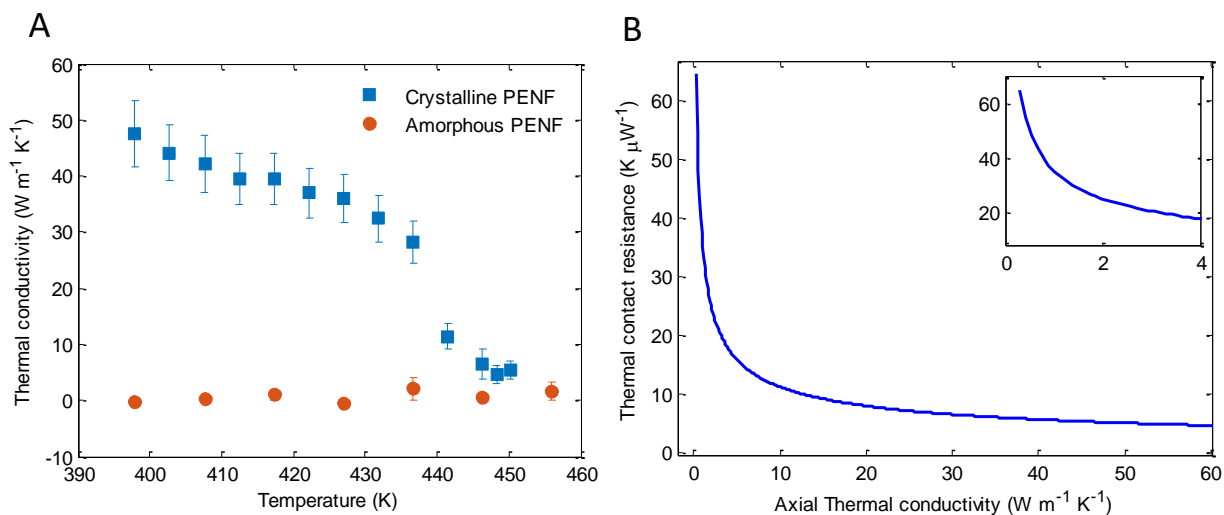


Figure 5.5: Thermal contact resistance. A) The thermal conductivity of crystalline PENF and amorphous PENF. B) Thermal contact resistance obtained using line contact model. The inset shows the thermal contact resistance for thermal conductivity from 0 to 4 W m⁻¹ K⁻¹.

Using the line contact model described in Section 4.4.1 of Chapter 4, the contact resistance for amorphous and crystalline portion was obtained. Fig. 5.5A shows measured thermal conductivity values for a fully crystalline PENF and an amorphous PENF. Fig. 5.5B clearly shows that the thermal contact resistance for an amorphous phase on the suspended platform is higher (~6X) than that of the crystalline phase. This is one of the main reasons why apparent amorphous length is higher than expected. Another possible reason is the over amorphization due to the Gaussian beam profile of the electron beam. The actual damage due to electron beam may be in an area larger than it is exposed.

5.5 Summary

In conclusion, for the first time, we have demonstrated a fully reversible, high-contrast PENF thermal switch. An unprecedented thermal switching factor $f = 10$ is observed by the

structural phase transition in crystalline PENF. By fabricating a heterogeneous amorphous-crystalline PE nanofiber, we also demonstrate a high-performance solid-state nanoscale thermal diode with a rectification factor $R = 25\%$, comparable with the experimentally reported values of existing solid-state nanoscale thermal diodes based on carbon nanotubes, boron nitride nanotubes, graphene and VO₂ nanobeams. The advanced nanoscale thermal components (thermal switches and diodes) demonstrated in this work can potentially perform as fundamental building blocks for actively regulating heat flow, and thus provide a robust platform for complex thermal control, which enables new applications for autonomous thermal management and efficient energy harvesting.

5.6 Chapter references:

- [1] G. Wehmeyer, T. Yabuki, C. Monachon, J. Wu, and C. Dames, “Thermal diodes, regulators, and switches: Physical mechanisms and potential applications,” *Appl. Phys. Rev.*, vol. 4, no. 4, 2017.
- [2] K. Kim and M. Kaviani, “Thermal conductivity switch: Optimal semiconductor/metal melting transition,” *Phys. Rev. B*, vol. 94, p. 155203, 2016.
- [3] C. W. Chang, D. Okawa, A. Majumdar, and A. Zettl, “Solid-state thermal rectifier,” *Science*, vol. 314, no. 5802, pp. 1121–4, Nov. 2006.
- [4] H. Wang, S. Hu, K. Takahashi, X. Zhang, H. Takamatsu, and J. Chen, “Experimental study of thermal rectification in suspended monolayer graphene,” *Nat. Commun.*, vol. 8, p. 15843, Jun. 2017.
- [5] J. Zhu, K. Hippalgaonkar, S. Shen, K. Wang, Y. Abate, S. Lee, J. Wu, X. Yin, A. Majumdar, and X. Zhang, “Temperature-Gated Thermal Rectifier for Active Heat Flow Control,” *Nano Lett.*, vol. 14, pp. 4867–4872, 2014.
- [6] J. Shin, M. Kang, T. Tsai, C. Leal, P. V Braun, and D. G. Cahill, “Thermally Functional Liquid Crystal Networks by Magnetic Field Driven Molecular Orientation,” vol. 10, p. 15, 2018.
- [7] S. Lee, K. Hippalgaonkar, F. Yang, J. Hong, C. Ko, J. Suh, K. Liu, K. Wang, J. J. Urban, X. Zhang, C. Dames, S. A. Hartnoll, O. Delaire, and J. Wu, “Anomalously low electronic thermal conductivity in metallic vanadium dioxide,” *Science (80-.)*, vol. 355, no. 6323,

- 2017.
- [8] T. Zhang and T. Luo, "Morphology-influenced thermal conductivity of polyethylene single chains and crystalline fibers," *J. Appl. Phys.*, vol. 112, no. 9, p. 094304, 2012.
 - [9] T. Zhang, X. Wu, and T. Luo, "Polymer Nanofibers with Outstanding Thermal Conductivity and Thermal Stability: Fundamental Linkage between Molecular Characteristics and Macroscopic Thermal Properties," *J. Phys. Chem. C*, vol. 118, no. 36, pp. 21148–21159, Sep. 2014.
 - [10] S. Shen, A. Henry, J. Tong, R. Zheng, and G. Chen, "Polyethylene nanofibres with very high thermal conductivities.," *Nat. Nanotechnol.*, vol. 5, no. 4, pp. 251–255, 2010.
 - [11] H. W. Starkweather, "The Effect of Heating Rate on the Melting of Polytetrafluoroethylene."
 - [12] Kohji Tashiro, A. Sono Sasaki, and M. Kobayashi, "Structural Investigation of Orthorhombic-to-Hexagonal Phase Transition in Polyethylene Crystal: The Experimental Confirmation of the Conformationally Disordered Structure by X-ray Diffraction and Infrared/Raman Spectroscopic Measurements," *Macromolecules*, vol. 29, no. 23, pp. 7460–7469, 1996.
 - [13] K. Tashiro, S. Sasaki, and M. Kobayashi, "Structural Investigation of Orthorhombic-to-Hexagonal Phase Transition in Polyethylene Crystal: The Experimental Confirmation of the Conformationally Disordered Structure by X-ray Diffraction and Infrared/Raman Spectroscopic Measurements," *Macromolecules*, vol. 29, pp. 7460–7469, 1996.
 - [14] W. N. dos Santos, J. A. de Sousa, and R. Gregorio, "Thermal conductivity behaviour of polymers around glass transition and crystalline melting temperatures," *Polym. Test.*, vol. 32, no. 5, pp. 987–994, Aug. 2013.
 - [15] B. Wunderlich and G. Czornyj, "A Study of Equilibrium Melting of Polyethylene," UTC, 1975.
 - [16] S. Tsubakihara, A. Nakamura, and M. Yasuniwa, "Hexagonal Phase of Polyethylene Fibers under High Pressure," *Polym. J.*, vol. 23, no. 11, pp. 1317–1324, Nov. 1991.
 - [17] S. Rastogi and J. A. Odell, "Stress stabilization of the orthorhombic and hexagonal phases of UHM PE gel-spun fibres," *Polymer (Guildf.)*, vol. 34, no. 7, pp. 1523–1527, 1993.
 - [18] T. Zhang and T. Luo, "Giant Thermal Rectification from Polyethylene Nanofiber Thermal Diodes," *Small*, vol. 11, no. 36, pp. 4657–4665, Sep. 2015.

Chapter 6: Ultra-high strength of crystalline polyethylene nanofibers

6.1 Abstract

The strength of PE nanofibers (PENF) was tested using a surface micro-machined stepper motor. The test platform was validated with silica nanofibers, and expected values of Young's Modulus were found. Due to their low surface energy, PENF slipped through the grips before they could be tested to failure. A new fabrication method (discussed in Chapter 3) was developed to address this problem. Dog-bone shaped PE nanofibers provided enough grip to successfully test PE nanofibers to failure. The highest strength measured to date for any polymer, 11.4 GPa, was achieved.

6.2 Mechanical measurement of polymer nanofibers

Young's modulus and strength in polymers increases in nanoscale fibers [1]–[5]. Due to the small volume, defects such as voids and impurities are significantly reduced whereas the confined size enhances the alignment of the backbone chain. However, experimental validation of mechanical enhancement of polymer nanofibers is difficult due to their minuscule size. Manipulation and positioning an individual nanofiber on to the desired location with nanoscale precision and high throughput is an important step in sample preparation. Owing to the small size of the nanofibers, it can be extremely difficult to prepare a specimen without damaging it. Nanometer resolution piezo-electric driven manipulators can be used to manipulate the nanofibers. However, the nanometer-scale size and the surface forces originating from van der Waals,

triboelectric or electrostatic attraction can still make manipulation challenging. For conducting materials, electron microscopes can be used to observe during manipulation, but in non-conducting samples an electron beam can damage the sample. We solved this problem by developing a novel sample mounting process discussed in Chapter 3.

For an accurate assessment of mechanical properties, the measurement system should have load resolution in the nanonewton range and displacement resolution in the nanometer range. Several experimental techniques have been developed in recent years such as resonance frequency measurement [6]–[9], nanoindentation [10]–[12], atomic force microscopy (AFM)-based measurements [5], [13], [14] and nano tensile measurements [1], [15], [16] for measuring mechanical property of 1D materials.

Some of these techniques such as resonance frequency measurement, however, are not suitable for polymer nanofibers as these techniques use electron microscopy to measure displacement [6]–[9]. Polymers degrade upon immediate exposure to electron beams. The electron beam induced swelling of crystalline PENF were discussed in Section 3.5.2 of Chapter 3. Loss of crystallinity and alignment in the fiber, which resulted in amorphous like thermal conductivity in PENF, was discussed in Section 4.4.6 of Chapter 4. Recently, a resonance shift based technique was employed to characterize a polymer nanofiber without exposure to the electron beam during the measurement, however, only elastic stiffness could be measured [17].

Nanoindentation has also been used to measure Young's modulus of polymer nanofibers [18] as well as inorganic materials such as silver nanowire [10] and ZnO nanowire [11], [12]. While it is suitable for probing isotropic material, polymer nanofibers are highly anisotropic because of the size confinement and drawing process usually associated with them. So, nanoindentation is not suitable to extract the axial mechanical property of polymer nanowires,

which is usually of interest. Also, the curvature of the nanofiber, tip-sample adhesion, surface roughness and the large stress concentration beneath the tip makes data interpretation difficult.

AFM-based measurement is one of the most extensively used methods for mechanical characterization of 1D material mainly because of its high load and deflection sensitivity. In addition, the AFM is a commercial tool, which makes it easily accessible. AFM-based measurements can be divided into two categories based on the mode of loading. Namely, bending and axial. Due to fewer assumptions in axial loading compared to bending, it is a preferred mode of testing. However axial loading proceeds with cantilever bending, therefore the test is prone to misalignment at large cantilever deflections [19]. In addition, electron microscopy is employed to resolve the nanometer-scale displacement [20]. Therefore, this method is not suitable for polymers.

Three-point bending test method has been successfully applied to the measurement of elastic modulus and yield strength of polymer nanowires such as PE nanofibers [5], conductive polypyrrole nanotubes [21], poly(L-lactic acid) (PLLA) nanofiber [14] as well as inorganic 1D materials such as gold nanowires [2], elastic modulus of cobalt oxide nanowires [22], silicon nanowires [23] and so on. This is a simple technique that can measure the strength and elastic modulus of the samples. The main limitation of the AFM bending test is its uncertainty stemming from the fourth power of diameter (two orders higher than the tensile test). Also, the cantilever tip should be calibrated before each measurement [24]. Data analysis becomes complicated during large deformation, fiber rotation, nanofiber sliding from the support and stress concentration from the AFM tip.

A tension test is most suitable for probing the mechanical properties of a polymer nanofiber as it requires the least number of assumptions. A commercial nano tensile testing system has been

used to test polymer submicron fibers [25]–[28]. This is a convenient apparatus; however, the force/displacement resolution may not be sufficient to probe fibers of diameters below 100 nm.

Several MEMS-based devices have been fabricated to perform a tensile test on 1D nanostructure samples with on-chip force sensors and on-chip actuators [29]–[31]. A MEMS device using an optical method to measure high-resolution displacement, as is compatible with polymers, was first fabricated by Kiuchi et al. [30]. They fabricated electrostatically actuated comb drive actuators to test carbon nanowires of 85 nm diameter and 4.6 μm gage length. They used a lever mechanism to amplify the displacement by a factor of 91 and imaged it optically under a stereomicroscope with a CCD camera [30]. A comb drive actuator does not provide the large range of displacement needed for testing ductile nanofibers, which reduces their suitability for most polymers. Displacement output is only up to a few tens of microns. Also, with increasing displacement of the sample, the net force output decreases significantly due to highly stiff springs attached to the comb drives to prevent pull-in instability [31].

Naraghi et al. have successfully fabricated and performed a MEMS-based nano tensile test on polymer nanofibers [1], [32], [33]. Highly ductile electrospun polyacrylonitrile (PAN) nanofibers were tested until failure. The test device consisted of specimen grips, a leaf-spring loadcell and a mount for external actuation with a precision piezoelectric actuator. The test process used optical metrology. The relative displacement of the gauges was extracted using digital image correlation (DIC). The accuracy of the DIC application to extract nanoscale displacement was verified using a piezoelectric actuator and found to be better than 50 nm. Engineering stress-strain curves were generated from the images acquired during the test process. In addition to stress-strain curves, the device was also used for strain rate measurements spanning six decades of strain rate from $2 \times 10^{-4} \text{ s}^{-1}$ to 200 s^{-1} [33], [34] as limited only by the frame rate of the charged coupled

device (CCD) used to acquire image during the test process [32]. Even though surface micromachined on-chip actuators provide the in-plane force necessary to avoid off-axis loading, they are limited by the force and displacement they can apply onto the specimen. Naraghi et al. also fabricated a new surface micro-machined MEMS device with an on-chip actuation with a wide range of force (30 nN – 300 μ N) and displacement (20 nm – 100 μ m) [1]. The mechanical measurement with this new on-chip device was consistent with the previously described off-chip testing platform. A load cell was connected in series with the sample and the actuator. Optical images of the load cell displacement were taken during the loading of the sample. Digital image correlation (DIC) was used to obtain a high-resolution displacement of the load cell from which force and elongation of the sample were deduced [1]. This is a novel method to test polymer nanofibers mechanical properties. However, the stiffness of the loadcell was too small to probe high stiffness high strength polymer nanofibers such as UHMWPE. Sahin et al. fabricated a stiffer loadcell to test for high stiffness micron scale carbon fiber. Due to the large size (>10X) of the specimen compared to a nanofiber, the specimen mount was also modified to keep the specimen near the neutral axis [35]. The force and displacement were extracted using DIC with a resolution better than ~25 nm.

Here we introduce a MEMS device with a different load cell design that produces good contrast for sub-pixel pattern matching to obtain high displacement resolution via optical methods. Also, we have fabricated several devices in a chip with different load cell stiffnesses compatible with low to high stiffness polymers.

6.3 Mechanical measurement MEMS platform

The tensile strength, σ_{ts} , of individual polyethylene nanofibers (PENF) was tested in tension using a microelectromechanical systems (MEMS) based device with an on-chip actuator that is a micro stepper motor with 60 nm step size and large in-plane force (up to 1 mN) [1], [36]. The optical metrology has a displacement resolution of 4 nm and a force resolution of 25 nN (with a 5.4 nN nm⁻¹ load cell) under a 50X objective. The MEMS device (Fig. 6.1) is fabricated with an on-chip actuator and a load cell spring in series. The sample is gripped between the load cell and a pad rigidly connected to the substrate. When an actuator takes a step to the right, it pulls the load cell and the specimen. Since they are in series, the force on the sample can be obtained from the load cell stiffness and its extension. Similarly, the specimen displacement can be obtained from the sample gauge displacement. After the mechanical measurement, the diameter and the length of the fiber were measured by SEM. A stress-displacement curve was generated, from which the σ_{ts} was obtained.

6.3.1 Fabrication

The MEMS platform was designed at CMU and fabricated by Sandia National Labs, Albuquerque, NM, USA, using Sandia Ultra-planar Multi-level MEMS technology (SUMMiT VTM) fabrication process [37]. This process involves five polycrystalline silicon layers with four mechanical layers, surface micromachined and then planarized with chemical mechanical polishing (CMP), with sacrificial oxide layers sandwiched between each polysilicon layers. This five-level process provides greater design freedom to make complicated interacting mechanical systems. The process exhibits a high degree of control. For example, the structural layer has a standard deviation of 6.3 nm for a 2.25 μ m layer thickness (0.3%) [38].

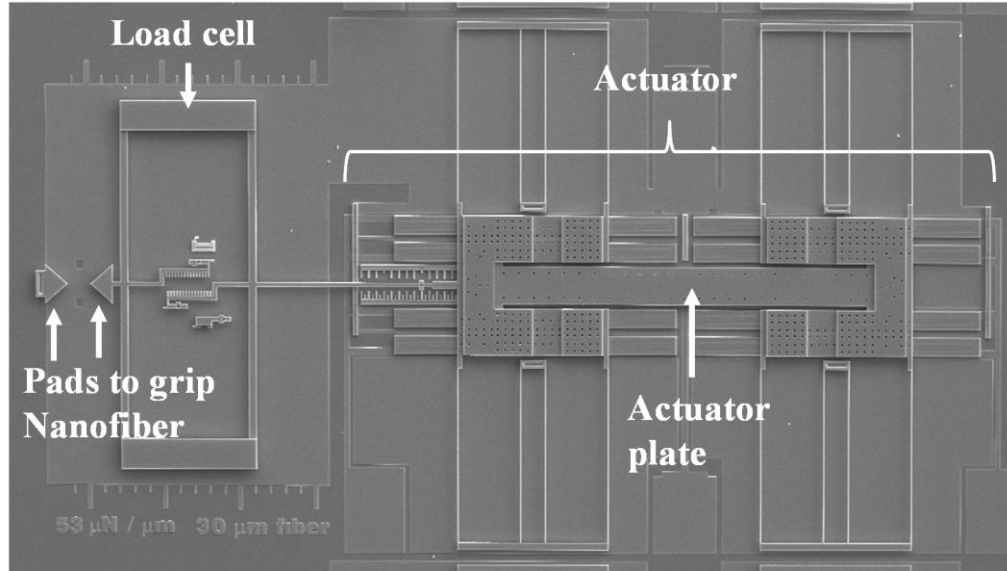


Figure 6.1: Optical image of a nanotractor. A nanofiber is clamped between the triangular pads.

6.3.2 Stepper motor (nanotractor)

The nanotractor is a surface micro-machined stepper motor with high-resolution in-plane force. It will be used to perform a tensile test on the polyethylene nanofiber. Fig. 6.1 shows a sample nanotractor. Using a 50X objective and the displacement resolution of ± 4 nm, the force resolution is for the softest load cell is ± 25 nN. The actuator is capable of stretching the nanofiber up to 75 μm , thus applying 250 % strain to these nanofibers. It can exert a large force (~ 1 mN).

An actuator plate moves similar to an inchworm where moderate out-of-plane displacement is converted into a small but consistent in-plane displacement. Each complete step forward is a result of a sequence of four actions onto the actuator as shown in Fig. 6.2. First, voltage is applied to a leading clamp as shown in Fig. 6.2a. This locks the clamps and keeps it from sliding. Then, voltage is applied to the actuation plate as shown in Fig. 6.2b. The electrostatic force pulls the plate down, causing it to bend and pull the trailing clamp with an attached tether forward. The tether connects the actuator plate to the load cell and sample. Grounded standoffs as shown in Fig.

6.2b prevent the shorting of the actuation plate with the substrate by limiting the out-of-plane displacement to $3\ \mu\text{m}$. Then, voltage is applied at the trailing clamp, which keeps it fixed at that position as shown in Fig. 6.2c. Finally, voltages at the leading clamp and the actuation plate are released as shown in Fig. 6.2d. This relaxes the out-of-plane bending of the actuation plate and the actuator moves forward, completing a step. The step size depends on the out-of-plane displacement amplitude of the actuation plate and its length. For the out-of-plane displacement amplitude $3\ \mu\text{m}$ and plate length $500\ \mu\text{m}$, the step size is $\sim 60\ \text{nm}$. The voltage sequence is repeated for multiple steps, enabling long-range travel. The voltages can also be sequenced to obtain reverse motion.

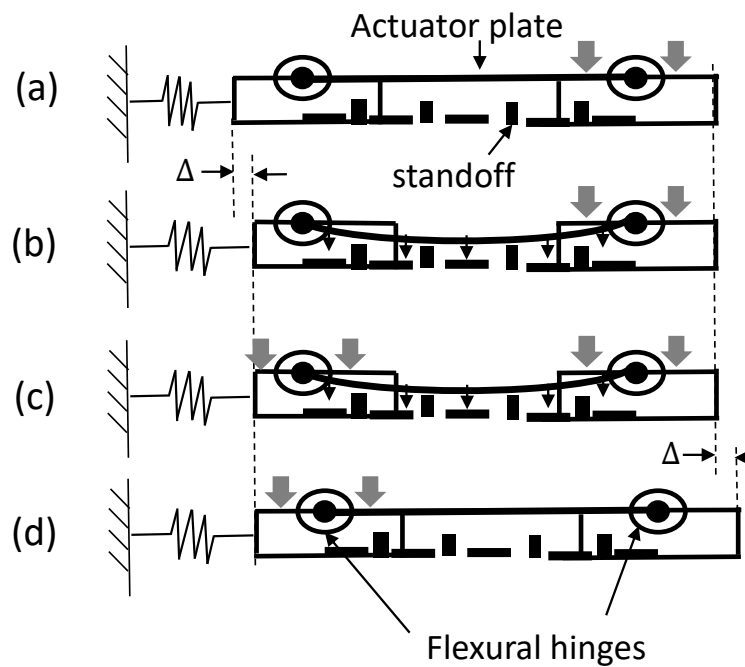


Figure 6.2: Voltage sequence applied to the actuator to obtain a step motion. a) The leading clamp is locked due to electrostatic force from applied voltage b) Voltage is applied to the actuation plate, which causes out of plane bending and pulls the trailing clamp by a step ($\sim 60\ \text{nm}$) c) Voltage is applied on the trailing clamp and locked d) Voltage is released at the leading clamp and the actuator plate, completing a step ($\sim 60\ \text{nm}$). Redrawn from [1].

6.3.3 Load cell

The load cell, as shown in Fig. 6.3, consists of four fixed guided beams (all same geometry) that determine the load cell stiffness and two gauges (combs) for displacement and force measurement. Two pairs of beams in the parallel arrangement are connected in series. The stiffness of the load cell is Ehw^3/L^3 , where E , h , w and L are Young's modulus, height, width and length of a beam, respectively. The load cell stiffnesses were designed such that they were stiff enough to exert enough force to test the samples until failure and compliant enough to have good force resolution. A nanofiber sample's stiffness is given as $k_S = E_S A_S / L_S$, where E_S , A_S and L_S are Young's modulus, area and length of the sample, respectively. Polyethylene nanofibers have very high Young's modulus near to theoretical limit [5]. Taking $E = 250$ GPa, $L = 30$ μm , and diameter = 50 nm to 250 nm, we get $k_S = 16.4$ N/m to 409 N/m. Four devices with different loadcell stiffness were fabricated to accommodate a large possible range of sample stiffness. The two metrology combs do not contribute to the stiffness of the load cell. They are used to perform sub-pixel pattern matching to obtain force and displacement of the sample discussed later in Section 6.4.2.

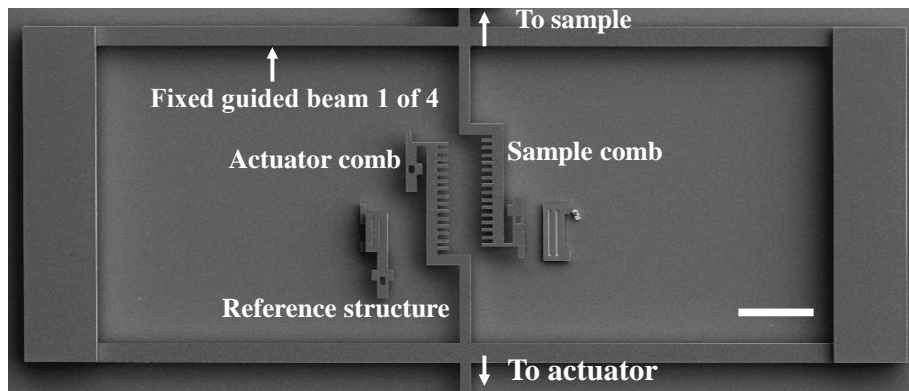


Figure 6.3: Load cell structure. Four guided beams and two combs with a fixed reference structure at the center. The scale bar is 40 μm .

In order to get an accurate force, the load cell stiffness needs to be assessed. SEM images of length and width of a load cell beam were recorded at five different locations and averaged. The height of the load cell is fabricated using MMPoly3 layer using the SUMMiT VTM process. We used nominal values for thickness, as it is well controlled. The estimated and designed values of the stiffness of the load cells are given below.

Table 6.1: Estimated stiffness of the loadcells.

Design	Length (μm)	Width (μm)	Height (μm)	Designed stiffness (N/m)	Estimated Stiffness (N/m)
1	200	4.89	2.25	5.7	5.39
2	200	7.39	2.25	19	18.62
3	200	10.34	2.25	53	50.99
4	200	13.85	2.25	125	122.50

6.4 Measurement method

6.4.1 Experimental setup

Measurements were carried out on a probe station equipped with a long working distance interferometer on a vibration isolation table at room temperature (RT), as shown in Fig. 6.4. A National Instruments PCI-6733 analog output card was used to apply voltages. A Tegam 2350 amplifier with a high bandwidth (DC to 2 MHz) and slew rate ($>250 \text{ V}/\mu\text{s}$) was used to amplify the applied voltages. A voltage of 200 V was used to actuate nanotractor. Load cell displacements were optically imaged through a 50X Mitutoyo long working distance objective (NA = 0.55) using

a Sony XCD SX910 camera at 1 frame/s and stored for later data analysis. Saved images were analyzed to measure load cell displacements with ~ 4 nm accuracy using sub-pixel pattern matching in Memscript, a MEMS software package developed by Sandia National Labs that employs National Instruments “NI Vision” commands. Load cell displacement measurements were used to calculate force and sample displacement. Details of the sub-pixel pattern matching method for accurate displacement extraction are given next and force and sample displacement measurement are given in Section 6.4.3.

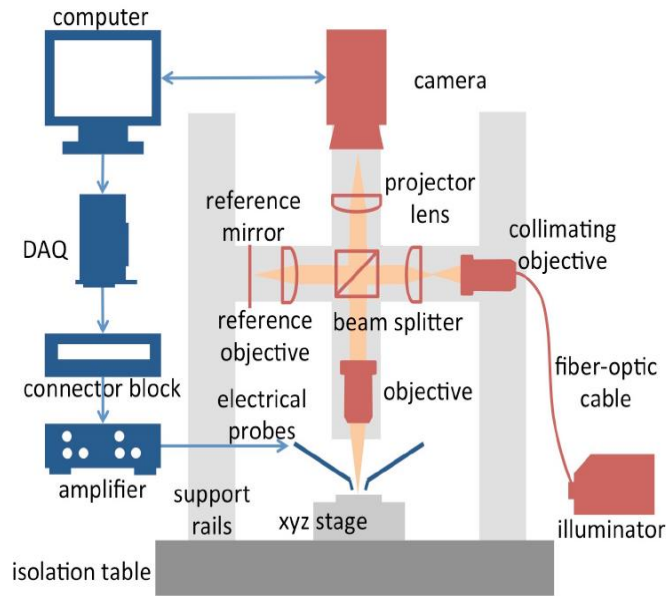


Figure 6.4: Schematic of the probe station with a long distance working objective [2].

6.4.2 Sub-pixel pattern matching

Nanoscale resolution of force and displacement without any electron beam exposure is a necessity for accurate mechanical characterization of polymer nanofibers. For a green light ($\lambda = 570$ nm) via 50X objective with $NA = 0.55$, the diffraction limit is $1.26 \mu\text{m}$. Direct optical

measurement is always diffraction limited, however, this problem can be circumvented by comparing an image with a reference image to measure the displacement.

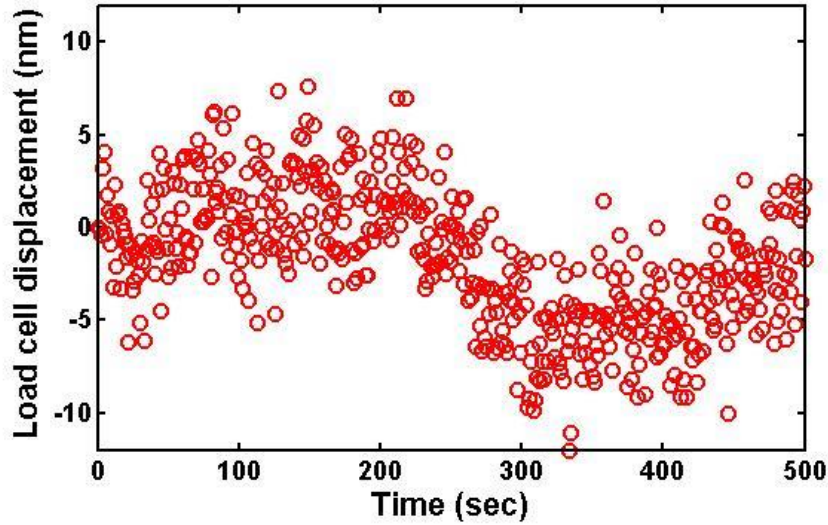


Figure 6.5: Pattern matching results of a load cell displacement from images taken at 50X on a stationary device. The standard deviation is ~ 4 nm.

In this work, we use sub-pixel pattern matching to obtain nanoscale resolution of load cell displacement used to calculate force and sample displacement. In sub-pixel pattern matching, a predetermined 2D pattern of a first image is iteratively searched in an expected window in subsequent images. Pattern positions (x , y and θ) with the highest match score are recorded. Sub-pixel displacement resolution is obtained by interpolating a pixel (bilinear in Memscript) on discrete structures such as edges or lines where a sharp contrast is achieved. Each pixel has a greyscale value from 2^n possible values where n is the number of bits per pixel ($n = 8$ in our case). A perfect edge with white (1) on one side and black (0) on other in a pixel could be interpolated with 2^n intensity values. In an ideal scenario with no noise and perfect contrast, a resolution of $\text{pixel}/2^n$ can be achieved. This would give 0.5 nm displacement resolution for an objective of 50X (pixel length is 121 nm for 50X objective). Considering noise, we achieved $\text{pixel}/30$ i.e ~ 4 nm

resolution (one standard deviation) as demonstrated by pattern matches on a stationary sample as shown in Fig. 6.5. Resolution can be improved with a large number of well-defined edges as provided here by the comb structures.

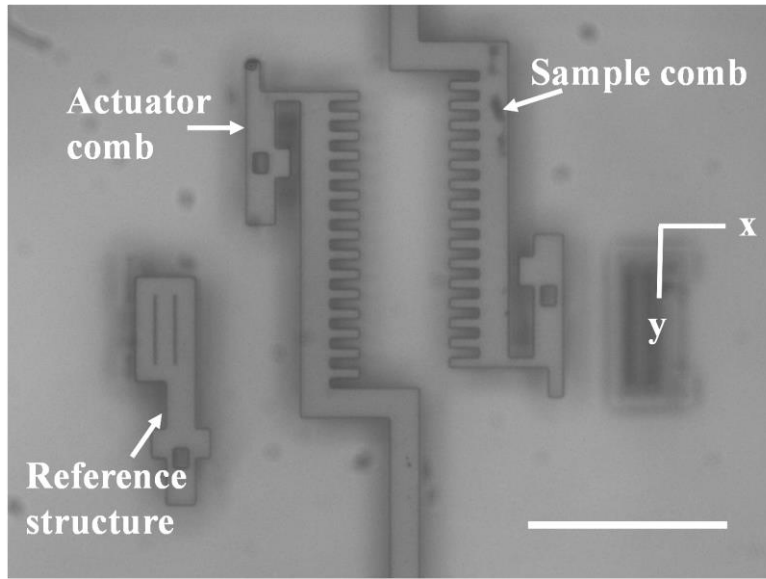


Figure 6.6: Optical image at 50X objective of combs and a reference structure used for sub-pixel pattern matching. The scale bar is 40 μm .

6.4.3 Force and displacement measurement on the specimen

The load cell has two comb structures, namely the sample comb and the actuator comb. One is attached to the sample end and the other to the actuator. Also, within a load cell is a reference structure fixed onto the substrate. Fig. 6.6 shows a typical optical image of these combs and reference structure with 50X objective used for sub-pixel pattern matching. Sub-pixel pattern matching, described in Section 6.4.2, was used to obtain the displacement of sample comb, actuator comb and reference structure. The nanofiber sample displacement (Δy_{sample}) is calculated from the sample comb displacement (Δy_{sample_comb}) and the reference structure displacement (Δy_{ref})

using equation 6.1. The reference structure displacement is subtracted to cancel the drift noise. The total actuator displacement ($\Delta y_{actuator}$) is calculated from actuator comb displacement ($\Delta y_{actuator_comb}$) and reference structure using equation 6.2. Total force acting on the nanofiber (f_{sample}) is obtained from the load cell displacement using equation 6.3 and equation 6.4.

$$\Delta y_{sample} = \Delta y_{sample_comb} - \Delta y_{ref} \quad (6.1)$$

$$\Delta y_{actuator} = \Delta y_{actuator_comb} - \Delta y_{ref} \quad (6.2)$$

$$\Delta y_{loadcell} = \Delta y_{actuator} - \Delta y_{sample} \quad (6.3)$$

$$f_{sample} = k \times \Delta y_{loadcell} \quad (6.4)$$

6.4.4 Stress-strain curve

Stress for a tensile test is $\sigma = F/A$ and strain is given by $\varepsilon = \Delta L/L$, where $\sigma, F, A, \varepsilon, \Delta L$ and L are the stress, applied force, cross section area, strain, displacement and initial length of the sample, respectively. The sample diameter was measured from SEM images to calculate the cross-section area of the sample. Length was also measured from the SEM image. A 3 nm platinum protective coating was applied to reduce charging and electron swelling effect before taking the SEM images. From this data, stress-strain curves were plotted.

6.4.5 Test method verification using silica nanofibers

Silica nanofibers were used to validate the experimental setup and estimated stiffness values. Fig. 6.6a shows a silica fiber on nanotractor ready for testing. Silica nanofiber samples were fabricated using a flame brushing technique [39], where a silica microwire was heated in the center using a butane torch and pulled at other two ends. It was stretched until broken and

nanofibers were obtained. The nanofiber was placed on a PDMS substrate. A tungsten tip with a tip diameter $\sim 1 \mu\text{m}$ connected to a high precision micro-manipulator was used to manipulate the silica nanofiber sample from PDMS to nanotractor. The cyanoacrylate glues were used to fix the sample onto the nanotractor. SEM image of the glass fiber is shown in Fig. 6.6c.

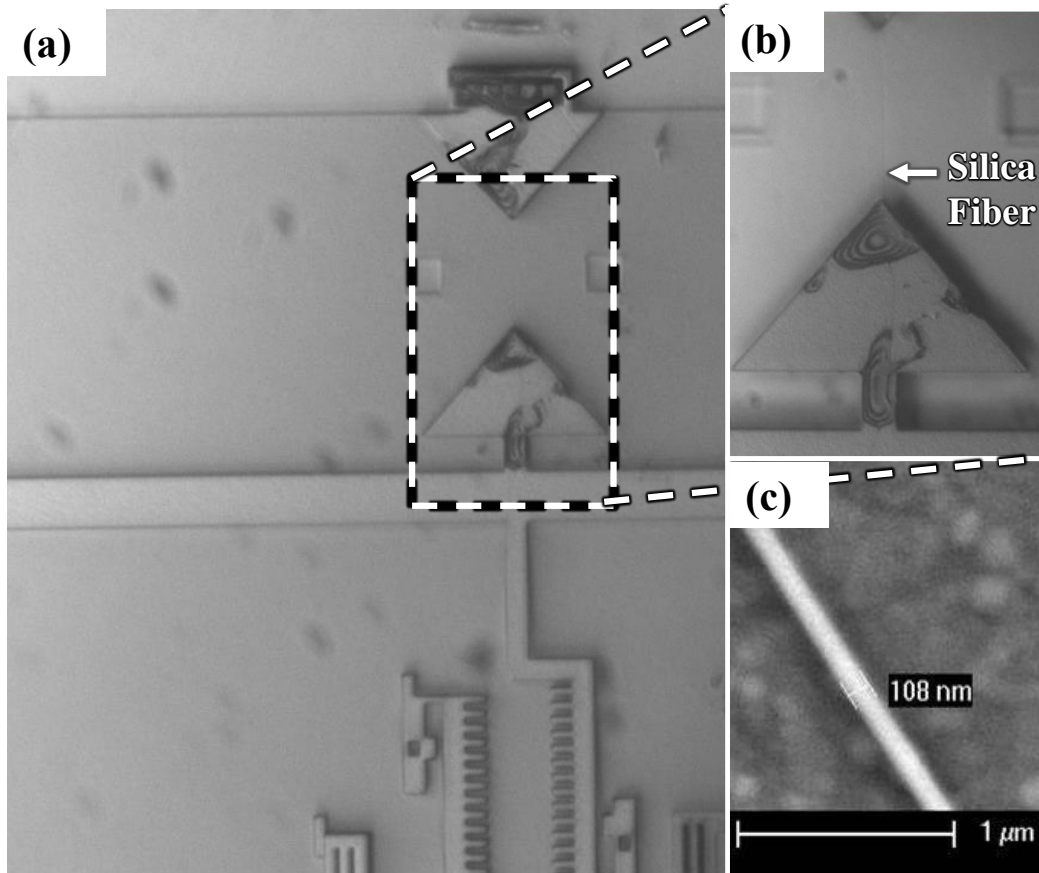


Figure 6.6: Silica fiber sample on a nanotractor a) Optical image of nanotractor sample with a silica fiber (20X objective) b) silica nanofiber gripped on a pad (50X objective) c) SEM image of the silica nanofiber.

Stress and strain were obtained from the force normalized over cross-section diameter and elongation over the gauge length. Fig. 6.7 shows the stress-strain curve of a silica nanofiber of diameter 108 nm. The fiber begins to experience stress once it is pulled taut. Fig. 6.7 shows that

the sample with a diameter of $D = 108$ nm became taut after 5 steps. Young's modulus is obtained from the slope of the stress-strain curve in the elastic region. The Young's modulus was found to be 67.7 GPa. The sample strength was 4.5 GPa and its elongation at failure was 9 %. The sample showed higher scatter of data near failure. The stiffest load cell was used in this test, resulting in low force resolution and high scatter. A second silica nanofiber was also tested with $D = 90.3$ nm (Fig. 6.7). Young's modulus derived from the stress-strain curve, as shown in Fig. 6.7, was 76.5 GPa. The diameter of this sample was 90.3 nm. The ultimate strength was 8.2 GPa, twice that of the previous sample. Elongation at failure was also observed to be higher than the previous sample at 13.8%. Table 6.2 tabulates the results.

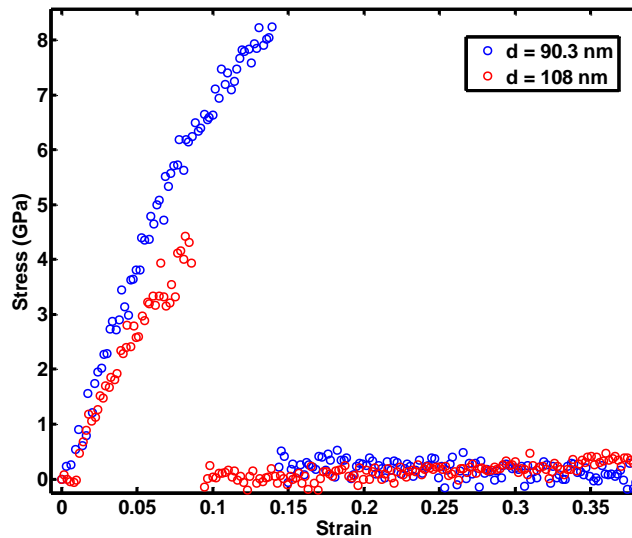


Figure 6.7: Stress-strain curve of the silica nanofibers a) $E = 67.7$ GPa was obtained for $d=108$ nm sample b) $E = 76.5$ GPa was obtained for $d = 90.3$ nm sample.

Table 6.2: Verification of measurement set up using silica nanofibers

Sample no.	Diameter (nm)	Failure strain (%)	Ultimate strength (GPa)	Young's modulus (GPa)
1	90.3	13.8	8.2	76.5
2	108	8.2	4.2	67.7

The Young's modulus values are close to bulk silica modulus (72 GPa) [40]. Silva et al. tested silica nanofibers using AFM cantilever bending test and showed that Young's modulus for silica nanofibers larger than 280 nm is similar to bulk [40]. Wang et. al.[41] obtained 27 ± 7 GPa for diameter between 43 nm and 95 nm and Dickin et. al.[42] obtained 47 ± 7 GPa for diameter between 80 nm and 98 nm. These measurements were done in TEM using resonance vibration method. Recent work [43] on a tensile test of silica nanofibers of dimensions 33.9 nm and 18.7 nm under TEM showed that Young's modulus was about 77.6 GPa, close to bulk silica. Our measurement method yielded Young's modulus values close to bulk modulus, validating our method.

Strengths are much higher than bulk silica (0.2 GPa) [3]. This is because of nanoscale size effect, where flaw density is significantly reduced and the probability of having a flaw larger than critical flaw is minimal. However, our values of silica nanofiber strength are somewhat lower than Brambilla and Payne [3], who measured an average strength of 10 GPa. Our fabrication method of using butane torch and strength test in high relative humidity (~70%) introduces hydroxyl group in the silica surface that may degrade the silica sample [3], [44].

We observed elongation as high as 13.8 % in the silica nanofibers. However, the SEM image of the fractured glass fiber, as shown in Fig. 6.8, shows a flat fracture surface and no diameter tapering, suggesting brittle failure.

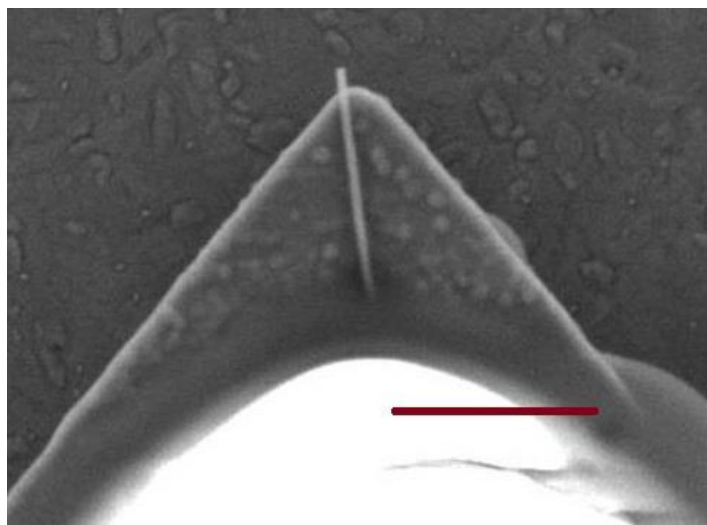


Figure 6.8: SEM image of a fractured silica fiber. Scale bar is 2 μm .

6.5 Results and discussions

6.5.1 Overview of samples

Six ultra-drawn PENFs with diameters ranging from 85 nm to 255 nm were tested. Three of the samples were fabricated using a two-stage tip drawing (Chapter 2, Section 2.3.2) and the other three samples were fabricated using local heat stretching (Chapter 3, Section 3.2.1). Fig. 6.9 shows an optical image of a representative sample fabricated using local heat stretching. All samples had a nominal gauge length of 30 μm . However, depending on where the glue attached to the sample, the actual length was between 30 and 40 μm . The tip-tip distance of the nanotractor pad (triangular pads) was measured from optical images calibrated with a known length on the same chip. The distance from tip to where the glue stopped was measured from an SEM image.

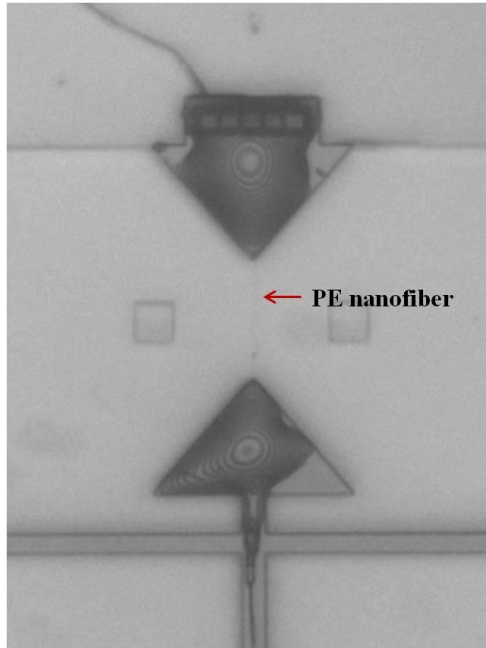


Figure 6.9: A representative sample ready for testing.

Prior to SEM, a 3 nm Pt was sputtered on the nanofiber to reduce the electron beam damage during SEM. The diameter measurement was done in the SEM using a low accelerating voltage (4 kV) to further reduce the beam damage. Astigmatism correction and focusing were performed away from sample position prior to imaging. When the samples were not in contact with the substrate upon breaking, significant coiling of the sample was noticed (discussed in Section 3.5.1). The coiling began upon immediate exposure of the electron beam. In that case, the diameter of the fiber near the pad was taken. The diameter, probably enlarged due to electron beam radiation (Section 3.5.2 in Chapter 3), gives a lower bound on the strength of the sample. The coiling of the fiber is, possibly, because of inelastic scattering of electrons providing sufficient energy to the molecules to relax to the isotropic state favored by entropy [45].

6.5.3 Gripping by mechanical locking using a dog-bone

The surface energy of PE is low (31 mJ m^{-2}) and the absence of a polar component (similar to PTFE 19 mJ m^{-2}) makes it difficult to wet with adhesives [46], [47]. There are several commercial adhesives such as Loctite 3032, Loctite 3035, Scotch weld DP 8005, Scotch weld DP 8010, Loctite plastic bonding system, and TAP poly-weld adhesive that are designed for low surface energy olefins such as polyethylene and polypropylene. However, their viscosity, working life and/or requirement to surface treat the sample made them unsuitable for this work. All available glues were tried. None worked successfully.

Increasing the surface energy of PE is the most common way at the macroscale to enhance PE adhesion. The surface energy can be altered by flame discharge, corona discharge, acid treatment and plasma treatment [47]. These surface treatments are destructive, which will alter the surface chemistry and property of the sample via oxidation. The length scale of the surface where these surface treatments affect the material is similar to the diameter of our sample [47]. Thus, these methods are not viable. Surface roughening is another method that has been frequently used at the macroscale. The glues within the rough surface provide additional force due to mechanical locking. However, with our sample size mechanical roughening of the fiber is not possible. Adhesion of an epoxy matrix with PE can also be enhanced by mixing reactive graphitic carbon nanofibers (r-GNF) [48]. However, the dispersion is always an issue when mixing r-GNF with glues. There have been previous measurements where an adhesive was used to fix the polyethylene nanofiber during an AFM based three-point bending test. This was successful because the applied force was three orders of magnitude smaller and tested for very small displacement [5].

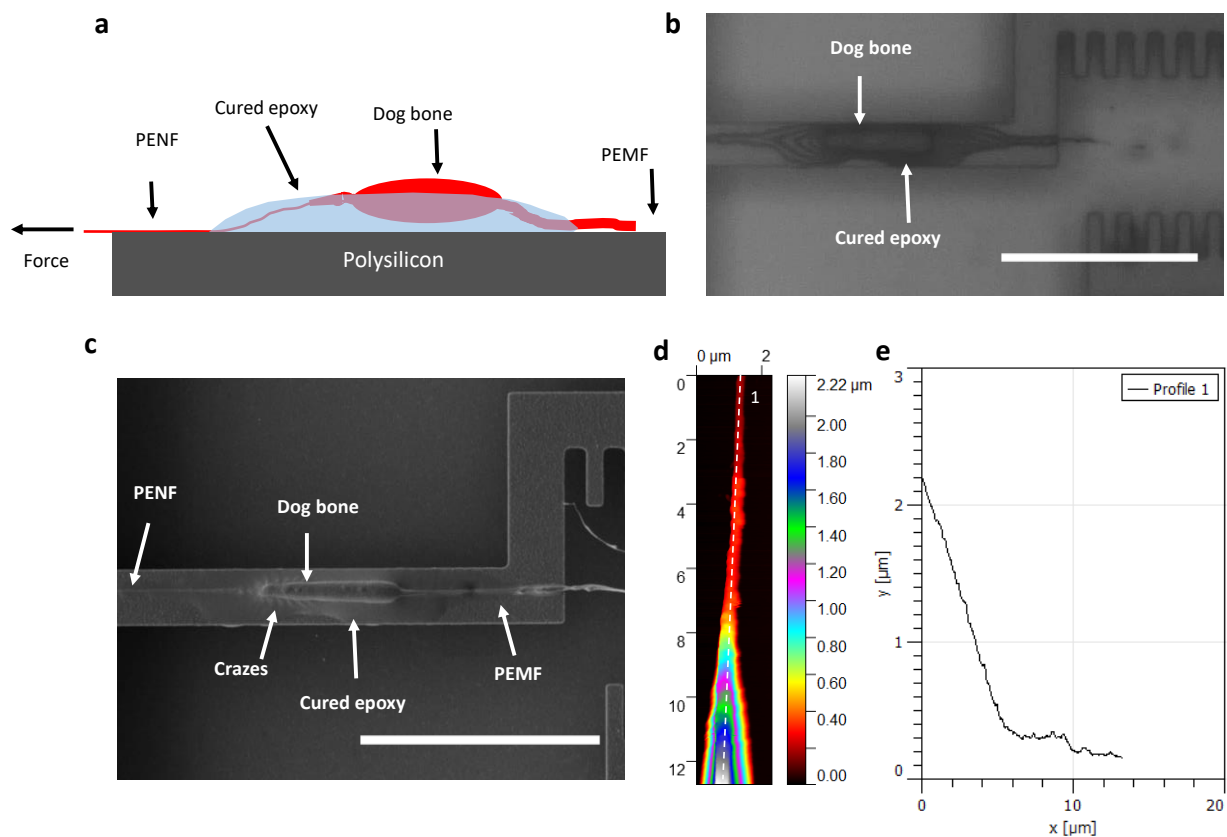


Figure 6.10: PE nanofiber (PENF) on the left side of the dog bone for additional mechanical gripping, with PE microfiber (PEMF) on the right. a) Schematic of the mechanical locking of the dog bone within cured epoxy. b) Optical image of the dog bone before testing. c) SEM image of the same dog bone after testing. The streaks at the left edge of the dog bone in c are crazes due to the deformation of the cured epoxy. They are only on the left side of the dog bone, indicating successful gripping of the test sample. d) Atomic force microscopy (AFM) image of a tip of a dog bone (SEM image not shown here). e) Height profile of the dog bone in d labeled ‘1’. Scale bars, 25 μm (b,c).

Here, we introduce a mechanical locking method to increase the gripping force. During localized drawing of a polyethylene microfiber (PEMF), the melt forms elongated globules at the edges of the PENF, similar to a dog bone, in response to the combined surface tension and drawing forces. Placing the glue (Gorilla epoxy) between the dog bone and the PENF yields mechanical

locking which provides a significant additional resisting force. Furthermore, the thicker section of the dog-bone ($3 - 5 \mu\text{m}$) makes it easy to locate and manipulate the sample under the optical microscope. A schematic of the dog bone within an epoxy is shown in Fig. 6.10a. Fig. 6.10c also shows local crazing of the glue as the dog bone is pulled into it, indicating successful mechanical locking. However, it also reveals that crazing is one slip mechanism. Fig. 6.10d and e show the taper at the tip of a dog-bone.

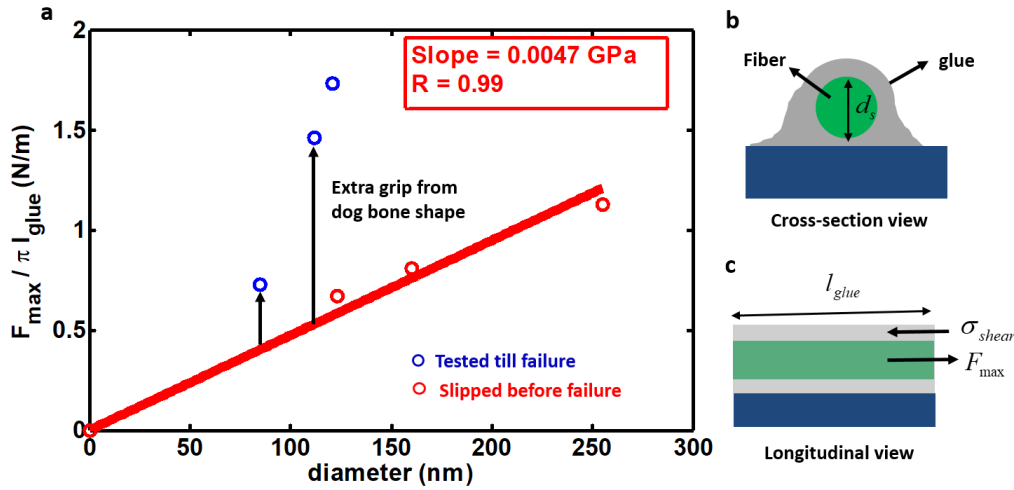


Figure 6.11: Estimation of glue shear strength. a) Shear force per unit glued length versus diameter of the fiber. The slope gives the shear modulus of glue with PE fiber. (b) and (c) are schematic cross-section and longitudinal views of the fiber in the glue.

6.5.4 Evaluation of glue adhesion and performance of dog-bone

From composites theory [49], the maximum force (F_{\max}) up to which a sample with a diameter d_s was tested before it slipped can be used to obtain the average shear strength (σ_{shear}) of glue/PE, given as

$$\sigma_{\text{shear}} = \frac{F_{\max}}{\pi d_s l_{\text{glue}}} \quad (6.5)$$

Equation 6.5 can be re-written as

$$\frac{F_{\max}}{\pi l_{\text{glue}}} = \sigma_{\text{shear}} d_s \quad (6.6)$$

where l_{glue} is the length of the nanofiber on which glue is applied. In Fig. 6.11a, $F_{\max}/\pi l_{\text{glue}}$ is plotted against d_s . The slipped samples have a slope of 4.7 MPa which is the shear strength of glue with the PE fiber. This is on par with the shear strength of Loctite® AA 3032/ Henkel which is a specialized glue for PE (6 MPa with high density PE). Samples tested till failure experience a significantly higher force per unit length. This additional force per unit length required to test till failure is contributed by the mechanical locking of the sample. Fig. 6.11b shows the schematic of fiber within the glue.

Now, we can also estimate the length of the glued section required to hold a typical 100 nm PENF with tensile strength (σ_{ts}) of 10 GPa. It can be shown that,

$$l_{\text{glue}} = \frac{\sigma_{\text{ts}} d_s}{4\sigma_{\text{shear}}} \approx 53 \mu\text{m}$$

This could not be achieved in the present experiment because the pad size is 30 μm .

6.5.4 Ultra high strength of crystalline PENF

The σ_{ts} of 11.4 ± 1.1 GPa was obtained for the nanofiber with a diameter of 85 nm. To our knowledge, this is the highest measured σ_{ts} for any polymer fiber reported including carbon fiber, Zylon®, Kevlar® and nylon fibers [26], [35], [50], [51] (Fig. 6.12). Even though the theoretical C-C bond strength (for chain scission) can be as high as 20 - 30 GPa, PE strength is limited by a slip that initiates at chain ends (6 – 8 GPa) [52]. The failure mode is a combination of chain slip and chain scission. A significantly minimized chain end density within the test length due to the

local heating based fabrication technique and short gage length (30 μm), comparable to the length of the PE molecule ($\sim 30 - 55 \mu\text{m}$ for ultra-high molecular weight PE), explains the high strength.

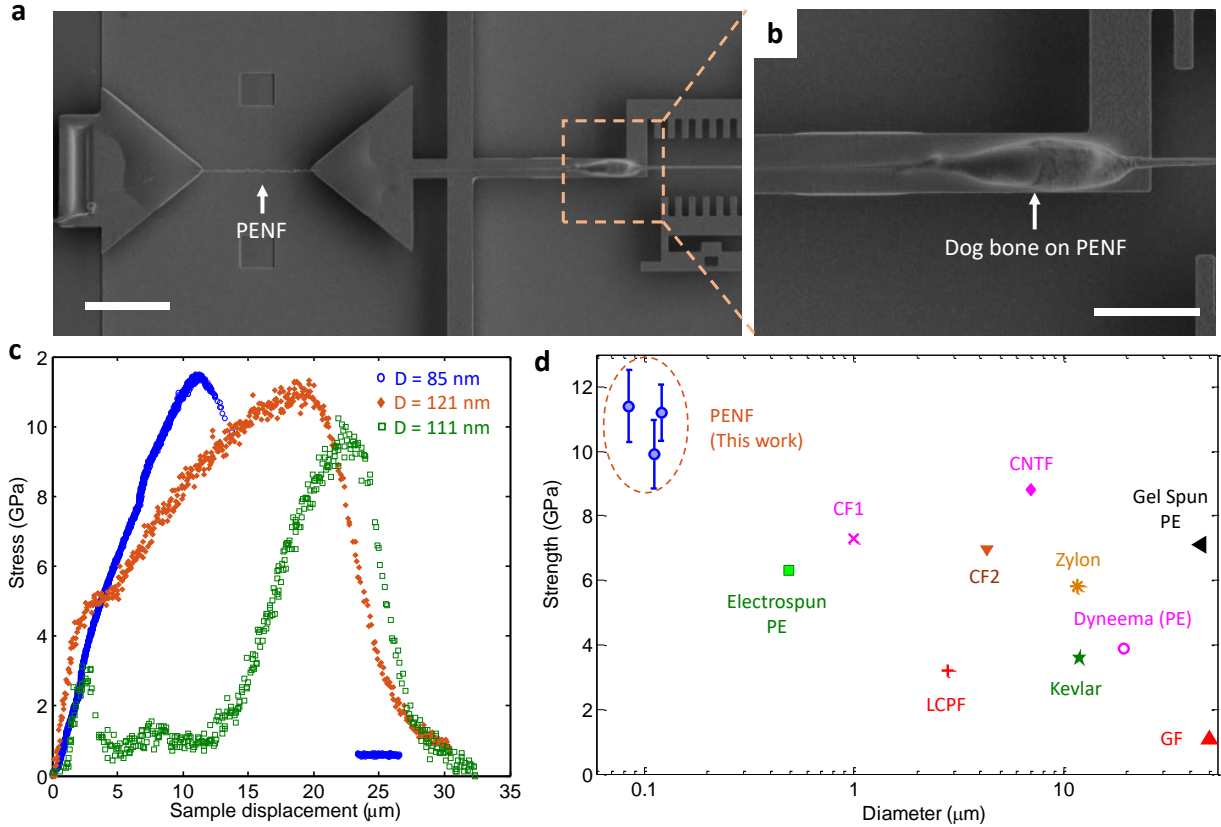


Figure 6.12: Mechanical characterization of PENF. a A PENF gripped between two pads. b Dog bone shape on a PENF which provides additional grip due to mechanical locking. High contrast at the edges of dog bone is from charging of cured epoxy. c Stress-displacement curve. d σ_{ts} of PENF compared to other fibers such as electrospun PE [3], CF1 [4] (Carbon fiber 1), CF2 (HexTow®/ Hexcel), CNTF [5] (Carbon nanotube fiber), PE [6] (Gel-spun PE fiber), Zylon®/ Toyobo, LCPF (Liquid crystal polymer fiber, Vectran™/ Kuraray), Kevlar®/ Du Pont, Dyneema®/ Royal DSM, and GF [7] (Graphene fiber). The error bars in PENF are calculated using uncertainty analysis (See Section 6.5.5). Scale bars, 25 μm (a), and 10 μm (b).

In addition, the diameter is not uniform over a length of 30 μm as discussed in Section 3.5.1 of Chapter 3. For mechanically tested samples, the narrow region along the sample used for calculating the σ_{ts} spans less than 1 μm (see Fig. 3.20 in Chapter 3). As this is much smaller than the length of a PE molecule, the likelihood of chain ends in the region is negligible. Therefore, these regions can sustain substantially larger stress limited by chain scission.

Two distinct failure mechanisms were observed when tested with low (5.4 N m^{-1}) and high (50.8 N m^{-1}) stiffness load cells. The sample tested with the low stiffness load cell exhibited ductile failure (Fig. 6.12c, $D = 85 \text{ nm}$), whereas that with the high stiffness load cell experienced extreme necking, where the diameter was reduced to less than 10 nm (see Section 6.5.7). This is because of the elastic strain energy $U = (1/2)k_L\delta_L^2 = (1/2)F^2/k_L$ stored in the loadcells. For a given load F , higher elastic strain energy is stored in the lower stiffness load cell. For small k_L (5.4 versus 50.8 N m^{-1}), F drops slowly during displacements after the σ_{ts} is reached, increasing the likelihood of instability.

6.5.5 Error analysis in stress using the Nanotractor Platform

Tensile strength (σ_{ts}) is the maximum stress that the sample can withstand before failing.

It can be expressed as

$$\sigma_{\text{ts}} = \frac{F_{\text{max}}}{A} \quad (6.7)$$

where F_{max} is the maximum force. This can be rewritten as

$$\sigma_{\text{ts}} = \frac{4k\Delta x_{\text{loadcell,max}}}{\pi d^2} \quad (6.8)$$

The total uncertainty in σ_{ts} is also estimated using the uncertainty propagation rule:

$$\left(\frac{\delta\sigma_{ts}}{\sigma_{ts}}\right)^2 = \left[\left(\frac{\delta k_L}{k_L}\right)^2 + \left(\frac{\delta(\Delta x_{loadcell})}{\Delta x_{loadcell}}\right)^2 + \left(2\frac{\delta d}{d}\right)^2\right] \quad (6.9)$$

The load cell stiffness k_L is given by

$$k_L = \frac{Ehw^3}{L^3} \quad (6.10)$$

$$\left(\frac{\delta k_L}{k_L}\right)^2 = \left(\frac{\delta E}{E}\right)^2 + \left(\frac{\delta h}{h}\right)^2 + \left(3\frac{\delta w}{w}\right)^2 + \left(3\frac{\delta L}{L}\right)^2 \quad (6.11)$$

Sample S1 with $d = 85 \pm 4$ nm was measured using a load cell with $k_L = 5.4$ N m⁻¹. The uncertainties in length and width of the load cell beam were calculated from five measurements along the load cell beam.

$$\left(\frac{\delta L}{L}\right) \sim 0.05 \% \quad \text{and} \quad \left(\frac{\delta w}{w}\right) = 0.6 \%$$

The error in Young's modulus of the polysilicon (164.3 ± 3.2 GPa) and beam height (2.25 μm, std 6.3 nm) has been measured on MEMS devices fabricated with SUMMiT VTM method [38], [53].

$$\left(\frac{\delta h}{h}\right) = 0.28 \% \quad \text{and} \quad \left(\frac{\delta E}{E}\right) = 2 \%$$

Thus, total uncertainty in stiffness $\left(\frac{\delta k_L}{k_L}\right)$ of the $k_L = 5.4$ N m⁻¹ loadcell is 2.7 %. The loadcell extension (12 μm) is significantly larger than pattern matching resolution (4 nm) so $\left(\frac{\delta(\Delta x_{loadcell})}{\Delta x_{loadcell}}\right) < 0.1 \%$. The major source of error is the fiber diameter:

$$\left(\frac{\delta d}{d}\right) = 4.7 \%$$

Using Equation 6.11, the uncertainty (one sigma) in stress is, $\left(\frac{\delta\sigma_{ts}}{\sigma_{ts}}\right) = 9.8 \%$

Other load cells will have even lesser error uncertainty as the width of the beam is measured more accurately. With respect to those load cells, other variables are the same.

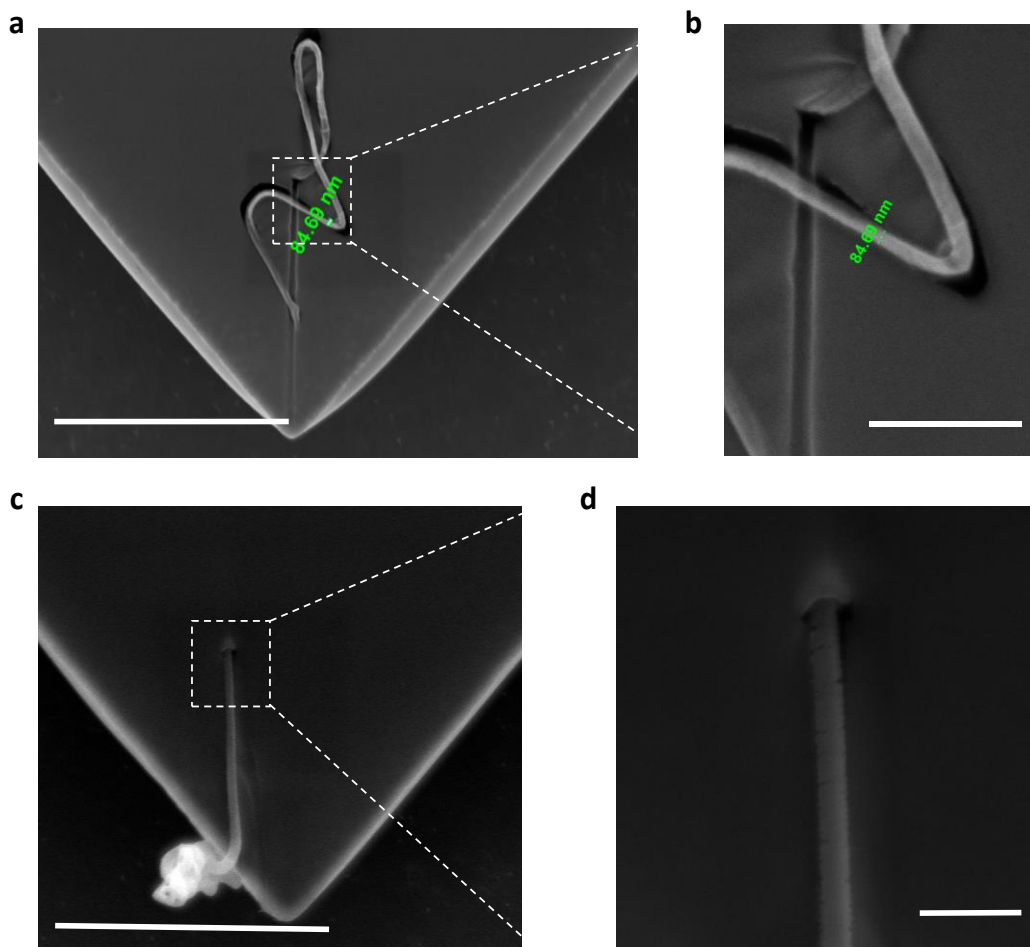


Figure 6.13: Diameter measurement for σ_{ts} evaluation. a) Fractured sample. b) Zoom in of inset of a. c) Extremely necked sample. The diameter is measured far away from necked region. The coiling is prominent in freely suspended sample compared to the sample on the substrate. Scale bars, 5 μm (a,c), 1 μm (b), 500 nm (d).

6.5.6 SEM of PENF post measurement

The PENF breaks during strength measurements and has free ends. When imaged in SEM, it coils rapidly due to irradiation near the free end similar to shrinkage with free ends [54]. This is attributed to the entropic relaxation of taut-tie molecules (TTM) [45] due to electron beam induced melting or chain scission. In the literature, the diameter of polymer fibers has been measured from an untested section [1]. However, this is not feasible here because the fiber exhibits tapering as

discussed in Section 3.5.1 of Chapter 3. Hence, the diameter is measured within the test section by SEM. As discussed in Section 6.5.4, the fiber fails by ductile failure (low k_L) or by extreme necking (high k_L). In the first case, the fiber diameter was measured (10 μm) away from the fractured end as shown in Fig. 6.13a. In a crystalline PEMF, the failure strain was 6.5 % at a strain rate comparable to this work (10^{-3} s^{-1}) [55]. So, assuming constant volume deformation, the diameter of the fiber decreases by 3.2 %. However, the controlled experiment (Section 3.5.2 of Chapter 3) showed that the measured diameter of the fiber was overestimated by 12 % due to irradiation. The value used to calculate strength is from SEM without correction, and therefore the reported strength is a lower bound.

In case of extreme necking, the local region can undergo large non-uniform deformation. Therefore, the diameter, in this case, was measured close to the clamped region as shown in Fig. 6.13c.

6.5.7 Extreme necking

As stated in the Section 6.5.4, the samples tested with the high stiffness load cell experienced extreme necking. Under electron beam irradiation, the free end of the PENF coils rapidly. Therefore, a measurement was performed using AFM on an extremely necked region of a mechanically probed sample. The AFM height values of 7, 1.4 and 1.2 nm in Fig. 6.14b are obtained from regions 1, 2 and 3 in Fig. 6.14a. This shows that the fibers deform by extreme necking rather than a typical local fracture with a short neck region.

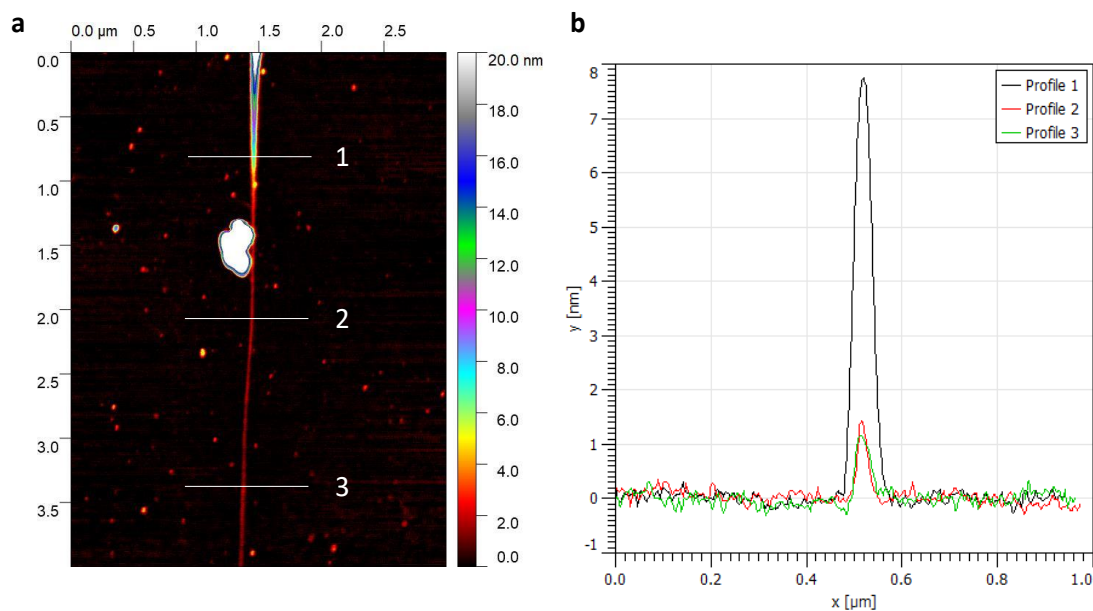


Figure 6.14: Extreme necking of PENF **a)** AFM image of the necked region **b)** Height profiles of lines shown in **(a)**.

6.6 Summary

Strength measurements on several UHMWPE nanofibers were conducted using a MEMS device. In the tensile tests, the grip strength to a PE nanofiber using an adhesive was insufficient because of the low surface energy of PE (31 mJ m^{-2}), and slip occurred before they were tested to failure. Dog bone shaped nanofibers were fabricated using a new fabrication method we developed (discussed in Chapter 3) to provide additional grip due to mechanical locking, enabling tensile strength to be measured. For an 85 nm fiber, the strength value of $11.4 \pm 1.1 \text{ GPa}$ was obtained. This is the highest measured strength of PE nanofiber as well as any polymer fiber.

Two distinct failure mechanisms were observed when tested with low (5.4 N m^{-1}) and high (50.8 N m^{-1}) stiffness load cells. The specimen tested with the low stiffness load cell exhibited ductile failure whereas the that with the high stiffness load cell experienced extreme necking, where the diameter was reduced to less than 10 nm.

The polymer nanofibers with lightweight-thermal-mechanical functionality could find general applications in aerospace and automotive systems, where a high strength-to-weight ratio is desirable. With the multi-functionality, the polymer nanofibers are purely electrically insulating and bio-compatible, which opens up unique applications in electronics and biology. Furthermore, integrating local heating as a secondary process on gel spun microfibers, which was reviewed in Section 2.3.1 of Chapter 2, could potentially realize making larger scale PE nanofibers.

6.7 Chapter references:

- [1] M. Naraghi, T. Ozkan, I. Chasiotis, S. S. Hazra, and M. P. de Boer, “MEMS platform for on-chip nanomechanical experiments with strong and highly ductile nanofibers,” *J. Micromech. Microeng.*, vol. 20, no. 12, p. 125022, 2010.
- [2] B. Wu, A. Heidelberg, and J. J. Boland, “Mechanical properties of ultrahigh-strength gold nanowires,” *Nat. Mater.*, vol. 4, no. 7, pp. 525–529, 2005.
- [3] G. Brambilla and D. N. Payne, “The Ultimate Strength of Glass Silica Nanowires,” *Nano Lett.*, vol. 9, no. 2, pp. 831–835, Feb. 2009.
- [4] S. Hoffmann, F. Östlund, J. Michler, H. J. Fan, M. Zacharias, S. H. Christiansen, and C. Ballif, “Fracture strength and Young’s modulus of ZnO nanowires,” *Nanotechnology*, vol. 18, no. 20, p. 205503, 2007.
- [5] P. Li, L. Hu, A. J. H. McGaughey, and S. Shen, “Crystalline polyethylene nanofibers with the theoretical limit of Young’s modulus,” *Adv. Mater.*, vol. 26, no. 7, pp. 1065–1070, 2014.
- [6] P. Poncharal, Z. L. Wang, D. Ugarte, and W. A. de Heer, “Electrostatic deflections and electromechanical resonances of carbon nanotubes,” *Science*, vol. 283, no. 5407, pp. 1513–6, Mar. 1999.
- [7] S. Perisanu, V. Gouttenoire, P. Vincent, A. Ayari, M. Choueib, M. Bechelany, D. Cornu, and S. T. Purcell, “Mechanical properties of SiC nanowires determined by scanning electron and field emission microscopies,” *Phys. Rev. B*, vol. 77, no. 16, p. 165434, Apr. 2008.
- [8] E. Zussman, X. Chen, W. Ding, L. Calabri, D. A. Dikin, J. P. Quintana, and R. S. Ruoff, “Mechanical and structural characterization of electrospun PAN-derived carbon nanofibers,” *Carbon N. Y.*, vol. 43, no. 10, pp. 2175–2185, 2005.
- [9] K. H. Liu, W. L. Wang, Z. Xu, L. Liao, X. D. Bai, and E. G. Wang, “In situ probing mechanical properties of individual tungsten oxide nanowires directly grown on tungsten tips inside transmission electron microscope,” *Appl. Phys. Lett.*, vol. 89, no. 22, p. 221908, 2006.

2006.

- [10] X. Li, H. Gao, C. J. Murphy, and K. K. Caswell, "Nanoindentation of Silver Nanowires," *Nano Lett.*, vol. 3, no. 11, pp. 1495–1498, Nov. 2003.
- [11] M. Y. Soomro, I. Hussain, N. Bano, E. Broitman, O. Nur, and M. Willander, "Nanoscale elastic modulus of single horizontal ZnO nanorod using nanoindentation experiment.," *Nanoscale Res. Lett.*, vol. 7, no. 1, p. 146, 2012.
- [12] S. J. Young, L. W. Ji, S. J. Chang, T. H. Fang, and T. J. Hsueh, "Nanoindentation of vertical ZnO nanowires," *Phys. E Low-dimensional Syst. Nanostructures*, vol. 39, no. 2, pp. 240–243, 2007.
- [13] E. P. S. Tan, C. N. Goh, C. H. Sow, and C. T. Lim, "Tensile test of a single nanofiber using an atomic force microscope tip," *Appl. Phys. Lett.*, vol. 86, no. 7, pp. 1–3, 2005.
- [14] E. P. S. Tan and C. T. Lim, "Physical properties of a single polymeric nanofiber," *Appl. Phys. Lett.*, vol. 84, no. 9, p. 1603, 2004.
- [15] Y. Zhu, C. Ke, and H. D. Espinosa, "Experimental Techniques for the Mechanical Characterization of One-Dimensional Nanostructures," *Exp. Mech.*, vol. 47, no. 1, pp. 7–24, Feb. 2007.
- [16] Y. Ura, K. Sugano, T. Tsuchiya, and O. Tabata, "Tensile testing of fullerene nano wire using electrostatic MEMS device," in *TRANSDUCERS 2009 - 2009 International Solid-State Sensors, Actuators and Microsystems Conference*, 2009, pp. 2062–2065.
- [17] P. A. Yuya, Y. Wen, J. A. Turner, Y. A. Dzenis, and Z. Li, "Determination of Young's modulus of individual electrospun nanofibers by microcantilever vibration method," *Appl. Phys. Lett.*, vol. 90, no. 11, p. 111909, Mar. 2007.
- [18] E. P. S. Tan and C. T. Lim, "Nanoindentation study of nanofibers," *Cit. Appl. Phys. Lett.*, vol. 87, p. 123106, 2005.
- [19] X. Li, X. Wang, W. C. Chang, Y. J. Chao, and M. Chang, "Effect of tensile offset angles on micro/nanoscale tensile testing," *Rev. Sci. Instrum.*, vol. 76, no. 3, 2005.
- [20] M.-F. Yu, O. Lourie, M. J. Dyer, K. Moloni, T. F. Kelly, and R. S. Ruoff, "Strength and breaking mechanism of multiwalled carbon nanotubes under tensile load," *Science*, vol. 287, no. 5453, pp. 637–40, Jan. 2000.
- [21] S. Cuenot, S. Demoustier-Champagne, and B. Nysten, "Elastic Modulus of Polypyrrole Nanotubes," 2000.
- [22] B. Varghese, Y. Zhang, L. Dai, V. B. C. Tan, C. T. Lim, and C.-H. Sow, "Structure-Mechanical Property of Individual Cobalt Oxide Nanowires," *Nano Lett.*, vol. 8, no. 10, pp. 3226–3232, Oct. 2008.

- [23] S. Hoffmann, I. Utke, B. Moser, J. Michler, S. H. Christiansen, V. Schmidt, S. Senz, P. Werner, U. Gösele, and C. Ballif, “Measurement of the Bending Strength of Vapor–Liquid–Solid Grown Silicon Nanowires,” *Nano Lett.*, vol. 6, no. 4, pp. 622–625, Apr. 2006.
- [24] W. Liu, K. Bonin, and M. Guthold, “Easy and direct method for calibrating atomic force microscopy lateral force measurements,” *Rev. Sci. Instrum.*, vol. 78, no. 6, p. 063707, Jun. 2007.
- [25] R. Inai, M. Kotaki, and S. Ramakrishna, “Structure and properties of electrospun PLLA single nanofibres,” *Nanotechnology*, vol. 16, no. 2, pp. 208–213, Feb. 2005.
- [26] J. H. Park and G. C. Rutledge, “Ultrafine high performance polyethylene fibers,” *J. Mater. Sci.*, vol. 53, 2017.
- [27] E. P. S. Tan, S. Y. Ng, and C. T. Lim, “Tensile testing of a single ultrafine polymeric fiber,” 2005.
- [28] E. P. S. Tan and C. T. Lim, “Mechanical characterization of nanofibers – A review,” *Compos. Sci. Technol.*, vol. 66, no. 9, pp. 1102–1111, 2006.
- [29] M. Yilmaz and J. W. Kysar, “Monolithic integration of nanoscale tensile specimens and MEMS structures,” *Nanotechnology*, vol. 24, no. 16, p. 165502, Apr. 2013.
- [30] M. Kiuchi, Y. Isono, S. Sugiyama, T. Morita, and S. Matsui, “Mechanical and electrical properties evaluation of carbon nanowire using electrostatic actuated nano tensile testing devices (EANAT),” in *5th IEEE Conference on Nanotechnology, 2005.*, pp. 640–643.
- [31] R. Legtenberg, A. W. Groeneveld, and M. Elwenspoek, “Comb-drive actuators for large displacements,” *J. Micromechanics Microengineering*, vol. 6, no. 3, pp. 320–329, Sep. 1996.
- [32] M. Naraghi, I. Chasiotis, H. Kahn, Y. Wen, and Y. Dzenis, “Novel method for mechanical characterization of polymeric nanofibers,” *Cit. Rev. Sci. Instruments*, vol. 78, p. 85108, 2007.
- [33] M. Naraghi, I. Chasiotis, H. Kahn, Y. Wen, and Y. Dzenis, “Mechanical deformation and failure of electrospun polyacrylonitrile nanofibers as a function of strain rate,” *Appl. Phys. Lett.*, vol. 91, no. 15, p. 151901, Oct. 2007.
- [34] M. Naraghi, P. V. Kolluru, and I. Chasiotis, “Time and strain rate dependent mechanical behavior of individual polymeric nanofibers,” *J. Mech. Phys. Solids*, vol. 62, pp. 257–275, 2014.
- [35] K. Şahin, N. A. Fasanella, I. Chasiotis, K. M. Lyons, B. A. Newcomb, M. G. Kamath, H. G. Chae, and S. Kumar, “High strength micron size carbon fibers from polyacrylonitrile–carbon nanotube precursors,” *Carbon N. Y.*, vol. 77, pp. 442–453, 2014.

- [36] M. P. deBoer, D. L. Luck, W. R. Ashurst, R. Maboudian, A. D. Corwin, J. A. Walraven, and J. M. Redmond, "High-Performance Surface-Micromachined Inchworm Actuator," *J. Microelectromechanical Syst.*, vol. 13, no. 1, pp. 63–74, Feb. 2004.
- [37] J. J. Sniegowski and M. P. de Boer, "IC-Compatible Polysilicon Surface Micromachining," *Annu. Rev. Mater. Sci.*, vol. 30, no. 1, pp. 299–333, Aug. 2000.
- [38] Sandia, "SUMMiT V □ Five Level Surface Micromachining Technology Design Manual," vol. 3.2, 2012.
- [39] L. Tong, R. R. Gattass, J. B. Ashcom, S. He, J. Lou, M. Shen, I. Maxwell, and E. Mazur, "Subwavelength-diameter silica wires for low-loss optical wave guiding," *Nature*, vol. 426, no. 6968, pp. 816–819, Dec. 2003.
- [40] E. C. C. M. Silva, L. Tong, S. Yip, and K. J. Van Vliet, "Size Effects on the Stiffness of Silica Nanowires," *Small*, vol. 2, no. 2, pp. 239–243, Feb. 2006.
- [41] Z. . Wang, R. . Gao, P. Poncharal, W. . de Heer, Z. . Dai, and Z. . Pan, "Mechanical and electrostatic properties of carbon nanotubes and nanowires," *Mater. Sci. Eng. C*, vol. 16, no. 1, pp. 3–10, 2001.
- [42] D. A. Dikin, X. Chen, W. Ding, G. Wagner, and R. S. Ruoff, "Resonance vibration of amorphous SiO₂ nanowires driven by mechanical or electrical field excitation," *J. Appl. Phys.*, vol. 93, no. 1, p. 226, 2003.
- [43] J. Luo, J. Wang, E. Bitzek, J. Y. Huang, H. Zheng, L. Tong, Q. Yang, J. Li, and S. X. Mao, "Size-Dependent Brittle-to-Ductile Transition in Silica Glass Nanofibers," *Nano Lett.*, vol. 16, no. 1, pp. 105–113, Jan. 2016.
- [44] J. L. Armstrong, M. J. Matthewson, and C. R. Kurkjian, "Humidity Dependence of the Fatigue of High-Strength Fused Silica Optical Fibers," *J. Am. Ceram. Soc.*, vol. 83, no. 12, pp. 3100–3109, Dec. 2000.
- [45] G. Capaccio and I. M. Ward, "Polymer Science Shrinkage, shrinkage force and the structure of ultra high modulus polyethylenes *)," *Colloid Polym. Sci.*, vol. 260, pp. 46–55, 1982.
- [46] D. K. Owens and R. C. Wendt, "Estimation of the surface free energy of polymers," *J. Appl. Polym. Sci.*, vol. 13, no. 8, pp. 1741–1747, Aug. 1969.
- [47] D. M. Brewis and D. Briggs, "Adhesion to polyethylene and polypropylene," *Polymer (Guildf.)*, vol. 22, no. 1, pp. 7–16, Jan. 1981.
- [48] S. Jana, A. Zhamu, W. H. Zhong, and Y. X. Gan, "Evaluation of adhesion property of UHMWPE fibers/nano-epoxy by a pullout test," *J. Adhes.*, vol. 82, no. 12, pp. 1157–1175, 2006.
- [49] K. K. Chawla, "Ceramic Matrix Composites," in *Composite Materials*, New York, NY: Springer New York, 1998, pp. 212–251.

- [50] E. Zussman, M. Burman, A. L. Yarin, R. Khalfin, and Y. Cohen, “Tensile deformation of electrospun nylon-6,6 nanofibers,” *J. Polym. Sci. Part B Polym. Phys.*, vol. 44, no. 10, pp. 1482–1489, May 2006.
- [51] J. Yao, C. Bastiaansen, and T. Peijs, “High Strength and High Modulus Electrospun Nanofibers,” *Fibers*, vol. 2, no. 2, pp. 158–186, Apr. 2014.
- [52] T. C. O’connor and M. O. Robbins, “Chain Ends and the Ultimate Strength of Polyethylene Fibers,” vol. 5, p. 51, 2016.
- [53] B. D. Jensen, M. P. de Boer, N. D. Masters, F. Bitsie, and D. A. LaVan, “Interferometry of actuated microcantilevers to determine material properties and test structure nonidealities in MEMS,” *J. Microelectromechanical Syst.*, vol. 10, no. 3, pp. 336–346, 2001.
- [54] M. Hoff~ and Z. Pelzbauer, “Relationship between thermal shrinkage and morphology of zone-drawn polyethylene*,” 1991.
- [55] B. Sanborn and T. Weerasooriya, “Tensile Properties of Dyneema SK76 Single Fibers at Multiple Loading Rates Using a Direct Gripping Method,” *Conf. Proc. Soc. Exp. Mech. Ser.*, vol. 65, no. VOLUME 1, pp. 1–4, 2015.

Chapter 7: Size-dependent creep master curve of electrospun polymer nanofibers

7.1 Abstract

The temperature and size-dependent elastic and viscoelastic behavior of electrospun polyacrylonitrile (PAN) nanofibers have been studied, and a master curve spanning ~10 decades (equivalent to 30 years at room temperature) has been developed. Elastic modulus and yield stress were found to increase with decreasing diameter. Based on the principle of a linear superposition, a variable stress creep measurement method was developed and compared with a conventional constant creep measurement technique. Using time-temperature superposition, the master curve was constructed for temperatures below the glass transition temperature. Thin specimens (~150 nm) are predicted to exhibit an order of magnitude less creep compared to thick specimens (~260 nm) after 30 years. The activation energy for creep process in thin PAN fibers was ~152 kJ mol⁻¹, 50 % larger than the thick fibers. Exposure of the PAN nanofibers to high energy electron beam increased the creep compliance significantly.

7.2 Introduction

Polymer nanofibers have garnered significant attention due to their strong size-dependent material properties. When their diameter is below ~1 μm, mechanical and thermal properties such as Young's modulus, tensile strength, and thermal conductivity are enhanced by several times to several orders of magnitude [1]–[6]. This has been reviewed in detail in Chapter 2. This notable heightening, coupled with the intrinsic properties of polymers such as their lightweight, chemical

resistance, and biocompatibility, opens up applications in tissue engineering, filtration, sensing, textiles, and composite reinforcements [7]–[11]. The size-dependent elastic-plastic behavior of nanofibers has been studied for several polymers [12]–[16]. However, for reliable design, their long-term mechanical behavior is in need of characterization.

The nanoscale size effect of mechanical properties in polymers is mainly due to (i) the reorganization of the interior core polymer chains and (ii) an increase in the relative amount of fluid-like chains on the surface. The increase in core molecule orientation and/or in crystallinity of a semi-crystalline polymer results in improved elastic-plastic properties [3], [12], [17]–[19], while an increase in the surface-to-volume ratio of a glassy polymer changes the rheological properties such as a decrease in the glass transition temperature, T_g [20], [21].

Polymers exhibit viscoelastic behavior, which is both dependent on time and temperature. For example, when a polymer is under a constant load much lower than the yield stress, the stiffness of the polymer decreases over time, resulting in a continued elongation of the polymer. This occurs because the molecules reorganize to reduce the localized stress by segmental rotation, flow or chain unfolding [22]. Similarly, at an elevated temperature near T_g , the polymer free volume increases and the molecules can slide past each other and disentangle at a higher rate [23]. Time and temperature are equivalent in that creep/relaxation behavior in the long-term can be simulated over a short-term by increasing the temperature [24]. Direct creep or stress relaxation tests for an extended period (years) are impractical due to time, cost, equipment and experimental stability. Therefore, time-temperature superposition has become a valuable tool to understand this long-term behavior using short-term tests [24]–[30].

The mechanical property measurement of nanofibers requires new characterization methods. A tensile test system can make elastic and plastic measurements [31]. In this case, the

nanofibers must maintain a constant nm-scale diameter over a length on the order of cm for good accuracy. Considering the aspect ratio is then on the order of 10^5 , this can be difficult to achieve experimentally. While scanning electron microscopy (SEM) can be used to obtain nanoscale deflections, its interpretation is limited by electron beam-induced damage such as the loss of orientation and crystallinity, mass loss, swelling and radiolysis [3], [32]–[34]. These effects can be minimized by using a low-dose and with infrequent imaging. Using low energy SEM imaging, Wingert et al. performed short-term viscoelastic measurements at room temperature (RT) in an atomic force microscopy (AFM) apparatus [35]. However, such mitigating modifications result in the poor temporal resolution [35]. The temporal resolution further compromises experiments at increasing temperature where shorter time relaxation modes are accessed.

Naraghi et al. demonstrated a technique based purely on optical metrology capable of measuring the viscoelastic response of a soft polymer nanofiber [36], [37]. They demonstrated a size effect on creep of electrospun PAN nanofibers where an increased orientation overwhelmed the increased surface effect and suppressed the creep rate. The measurement system required manual feedback to keep the creep stress constant. Although the system could measure room temperature creep, creep measurements at a higher temperature would require rapid feedback, not feasible manually due to the fast relaxation.

Here, based on the principle of linear superposition, we demonstrate that a variable stress technique can be applied to a polymer nanofiber to measure the linear viscoelastic behavior at an elevated temperature. This also eliminates the need to apply feedback to keep the stress constant, thus making it feasible to acquire an accurate relaxation time at higher temperatures. In addition, we demonstrate a size-dependent master curve of polymer nanofiber which shows that a thinner nanofiber exhibits less creep. We attribute this to an increased orientation of the polymer core

molecules. The master curve allows an estimate of polymer nanofiber viscoelastic behavior below T_g up to 30 years. After that duration, it is estimated that the creep compliance of a 260 nm PAN nanofiber is an order of magnitude larger than that of a 150 nm PAN nanofiber. The activation energy in the thicker PAN nanofiber was 103 kJ/mol This was 50 % larger than the thinner nanofiber. When the orientation of PAN nanofibers was removed by exposing PAN nanofiber to high energy electron beams in SEM, the creep compliance increased by several times.

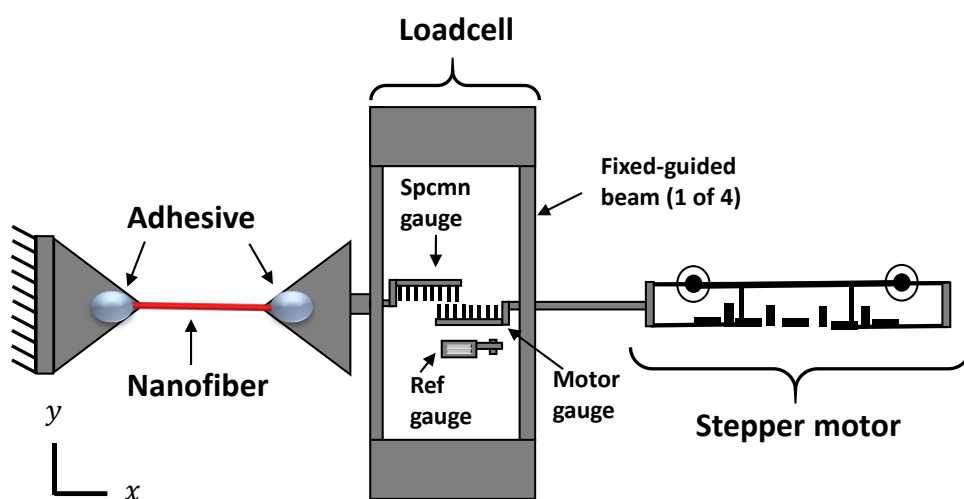


Figure 7.1: Test platform schematic (not to scale).

7.3 Experimental methods

7.3.1 Specimen preparation and test platform

PAN nanofibers were fabricated by electrospinning [38]. Accordingly, PAN with a molecular weight of $150,000 \text{ g mol}^{-1}$ was dissolved in dimethylformamide (DMF) (Sigma-Aldrich) to obtain a 10 wt. % solution. The feed rate of the polymer solution during electrospinning was 2.0 ml h^{-1} to achieve a stable electrospinning jet. Highly aligned polymer nanofibers were obtained by using a rotating drum collector at electrospinning voltage and distance of 25 kV and 20 cm,

respectively. The temperature and humidity within the electrospinning chamber is ~ 25 °C and 20 % - 30 %.

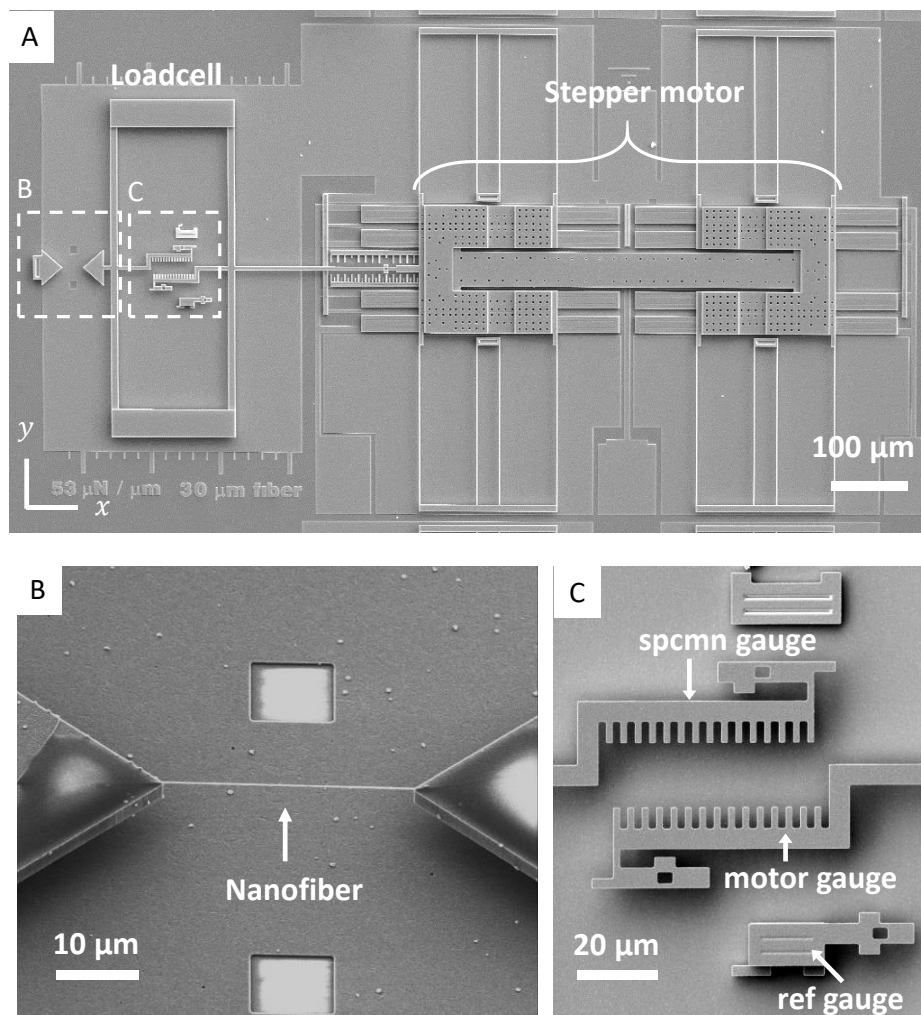


Figure 7.2: SEM images of (A) the full test platform with the stepper motor on the right, (B) the gauge section with a mounted nanofiber and (C) the comb fingers and reference gauge used for displacement metrology.

Three types of experiments were performed in this study: (i) size-dependent uniaxial tensile tests (ii) constant load creep tests and (iii) variable stress creep tests. They were conducted using a microelectromechanical system (MEMS) based device on individual PAN nanofibers. A detailed

discussion of the MEMS-based test platform can be found in Section 6.3 in Chapter 6. Briefly, the test platform has an on-chip surface micromachined stepper motor which takes 60 nm steps driven by electrostatic forces [39]. The detailed actuation mechanism has been discussed in Section 6.3.2 in Chapter 6. The stepper motor can apply high in-plane force (1 mN) and stretch the nanofiber up to 75 μm , thereby applying up to 250 % strain on the 30 μm nominal gage length nanofibers. Fig. 7.1 shows the schematic of the test platform (not to scale) with the stepper motor on the right. It was fabricated using the SUMMiT VTM (Sandia Ultra-planar Multi-level MEMS Technology 5) process [40]. Fig. 7.2A shows an SEM image of the full MEMS platform.

A polymer nanofiber sample is gripped by fixed and moveable pads (Fig. 7.2B). The movable pad and a load cell are tethered to the stepper motor. When it takes a step to the right, it displaces the load cell and once taut, the test specimen. Because the load cell and the specimen are in series, they experience an equal load and each stretches proportional to its stiffness. The load cell consists of four fixed-guided beams (Figs. 7.1, 7.2A), which determine the load cell stiffness, and two gauges – from which displacement and force are determined (Figs. 7.1, 7.2C). The length and width of the fixed-guided beams are obtained from the SEM images, whereas the thickness is determined by the Sandia SUMMiT VTM process [41]. Its estimated stiffness is $k_L=5.4 \text{ nN nm}^{-1}$, while the uncertainty in stiffness is $\pm 2.7 \%$ (one standard deviation). The detailed derivation of the uncertainty of the loadcell stiffness can be found in Section 6.3.3 in Chapter 6. The load cell gauges and a fixed reference (Fig. 7.2C) are optically imaged throughout the test with a charged coupled device (CCD) camera. The images are saved for later data analysis using sub-pixel pattern matching to extract force and displacement of the fiber. The force exerted on the specimen is $F = k_L \times (x_{\text{motor gauge}} - x_{\text{specmn gauge}})$, where x represents position. The nanofiber diameter (D) was measured after mechanical testing using SEM in a region just outside the epoxy grips. Stress was

calculated as $\sigma = 4F/(\pi D^2)$. Engineering strain was obtained as $\varepsilon = (x_{\text{spcmn gauge}} - x_{\text{ref gauge}})/L_f$ where L_f is the initial length of the nanofiber. The sub-pixel pattern matching provides displacement and force resolution of ± 6 nm and ± 32 nN (one standard deviation).

An individual nanofiber of 250 – 500 μm length was cut using a custom micro-heater. The nanofiber was manipulated onto the test platform pads, and firmly attached with epoxy using a sharp tungsten tip mounted on a precision XYZ manipulator. Next, the epoxy was cured for 24 h. Then, measurements were carried out on a probe station equipped with a long working distance microscope (numerical aperture $NA = 0.55$) on a vibration isolation table.

For the temperature-dependent creep tests, the MEMS device was placed on a temperature-controlled plate (Agilent N9657A) and tested in laboratory air and ambient relative humidity of 70 ± 10 %. A normal force of several mN is applied to the stepper motor friction clamps, whereas the axial force in the fiber is at the μN scale. Therefore, an important feature of this test platform, especially important for the variable stress creep test, is that its drift relative to the substrate is negligible [42] given this large normal to tangential force ratio, which is well above the clamp coefficient of friction of 0.3. (Note that substrate drift is subtracted out from the measurements). The total measured creep is the sum of the creep in the specimen and in the grip, both of which depend on the applied force. Due to the large contact area between the nanofiber and epoxy compared to the cross-section area of the nanofiber, a negligible shear stress ($>10^2$ times) is present at the interface compared to the tensile stress on the fiber. Therefore, the contribution from the creep in epoxy [43], [44] is expected to be negligible.

Thermogravimetric analysis of PAN below 200 $^\circ\text{C}$ in the air does not reveal any different degradation compared to nitrogen or oxygen environments [45]. Therefore, our tests below T_g ,

which is 105 °C for electrospun PAN nanofibers [38], in laboratory air are not expected to give different results if tested in those common pure gases.

7.3.2 Mechanical test protocols

7.3.2.1 Uniaxial tensile test

For a uniaxial tensile test, nanofibers of various diameters D were chosen and tested on the probe station. The stepper motor was actuated at 1 step s^{-1} , corresponding to a nominal strain rate of $2 \times 10^{-3} s^{-1}$, while load cell displacements were optically imaged with a 50X objective (NA = 0.55) using a charge coupled device (CCD) camera at 1 frame s^{-1} and stored for data analysis.

After the measurement, specimen stress and the strain were evaluated from recorded images as described in the section above. An engineering stress-strain curve was plotted. Elastic modulus was obtained from the slope of the initial linear regime of the curve. The stress at which line with a slope of Young's modulus offset by 0.2 % was taken as the yield strength.

7.3.2.2 Conventional creep test

In a conventional creep test, a creep stress (σ_{creep}) is applied instantaneously and kept constant while the corresponding strain as a function of time $\varepsilon(t)$ is measured. Then, creep compliance $D(t)$ is defined as

$$D(t) = \frac{\varepsilon(t)}{\sigma_{creep}} \quad (1)$$

At the macroscale, this is easily realized with a dead load and a strain gauge.

In our experiments, we used feedback to simulate a conventional creep experiment. The motor was stepped at 1 Hz until the fiber was taut and then σ_{creep} was rapidly applied. Naraghi et al. found that PAN nanofibers with D from 240 to 340 nm were in the linear viscoelastic (LVE) regime at RT when the stress was below 70 MPa [36]. This corresponds to a strain of $\sim 2\%$. Because the fiber diameter is only accurately measured post-test by SEM, a fiber strain rather than a fiber stress was applied in the creep tests. This was done by moving stepper motor 10-13 steps at 100 Hz, equivalent to 2% nominal strain in the absence of a load cell. The actual strain on the specimen is lower than that due to the displacement of the load cell in series. This was found to be a safe approach to stay within the LVE limit.

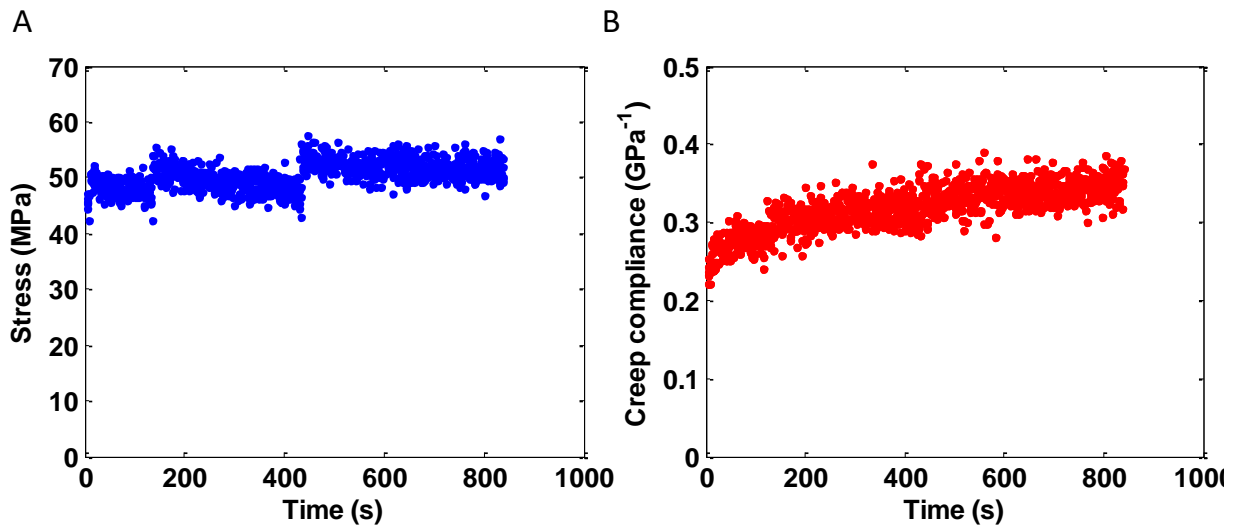


Figure 7.3: Data from a conventional creep test at RT. (A) Approximately constant creep stress as maintained by feedback (B) the corresponding creep compliance curve.

The stepper motor displacement is the sum of the load cell opening and the fiber displacement. After load application, the specimen creeps. The load cell closes in response to the specimen extension, and the tensile force gradually decreases. A force feedback mechanism was

implemented to minimize the load relaxation and to keep the creep stress nearly constant. Accordingly, when the load cell opening reduced by more than 30 nm, a feedback step was applied.

The load cell opening was thus monitored to determine when the feedback step should be applied. The camera image acquisition speed was 15 frames s⁻¹ and the feedback algorithm was ultimately limited by the sub-pixel pattern matching, resulting in a maximum of 2 feedbacks s⁻¹. At room temperature (RT), the relaxation time was several times slower than the feedback capability, thus the creep test was feasible, similar to ref. [36], but now as an automatic process.

In Fig. 7.3A, data for a PAN nanofiber (diameter 280 nm) subjected to a nearly constant σ_{creep} (50.5 ± 2.5 MPa (1 standard deviation)) within the LVE regime with feedback is shown. The deviation could be minimized with a load cell of lower stiffness and/or a stepper motor with smaller step size. The necessity of feedback became infrequent after the first at 50 s and the duration between corrections became longer after each feedback. However, due to the feedback mechanism, the serrated nature of the stress profile is apparent (Fig. 7.3A). The average stress was taken as the creep stress, and the creep compliance (Fig. 7.3B) was obtained per equation 1. The creep compliance increases with time. Our 800 s creep compliance ($\sim 0.34 \pm 0.02$ GPa⁻¹) is slightly larger than that of Naraghi et al. [36] (~ 0.28 GPa⁻¹) for a similar diameter fiber, possibly because of a lesser degree of molecular orientation from different electrospinning parameters. In any case, the creep compliance is in reasonable agreement with given the reported scatter in Naraghi et al.'s data [36].

7.3.2.3 Variable stress creep test

The PAN nanofiber creep rate was observed to increase rapidly with temperature. Thus, while RT creep could be adequately assessed, a revised method was necessary to test its creep

properties at higher temperatures with this test platform.

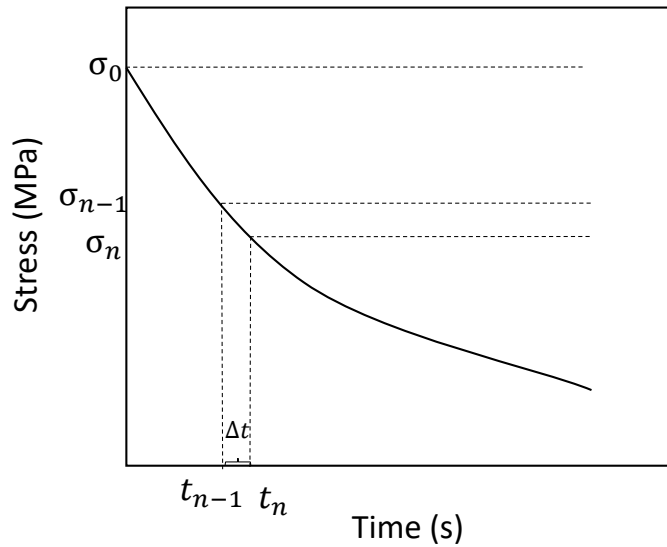


Figure 7.4: An example of variable creep stress.

Creep compliance can also be obtained with a variable stress input within the LVE [30], which eliminates the need for feedback. The variable stress can be represented as a series of constant stresses each of which begins loading at a different time. The variable stress $\sigma(t)$ shown in Fig. 7.4 can be expressed as

$$\sigma(t) = \sigma_0 H(t) + \sum (\sigma_n - \sigma_{n-1}) H(t - t_n) \quad (2)$$

For an LVE material, the creep compliance is independent of the stress input. Thus, using the Boltzmann superposition principle strain can be obtained by adding the response of each individual step stress

$$\varepsilon(t) = \int_0^t D(t - \tau) \frac{d\sigma}{d\tau} d\tau \quad (3)$$

In this process, the nanofiber is actuated to a strain value within the LVE regime, similar to the conventional creep test process described above. After the actuation, the stepper motor is fixed.

The application of the stress causes the sample to creep. The load cell closes equivalent to the sample extension from creep. No feedback is applied, and the stress is allowed to relax. All these processes are recorded with a CCD at an effective rate of 10 frames s^{-1} to allow for storage of the recorded image. The variable stress and strain are analyzed from the saved images. The sequence to obtain creep compliance with a variable stress-based creep measurement is discussed next. Taking the Laplace transform of equation 3 and rearranging gives

$$D(s) = \frac{\varepsilon(s)}{s\sigma(s)}. \quad (4)$$

The Laplace transform of stress, $\sigma(s)$, and strain, $\varepsilon(s)$, are obtained from the functional form of stress $\sigma(t)$ and strain $\varepsilon(t)$, which are obtained after curve fitting the raw data. Then, the creep compliance is obtained from an inverse Laplace transform of equation 4,

$$D(t) = \mathcal{L}^{-1}(D(s)). \quad (5)$$

The advantage of this process is that it does not require feedback and thus it can capture the creep process accurately even at an elevated temperature. To minimize erroneous readings due to out-of-plane microscope drift, an autofocus routine at intervals on the order of hundreds of seconds was employed.

The application of the Boltzmann superposition principle to obtain a creep compliance from a variable stress application is limited to the LVE regime, where stress is linearly proportional to strain in an isochronous curve. To ascertain the LVE regime, a $D = 220$ nm PAN nanofiber was tested at different stress levels (Fig. 7.5A) ranging from LVE to the non-linear viscoelastic regimes and the resulting strain (Fig. 7.5B) was recorded. The total strain during this test was up to 8 %, but the strain increments were each below 2%, so that in each increment the linearity of stress versus strain could be probed from low to high stress. With increasing temperature, shorter time relaxation modes are activated resulting in the LVE shift to a lower stress or a higher strain [46].

The LVE regime at 100 °C was measured and previous work by Naraghi et al. [36] was used for a room temperature (RT) LVE regime estimate as described in section II.2.2.

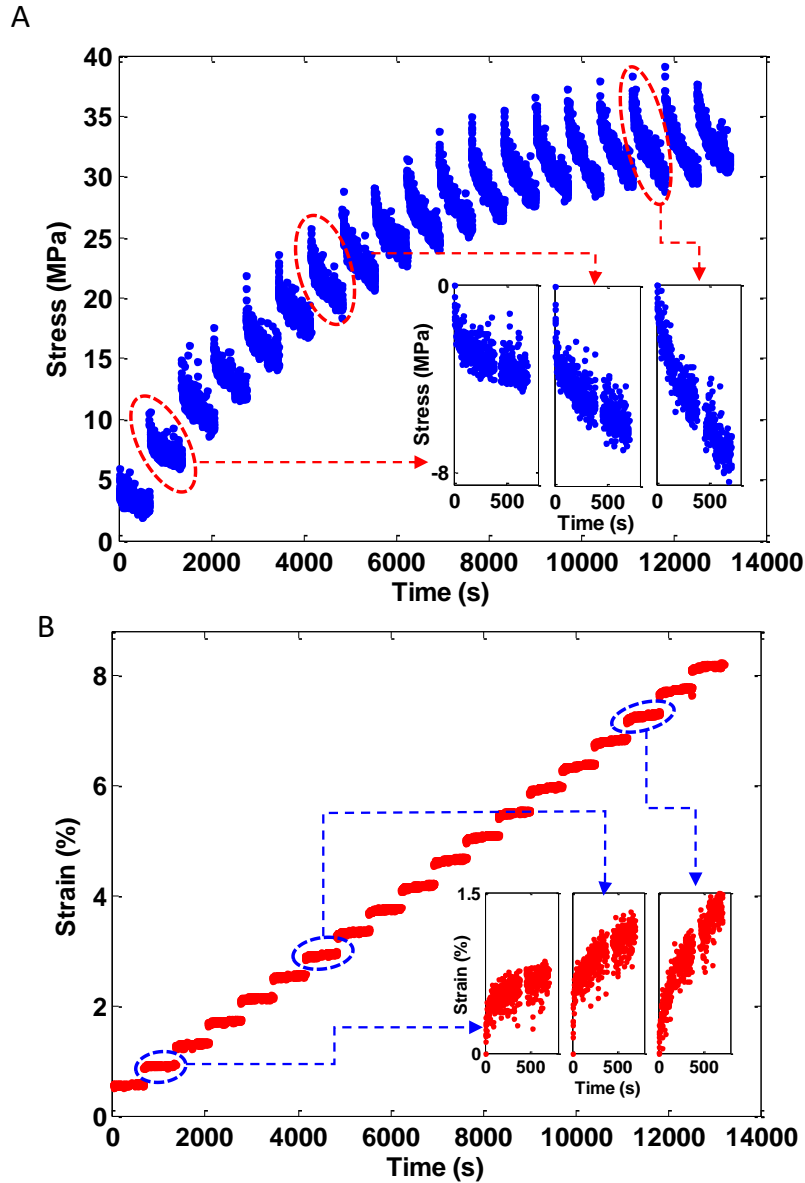


Figure 7.5: Data taken to determine the limit of the linear viscoelasticity (LVE) regime at 100 °C (A) Multiple levels of variable stresses. The insets show individual levels of variable stress. (B) The corresponding strain. The insets show the respective strains. In the insets, the stress and strains values are shifted such that their origins begin at their initial value.

For each stress level, the actuator took 3 steps and was held for ~650 s before increasing the stress to the next level. After 400 s, the microscope objective was again autofocused on the load cell gages, which required 60 s. The insets of Figs. 5A and B show magnified stress-time and strain-time data at three different loadings. Since the stress and the strain data were not collected during the autofocus routine, this interval appears as a gap. The stress and the strain values in the insets are shifted such that the origins begin at their initial values.

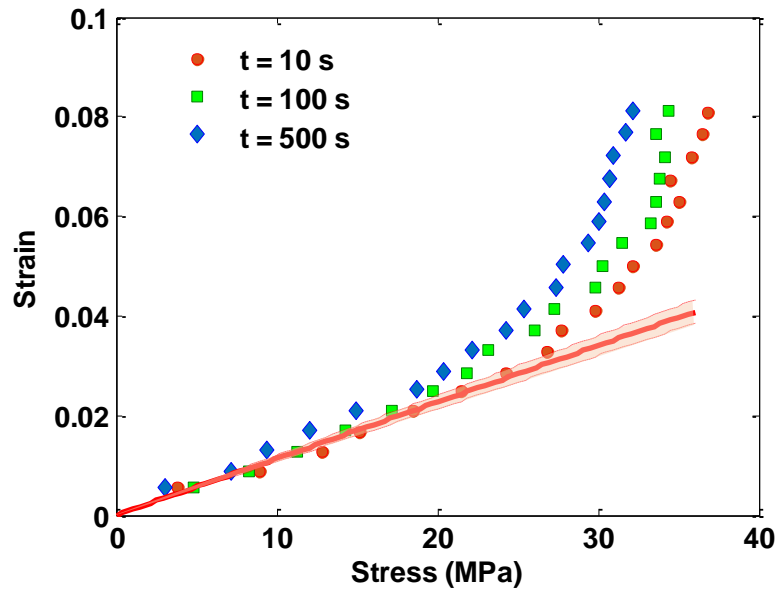


Figure 7.6: Isochronous engineering stress-strain curves at 100 °C to determine the limit of linear viscoelastic (LVE) behavior. A least squares linear fit with a 95 % confidence interval on the 10 s stress-strain data is shown.

Fig. 7.6 shows the resulting isochronous engineering stress-strain curves for times $t = 10$, 100 and 500 s after the application of stress at each level shown in Fig. 7.5. To determine stress and strain, the data were chosen to be within ± 1 , 3 and 10 s of times $t = 10$, 100 and 500 s,

respectively. A least squares linear fit for the 10 s isochronous curve indicates that the material is linear below ~25 MPa or ~3 % initial strain at 100 °C. The solid line is the least squares fit whereas the dashed lines represent the 95 % confidence interval boundaries.

Given Naraghi et al.'s data [36] and the Fig. 7.6 results, the creep strain initially applied to specimens as reported in the Results section below was limited to 2 % at RT and 3 % at 100 °C. Also, the specimens were heated at a slow heating rate (2 K min⁻¹) and held at a set temperature for 1 h before conducting a test.

7.3.2.4 Time-temperature superposition and generating a master curve

Time-temperature superposition (TTSP) is a well-established technique where short-term rheological properties of a polymer are shifted and superposed to obtain a larger frequency/time domain behavior also referred to as a master curve [24]. The underlying concept is that the viscoelastic behavior at a certain time and temperature is equivalent to a longer time at a lower temperature. The viscoelastic measurements are generally taken over three decades of time. Using TTSP, it is possible to estimate the viscoelastic behavior over ten to fifteen decades of time. An isothermal creep compliance curve is shifted horizontally on a log time-scale compared to a reference temperature curve to obtain a smooth curve that spans the much longer time. The horizontal shift factor ($\log a_T$), for a polymer above T_g , is obtained from the well-known William-Landel-Ferry (WLF) equation [24]. Our tests are limited to temperatures from RT to the PAN nanofiber T_g . For a polymer below T_g , an Arrhenius type equation can be applied [25] to obtain the horizontal shift factor as shown below

$$\log a_T = \frac{\Delta H}{2.3R} \left(\frac{1}{T_0} - \frac{1}{T} \right) \quad (6)$$

where ΔH is the activation energy for the creep, R is the gas constant and T_0 is the reference

temperature. For a thermorheologically complex material where density changes with temperature, a small vertical shift factor is also required to obtain a smooth master curve [47], [48].

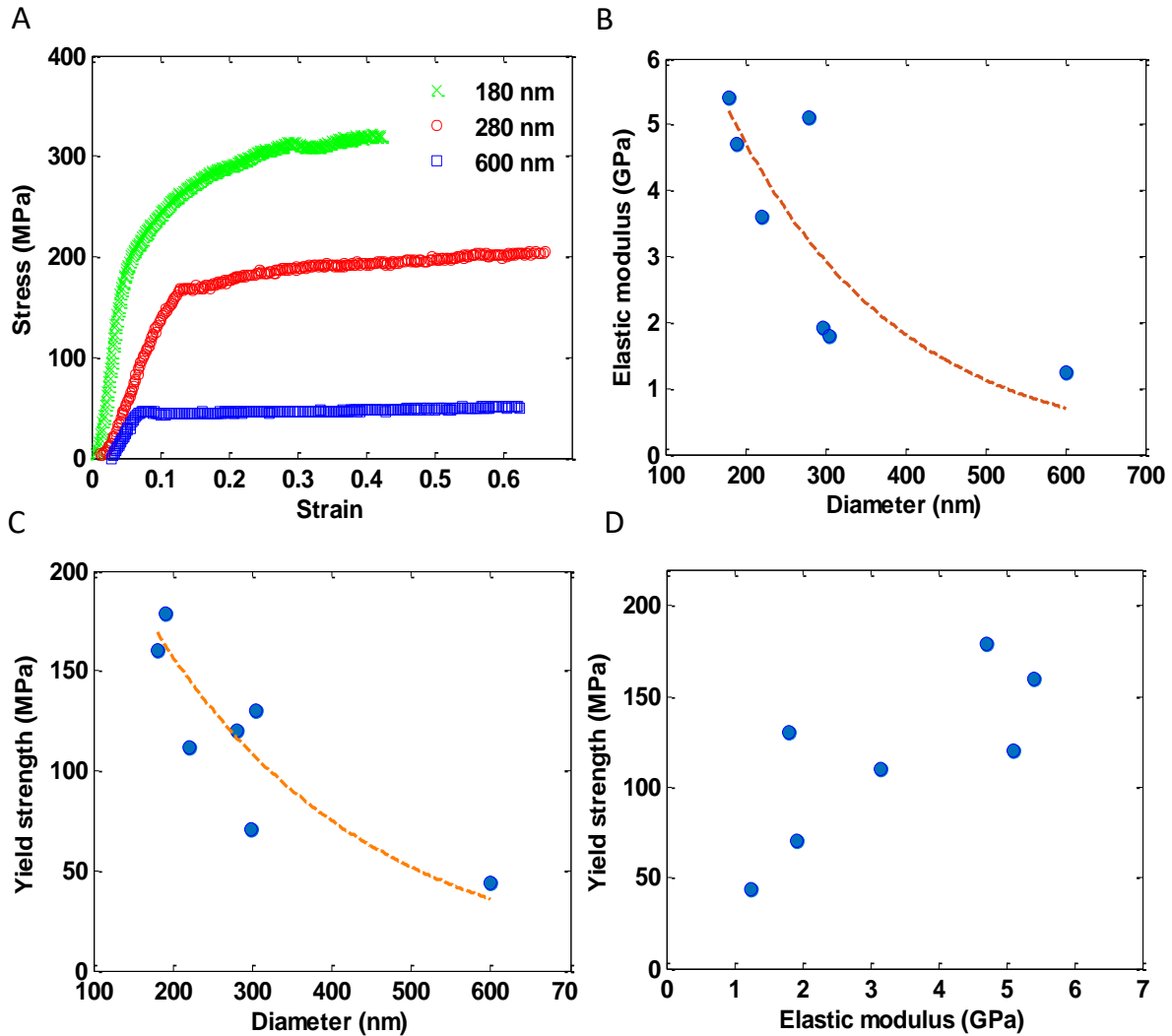


Figure 7.7: Elastic-plastic behavior of PAN nanofiber. (A) Engineering stress-strain curves for three different diameters. (B) Elastic modulus vs diameter. (C) Yield strength vs diameter. (D) The elastic modulus vs yield strength shows a positive correlation. Dashed lines are exponential curves that indicate the data trends.

7.4 Results

7.4.1 Size-dependent tensile properties:

Tensile measurements were performed on electrospun PAN nanofibers with diameters D between 180 nm and 600 nm. From the stress-strain curves (Fig. 7.7A), the elastic modulus and the yield strength were obtained. The elastic modulus (Fig. 7.7B) and the yield strength were found to increase significantly below 300 nm (Fig. 7.7C). The dashed lines in Figs. 7.7B and C indicate the data trend. Thinner fibers show an increased modulus with increased yield strength as demonstrated by a positive correlation between them (Fig. 7.7D). The size-dependent elastic behavior of PAN nanofiber is consistent with the previous measurements on PAN nanofiber [36] and other electrospun polymer nanofibers [16], [49]. Above 300 nm, the elastic modulus of PAN nanofiber is comparable to that of bulk PAN ($\sim 1.1 - 3$ GPa) [12]. The increasing modulus and strength below 300 nm have been attributed to increasing molecular orientation during electrospinning. This also leads to a reduction in ductility on samples below 300 nm.

7.4.2 Variable stress creep experiment

Fig. 7.8 shows a typical variable stress curve and a strain response of a PAN nanofiber sample (240 nm), in this case, tested at 60 °C. The raw data was fit with a time-dependent function as shown by the green dashed line. Using equations 5 and 6, the creep compliance was obtained. Fig. 7.9 shows the temperature-dependent creep compliances of PAN nanofibers with $D = 260 \pm 80$ nm. The samples were tested at temperatures between RT and close to T_g (105 °C [38]). The creep compliance shows a transient behavior up to 2000 s followed by a steady-state behavior limited by the steady state viscosity of the material. It also increases with the increase in temperature mainly because shorter time relaxation modes become accessible.

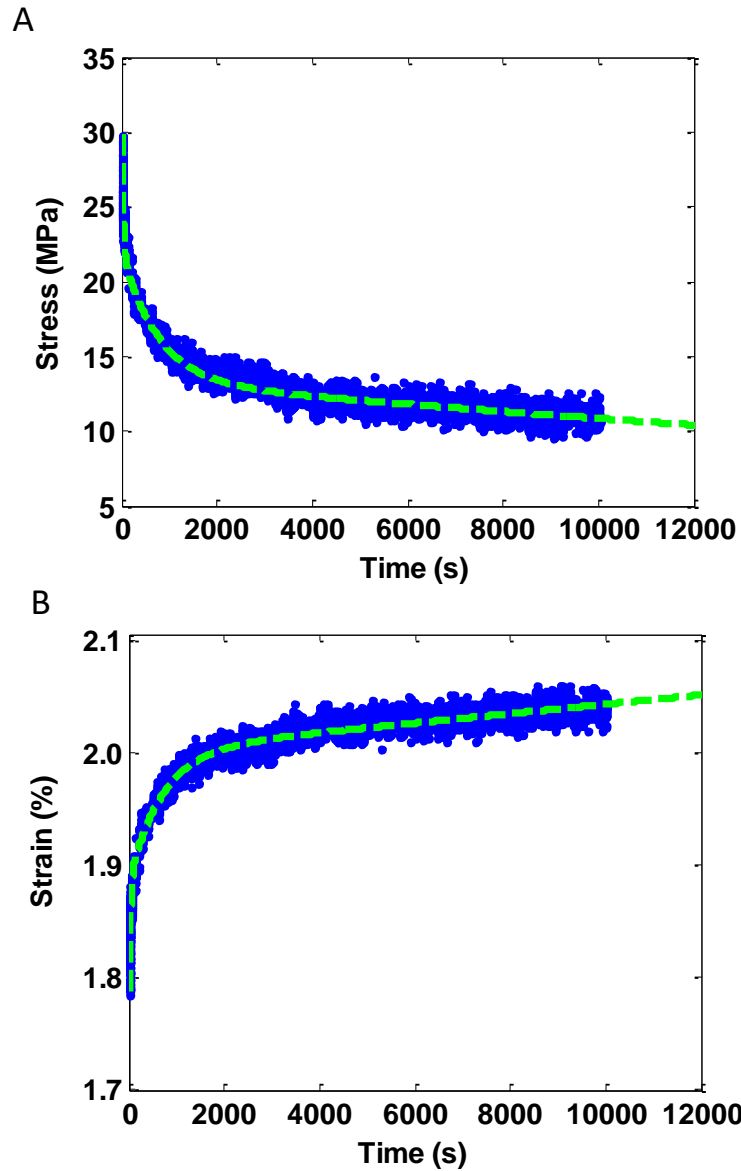


Figure 7.8: Representative sample with (A) stress and (B) strain curve fitting.

Fig. 7.10A shows a smooth master curve spanning 9 decades of time obtained by horizontally shifting the creep compliances at different temperatures with reference to the RT creep compliance. The first 20 s transient creep response was removed before the shift. In some thermorheologically complex material where density changes with temperature, a small vertical shift is necessary [48]. In order to generate a master curve (Fig. 7.10A), a vertical shift of 0.028

was used only for 104 °C, the temperature close to T_g suggesting that PAN fiber may be thermorheologically simple below T_g . Bulk PAN [27] and several other polymers such as aramid fibers [50] wood-plastic composite [51] have also exhibited thermorheological simplicity [51] whereas semi-crystalline polymers are known to exhibit thermorheological complexity [52], [53].

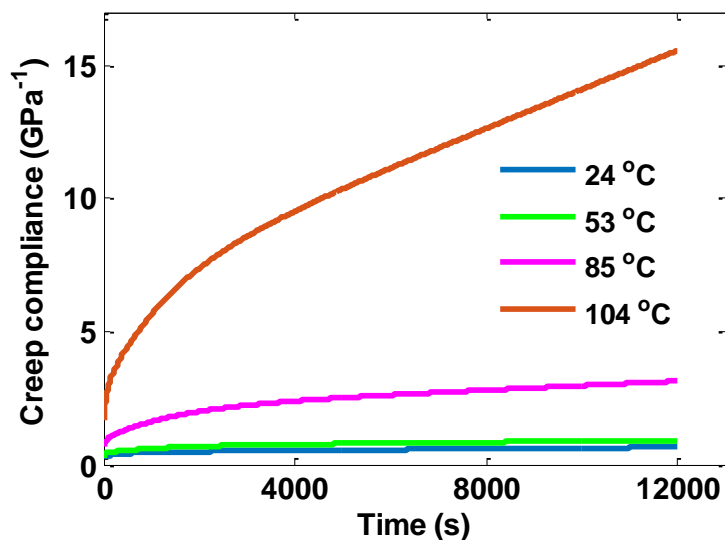


Figure 7.9: Creep compliance as a function of temperatures. The nanofiber diameters for each tested temperature of 24 °C, 53 °C, 85 °C and 104 °C were 240 nm, 190 nm, 232 nm and 375 nm respectively.

The horizontal shift factors used for the master curve are shown in Fig. 7.10B. A linear fit between the horizontal shift factors and the inverse of absolute temperatures gives the activation energy for the creep of PAN nanofiber. The apparent activation energy of creep/relaxation increases significantly close to the glass transition temperature [27]. Therefore, the shift factor of measurement close to T_g was excluded. An apparent activation energy of $\sim 103 \text{ kJ mol}^{-1}$ was obtained. The value is near the previously reported activation energies for bulk PAN 110 kJ mol^{-1}

[27] below T_g and also several other polymers below T_g such as poly(methyl methacrylate) (PMMA) 84.1 kJ mol⁻¹ [54], acrylonitrile butadiene (ABS) 75.6 kJ mol⁻¹ [55] and aramid fibers 116.3 - 147.3 kJ mol⁻¹ [50].

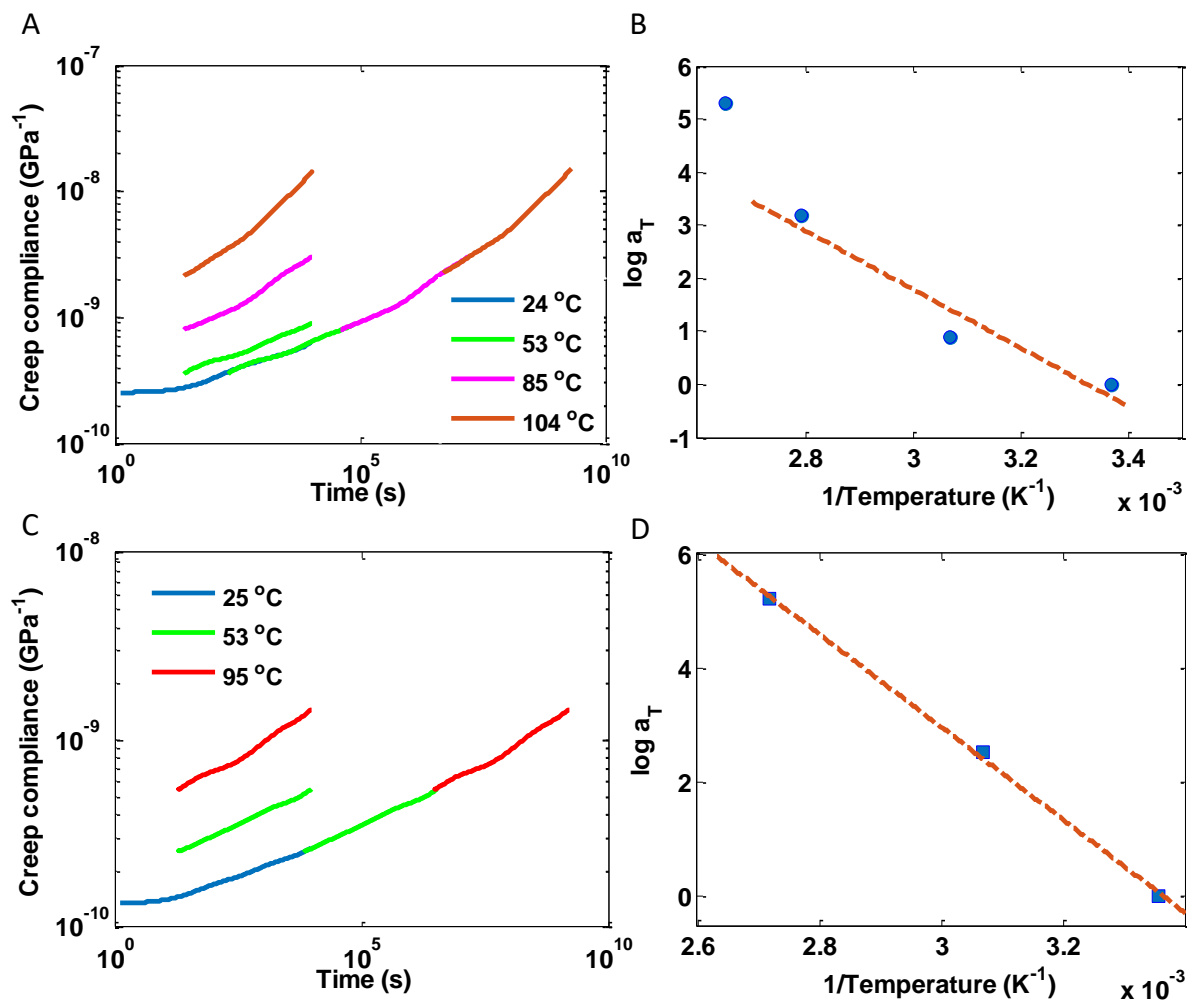


Figure 7.10: TTSP with RT as the reference temperature. (A) Master curve for nanofibers with an average diameter of 260 nm (B) Horizontal shift factor vs inverse of absolute temperature. The dashed line is a linear curve fit excluding the data close to T_g . (C) Master curve for nanofibers with an average diameter of 150 nm. The nanofiber diameters for each tested temperature of 25 °C, 53 °C, and 95 °C were 160 nm, 145 nm, and 145 nm respectively. (D) Horizontal shift factor vs inverse of absolute temperature.

A similar master curve was generated for thin fibers ($D=150 \pm 10$ nm). Figs. 7.10C and D show the associated master curve and horizontal shift factors, respectively. The activation energy of the thin PAN nanofiber, 152 kJ mol^{-1} , is 50 % larger than thick PAN nanofiber. The surface-to-volume ratio is larger in thin PAN nanofiber. Therefore, the data implies that the orientation effect outweighs the surface effect.

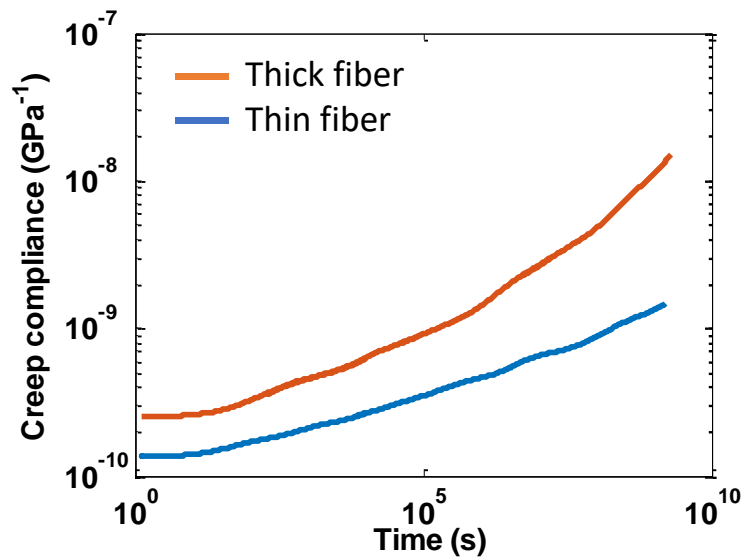


Figure 7.11: Comparison of the master curves of thick (average diameter 250 nm) and thin fiber (average diameter 150 nm). RT is the reference temperature.

Fig. 7.11 shows the size-dependent master curve for PAN nanofiber. Similar to the size-dependent creep compliance [36], the PAN nanofiber master curve shows size-dependence, where thinner fiber creeps less. After 30 years, the creep of thin PAN nanofiber is an order of magnitude smaller than thick PAN nanofiber.

The orientation of the PAN nanofiber was removed by exposing the PAN nanofiber to a high energy electron beam in SEM. The creep compliance of the randomly oriented fiber ($D=220$ nm) then increased by a factor of 5 to 10 compared with the partially oriented fibers ($D=160$ and 240 nm), Fig. 12. This indicates how much globally unoriented molecules increase the creep compliance.

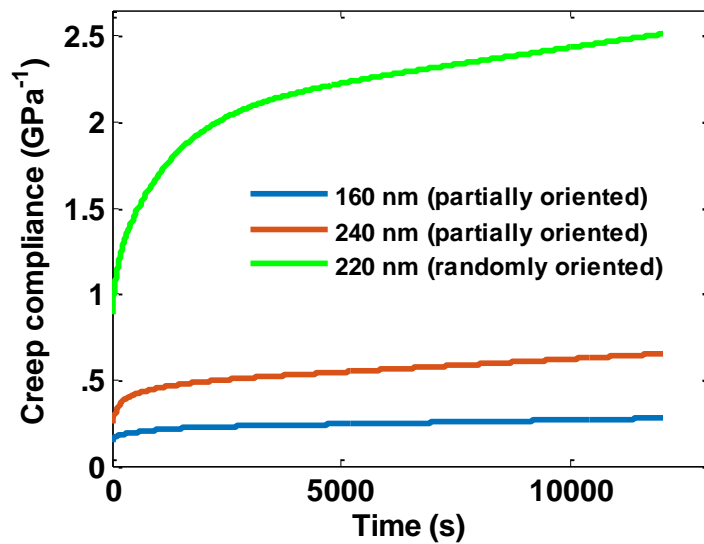


Figure 7.12: Creep compliances of the partially oriented versus a randomly oriented PAN nanofiber.

7.5 Summary and Concluding Remarks

A new test platform (Figs. 7.1 and 7.2) to measure polymer nanofiber creep versus temperature, resulting in the first TTSP curves of PAN nanofibers from RT to T_g , has been demonstrated. The advantages of the method are (i) that the fibers are short and therefore exhibit minimal cross-section variation, (ii) that the deformation measurements are optical and therefore

not susceptible to electron-induced bond damage and (iii) that the platform is not susceptible to drift, thereby minimizing experimental error. With the platform, at RT results in agreement with other literature [36] were obtained in a conventional creep test using feedback (Fig. 7.3). To enable creep measurements up to T_g (105 °C), a variable stress relaxation method was proposed. To implement this method, we first showed that the LVE regime extends up to 3 % strain for PAN at 100 °C (Figs. 7.5 and 7.6), and then upon the principle of linear superposition, applied standard Laplace transform techniques to extract the creep compliance curves.

With this new platform, elastic modulus and yield strength of PAN nanofibers with diameters from 180 to 600 nm were found to increase significantly with decreasing diameter below 300 nm, consistent with previous measurements on as electrospun PAN nanofibers [36], [37], [56] and several other polymer nanofibers [16], [49]. The increasing modulus and strength were attributed to the increasing orientation with decreasing diameter [12], and the data taken here substantiates those results. The ductility was found to reduce below 300 nm.

The creep compliance showed a monotonically increasing trend with time and temperature. The steady-state creep compliance at 5000 s was slightly larger ($\sim 0.4 - 0.5 \text{ GPa}^{-1}$) than that of Naraghi et al. ($\sim 0.3 - 0.4 \text{ GPa}^{-1}$) for a similar diameter fiber, possibly because of a lesser degree of molecular orientation due to different electrospinning parameters [36]. The steady-state creep compliance near T_g was almost 25 times larger than at RT. Using TTSP, a size-dependent creep compliance master curve was generated. The creep compliance decreased with diameter consistent with the previous measurement by Naraghi et al. [36]. After 30 years, the creep compliance of thin PAN nanofiber ($\sim 150 \text{ nm}$) is an order of magnitude smaller than that of thick PAN nanofiber ($\sim 260 \text{ nm}$). Using an Arrhenius equation for the horizontal shift factor below T_g , an activation energy for the creep process was estimated. The activation energy for 150 nm thin fiber, 152 kJ mol^{-1} , was 50

% higher than the 260 nm thick fiber and of similar magnitude as other polymers such as bulk PAN, PMMA, ABS and aramid fibers [27], [50], [54], [55]. The increase in activation energy and a decrease in creep compliance were attributed to the increased molecular orientation with diameter [12].

The jet instability causing whiplash motion leads to the increase in molecular orientation during electrospinning. The role of molecular orientation was further studied by randomizing PAN with high energy electron beam in SEM. The creep compliance of the electron – beam exposed fiber ($D=220$ nm) increased by a factor of 5 to 10 compared with the partially oriented fibers of similar size. This indicates how much the unoriented molecules created as a result of the damage, increase the creep compliance.

In addition to size-dependent elastic-plastic properties of PAN nanofiber, these findings show a size-dependent creep master curve. Thin PAN nanofiber (150 nm) have 50 % higher creep activation energy than thick fiber (260 nm) and exhibit an order of magnitude smaller creep compliance after 30 years. This reduction in creep compliance with size is attributed to the molecular orientation due to jet instability during electrospinning. Removing the orientation by exposing the fiber to SEM increased the creep compliance by 5-10 times.

7.6 Chapter references:

- [1] M. Naraghi, I. Chasiotis, H. Kahn, Y. Wen, and Y. Dzenis, “Novel method for mechanical characterization of polymeric nanofibers,” *Cit. Rev. Sci. Instruments*, vol. 78, p. 85108, 2007.
- [2] P. Li, L. Hu, A. J. H. McGaughey, and S. Shen, “Crystalline polyethylene nanofibers with the theoretical limit of Young’s modulus,” *Adv. Mater.*, vol. 26, no. 7, pp. 1065–1070, 2014.

- [3] R. Shrestha, P. Li, B. Chatterjee, T. Zheng, X. Wu, Z. Liu, T. Luo, S. Choi, K. Hippalgaonkar, M. P. de Boer, and S. Shen, “Crystalline polymer nanofibers with ultra-high strength and thermal conductivity,” *Nat. Commun.*, vol. 9, no. 1, p. 1664, 2018.
- [4] S. Shen, A. Henry, J. Tong, R. Zheng, and G. Chen, “Polyethylene nanofibres with very high thermal conductivities,” *Nat. Nanotechnol.*, vol. 5, no. 4, pp. 251–255, 2010.
- [5] Z. Zhong, M. C. Wingert, J. Strzalka, H.-H. Wang, T. Sun, J. Wang, R. Chen, and Z. Jiang, “Structure-induced enhancement of thermal conductivities in electrospun polymer nanofibers,” *Nanoscale*, vol. 6, no. 14, p. 8283, 2014.
- [6] V. Singh, T. L. Bougher, A. Weathers, Y. Cai, K. Bi, M. T. Pettes, S. A. McMenamin, W. Lv, D. P. Resler, T. R. Gattuso, D. H. Altman, K. H. Sandhage, L. Shi, A. Henry, and B. A. Cola, “High thermal conductivity of chain-oriented amorphous polythiophene,” *Nat. Nanotechnol.*, vol. 9, no. 5, pp. 384–90, 2014.
- [7] S. Agarwal, J. H. Wendorff, and A. Greiner, “Progress in the Field of Electrospinning for Tissue Engineering Applications,” *Adv. Mater.*, vol. 21, no. 32–33, pp. 3343–3351, Sep. 2009.
- [8] I. S. Chronakis, “Novel nanocomposites and nanoceramics based on polymer nanofibers using electrospinning process—A review,” *J. Mater. Process. Technol.*, vol. 167, no. 2, pp. 283–293, 2005.
- [9] Z.-M. Huang, Y. Z. Zhang, M. Kotaki, and S. Ramakrishna, “A review on polymer nanofibers by electrospinning and their applications in nanocomposites,” *Compos. Sci. Technol.*, vol. 63, no. 15, pp. 2223–2253, Nov. 2003.
- [10] J. Fang, H. Niu, T. Lin, and X. Wang, “Applications of electrospun nanofibers,” *Sci. Bull.*, vol. 53, no. 15, pp. 2265–2286, Aug. 2008.
- [11] M. Á. R. Calderón and W. Zhao, “Applications of Polymer Nanofibers in Bio-Materials, Biotechnology and Biomedicine: A Review,” in *TMS 2014: 143rd Annual Meeting & Exhibition*, Cham: Springer International Publishing, 2014, pp. 401–414.
- [12] M. Naraghi, S. N. Arshad, and I. Chasiotis, “Molecular orientation and mechanical property size effects in electrospun polyacrylonitrile nanofibers,” *Polymer (Guildf.)*, vol. 52, no. 7, pp. 1612–1618, 2011.
- [13] J. H. Park and G. C. Rutledge, “Ultrafine high performance polyethylene fibers,” *J. Mater. Sci.*, vol. 53, 2017.
- [14] M. Burman, A. Arinstein, and E. Zussman, “Free flight of an oscillated string pendulum as a tool for the mechanical characterization of an individual polymer nanofiber,” *Cit. Appl. Phys. Lett*, vol. 93, p. 193118, 2008.
- [15] S. Cuenot, S. Demoustier-Champagne, and B. Nysten, “Elastic Modulus of Polypyrrole Nanotubes,” 2000.

- [16] M. K. Shin, S. I. Kim, S. J. Kim, S.-K. Kim, H. Lee, and G. M. Spinks, "Size-dependent elastic modulus of single electroactive polymer nanofibers," *Appl. Phys. Lett.*, vol. 89, no. 23, p. 231929, Dec. 2006.
- [17] C. T. Lim, E. P. S. Tan, and S. Y. Ng, "Effects of crystalline morphology on the tensile properties of electrospun polymer nanofibers," *Cit. Appl. Phys. Lett*, vol. 92, p. 141908, 2008.
- [18] J. Yao, C. Bastiaansen, and T. Peijs, "High Strength and High Modulus Electrospun Nanofibers," *Fibers*, vol. 2, no. 2, pp. 158–186, Apr. 2014.
- [19] M. D. Shelby and G. L. Wilkes, "The effect of molecular orientation on the physical ageing of amorphous polymers—dilatometric and mechanical creep behaviour," *Polymer (Guildf)*, vol. 39, no. 26, pp. 6767–6779, Dec. 1998.
- [20] Z. Yang, Y. Fujii, F. K. Lee, C.-H. Lam, and O. K. C. Tsui, "Glass transition dynamics and surface layer mobility in unentangled polystyrene films.," *Science*, vol. 328, no. 5986, pp. 1676–9, Jun. 2010.
- [21] Y. Chai, T. Salez, J. D. McGraw, M. Benzaquen, K. Dalnoki-Veress, E. Raphaël, and J. A. Forrest, "A direct quantitative measure of surface mobility in a glassy polymer.," *Science*, vol. 343, no. 6174, pp. 994–9, Feb. 2014.
- [22] I. M. Ward and J. Sweeney, *Mechanical properties of solid polymers*. .
- [23] H. Higuchi, A. M. Jamieson, and R. Simha, "Free volume quantities and viscoelasticity of polymer glasses," *J. Polym. Sci. Part B Polym. Phys.*, vol. 34, no. 8, pp. 1423–1426, Jun. 1996.
- [24] M. L. Williams, R. F. Landel, and J. D. Ferry, "The Temperature Dependence of Relaxation Mechanisms in Amorphous Polymers and Other Glass-forming Liquids," *J. Am. Chem. Soc.*, vol. 77, no. 14, pp. 3701–3707, 1955.
- [25] P. A. O'connell and G. B. Mckenna, "Arrhenius-type temperature dependence of the segmental relaxation below T_g," *J. Chem. Phys.*, vol. 110, p. 11054, 1999.
- [26] A. V. Tobolsky and J. R. McLoughlin, "Elastoviscous properties of polyisobutylene. V. The transition region," *J. Polym. Sci.*, vol. 8, no. 5, pp. 543–553, May 1952.
- [27] E. V. Thompson, "Mechanical Properties of Cast Acrylonitrile Polymers. 1. Polyacrylonitrile," *Macromolecules*, vol. 13, no. 1, pp. 132–136, Jan. 1980.
- [28] N. Phan-Thien, "On the Time-Temperature Superposition Principle of Dilute Polymer Liquids," *J. Rheol. (N. Y. N. Y.)*, vol. 23, no. 4, pp. 451–456, Aug. 1979.
- [29] M. Tajvidi, R. H. Falk, and J. C. Hermanson, "Time-temperature superposition principle applied to a kenaf-fiber/high-density polyethylene composite," *J. Appl. Polym. Sci.*, vol. 97, no. 5, pp. 1995–2004, Sep. 2005.

- [30] P. A. O’Connell and G. B. McKenna, “Rheological Measurements of the Thermoviscoelastic Response of Ultrathin Polymer Films,” *Science*, vol. 307, no. 5716, pp. 1760–1763, Mar. 2005.
- [31] D. Papkov, Y. Zou, M. N. Andalib, A. Goponenko, S. Z. D. Cheng, and Y. A. Dzenis, “Simultaneously Strong and Tough Ultrafine Continuous Nanofibers,” 2013.
- [32] D. T. Grubb and G. W. Groves, “Rate of damage of polymer crystals in the electron microscope: Dependence on temperature and beam voltage,” *Phil. Mag.*, vol. 24, pp. 815–828, 1971.
- [33] L. Reimer and A. Schmidt, “The shrinkage of bulk polymers by radiation damage in an SEM,” *Scanning*, vol. 7, no. 1, pp. 47–53, 1985.
- [34] R. F. Egerton, P. Li, and M. Malac, “Radiation damage in the TEM and SEM,” *Micron*, vol. 35, no. 6, pp. 399–409, 2004.
- [35] M. C. Wingert, Z. Jiang, R. Chen, and S. Cai, “Strong size-dependent stress relaxation in electrospun polymer nanofibers.”
- [36] M. Naraghi, P. V. Kolluru, and I. Chasiotis, “Time and strain rate dependent mechanical behavior of individual polymeric nanofibers,” *J. Mech. Phys. Solids*, vol. 62, pp. 257–275, 2014.
- [37] M. Naraghi, I. Chasiotis, H. Kahn, Y. Wen, and Y. Dzenis, “Mechanical deformation and failure of electrospun polyacrylonitrile nanofibers as a function of strain rate,” *Appl. Phys. Lett.*, vol. 91, no. 15, p. 151901, Oct. 2007.
- [38] J. Cai, S. Chawla, and M. Naraghi, “Microstructural evolution and mechanics of hot-drawn CNT-reinforced polymeric nanofibers,” *Carbon N. Y.*, vol. 109, pp. 813–822, Nov. 2016.
- [39] M. P. deBoer, D. L. Luck, W. R. Ashurst, R. Maboudian, A. D. Corwin, J. A. Walraven, and J. M. Redmond, “High-Performance Surface-Micromachined Inchworm Actuator,” *J. Microelectromechanical Syst.*, vol. 13, no. 1, pp. 63–74, Feb. 2004.
- [40] J. J. Sniegowski and M. P. de Boer, “IC-Compatible Polysilicon Surface Micromachining,” *Annu. Rev. Mater. Sci.*, vol. 30, no. 1, pp. 299–333, Aug. 2000.
- [41] Sandia, “SUMMiT V □ Five Level Surface Micromachining Technology Design Manual,” vol. 3.2, 2012.
- [42] A. D. Corwin and M. P. de Boer, “Frictional Aging and Sliding Bifurcation in Monolayer-Coated Micromachines,” *J. Microelectromechanical Syst.*, vol. 18, no. 2, pp. 250–262, Apr. 2009.
- [43] E. Kontou, “Tensile Creep Behavior of Unidirectional Glass-Fiber Polymer Composites,” 2005.

- [44] R. J. Crowson and R. G. C. Arridge, "Linear viscoelastic properties of epoxy resin polymers in dilatation and shear in the glass transition region. 1. Time-temperature superposition of creep data," *Polymer (Guildf)*, vol. 20, pp. 737–746, 1979.
- [45] N. Grassie and R. McGuchan, "Pyrolysis of polyacrylonitrile and related polymers," *Eur. Polym. J.*, vol. 6, pp. 1277–1291, 1970.
- [46] O. Starkova and A. Aniskevich, "Limits of linear viscoelastic behavior of polymers," *Mech. Time-Dependent Mater.*, vol. 11, no. 2, pp. 111–126, Nov. 2007.
- [47] D. G. Fesko and N. W. Tschoegl, "Time-temperature superposition in thermorheologically complex materials," *J. Polym. Sci. Part C Polym. Symp.*, vol. 35, no. 1, pp. 51–69, Mar. 2007.
- [48] J. D. Ferry, *Viscoelastic properties of polymers*, 3rd ed. Wiley, 1980.
- [49] Q. Fu, Y. Jin, X. Song, J. Gao, X. Han, X. Jiang, Q. Zhao, and D. Yu, "Size-dependent mechanical properties of PVA nanofibers reduced via air plasma treatment," *Nanotechnology*, vol. 21, no. 9, p. 095703, Mar. 2010.
- [50] K. G. N. C. Alwis and C. J. Burgoyne, "Time-Temperature Superposition to Determine the Stress-Rupture of Aramid Fibres," *Appl Compos Mater*, vol. 13, pp. 249–264, 2006.
- [51] F.-C. Chang, F. Lam, and J. F. Kadla, "Application of time–temperature–stress superposition on creep of wood–plastic composites," *Mech. Time-Dependent Mater.*, vol. 17, no. 3, pp. 427–437, Aug. 2013.
- [52] F. Schwarzl and A. J. Staverman, "Time-Temperature Dependence of Linear Viscoelastic Behavior," *J. Appl. Phys.*, vol. 23, no. 8, p. 581, 1952.
- [53] A. D. Drozdov, "Effect of temperature on the viscoelastic and viscoplastic behavior of polypropylene," *Mech Time-Depend Mater*, vol. 14, pp. 411–434, 2010.
- [54] Y. Lin, Y. Shangguan, M. Zuo, E. Harkin-Jones, and Q. Zheng, "Effects of molecular entanglement on molecular dynamics and phase-separation kinetics of poly(methyl methacrylate)/poly(styrene-co-maleic anhydride) blends," *Polymer (Guildf)*, vol. 53, no. 6, pp. 1418–1427, Mar. 2012.
- [55] R. S. Moore and C. Gieniewski, "Interpretation of the tensile creep response of an ABS polymer," *Polym. Eng. Sci.*, vol. 9, no. 3, pp. 190–196, May 1969.
- [56] M. Naraghi, T. Ozkan, I. Chasiotis, S. S. Hazra, and M. P. de Boer, "MEMS platform for on-chip nanomechanical experiments with strong and highly ductile nanofibers," *J. Micromech. Microeng.*, vol. 20, no. 12, p. 125022, 2010.
- [57] J. Z. Yu, E. Korkmaz, M. I. Berg, P. R. LeDuc, and O. B. Ozdoganlar, "Biomimetic scaffolds with three-dimensional undulated microtopographies," *Biomaterials*, vol. 128, pp. 109–120, 2017.

Chapter 8: Summary and suggestions for future work

8.1 Summary

The objective of this thesis was to study the thermal, and mechanical properties of individual nanofibers and couple the properties with their molecular structure. In order to complete the research objective, a new technique to fabricate highly crystalline nanofibers and manipulate them within an optical framework were developed. This chapter summarizes the major findings of Chapters 3 through 7 and then suggests possible for future works.

A new technique was developed in Chapter 3 to fabricate highly crystalline and oriented polyethylene nanofiber (PENF) with a diameter in the range of 10 – 100 nm. The molecular orientation of the backbone chain was studied using Micro-Raman which indicated qualitatively that the molecular orientation increases from powder to microfiber and then nanofiber. The amorphous phase fraction was also significantly reduced. Selected area electron diffraction (SAED) patterns taken with a cryogenic transmission electron microscope (TEM) further verified that the polyethylene (PE) nanofibers were highly crystalline and assumed an orthorhombic lattice structure. A twinning on {310} plane and a small volume fraction of monoclinic phase was also observed. One of the main obstacles for mechanical and thermal experimentation with crystalline polymer nanofibers was their manipulation and mounting onto the test platforms. A new robust method for manipulating and mounting polymer nanofibers under an optical microscope was developed. In this method, a macrostructure (polymer nanofiber on bulk micro-machined silicon frame) is manipulated instead of the individual nanostructure. The techniques developed in Chapter 3 were utilized to successfully make specimens for thermal characterization as described in Chapters 4 and 5 and for strength measurement as in Chapter 6.

Thermal transport in PENF was studied in chapter 4. The thermal contact resistance of a PENF onto a suspended thermal device was found to be significant. A common approach to grip and minimize thermal contact resistance of 1D structures, namely focused ion beam-based Pt deposition, was found to amorphize PENF, which degraded the thermal conductivity. A capillary-induced Van der Waals contact method was developed, which minimized the contact resistance. The thermal measurement revealed a unique low dimensionality phonon physics for thermal transport in a crystalline PENF. The thermal conductivity increased with increasing temperature following an unusual $\sim T^1$ trend below 100 K and eventually peaked at 130–150 K, reaching a metal-like value of $90 \text{ W m}^{-1} \text{ K}^{-1}$, and then decayed as $1/T$. The linear increase in thermal conductivity at low temperature was attributed to extrinsic scattering mechanisms such as boundary and defects. This also means that the thermal conductivity trend is dependent on the heat capacity, which was attributed to the one-dimensionality of backbone chains due to strong C–C covalent bond along the chains that dominate over the van der Waals interactions in other directions. The $1/T$ trend was consistent with the trend of a crystalline dielectric material with a low defect density.

In Chapter 5, upon examining the thermal transport at high temperature, a phase transformation from the orthorhombic to the hexagonal phase was discovered, consistent with constrained PE microfibers. Consequently, a new fully reversible, high-contrast PE nanofiber thermal switch at $\sim 435 \text{ K}$ was demonstrated. An unprecedented thermal switching factor $f = 10$ was observed due to the orthorhombic to hexagonal structural phase transition, where the switching factor $f = G_{\text{on}}/G_{\text{off}}$ is defined as the ratio of on-state high thermal conductance G_{on} to the off-state low thermal conductance G_{off} . The phase transformation was found to be thermally stable and fully reversible. It was found that PE chains transition from a highly ordered *all-trans*

conformation in the orthorhombic phase to one with the rotational disorder, namely, a combined *trans* and *gauche* conformation during the phase transformation to hexagonal phase. This phase still has the long-range order of molecular chains but lacks the short-range conformation order of CH₂ units due to conformational rotations. The chain segmental rotations due to the relatively weak dihedral energy barrier introduces morphology disorder along the chains that can significantly interrupt phonon transport along the chains. Therefore, thermal conductance in the hexagonal phase decreased significantly. The hexagonal phase melting temperature was found to be ~470 K, much higher than that reported in PE microfiber (452 K). This was attributed to the constraint and stress on the specimen against melting, favoring low entropy in the oriented melt. On further heating the specimen, a degradation temperature of 557 K was found where the fiber thermally degraded and broke between the suspended pads.

In Chapter 5, by fabricating the heterogeneous amorphous-crystalline PENF, a high-performance solid-state nanoscale thermal diode with a rectification factor $R = 25\%$, comparable to existing solid-state nanoscale thermal diodes based on carbon nanotubes, boron nitride nanotubes, graphene and VO₂ nanobeams, was demonstrated. Thermal rectification demonstrates the amount of heat flux asymmetry when the thermal bias direction is reversed. Thermal rectification was found to be significantly smaller than predicted (~120 %) by a molecular dynamics simulation for an optimized amorphous length to crystalline length ratio in a heterogeneous system. The thermal contact resistance between an amorphized PENF and a suspended thermal device was found to be much higher (~6X) than that of a crystalline PENF, which changed the apparent amorphous to crystalline length ratio. The thermal contact ratio between an amorphous PE and a suspended pad was ~6 times larger than a crystalline PE and a suspended thermal device.

The strength of PENF, fabricated using the techniques developed in Chapter 3, was studied in Chapter 6. In tensile tests, the grip strength to a PE nanofiber using an adhesive was insufficient because of the low surface energy of PE (31 mJ m^{-2}), and slip occurred before they were tested to failure. A dog bone-shaped nanofiber was designed and fabricated to provide additional grip due to mechanical locking, enabling the tensile strength to be measured. An ultimate tensile strength (11.4 GPa) was obtained. This is one of the highest tensile strengths measured to date for a polymer or a polymer composite.

In Chapter 7, a variable stress-based creep measurement technique was developed to eliminate the necessity of the feedback to keep a creep stress constant. This was particularly important to measure the creep properties at an elevated temperature. From the temperature-dependent creep compliance curves, a master curve spanning 30 years was developed. A thin PAN nanofiber ($\sim 150 \text{ nm}$) is predicted to give rise to an order of magnitude less creep compared to a thick fiber ($\sim 250 \text{ nm}$) after 30 years at room temperature. The activation energy for creep process in thin PAN fiber was $\sim 152 \text{ kJ mol}^{-1}$, 50 % larger than the thick fiber. The reduction in creep compliance for the thin fiber was attributed to increased orientation within the core molecules. After removing the orientation of core PAN molecules by the exposure to high energy electron beam, higher creep compliance than that of the oriented specimens was obtained. This indicates the role of globally random molecules.

8.2 Future work suggestions

Some of the potential future work are suggested in this section.

8.2.1 Thermo-mechanical measurement of a PENF

It has been observed that highly oriented PE microfibers exhibit a negative coefficient of thermal expansion, which also depends on crystallinity and molecular orientation [1]–[4]. The thermal and mechanical testing techniques established in this thesis are uniquely suited for characterizing the negative coefficient of thermal expansion of individual PENFs.

An optical-metrology based thermo-mechanical measurement technique can be developed using the suspended microthermal device in Chapters 4 and 5 and sub-pixel pattern matching discussed in Chapter 6. The metal serpentine lines in the microthermal device allow for the high contrast image necessary for high-resolution pattern matching. The pattern matching can be used to acquire nanoscale displacement of the suspended platforms to detect a change in length of the supported PENF. The microthermal device can also be used to obtain the local temperature of the PENF. In addition, the highly compliant suspended beams are uniquely suited for zero stress dilatometry.

In addition to the coefficient of thermal expansion, this measurement technique can also be used to detect relaxation mechanisms in crystalline PENF which has been known to depend on the crystal thickness. Furthermore, this system is also suited to measure any phase transition temperature. During the phase transition, the separation gap between the suspended platforms changes significantly, which can be extracted from the images using the sub-pixel pattern matching.

8.2.2 Conducting polymer nanofiber

Recently, Zhang *et al.* [5] performed a large-scale molecular dynamics simulation to elucidate the fundamental link between molecular characteristics and possible thermal conductivity enhancement in polymers as well as thermal stability. They noted that due to the overlap of the *p*-orbitals in π -conjugated polymers such as polyaniline (PA), polythiophene (PT), poly(*p*-phenylene) (PPP) among others, such polymers have higher thermal conductivities compared to a linear polymer such as PE. In addition, they also exhibit good thermal stability. Conducting polymers such as polythiophene also exhibit an orthorhombic to a hexagonal lattice transformation. The fabrication technique established in this thesis is suited to produce a highly crystalline backbone molecule oriented by the high strain rate drawing. Including thermal conductivity, the high crystallinity achieved due to drawing can also increase electrical conductivity. The thermal and electrical multifunctionality with intrinsic chemical resistance and biocompatibility in a polymer nanofiber open applications such as sensing for biomedical application.

8.3 Chapter references:

- [1] J. A. O. Bruno, N. L. Allan, T. H. K. Barron, and A. D. Turner, "Thermal expansion of polymers: Mechanisms in orthorhombic polyethylene," *Phys. Rev. B.*, vol. 58, no. 13, pp. 8416–8427, 1998.
- [2] B. H. Kim and R. De Batist, "Negative coefficient of thermal expansion in polyethylene," *J. Polym. Sci. Polym. Lett. Ed.*, vol. 11, no. 2, pp. 121–122, Feb. 1973.
- [3] C. L. Choy, F. C. Chen, and K. Young, "Negative thermal expansion in oriented crystalline polymers," *J. Polym. Sci. Polym. Phys. Ed.*, vol. 19, no. 2, pp. 335–352, Feb. 1981.
- [4] R. H. Baughman, "Negative thermal expansion in crystalline linear polymers," *J. Chem. Phys.*, vol. 58, no. 7, p. 2976, Aug. 1973.

- [5] T. Zhang, X. Wu, and T. Luo, "Polymer Nanofibers with Outstanding Thermal Conductivity and Thermal Stability: Fundamental Linkage between Molecular Characteristics and Macroscopic Thermal Properties," *J. Phys. Chem. C*, vol. 118, no. 36, pp. 21148–21159, Sep. 2014.

Appendix

A. Sample collector fabrication

The Sample collector was fabricated using a microfabrication process, as shown in Fig. A.1. The selectivity of a traditional oxide mask for silicon etching is insufficient for a through etch. 4" (100) silicon wafers coated with 300 nm LPCVD silicon nitride (SiN) on both sides were purchased from WRS materials. First, HMDS vapor was primed on the SiN surface at 150 °C for 5 minutes as an adhesion promoter. Then, AZ 4210 photoresist was spin-coated followed by a soft bake at 95 °C for 1 minute. Spin coating was done at 4000 rpm resulting in 2.1 μm thick photoresist on the wafer. The photoresist was patterned using a Karl Suss MA6 aligner. The aligner exposes the photoresist with the ultra-violet light of wavelength 320 nm at 5 mW/cm² for 80 seconds. The exposed photoresist is then developed by immersing the wafer in a developer (a mixture of AZ 400K and DI water at 1:4) for 120 seconds. After developing, the wafer is cleaned in deionized (DI) water and blow dried using nitrogen.

The pattern on photoresist was transferred onto SiN by using reactive ion etching (RIE) using a Plasma-therm 790 RIE system. The wafer sample was placed in a vacuum chamber with a bias voltage of 315 volts. A mixture of reactive gases, tetrafluoromethane (CF₄) and oxygen (O₂), filled the chamber at flow rates of 19.5 sccm and 0.5 sccm, respectively, at a total pressure of 35 mT. An RF power of 60 watts was applied to induce plasma. The fluorine in CF₄ reacts with the silicon in silicon nitride forming silicon tetrafluoride (SiF₄) gas. Carbon can form polymer deposit onto the surface reducing the etch rate. So, the fluorine/carbon ratio determines the SiN etch rate. A higher ratio provides a higher etch rate. Oxygen can react with the carbon forming volatile gas increasing the fluorine to carbon ratio and thus increase the reaction rate. However, it also etches

the photoresist, so care should be taken. We obtained an average etch rate of 26 nm/min with decreasing etch rate because of polymer deposit. The total etching duration was 12.5 minutes to ensure all silicon nitride had been etched. After 6 minutes of etch time, the etching was stopped and argon gas was used to purge the chamber for 2 minutes at 200 mT. This process was done to get rid of any polymer deposit on the surface that could hinder the SiN etching. After complete etching, oxygen plasma was introduced in the chamber for 5 minutes at 50 mT and 100W to get rid of the photoresist and any polymer formed on the etched surface. The chamber was once again purged using Argon gas at 200 mT for 2 minutes. The wafer samples were cleaned using acetone, isopropanol alcohol and DI water, respectively. Silicon wafer with patterned SiN was then through etched using KOH.

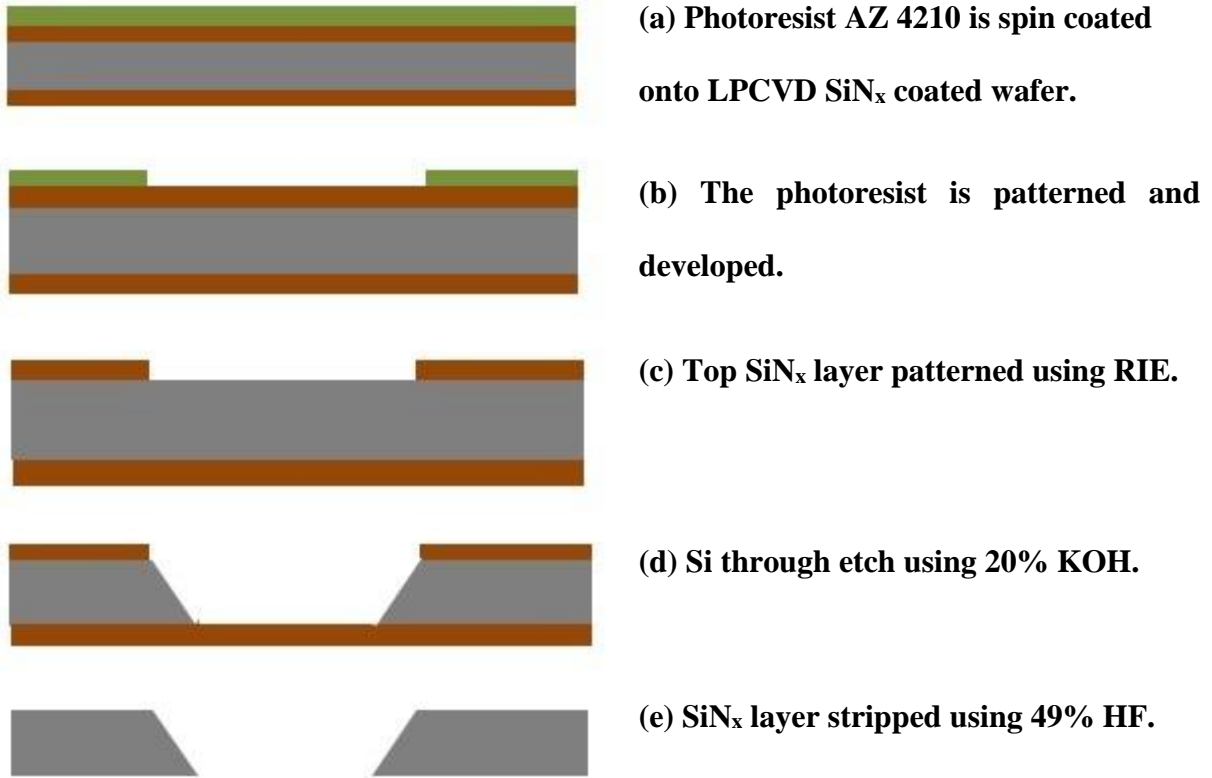


Figure A.1: Micro fabrication processes of the sample collector.

KOH etching of silicon depends on the crystal orientation of silicon, solution concentration and temperature. KOH pellets were mixed with DI water to obtain 20% solution, an optimum KOH concentration for (100) Si etch [1]. The solution was heated to 80 °C and the wafer was placed in the sample. The hydrogen bubbles were seen as soon as the sample was placed in the solution. The solution on glassware was covered with an aluminum thin film to reduce the evaporation loss of water. It significantly reduced the KOH concentration increase of the solution by condensing the vapor back into the solution. However, aluminum thin film reacted with the vapor and some holes were apparent in the cover film. The etch duration was 7 hrs with an average etch rate of 78.5 μm/hr. It is lesser than an etch rate for 20% KOH at 80 °C [1]. Water evaporation increases the

concentration of KOH and thereby decreases the average etching rate. Etching stops at the end of SiN_x layer. KOH etching is an anisotropic etch with (111) plane etching slower than (110) and (100) resulting in a characteristic pyramid like structure with 54.7° [1]. At the end of KOH etch, we obtained square holes with the slanted wall (54.7°). The sample was rinsed in DI water several times before HF etching of the SiN_x mask.

The SiN_x mask layer was removed using 49% hydrofluoric acid (HF). It was etched for 15 minutes for complete removal of SiN_x. The wafer was then diced into individual sample collector.

B. Microheater

The microheater is a sharply bent tungsten wire locally etched at the tip to 5 – 10 μm. It is joule-heated to a temperature exceeding 500 °C locally at the tip. It is used to fabricate a nanofiber sample by local heating a pre-tensile stressed fiber and also later to cut the fiber by local melting to limit within the testing device. The steps used to make it are described next.

B.1 Microheater fabrication

The microheater was fabricated from a 50 μm tungsten wire purchased from ESPI metals. A sharp edge was bent and adhered on a glass slide. The protruding bent edge was submerged on a beaker with 30% H₂O₂ solution at room temperature with magnetic stirrer. The wire was etched until the final diameter at the tip reached 5 – 10 μm as shown in Fig. B.1a. The ends of the wire were attached with copper tape for electrical attachment. Fig. B.1b shows a fabricated microheater.

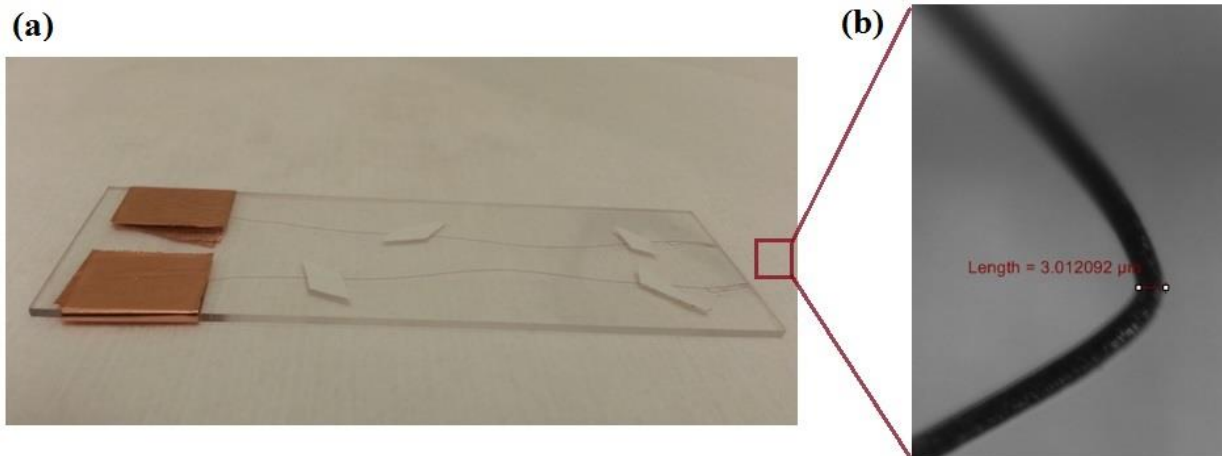


Figure B.1: Microheater used for local heat stretching and cutting PE fiber. a) microheater b) tungsten tip of microheater with diameter $\sim 3\mu\text{m}$.

Chapter references:

- [1] H. Seidel, L. Csepregi, A. Heuberger, and H. Baumgärtel, “Anisotropic Etching of Crystalline Silicon in Alkaline Solutions,” *J. Electrochem. Soc.*, vol. 137, no. 11, p. 3612, 1990.